

A Tale of two Higgs: Search for pair
production of Higgs bosons in the $b\bar{b}b\bar{b}$
final state using proton–proton collisions at
 $\sqrt{s} = 13$ TeV with the ATLAS detector

A DISSERTATION PRESENTED

BY

BAOJIA TONG

TO

THE DEPARTMENT OF PHYSICS

IN PARTIAL FULFILLMENT OF THE REQUIREMENTS

FOR THE DEGREE OF

DOCTOR OF PHILOSOPHY

IN THE SUBJECT OF

PHYSICS

HARVARD UNIVERSITY
CAMBRIDGE, MASSACHUSETTS

MAY 2018

©2017-2018 – BAOJIA TONG
ALL RIGHTS RESERVED.

A Tale of two Higgs: Search for pair production of Higgs bosons in the $b\bar{b}b\bar{b}$ final state using proton–proton collisions at $\sqrt{s} = 13$ TeV with the ATLAS detector

ABSTRACT

This thesis presents a search for Higgs boson pair production, with the $b\bar{b}b\bar{b}$ final state. This search uses the full 2015 and 2016 data collected by the ATLAS Collaboration at $\sqrt{s} = 13$ TeV, corresponding to $3.2 \pm 0.2 \text{ fb}^{-1}$ of 2015 and $32.9 \pm 1.1 \text{ fb}^{-1}$ of 2016 pp collision data. Improvements with respect to the previous analysis come from the increased dataset, detailed background estimation and additional signal regions. Search sensitivity is specially enhanced for the resonance signals between 2500 GeV and 3000 GeV. The data is found to be compatible with the Standard Model predictions, and no signs of new physics have been observed. The results are interpreted in the context of the bulk Randall-Sundrum warped extra dimension model with a Kaluza-Klein graviton $k/\bar{M}_{\text{Pl}} = 1.0$ or 2.0 decaying to hh , and the Type 2 two-Higgs doublet model (2HDM) where the neutral heavy CP-even H scalar decays to hh .

Contents

o INTRODUCTION	I
1 THEORY AND MOTIVATION	4
1.1 The Standard Model and the Higgs Boson	4
1.2 Standard Model di-Higgs production	6
1.3 Beyond the Standard Model physics di-Higgs production	8
1.4 Di-Higgs decay and LHC previous search results	12
1.5 Resolved and Boosted	14
2 LHC AND ATLAS	16
2.1 The Large Hadron Collider	17
2.2 A Toroidal LHC ApparatuS	20
3 RECONSTRUCTION AND OBJECTS	25
3.1 ID Tracks and Vertices	26
3.2 Jets	27
3.3 Flavor Tagging	32
3.4 Leptons	35
4 DATA AND SIMULATION	37
4.1 Data	37
4.2 MC	39
4.3 Signal	40
5 EVENT SELECTION	42
5.1 Data Cleaning	42
5.2 Trigger	44
5.3 Object Selection	45
5.4 Resolved Veto	50
5.5 2D Higgs Mass Cut	53

5.6	Number of b -tagging requirement	54
5.7	Signal efficiency and cutflow	56
6	BACKGROUND ESTIMATION	59
6.1	Overview	59
6.2	Definition of the sideband and control regions	61
6.3	QCD multi-jets	64
6.4	$t\bar{t}$	65
6.5	Fitting procedure for QCD and $t\bar{t}$ normalization	66
6.6	QCD reweighting	69
6.7	m_{2J} in the sideband region	73
6.8	m_{2J} in the control region	74
6.9	m_{2J} rescale and smoothing in the signal region	75
6.10	Yields	76
7	SYSTEMATICS	81
7.1	Overview	81
7.2	Theoretical uncertainties	82
7.3	Uncertainties on detector and reconstruction	84
7.4	Uncertainty on $t\bar{t}$ generator	86
7.5	Uncertainty on μ_{qcd} estimation	87
7.6	Validation in low mass and high mass signal region	90
7.7	Uncertainty on the shape of $t\bar{t} m_{2J}$ in the $4/3b$ signal region	95
7.8	Uncertainty on the shape of the QCD distribution in the signal region	95
7.9	Uncertainty on smoothing function in the signal region	96
7.10	Summary of systematics	99
8	RESULT	103
8.1	Boosted signal region	103
8.2	Resolved signal region	106
8.3	Statistical analysis	107
8.4	Boosted and resolved combined limits	112
9	CONCLUSION	115
APPENDIX A	BOOSTED SIDEBAND REGION KINEMATIC DISTRIBUTIONS	117

APPENDIX B BOOSTED CONTROL REGION KINEMATIC DISTRIBUTIONS	130
APPENDIX C BOOSTED SINGAL REGION KINEMATIC DISTRIBUTIONS	143
APPENDIX D CONSTANT μ_{qcd} VALIDATION	158
APPENDIX E REWEIGHTING DETAILS	165
APPENDIX F EFFECTS ON YIELD PREDICTION FROM VARIATIONS OF THE SIDEBAND AND CONTROL REGIONS	179
REFERENCES	201

Listing of figures

1.1	Fermions and bosons of the Standard Model and their properties ¹ , where all the values are measured experimentally.	5
1.2	Leading order Feynman diagrams contributing to di-Higgs production via gluon-gluon fusion, through the Higgs-fermion Yukawa interactions 1.2a and the Higgs boson self-coupling 1.2b. Only Figure 1.2b probes λ_{hhh}	6
1.3	Leading order Feynman diagrams contributing to Higgs pair production via VBF.	7
1.4	Total cross sections (y-axis) at the NLO in QCD for the six largest di-Higgs production channels at pp colliders at different energy (x-axis). Gluon-gluon fusion, VBF, top-pair, W^\pm, Z and single-top associated di-Higgs productions are shown. The thickness of the lines corresponds to the uncertainties added linearly. H refers to the SM Higgs.	7
1.5	BSM Higgs boson pair production: non-resonant production proceeds through changes in the SM Higgs couplings in 1.5a and 1.5b, resonant production proceeds through 1.5c an intermediate resonance, X. H and b both refers to the SM Higgs.	9
1.6	Total cross sections (y-axis) at the LO and NLO in QCD for di-Higgs production channels, at the $\sqrt{s} = 14$ TeV LHC as a function of the self-interaction coupling λ (x-axis) . The dashed (solid) lines and light- (dark-) color bands correspond to the LO (NLO) results and to the scale and PDF uncertainties added linearly. The SM values of the cross sections are obtained at $\frac{\lambda}{\lambda_{SM}} = 1$, indicated by the red vertical line. H refers to the SM Higgs.	9
1.7	Parton luminosity ratios as a function of resonance mass M_X for $13/8$ TeV ² . 1, 2, and 3 TeV M_X ratios are indicated by red lines. For a 2 TeV X , the luminosity ratio is almost 10.	11
1.8	Summary of di-Higgs final states and their ratios. Top left, $b\bar{b}b\bar{b}$, has the largest branching ratio.	12

1.9	The observed and expected 95% CL upper limits of $\sigma(gg \rightarrow H) \times BR(H \rightarrow bb)$ at $\sqrt{s} = 8\text{TeV}$ as functions of the heavy Higgs boson mass m_H , combining resonant searches in Higgs boson pair to $b\bar{b}\tau^+\tau^-$, $W^+W^-\gamma\gamma$, $b\bar{b}\gamma\gamma$, and $b\bar{b}b\bar{b}$ final states. The expected limits from individual searches are also shown. The green and yellow bands represent $\pm 1\sigma$ and $\pm 2\sigma$ uncertainty ranges of the expected combined limits. The improvement above $m_H = 500\text{ GeV}$ reflects the sensitivity of the $b\bar{b}b\bar{b}$ analysis. The results beyond 1TeV are only from the $b\bar{b}b\bar{b}$ final state alone.	13
1.10	Cartoon for $X \rightarrow hh \rightarrow b\bar{b}b\bar{b}$, with resolved event topology (left) and boosted event topology (right).	14
2.1	A schematic view of the LHC ring ³ . LINAC ₂ , Booster, PS, SPS, and LHC accelerate the protons in order. Four main experiments are located at interaction points along the ring. ATLAS and CMS are general purpose experiments, while ALICE focuses on heavy ion collisions and LHC _b is dedicated to B physics.	17
2.2	The luminosity-weighted distribution of the mean number of interactions per crossing for the 2015 and 2016 $p\bar{p}$ collision data at 13 TeV centre-of-mass energy. ⁴	19
2.3	A detailed computer-generated image of the ATLAS detector and its systems.	20
2.4	Geometry of IBL, PIXEL and SCT detectors in Run2.	22
2.5	The overall layout of the ATLAS Muon Spectrometer.	22
2.6	Cumulative luminosity vs. time delivered to (green) and recorded by ATLAS (yellow) during stable beams for $p\bar{p}$ collisions at 13 TeV centre-of-mass energy.	24
3.1	Illustration of particle interactions in ATLAS.	26
3.2	Two collision events recorded in June 2015 with a high leading jet p_T shown in rapidity-azimuthal angle parameter space. The dots are calorimeter-cell clusters with positive energy. Only the two leading jets are shown, with their area demarcated by a colored circle, and with grey regions denoting the corresponding k_t sub-jets of size $R_{sub} = 0.2$. The colour of both jets and clusters corresponds to their p_T	28
3.3	For the trimming algorithm using calorimeter cell clusters as inputs to the anti- k_t jet reconstruction algorithm with $R = 1.0$, a comparison of the jet mass distribution for QCD background jets and W boson jets low p_T and high p_T kinematic regions, as determined by the untrimmed truth jet p_T . The trimming parameter choices shown here are $R_{sub} = 0.1, 0.2$, and 0.3 for a fixed cut at 5%.	29

3.4	Uncalibrated (dashed line) and calibrated (solid line) reconstructed jet mass distribution 3.4a, and the jet mass resolution vs jet p_T 3.4b for calorimeter-based jet mass, m_{calo} (red), track-assisted jet mass m_{TA} (black) and the invariant mass of four-vector sum of tracks associated to the large-radius calorimeter jet m_{track} (blue) for W/Z-jets ⁵	30
3.5	Secondary vertex reconstruction rate and MV_{2c10} output for b-jets (solid blue), c-jets (dashed green) and light-jets (dotted red) evaluated with simulated $t\bar{t}$ events.	33
3.6	b -jet efficiency for the fixed cut working point with a b -jet efficiency of 77% as a function of the jet p_T for the comparison between the MV_{2c10} b -tagging algorithm employed for the 2016 analyses (2016 config) and the previous version of the tagger, MV_{2c20} (2015 config), which has 15% c -fraction in the training	34
3.7	Light-flavour jet and c -jet rejection as a function of jet p_T for the previous (2015 config) MV_{2c20} and the current MV_{2c10} configuration (2016 config). A fixed cut at 77% b -jet efficiency operating point is used ⁶	35
5.1	2015 ATLAS boosted di-Higgs event candidate's event display. The data is taken in run 282712, lumiblock 503 and has event number 595661746. ID is in gray, ECAL is in green, HCAL is in red and MS is in blue. Only tracks with $p_T > 25$ GeV are shown. Jets are gray cones, and ID tracks are colored lines in the ID. There are 2 b tagged tracks within in each of the large- R jets. The one large- R jet has 119 GeV mass and 543 GeV p_T , and the other one has 127 GeV mass and 413 GeV p_T . The ΔR between the two large- R jet is 3.54 and the invariant mass of the two large- R jets is 1336 GeV.	43
5.2	Different trigger efficiencies as a function of the signal resonance mass with respect to all events with no selection (left) and with respect to events passing the two large- R jets $p_T > 400$ GeV and leading/subleading jet $p_T > 250$ GeV (right). For 1.4 TeV signal, the trigger efficiency is about 98%.	44
5.3	Large- R jet trigger efficiencies, defined as the fraction of events fired trigger with a given highest large- R jet p_T , measured in 2015 Data (<code>HLT_j360_a10_lcw</code> , left) and 2016 Data (<code>HLT_j420_a10_lcw</code> , right) and MC.	45
5.4	Percentages of truth Higgs to large- R jet $\Delta R < 1.0$ matching as a function of G_{KK}^* mass. Both Higgs almost never match to the same large- R jet.	46
5.5	Normalized ΔR between the truth Higgs (leading on left, subleading on right) and the truth children b -quarks for G_{KK}^* MCs. Lines are drawn at $\Delta R = 0.4$ (R of small- R jets) and $\Delta R = 1.0$ (R of large- R jets).	47

§.6	Percentage of $\Delta R < 0.2$ matching truth b 's to track jets (leading Higgs on the left, sub-leading Higgs on the right) for different G_{KK}^* mass. The cases listed in the legend are orthogonal to each other. The cases not listed on the legend (including when a truth b is not contained in the large- R jet) happen in total at most 1.6% of the time for a given G_{KK}^* mass.	48
§.7	Kinematics of 1 TeV G_{KK}^* before and after muon-in-jet corrections. The reconstructed Higgs masses (top row, left for leading large- R jet, right for subleading large- R jet) are closer to 125 GeV after the correction, which improves the signal efficiency for the signal region selection by $\sim 10\%$ (bottom row, left for m_{JJ} , right for event distribution differences on the leading-subleading large- R jet mass plane.).	49
§.8	After large- R jet requirements, normalized $\Delta\eta_{JJ}$ distribution in 1.5 TeV G_{KK}^* and data, where the data consists of mostly multijet events ($> 90\%$). The background multijet event is flatter in $\Delta\eta_{JJ}$ distribution.	50
§.9	Event display of the same event using §.9a resolved and §.9b boosted topologies. The resolved reconstruction gives a m_{4J} of 873 GeV, and the boosted reconstruction gives m_{2J} of 852 GeV.	51
§.10	For RSG $c = 1.0$ samples, number of events as a function of leading Higgs candidate mass and subleading Higgs candidate mass, for 1.2 TeV (left) signal and 2 TeV (right) signal samples. The red dotted line in the center correspond to the signal region, passing $X_{bb} < 1.6$.	53
§.11	Signal fraction in different b -tag categories (left) and detailed fraction in different number of track jet and b -tag categories (right) as a function of signal resonance mass hypothesis for selection cuts. The efficiencies are relative to the total number of events passing the 2D mass cut.	56
§.12	Absolute (left) and relative (right) signal efficiency as a function of RSG $c=1.0$ signal resonance mass hypothesis for selection cuts. The relative efficiency is defined from the previous cut, where the order of cuts is given by the legend. PassTrig means the event passes the trigger selection; PassDiJetPt means the event passes the leading and sub-leading jet p_T cuts; PassDiJetEta means the event passes the leading and sub-leading jet η cuts; Pass-DeltaH means the events passes the $ \Delta\eta < 1.7$ cut; PassBJetSkim means the event contains at least two b -tagged track jets, inclusive of 2 b , 2 bs , 3 b and 4 b configurations; PassSignal means the event passes the signal region cut $X_{bb} < 1.6$.	57

6.1	The m_J^{lead} vs m_J^{subl} distribution of the $2bs$ data. The signal region is the area surrounded by the inner (red) dashed contour line, centered on ($m_J^{\text{lead}}=124$ GeV, $m_J^{\text{subl}}=115$ GeV). The control region is the area between the signal region and the intermediate (orange) contour line. The sideband region is the area between the control region and the outer (yellow) contour line.	62
6.2	Detailed signal efficiency in different signal/control/sideband regions as in n -tag regions and inclusive b-tagged regions, which include $2b$, $1b$ and ob as well, (bottom right) as a function of G_{KK}^* resonance mass for selection cuts. The efficiencies are relative to the total number of events in the preselection.	63
6.3	Normalized of $2bs$, $3b$, and $4b\bar{t}\bar{t}$ MC m_{2J} distribution in the signal region. The uncertainties are statistical.	66
6.4	Simultaneous fit of μ_{qcd} and $\alpha_{\bar{t}\bar{t}}$ in $4b$ (top) and $3b$ (middle) and $2bs$ (bottom) sideband region using leading large- R jet mass.	68
6.5	Comparison of different track jet p_T distributions. The top row is for leading Higgs candidate, and the bottom row is for subleading Higgs candidate. The left column is for the leading track jet of the Higgs candidate, and the right column is for the subleading track jet of the Higgs candidate. Shown in the plot are data distributions, inclusive of SB, CR, and SR regions for ob and $1b$, while for $2bs$ only the SB region is shown. At the bottom ratio plot, all the ratio are taken with respect to the ob tagged distribution.	70
6.6	The m_{2J} distributions in the sideband region of the boosted analysis for the data and the predicted background for (top left) the four-tag, (top right) the three-tag, and (bottom) the two-tag split samples. The data-to-background ratio (bottom panels) shows the statistical uncertainties as the grey hatched band.	73
6.7	The m_{2J} distributions in the control region of the boosted analysis for the data and the predicted background for (top left) the four-tag, (top right) the three-tag, and (bottom) the two-tag split samples. The data-to-background ratio (bottom panels) shows the statistical uncertainties as the gray hatched band.	74
6.8	Normalized scaled m_{2J} distributions for the $4b$ (left), $3b$ (middle), and $2bs$ (right) signal regions. For comparison, the unscaled m_{2J} distributions are shown on the same plot.	
	75

6.9	Fits for scaled background smoothing are shown for QCD (left column) and $t\bar{t}$ (right column) in the $4b$ (top), $3b$ (middle), and $2bs$ (bottom) signal region. The left figures show the distributions with linear y -axis scale along with the fit central value and variations. The right figures show the distributions with log y -axis scale along with the fit central value and the fit variations as determined by the varying the fit parameters within uncertainties whilst taking into account parameter correlations.	77
6.10	Background prediction for $4b$ (top), $3b$ (middle), and $2bs$ (bottom) signal region using scaled di-jet mass before (left) and after smoothing (right). The uncertainty band includes only fit statistical uncertainties.	78
7.1	Impact of efficiency scale factor w_{sf} and inefficiency scale factor w_{sf}^{anti} on 2 TeV G_{KK}^* with $c = 1.0$. $4b$ signal region (left), $3b$ signal region (middle), and $2bs$ signal region are shown.	86
7.2	Total background estimation ($qcd + t\bar{t}$) with different $t\bar{t}MC$ variations. The different variations agree with the default within the statistical uncertainties.	87
7.3	Illustration of ZZ (left) and TT (right) signal region as shown in the orange shaded region. Control region shown in green, and sideband region in blue. The white circle in the middle is the real signal region, and it is blinded.	90
7.4	ZZ signal region distribution of m_{2J} (left column) and leading large-R jet mass (right column) in low mass signal, for $4b$ (top row), $3b$ (middle row) and $2b$ split (bottom row). The plots are with only statistical uncertainty.	92
7.5	TT signal region distribution of m_{2J} (left column) and leading large-R jet mass (right column) in low mass signal, for $4b$ (top row), $3b$ (middle row) and $2b$ split (bottom row). The plots are with only statistical uncertainty.	93
7.6	The shape of $t\bar{t}$ m_{2J} in the sideband region, comparing the $3b$ shape with that of the $2bs$, in order to asses the systematic effect of additional b -tags changing the dijet mass distribution. The m_{jj} distributions is shown on the left, and the ratio of $3b$ to $2bs$ distributions on the right.	95
7.7	Dijet mass distribution in the CR along with the prediction (left) and the ratio of the prediction to the CR distribution (right) for the $2bs$ (top) $3b$ (middle) and $4b$ (bottom) samples. Ratios are from the smoothed distributions, the data uncertainty band contains the smoothing parameter variations, and the prediction uncertainty band also contains smoothing parameter variations.	97

7.8	Dijet mass distribution SR prediction fit with several fit ranges (left) and the ratio of nominal to fits with different fit ranges (right) for the $2bs$ (top) $3b$ (middle) and $4b$ (bottom) samples.	98
7.9	Dijet mass distribution SR prediction fit with several fit functions (left) and the ratio of nominal to fits with different fit functions (right) for the $2b$ (top) $3b$ (middle) and $4b$ (bottom) samples. The additional fit functions are from Table 7.6.	100
7.10	Impact of each systematic on the signal prediction as a function of the signal mass, in the $4b$ (left) and $3b$ (middle) and $2bs$ signal regions.	101
8.1	Unscaled m_{2J} distribution in the $4b$ Signal Region after unblinding. The left plot is on linear scale and the right plot is on log scale.	104
8.2	Unscaled m_{2J} distribution in the $3b$ Signal Region after unblinding. The left plot is on linear scale and the right plot is on log scale.	104
8.3	Unscaled m_{2J} distribution in the $2bs$ Signal Region after unblinding. The left plot is on linear scale and the right plot is on log scale.	105
8.4	Scaled m_{2J} distribution in the $4b$ Signal Region after unblinding. The left plot is on linear scale and the right plot is on log scale.	105
8.5	Scaled m_{2J} distribution in the $3b$ Signal Region after unblinding. The left plot is on linear scale and the right plot is on log scale.	105
8.6	Scaled m_{2J} distribution in the $2bs$ Signal Region after unblinding. The left plot is on linear scale and the right plot is on log scale.	106
8.7	Distributions of m_{4j} in the signal region of the resolved analysis for (a) 2015 data and (b) 2016 data, compared to the predicted backgrounds. The hatched bands shown in the bottom panels represent the combined statistical and systematic uncertainties in the total background estimates. The expected signal distributions of G_{KK}^* resonances with masses of 800 and 1200 GeV, the 280 GeV scalar sample and SM non-resonant di-Higgs production ($\times 100$) are also shown. The scalar sample is normalized to a cross section times branching ratio of 2.7 pb.	107
8.8	Local p_0 of the (a) scalar, (b) $c=1$ Graviton and (c) $c=2$ Graviton.	109
8.9	The impact of nuisance parameters on the fitted cross section, ranked by their post-fit impact. The signal mass used in this fits is 2000 GeV, and the signal model is (a) narrow scalar, (b) G_{KK}^* with $c = 1$ and (c) G_{KK}^* with $c = 2$	110
8.10	Post-fit signal region scaled m_{2J} distributions after fitting the data with the 2 TeV G_{KK}^* with $c = 1.0$ hypothesis. The signal strength is slightly positive.	110

8.11	The expected and observed 95% C.L. upper exclusion limits for the boosted $4b$ analysis calculated including all systematic uncertainties for the narrow scalar model (top), $G_{KK}^*c = 1.0$ (middle), and $G_{KK}^*c = 2.0$ (bottom). The dot-dashed line shows the expected limit when only statistical uncertainties are included. The limits are derived within the asymptotic approximation.	III
8.12	The expected and observed 95% C.L. upper exclusion limits for the boosted $4b$ analysis calculated including all systematic uncertainties for the narrow scalar model. The dot-dashed line shows the expected limit when only statistical uncertainties are included. The limits are derived within the asymptotic approximation.	II3
8.13	The expected and observed 95% C.L. upper exclusion limits for the boosted $4b$ analysis calculated including all systematic uncertainties for the $c=1.0$ Graviton. The dot-dashed line shows the expected limit when only statistical uncertainties are included. The limits are derived within the asymptotic approximation.	II4
8.14	The expected and observed 95% C.L. upper exclusion limits for the boosted $4b$ analysis calculated including all systematic uncertainties for the $c=2.0$ Graviton. The dot-dashed line shows the expected limit when only statistical uncertainties are included. The limits are derived within the asymptotic approximation.	II4
A.1	Kinematics (p_T , mass, η , ϕ) of the lead large- R jet in data and prediction in the sideband region after requiring $4 b$ -tags.	II8
A.2	Kinematics (p_T , mass, η , ϕ) of the subleading large- R jet in data and prediction in the sideband region after requiring $4 b$ -tags.	II9
A.3	First two rows show the p_T of the lead (left) and sub-lead (right) small- R track jets associated to the lead (first-row) and sub-lead (second-row) large- R jet in data and prediction in the sideband region after requiring $4 b$ -tags. Third row shows the ΔR between two leading small- R track-jets associated to the leading (left) and sub-leading (right) large- R jet.	I20
A.4	Kinematics (invariant mass, ΔR , $\Delta\eta$ and $\Delta\phi$) of two large- R jets in data and prediction in the sideband region after requiring $4 b$ -tags.	I21
A.5	Kinematics (p_T , mass, η , ϕ) of the lead large- R jet in data and prediction in the sideband region after requiring $3 b$ -tags.	I22
A.6	Kinematics (p_T , mass, η , ϕ) of the subleading large- R jet in data and prediction in the sideband region after requiring $3 b$ -tags.	I23

A.7	First two rows show the p_T of the lead (left) and sub-lead (right) small- R track jets associated to the lead (first-row) and sub-lead (second-row) large- R jet in data and prediction in the sideband region after requiring 3 b -tags. Third row shows the ΔR between two leading small- R track-jets associated to the leading (left) and sub-leading (right) large- R jet.	124
A.8	Kinematics (invariant mass, ΔR , $\Delta\eta$ and $\Delta\phi$) of two large- R jets in data and prediction in the sideband region after requiring 3 b -tags.	125
A.9	Kinematics (p_T , mass, η , ϕ) of the lead large- R jet in data and prediction in the sideband region after requiring 2 b -tags split.	126
A.10	Kinematics (p_T , mass, η , ϕ) of the subleading large- R jet in data and prediction in the sideband region after requiring 2 b -tags split.	127
A.11	First two rows show the p_T of the lead (left) and sub-lead (right) small- R track jets associated to the lead (first-row) and sub-lead (second-row) large- R jet in data and prediction in the sideband region after requiring 2 b -tags split. Third row shows the ΔR between two leading small- R track-jets associated to the leading (left) and sub-leading (right) large- R jet.	128
A.12	Kinematics (invariant mass, ΔR , $\Delta\eta$ and $\Delta\phi$) of two large- R jets in data and prediction in the sideband region after requiring 2 b -tags split.	129
B.1	Kinematics (p_T , mass, η , ϕ) of the lead large- R jet in data and prediction in the control region after requiring 4 b -tags.	131
B.2	Kinematics (p_T , mass, η , ϕ) of the subleading large- R jet in data and prediction in the control region after requiring 4 b -tags.	132
B.3	First two rows show the p_T of the lead (left) and sub-lead (right) small- R track jets associated to the lead (first-row) and sub-lead (second-row) large- R jet in data and prediction in the control region after requiring 4 b -tags. Third row shows the ΔR between two leading small- R track-jets associated to the leading (left) and sub-leading (right) large- R jet.	133
B.4	Kinematics (invariant mass, ΔR , $\Delta\eta$ and $\Delta\phi$) of two large- R jets in data and prediction in the control region after requiring 4 b -tags.	134
B.5	Kinematics (p_T , mass, η , ϕ) of the lead large- R jet in data and prediction in the control region after requiring 3 b -tags.	135
B.6	Kinematics (p_T , mass, η , ϕ) of the subleading large- R jet in data and prediction in the control region after requiring 3 b -tags.	136

B.7 First two rows show the p_T of the lead (left) and sub-lead (right) small- R track jets associated to the lead (first-row) and sub-lead (second-row) large- R jet in data and prediction in the control region after requiring 3 b -tags. Third row shows the ΔR between two leading small- R track-jets associated to the leading (left) and sub-leading (right) large- R jet.	137
B.8 Kinematics (invariant mass, ΔR , $\Delta\eta$ and $\Delta\phi$) of two large- R jets in data and prediction in the control region after requiring 3 b -tags.	138
B.9 Kinematics (p_T , mass, η , ϕ) of the lead large- R jet in data and prediction in the control region after requiring 2 b -tags split.	139
B.10 Kinematics (p_T , mass, η , ϕ) of the subleading large- R jet in data and prediction in the control region after requiring 2 b -tags split.	140
B.11 First two rows show the p_T of the lead (left) and sub-lead (right) small- R track jets associated to the lead (first-row) and sub-lead (second-row) large- R jet in data and prediction in the control region after requiring 2 b -tags split. Third row shows the ΔR between two leading small- R track-jets associated to the leading (left) and sub-leading (right) large- R jet.	141
B.12 Kinematics (invariant mass, ΔR , $\Delta\eta$ and $\Delta\phi$) of two large- R jets in data and prediction in the control region after requiring 2 b -tags split.	142
C.1 Kinematics (p_T , mass, η , ϕ) of the lead large- R jet in data and prediction in the signal region after requiring 4 b -tags.	146
C.2 Kinematics (p_T , mass, η , ϕ) of the subleading large- R jet in data and prediction in the signal region after requiring 4 b -tags.	147
C.3 First two rows show the p_T of the lead (left) and sub-lead (right) small- R track jets associated to the lead (first-row) and sub-lead (second-row) large- R jet in data and prediction in the signal region after requiring 4 b -tags. Third row shows the ΔR between two leading small- R track-jets associated to the leading (left) and sub-leading (right) large- R jet.	148
C.4 Kinematics (invariant mass, ΔR , $\Delta\eta$ and $\Delta\phi$) of two large- R jets in data and prediction in the signal region after requiring 4 b -tags.	149
C.5 Kinematics (p_T , mass, η , ϕ) of the lead large- R jet in data and prediction in the signal region after requiring 3 b -tags.	150
C.6 Kinematics (p_T , mass, η , ϕ) of the subleading large- R jet in data and prediction in the signal region after requiring 3 b -tags.	151

C.7	First two rows show the p_T of the lead (left) and sub-lead (right) small- R track jets associated to the lead (first-row) and sub-lead (second-row) large- R jet in data and prediction in the signal region after requiring 3 b -tags. Third row shows the ΔR between two leading small- R track-jets associated to the leading (left) and sub-leading (right) large- R jet.	152
C.8	Kinematics (invariant mass, ΔR , $\Delta\eta$ and $\Delta\phi$) of two large- R jets in data and prediction in the signal region after requiring 3 b -tags.	153
C.9	Kinematics (p_T , mass, η , ϕ) of the lead large- R jet in data and prediction in the signal region after requiring 2 b -tags split.	154
C.10	Kinematics (p_T , mass, η , ϕ) of the subleading large- R jet in data and prediction in the signal region after requiring 2 b -tags split.	155
C.11	First two rows show the p_T of the lead (left) and sub-lead (right) small- R track jets associated to the lead (first-row) and sub-lead (second-row) large- R jet in data and prediction in the signal region after requiring 2 b -tags split. Third row shows the ΔR between two leading small- R track-jets associated to the leading (left) and sub-leading (right) large- R jet.	156
C.12	Kinematics (invariant mass, ΔR , $\Delta\eta$ and $\Delta\phi$) of two large- R jets in data and prediction in the signal region after requiring 2 b -tags split.	157
D.1	$1b$ over $0b$ μ_{qcd} values evaluated in data, with the N_{event} weighted mean and the Gaussian fit mean listed.	159
D.2	$2b$ over $1b$ μ_{qcd} values evaluated in data, with the N_{event} weighted mean and the Gaussian fit mean listed.	159
D.3	$2bs$ over $1b$ μ_{qcd} values evaluated in data, with the N_{event} weighted mean and the Gaussian fit mean listed.	160
D.4	$3b$ over $2b$ μ_{qcd} values evaluated in data, with the N_{event} weighted mean and the Gaussian fit mean listed. SR is blinded.	160
D.5	$4b$ over $2b$ μ_{qcd} values evaluated in data, with the N_{event} weighted mean and the Gaussian fit mean listed. SR is blinded.	161
D.6	$1b$ over $0b$ μ_{qcd} values evaluated in dijet MC, with the N_{event} weighted mean and the Gaussian fit mean listed.	162
D.7	$2b$ over $1b$ μ_{qcd} values evaluated in dijet MC, with the N_{event} weighted mean and the Gaussian fit mean listed.	162

D.8	$2b$ s over $1b$ μ_{qcd} values evaluated in dijet MC, with the N_{event} weighted mean and the Gaussian fit mean listed.	163
D.9	$3b$ over $2b$ μ_{qcd} values evaluated in dijet MC, with the N_{event} weighted mean and the Gaussian fit mean listed.	163
D.10	$4b$ over $2b$ μ_{qcd} values evaluated in dijet MC, with the N_{event} weighted mean and the Gaussian fit mean listed.	164
E.1	For $2b$ s background estimate: the fits to the ratio of the data in the $1b$ category, of the sub-leading Higgs candidate $1b$ -tagged events's subleading Higgs candidate distributions(black point), over the leading Higgs candidate $1b$ -tagged events's subleading Higgs candidate distributions(yellow). Distributions and fits to the estimated QCD background for large- R jet p_T (left), the large- R jet's leading trackjet p_T (middle), and large- R jet's subleading trackjet p_T (right) are shown. Figures are before reweighting (top row), after the first iteration(second row), after the fourth iteration(third row), and after the last iteration (bottom row). The green line is the spline fit; the red line is a polynomial fit; the blue line is the spline interpolation.	167
E.2	For $2b$ s background estimate: the fits to the ratio of the data in the $1b$ category, of the leading Higgs candidate $1b$ -tagged events's leading Higgs candidate distributions(black point), over the subleading Higgs candidate $1b$ -tagged events's leading Higgs candidate distributions(yellow). Distributions and fits to the estimated QCD background for large- R jet p_T (left), the large- R jet's leading trackjet p_T (middle), and large- R jet's subleading trackjet p_T (right) are shown. Figures are before reweighting (top row), after the first iteration(second row), after the fourth iteration(third row), and after the last iteration (bottom row). The green line is the spline fit; the red line is a polynomial fit; the blue line is the spline interpolation.	168
E.3	For $3b$ background estimate: the fits to the ratio of the data in the $2b$ category, of the sub-leading Higgs candidate $2b$ -tagged events's subleading Higgs candidate distributions(black point), over the leading Higgs candidate $1b$ -tagged events's subleading Higgs candidate distributions(yellow). Distributions and fits to the estimated QCD background for large- R jet p_T (left), the large- R jet's leading trackjet p_T (middle), and large- R jet's subleading trackjet p_T (right) are shown. Figures are before reweighting (top row), after the first iteration(second row), after the fourth iteration(third row), and after the last iteration (bottom row). The green line is the spline fit; the red line is a polynomial fit; the blue line is the spline interpolation.	169

E.8	Reweighted $3b$ sideband region predictions comparison. Top row is the dijet Mass, second row is leading large- R jet p_T , third row is the leading large- R jet's leading trackjet p_T and the last row subleading large- R jet's leading trackjet p_T . On the left are the distributions before reweighting, and on the right are the distributions after reweighting. . .	174
E.9	Reweighted $4b$ sideband region predictions comaprison. Top row is the dijet Mass, second row is leading large- R jet p_T , third row is the leading large- R jet's leading trackjet p_T and the last row subleading large- R jet's leading trackjet p_T . On the left are the distributions before reweighting, and on the right are the distributions after reweighting. . .	175
E.10	Reweighted $2bs$ control region predictions comaprison. Top row is the dijet Mass, second row is leading large- R jet p_T , third row is the leading large- R jet's leading trackjet p_T and the last row subleading large- R jet's leading trackjet p_T . On the left are the distributions before reweighting, and on the right are the distributions after reweighting. . .	176
E.11	Reweighted $3b$ control region predictions comaprison. Top row is the dijet Mass, second row is leading large- R jet p_T , third row is the leading large- R jet's leading trackjet p_T and the last row subleading large- R jet's leading trackjet p_T . On the left are the distributions before reweighting, and on the right are the distributions after reweighting. . .	177
E.12	Reweighted $4b$ control region predictions comaprison. Top row is the dijet Mass, second row is leading large- R jet p_T , third row is the leading large- R jet's leading trackjet p_T and the last row subleading large- R jet's leading trackjet p_T . On the left are the distributions before reweighting, and on the right are the distributions after reweighting. . .	178
F.1	In $1b$ data, with low-mass CR variation, new SB and CR $m_J^{\text{lead}} - m_J^{\text{subl}}$ distribution. . .	181
F.2	In $1b$ data, with high-mass CR variation, new SB and CR $m_J^{\text{lead}} - m_J^{\text{subl}}$ distribution. . .	182
F.3	In $1b$ data, with signal-depletion (small) CR variation, new SB and CR $m_J^{\text{lead}} - m_J^{\text{subl}}$ distribution. . .	182
F.4	In $1b$ data, with low-mass SB variation, new SB and CR $m_J^{\text{lead}} - m_J^{\text{subl}}$ distribution. . .	183
F.5	In $1b$ data, with high-mass SB variation, new SB and CR $m_J^{\text{lead}} - m_J^{\text{subl}}$ distribution. . .	183
F.6	In $1b$ data, with small SB variation, new SB and CR $m_J^{\text{lead}} - m_J^{\text{subl}}$ distribution. . .	184
F.7	In $1b$ data, with large SB variation, new SB and CR $m_J^{\text{lead}} - m_J^{\text{subl}}$ distribution. . .	184
F.8	Comparisons of the nominal QCD shape prediction (black) with the results of control and sideband region variations (red). The ratio of the shape from each variation to the nominal shape is shown in the lower panel. The left column shows the relevant distributions for the $4b$ signal region, the middle column is for the $3b$ signal region, and the left column is for the $2bs$ signal region. The top row is for high CR variation, the middle row is for the low CR variation, and the bottom row is for the small CR variation. . .	199

Listing of tables

2.1 LHC nominal and operational parameters	19
5.1 Physics objects and their technical names in the boosted analysis.	45
5.2 The selection efficiency for $G_{KK}^* \rightarrow hh \rightarrow b\bar{b}b\bar{b}$ events ($c = 1.0$) at each stage of the event selection. Uncertainties are the MC stat uncertainty only.	57
5.3 The selection efficiency for $G_{KK}^* \rightarrow hh \rightarrow b\bar{b}b\bar{b}$ events ($c = 2.0$) at each stage of the event selection. Uncertainties are the MC stat uncertainty only.	58
5.4 The selection efficiency for $H \rightarrow hh \rightarrow b\bar{b}b\bar{b}$ events at each stage of the event selection.	58
6.1 Definitions of the signal region, the control region and the sideband region.	61
6.2 Background scaling parameters (μ_{qcd} and $\alpha_{t\bar{t}}$) estimated from fits to the m_J^{lead} distributions in $4b/3b/2bs$ sideband regions. $\varrho(\mu_{qcd}, \alpha_{t\bar{t}}) = \frac{\text{Cov}(\mu_{qcd}, \alpha_{t\bar{t}})}{\sigma_{\mu_{qcd}} \sigma_{\alpha_{t\bar{t}}}}$	69
6.3 Background scaling parameters (μ_{qcd} and $\alpha_{t\bar{t}}$) estimated from fits to the m_J^{lead} distributions in $4b/3b/2bs$ sideband regions post reweighting. $\varrho(\mu_{qcd}, \alpha_{t\bar{t}}) = \frac{\text{Cov}(\mu_{qcd}, \alpha_{t\bar{t}})}{\sigma_{\mu_{qcd}} \sigma_{\alpha_{t\bar{t}}}}$	72
6.4 Smoothing parameters in $4b$ and $3b$ and $2bs$ signal regions for scaled mass distributions, the correlation between parameters is almost always 0.99.	76
6.5 Expected yields for backgrounds in the $4b$ signal region, control region, and sideband region, along with the observed number of data events. The signal predictions for $G_{KK}^* m = 1.0, 1.5, 2.0$ TeV with $c = 1.0$. The uncertainty listed is statistical, without fit uncertainty.	79
6.6 Expected yields for backgrounds in the $3b$ signal region, control region, and sideband region, along with the observed number of data events. The signal predictions for $G_{KK}^* m = 1.0, 1.5, 2.0$ TeV with $c = 1.0$. The uncertainty listed is statistical, without fit uncertainty.	79
6.7 Expected yields for backgrounds in the $2bs$ signal region, control region, and sideband region, along with the observed number of data events. The signal predictions for $G_{KK}^* m = 1.0, 1.5, 2.0$ TeV with $c = 1.0$. The uncertainty listed is statistical, without fit uncertainty.	80

7.1	Agreement between data and prediction in $4b$ tag CR. Showing stat uncertainty only.	89
7.2	Agreement between data and prediction in $3b$ tag CR. Showing stat uncertainty only.	89
7.3	Agreement between data and prediction in $2bs$ tag CR. Showing stat uncertainty only.	89
7.4	Data and prediction in ZZ SR in $4b$, $3b$ and $2bs$ regions.	91
7.5	Data and prediction in TT SR in $4b$, $3b$ and $2bs$ regions.	94
7.6	Functions used to fit the QCD dijet mass distributions, where $x = m_{jj}/\sqrt{s}$	99
7.7	Percent impact of the dominant systematics on the background acceptance and on the signal acceptance of G_{KK}^* with $c = 1.0$ in the $4b$ signal region.	102
7.8	Percent impact of the dominant systematics on the background acceptance and on the signal acceptance of G_{KK}^* with $c = 1.0$ in the $3b$ signal region.	102
7.9	Percent impact of the dominant systematics on the background acceptance and on the signal acceptance of G_{KK}^* with $c = 1.0$ in the $2bs$ signal region.	102
8.1	Unblinded Signal Region predictions and results. All systematic uncertainties are included for backgrounds. The Poisson uncertainty in data is shown for comparison.	104
8.2	The number of predicted background events in the signal region (SR) for the resolved analysis compared to the data, for the 2015 and 2016 datasets. The yields for three potential signals, an 800 GeV G_{KK}^* resonance with $k/\bar{M}_{Pl} = 1$, a scalar with a mass of 280 GeV, and SM non-resonant Higgs boson pair production, are also shown. The scalar sample is normalized to a cross section times branching ratio of 2.7 pb. The quoted uncertainties include both the statistical and systematic uncertainties, and the total uncertainty considers correlations. The numbers of observed and predicted events are also given in the control region (CR).	107
8.3	95% CL exclusion limits for SM non-resonant di-Higgs production, in units of the SM prediction for $\sigma(pp \rightarrow hh \rightarrow b\bar{b}b\bar{b})$	113
C.1	$4b$ unblinded Signal Region predictions and results. All systematic uncertainties included for backgrounds. For Data, the statistical uncertainty is shown. Mass range is broken into greater than 1 TeV, 1.5 TeV, 2 TeV, 2.5 TeV, and 3 TeV intervals.	144
C.2	$3b$ unblinded Signal Region predictions and results. All systematic uncertainties included for backgrounds. For Data, the statistical uncertainty is shown. Mass range is broken into greater than 1 TeV, 1.5 TeV, 2 TeV, 2.5 TeV, and 3 TeV intervals.	144
C.3	$2bs$ unblinded Signal Region predictions and results. All systematic uncertainties included for backgrounds. For Data, the statistical uncertainty is shown. Mass range is broken into greater than 1 TeV, 1.5 TeV, 2 TeV, 2.5 TeV, and 3 TeV intervals.	144

C.4	$4b$ unblinded Scaled dijet mass Region predictions and results. All systematic uncertainties included for backgrounds. For Data, the statistical uncertainty is shown. Mass range is broken into greater than 1 TeV, 1.5 TeV, 2 TeV, 2.5 TeV, and 3 TeV intervals.	145
C.5	$3b$ unblinded Scaled dijet mass Signal Region predictions and results. All systematic uncertainties included for backgrounds. For Data, the statistical uncertainty is shown. Mass range is broken into greater than 1 TeV, 1.5 TeV, 2 TeV, 2.5 TeV, and 3 TeV intervals. . . .	145
C.6	$2bs$ unblinded Scaled dijet mass Signal Region predictions and results. All systematic uncertainties included for backgrounds. For Data, the statistical uncertainty is shown. Mass range is broken into greater than 1 TeV, 1.5 TeV, 2 TeV, 2.5 TeV, and 3 TeV intervals. . . .	145
F.1	Background prediction in SR/CR/SB for High CR in $4b$ region.	185
F.2	Background prediction in SR/CR/SB for Low CR in $4b$ region.	185
F.3	Background prediction in SR/CR/SB for Small CR in $4b$ region.	186
F.4	Background prediction in SR/CR/SB for High SB in $4b$ region.	186
F.5	Background prediction in SR/CR/SB for Low SB in $4b$ region.	187
F.6	Background prediction in SR/CR/SB for Large SB in $4b$ region.	187
F.7	Background prediction in SR/CR/SB for Small SB in $4b$ region.	188
F.8	Background prediction in SR/CR/SB for High CR in $3b$ region.	189
F.9	Background prediction in SR/CR/SB for Low CR in $3b$ region.	189
F.10	Background prediction in SR/CR/SB for Small CR in $3b$ region.	190
F.11	Background prediction in SR/CR/SB for High SB in $3b$ region.	190
F.12	Background prediction in SR/CR/SB for Low SB in $3b$ region.	191
F.13	Background prediction in SR/CR/SB for Large SB in $3b$ region.	191
F.14	Background prediction in SR/CR/SB for Small SB in $3b$ region.	192
F.15	Background prediction in SR/CR/SB for High CR in $2bs$ region.	193
F.16	Background prediction in SR/CR/SB for Low CR in $2bs$ region.	193
F.17	Background prediction in SR/CR/SB for Small CR in $2bs$ region.	194
F.18	Background prediction in SR/CR/SB for High SB in $2bs$ region.	194
F.19	Background prediction in SR/CR/SB for Low SB in $2bs$ region.	195
F.20	Background prediction in SR/CR/SB for Large SB in $2bs$ region.	195
F.21	Background prediction in SR/CR/SB for Large SB in $2bs$ region.	196
F.22	Variation in Prediction in $4b$ SR region.	197
F.23	Variation in Prediction in $3b$ SR region.	197
F.24	Variation in Prediction in $2bs$ SR region.	198

VERITAS SHALL MAKE YOU FREE.

Acknowledgments

THANKS TO EVERYONE WORKING AT CERN. CERN is a unique and special place. I love how the streets are named by physicists. Without the support from the IT department, I could not log into lxplus, check the twikis and finish my work. CERN user's office also made traveling to Europe a much nicer and easier experience for me.

THANKS TO EVERYONE WORKING ON THE LARGE HADRON COLLIDER. Without a fully functional accelerator, there would have been no data for me to study. The LHC performed outstandingly since 2015, and all the valuable data in this thesis is produced from it.

THANKS TO EVERYONE THE ATLAS COLLABORATION, who has supported this remarkable program and has contributed to every bit of the result in my thesis. I am standing on the ATLAS(member)'s shoulders—eight floors high and don't shrug. Without the excellent work on detector design, commissioning, operational works, reconstruction, data processing, performance studies and recommendations, software support, computing support, and analysis discussions and guidance, I could not have completed this thesis. I sincerely thank all ATLAS members for their work.

*It was the best of times, it was the worst of times, it was
the age of wisdom, it was the age of foolishness, it was
the epoch of belief, it was the epoch of incredulity, it was
the season of Light, it was the season of Darkness, it was
the spring of hope, it was the winter of despair, we had
everything before us, we had nothing before us, we were
all going direct to Heaven, we were all going direct the
other way. In short, the period was so far like the present
period, that some of its noisiest authorities insisted on
its being received, for good or for evil, in the superlative
degree of comparison only.*

Charles Dickens

0

Introduction

In 2012, the Higgs boson was discovered by the ATLAS and CMS experiment at the LHC. The particle physics community faced a period just like at the beginning of *A Tale of Two Cities*. It was the best of times, as the Standard Model was a great success. It was the worst of times, as there were very few experimental clues for physics beyond the Standard Model. But with the LHC's increase in collision energy, it is a great time to search for beyond the Standard Model physics. The newly discovered Higgs boson can be used as a tool in these searches. Higgs pair production is particularly interesting. It has a low cross section in the Standard Model. However, new physics can modify its production process. Especially, two Higgs bosons can be produced through heavy resonances particles. This gives a clear signature at the collider experiments.

This search focuses on the dominant $b \rightarrow b\bar{b}$ decay mode to search for Higgs boson pair production. The “resolved” analysis is used for hh systems in which the Higgs bosons have Lorentz boosts low enough that four b -jets can be reconstructed. The “boosted” analysis is used for those hh systems in which the Higgs bosons have higher Lorentz boosts, which prevents the Higgs boson decay products from being resolved in the detector as separate b -jets. Instead, each Higgs boson candidate consists of a single large-radius jet, and b -decays are identified using smaller-radius jets built from charged-particle tracks. Two analyses are complementary in their acceptance, each employing a unique technique to reconstruct the Higgs boson. This thesis focuses on the boosted analysis due to its great sensitivity for heavy resonance signals.

In the boosted analysis, an additional signal-enriched sample is utilized with respect to the former ATLAS publication⁷. The dataset comprises the 2015 and 2016 data, corresponding to 36.1 fb^{-1} for the boosted analysis. The results are obtained using the resolved analysis for a resonance mass between 260 GeV and 1400 GeV, and the boosted analysis between 800 GeV and 3000 GeV. The main background is multijet production, which is estimated from data; the sub-leading background is $t\bar{t}$, which is estimated using both data and simulations. The two analyses employ orthogonal selections, and a statistical combination is performed in the mass range where they overlap. The final discriminants are the four-jet and dijet invariant mass distributions in the resolved and boosted analyses, respectively. Limits are set for the following benchmark signals: a spin-2 graviton decaying into Higgs bosons, a scalar resonance decaying into a Higgs boson pair, and SM non-resonant Higgs boson pair production.

This dissertation begins by discussing the status of di-Higgs. Chapter 1 gives an overview of double Higgs production in the Standard Model and beyond. Chapter 2 presents details regarding the Large Hadron Collider and the ATLAS experiment. Chapter 3 discusses reconstruction of physics objects. Chapter 4 lists the dataset and simulation samples. Chapter 5 shows the event selection.

Chapter 6 discusses the background estimation in details. Chapter 7 presents the systematics. Finally, the results are shown in Chapter 8. A brief summary and outlook is presented in the conclusion. Many detailed plots and supporting material are shown in the appendices, to keep the main chapters concise.

Knowledge knows no bounds.

Creator

1

Theory and Motivation

I.I THE STANDARD MODEL AND THE HIGGS BOSON

The Standard Model(SM)^{1,8,9,10} is a quantum field theory describing the interactions of elementary particles through the strong, weak and electromagnetic forces. The elementary particles and their properties are shown in Figure I.I. So far, the SM predictions of particle interactions agree extremely well with experimental observations.

In the SM, the Higgs mechanism introduces a complex scalar Higgs field, φ , with nonzero vacuum expectation values. The scalar Higgs potential is $V(\varphi) = -v^2\lambda_v\varphi^\dagger\varphi + \lambda_v(\varphi^\dagger\varphi)^2$. Through spontaneous symmetry breaking, W^\pm and Z bosons acquire their masses. This process also predicts an extra scalar, the Higgs boson. The SM Lagrangian containing Higgs couplings, $\mathcal{L}_{\text{Higgs}}$, is shown

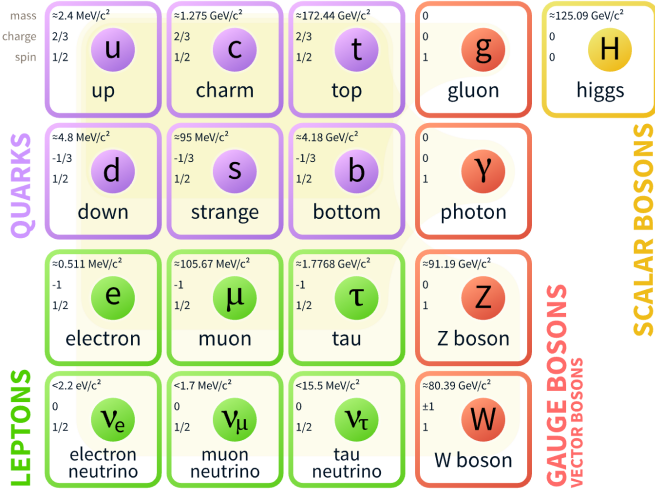


Figure 1.1: Fermions and bosons of the Standard Model and their properties¹, where all the values are measured experimentally.

in Eq I.I.

$$\mathcal{L}_{\text{Higgs}} = -\lambda_{h\bar{f}f} b\bar{f} + \delta_V V_\mu V^\mu (\lambda_{hvv} b + \lambda_{hhvv} b^2) + \lambda_{hh} b^2 + \lambda_{hhh} b^3 + \lambda_{hhhh} b^4 \quad (\text{I.I})$$

where

- $v \sim 246 \text{ GeV}$, is the non-zero expectation value of the Higgs field;
- $\lambda_v \sim -0.13$, the coefficient for the quartic potential term, is constrained from Higgs mass;
- $m_h = \sqrt{2\lambda_v v} = 125.09 \pm 0.24 \text{ GeV}$, is the Higgs mass; this was discovered in 2012^{II,12};
- $V = W^\pm$ or Z , $\delta_W = 1$, $\delta_Z = \frac{1}{2}$;
- $\lambda_{h\bar{f}f} = \frac{m_f}{v}$, is the Higgs to fermion coupling; m_f is the mass of the fermion;
- $\lambda_{hvv} = \frac{2m_v^2}{v}$, is the Higgs to boson coupling; m_v is the mass of the boson;
- $\lambda_{hhvv} = \frac{m_v^2}{v^2}$, is the Higgs-Higgs to boson-boson coupling;
- $\lambda_{hh} = \frac{m_h^2}{2}$, is the Higgs mass term;

- $\lambda_{hhh} = \frac{m_h^2}{2v} = \lambda_{\nu\nu}$, or λ_{hhh} , is the Higgs self-coupling;
- $\lambda_{hhhh} = \frac{m_h^2}{8v^2}$, is the Higgs quartic-coupling.

What's particularly interesting and has not been measured experimentally is λ_{hhh} . The SM predicts $\lambda_{hhh} = \frac{m_h^2}{2v}$, which is referred as λ_{SM} in this thesis. Measuring λ_{hhh} directly probes the quartic term in the Higgs potential. Also, the $\lambda_{hhh} b^3$ term shows one way for double Higgs production within the SM. Double Higgs production is also known as *di-Higgs* or *Higgs pair production*.

1.2 STANDARD MODEL DI-HIGGS PRODUCTION

There are two main production diagrams of di-Higgs at the LHC, both shown in Figure 1.2. In the gluon-gluon fusion process, di-Higgs are produced through a box or a triangle loop. Only the triangle loop 1.2b probes the λ_{hhh} . In the triangle diagram, the middle Higgs boson acts as a propagator (off-shell), and the two Higgs bosons in the final state are on-shell. The diagram with an on-shell middle Higgs and two off-shell Higgs bosons in the final state is strongly disfavored¹. The box and triangle diagrams interfere destructively, which makes the overall production rate smaller than what would be expected in the absence of a λ_{hhh} term.

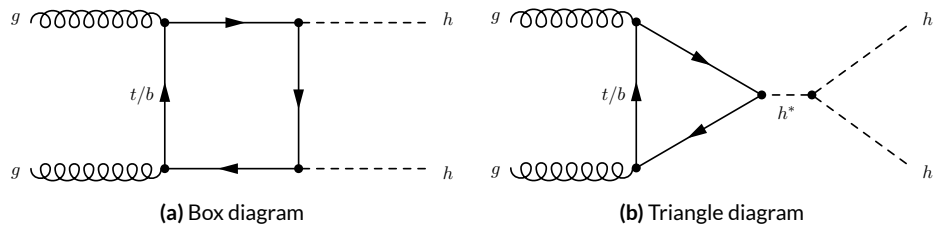


Figure 1.2: Leading order Feynman diagrams contributing to di-Higgs production via gluon-gluon fusion, through the Higgs-fermion Yukawa interactions 1.2a and the Higgs boson self-coupling 1.2b. Only Figure 1.2b probes λ_{hhh} .

Many other different production modes of di-Higgs exist. The Feynman diagrams for VBF production are shown in 1.3. Figure 1.4¹³ compares the cross sections of gluon-gluon fusion, Vector Boson Fusion (VBF), top-pair, W^\pm , Z and single-top associated di-Higgs production. It shows that gluon-gluon fusion is the dominant production channel for di-Higgs at pp colliders.

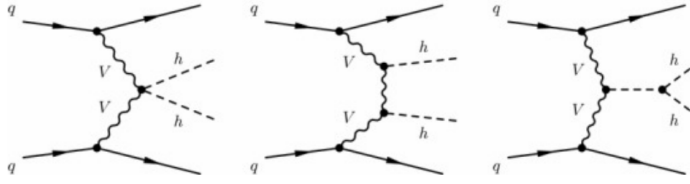


Figure 1.3: Leading order Feynman diagrams contributing to Higgs pair production via VBF.

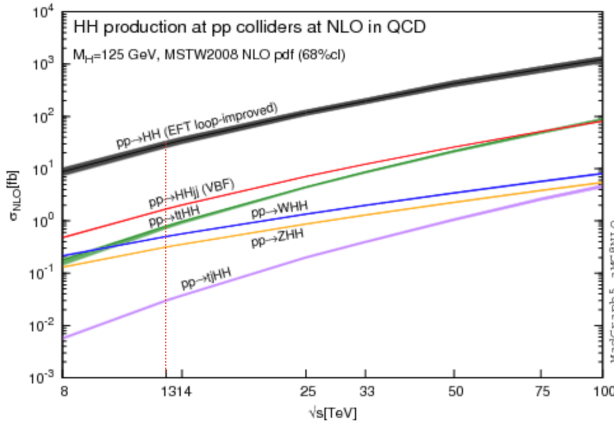


Figure 1.4: Total cross sections (y-axis) at the NLO in QCD for the six largest di-Higgs production channels at pp colliders at different energy (x-axis). Gluon-gluon fusion, VBF, top-pair, W^\pm , Z and single-top associated di-Higgs productions are shown. The thickness of the lines corresponds to the uncertainties added linearly. H refers to the SM Higgs.

For p-p collisions at $\sqrt{s} = 13$ TeV, the total cross section for SM di-Higgs production¹⁴ is evaluated at next-to-next-to-leading order (NNLO) with the summation of logarithms at next-to-next-leading-logarithm (NNLL) accuracy and including finite top-quark mass effects at next-to-leading order (NLO). The uncertainties are from energy scale and parton distributions functions (PDF):

- Gluon gluon fusion: $\sigma_{gg \rightarrow HH} = 33.49^{+4.3\%}_{-6.0\%} \pm 2.1\% \text{ fb.}$
- Vector boson fusion: $\sigma_{VBF \rightarrow HH} = 1.62^{+2.3\%}_{-2.7\%} \pm 2.3\% \text{ fb.}$
- Gluon gluon fusion to Triple-Higgs: $\sigma_{gg \rightarrow HHH} = 0.06332^{+16.1\%}_{-14.1\%} \pm 3.4\% \text{ fb.}$

This means inside the 2015 and 2016 ATLAS 36 fb^{-1} data, the SM expectation is around one thousand di-Higgs events and only two triple Higgs events.

1.3 BEYOND THE STANDARD MODEL PHYSICS DI-HIGGS PRODUCTION

The SM works extremely well, yet the Higgs boson mass at 125 GeV requires extreme fine-tuning for radiative corrections. The presence of new physics at the TeV scale would help solve the naturalness problem.

BSM physics could significantly enhance the production of di-Higgs at the LHC. This is separated into two categories: non-resonant and resonant production. The non-resonant production generally refers to modifications of the Higgs couplings, either the Higgs self-coupling or the Higgs-top couplings. Resonant production refers to the case when a particle with invariant mass greater than twice the Higgs mass decays directly into two Higgs bosons. The non-resonant and resonant production also differ from the invariant mass distribution of the di-Higgs at the truth level. In the non-resonant case, the invariant mass distribution has no clear peak, whereas in the resonant case, the invariant mass distribution usually forms a peak with model dependent width.

1.3.1 BSM NON-RESONANT DI-HIGGS

Enhanced non-resonant Higgs boson pair production is predicted in many models. BSM models featuring direct $t\bar{t}hh$ vertices^{15,16} or new light colored scalars¹⁷ could augment the vertex strength, shown as the red dots in Figure 1.5. A direct modification of the Higgs self-coupling coefficient in Eq 1.1, from $\lambda_{sm} bbb$ to λbbb , is also possible. This is shown as the green dot in Figure 1.5b.

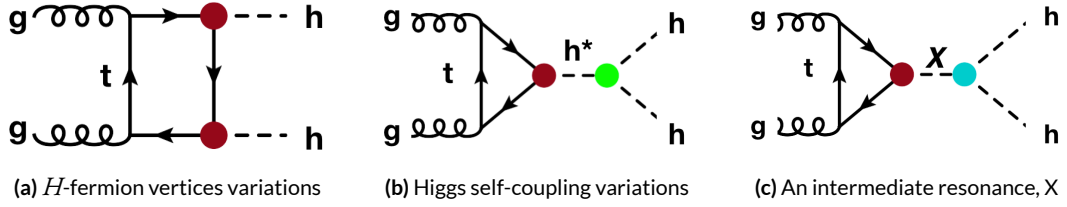


Figure 1.5: BSM Higgs boson pair production: non-resonant production proceeds through changes in the SM Higgs couplings in 1.5a and 1.5b, resonant production proceeds through 1.5c an intermediate resonance, X . H and h both refers to the SM Higgs.

The non-resonant di-Higgs enhancement is usually described by the di-Higgs cross section ratio between a BSM λ coupling scenario and the λ_{SM} coupling scenario. $\frac{\lambda}{\lambda_{\text{SM}}}$ indicates the ratio between the BSM model λ and λ_{SM} . From the SM electroweak measurements, the self coupling term is constrained to $-14 \leq \frac{\lambda}{\lambda_{\text{SM}}} \leq 17.4$ ¹⁸. Variations of λ have a non-trivial effect on di-Higgs production cross section, shown in Figure 1.6¹³. In the regime of relatively high trilinear coupling, the observation will be an excess of di-Higgs events with respect to the expected background. A simple limit can be set in this case.

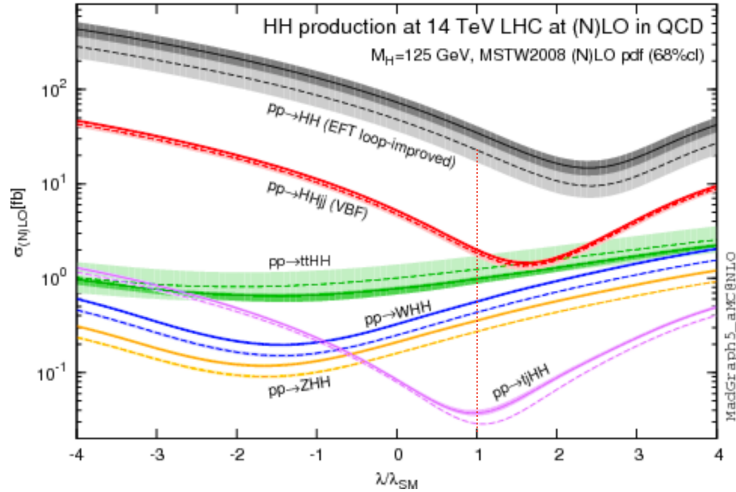


Figure 1.6: Total cross sections (y-axis) at the LO and NLO in QCD for di-Higgs production channels, at the $\sqrt{s} = 14$ TeV LHC as a function of the self-interaction coupling λ (x-axis). The dashed (solid) lines and light- (dark-) color bands correspond to the LO (NLO) results and to the scale and PDF uncertainties added linearly. The SM values of the cross sections are obtained at $\frac{\lambda}{\lambda_{\text{SM}}} = 1$, indicated by the red vertical line. H refers to the SM Higgs.

1.3.2 BSM RESONANT DI-HIGGS

Resonant Higgs boson pair production is also predicted by many models. Extensions of the Higgs sector, such as two-Higgs-doublet models(2HDM)^{19,20}, propose the existence of a heavy spin-0 scalar H that can decay into di-Higgs. The bulk Randall-Sundrum model^{21,22}, which features spin-2 Kaluza-Klein gravitons, G_{KK}^* , could also subsequently decay to pairs of Higgs bosons. These proposed heavy particles, heavy CP-even scalar H and G_{KK}^* , are represented as X in Figure 1.5c.

The 2HDM is a simple extension of the SM which has large resonance effects¹⁴. The 2HDM consists of 5 physical Higgs bosons: h (light scalar Higgs), H (heavy scalar Higgs), A (heavy pseudoscalar Higgs), and H^\pm (two charged Higgs). The 2HDM can introduce tree level flavor changing neutral currents. To avoid this, models impose discrete symmetries in which the charged fermions only couple to one of the Higgs doublets. One version is type II 2HDM, in which all positively charged quarks couple to one doublet and the negatively charged quarks and leptons couple to the other. The type II model is the Minimal Supersymmetric Standard Model(MSSM)'s Higgs sector.

Resonant di-Higgs production in 2HDM models can proceed through decays of the heavy CP-even Higgs $H \rightarrow hh$. The branching ratio for $H \rightarrow hh$ depends on the model type as well as the values of $\tan\beta$ and $\cos(\beta - \alpha)$. $\tan\beta = \frac{v_{\text{doublet}}}{v_{\text{SM}}}$ is the ratio of the vacuum expectation values of the two Higgs doublets. α is the mixing angle between the heavy H and light h fields. The limit where $\cos(\beta - \alpha) = 0$ is called the alignment limit, and in this limit the light Higgs h has the same couplings as a SM Higgs. Near the alignment limit there is some unprobed phase space depending on the exact models and values of $\tan\beta$, and they are particularly interesting to be searched for at the LHC.

The Randall-Sundrum model proposes a five-dimensional warped spacetime that contains two manifolds: one where the force of gravity is very strong and a second manifold at the TeV scale

corresponding to the known SM sector. The experimental consequence of this theory is a series of widely mass-spaced Kaluza-Klein graviton resonances, G_{KK}^* . In cases where the fermions are localized to the SM brane, production of gravitons from fermion pairs is suppressed and the primary mode of production of G_{KK}^* is gluon fusion. These gravitons further decay to di-Higgs, with branching fraction ranging from 6.43% for gravitons with a mass of 500 GeV to 7.66% at 3 TeV. Randall-Sundrum models have two free parameters - the mass of the graviton and $c = k/\bar{M}_{\text{pl}}$, where \bar{M}_{pl} is the reduced Planck mass and k is the curvature scale of the extra dimension. The width of the graviton increases with both mass and c .

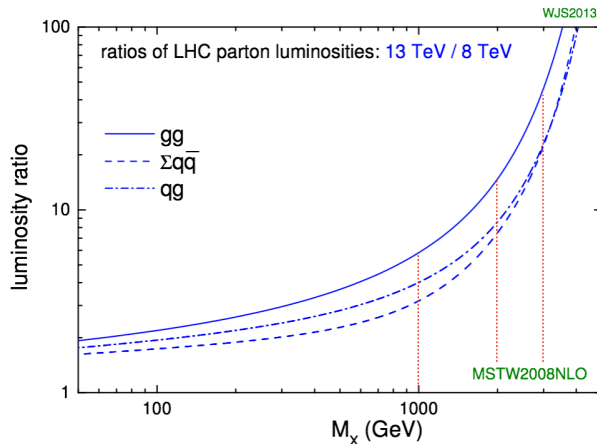


Figure 1.7: Parton luminosity ratios as a function of resonance mass M_X for 13/8 TeV². 1, 2, and 3 TeV M_X ratios are indicated by red lines. For a 2 TeV X , the luminosity ratio is almost 10.

In model dependent searches, based on fixed assumptions of the resonance particles' branching ratio, other search channels like resonance VV or $t\bar{t}$ are more sensitive compared to di-Higgs²³. In order to constrain more BSM physics phase space, di-Higgs search results need to be interpreted in different baseline models, covering both narrow and wide resonances.

It is easy theoretically for new heavy resonance particles to interact with the SM through the Higgs as a mediator. This usually results in resonance di-Higgs production. With the increased center of mass collision energy from 8 TeV to 13 TeV in LHC Run 2, the production cross section for particles with TeV mass grows, as shown in Figure 1.7. In the case of a 2 TeV M_X , the cross section gain is almost a factor of 10. Therefore, it was particularly important to focus on resonant searches above TeV region.

1.4 DI-HIGGS DECAY AND LHC PREVIOUS SEARCH RESULTS

The Higgs boson decays into other elementary particles in 1.56^{-22} s. Therefore, searching for di-Higgs requires reconstructing the Higgs boson from the decay products. Di-Higgs decay is a combination of single Higgs decay, which is determined by the Higgs coupling terms to fermions and bosons are shown in Equation 1.1. The branching ratios of different di-Higgs final states are shown in Figure 1.8.

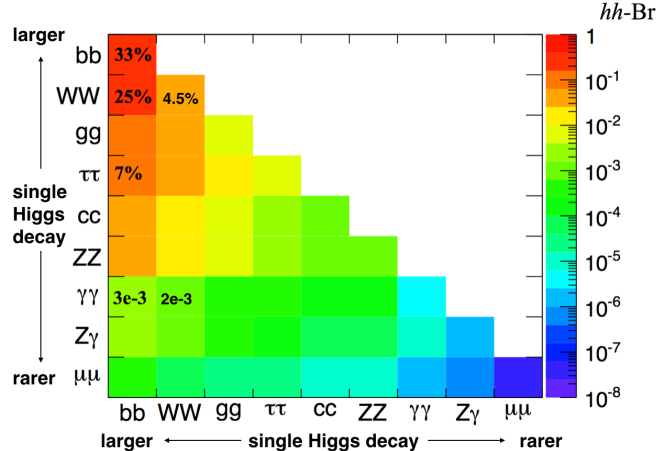


Figure 1.8: Summary of di-Higgs final states and their ratios. Top left, $b\bar{b}b\bar{b}$, has the largest branching ratio.

Previous searches for Higgs boson pair production have not found any significant signals. Using 8 TeV data, ATLAS has examined the $b\bar{b}b\bar{b}$ ²⁴, $b\bar{b}\gamma\gamma$ ²⁵, $b\bar{b}\tau^+\tau^-$ and $W^+W^-\gamma\gamma$ channels, all of

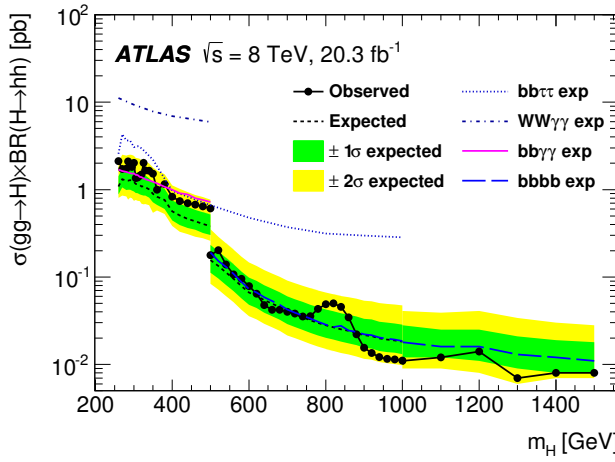


Figure 1.9: The observed and expected 95% CL upper limits of $\sigma(\text{gg} \rightarrow H) \times \text{BR}(H \rightarrow \text{bb})$ at $\sqrt{s} = 8$ TeV as functions of the heavy Higgs boson mass m_H , combining resonant searches in Higgs boson pair to $b\bar{b}\tau^+\tau^-$, $W^+W^-\gamma\gamma$, $b\bar{b}\gamma\gamma$, and $b\bar{b}b\bar{b}$ final states. The expected limits from individual searches are also shown. The green and yellow bands represent $\pm 1\sigma$ and $\pm 2\sigma$ uncertainty ranges of the expected combined limits. The improvement above $m_H = 500$ GeV reflects the sensitivity of the $b\bar{b}b\bar{b}$ analysis. The results beyond 1 TeV are only from the $b\bar{b}b\bar{b}$ final state alone.

which were combined²⁶. The resonant search combination result is shown in Figure 1.9. The best non-resonant $\sigma(pp \rightarrow bb)$ cross section limit in Run 1 is the ATLAS combination, at 0.69 pb. This corresponds to $|\frac{\lambda}{\lambda_{\text{SM}}}| < 70$. Different di-Higgs search challenges and perspectives are summarized below:

- $b\bar{b}b\bar{b}$: b -jet trigger efficiency limits the low mass resonance searches, but for high mass resonances above 500 GeV, the branching ratio of this channel provides a decisive advantage. It is great for non-resonant searches as well.
- $b\bar{b}W^+W^-$: Despite the second largest branching ratio, large background from $t\bar{t}$ limits this search sensitivity.
- $b\bar{b}\gamma\gamma$: This channel benefits from good double photon trigger efficiency, a good photon reconstruction efficiency and a low SM background. Most sensitive at low mass $m_X \leq 350$ GeV. At higher masses, the smaller branching ratio and the merging of photons hurt the search sensitivity. Great for non-resonant searches.
- $b\bar{b}\tau^+\tau^-$: An intermediate choice between $b\bar{b}b\bar{b}$ and $b\bar{b}\gamma\gamma$ for resonance searches. Yet this channel contributes to the non-resonant result significantly.

- $W^+W^-\gamma\gamma$: Suffers from much lower branching ratio and lower reconstruction efficiency of the W^+W^- compared to $b\bar{b}$.
- $W^+W^-\tau\tau, W^+W^-W^+W^-, b\bar{b}ZZ$: There are no search results on these channels yet. But because of the relatively large branching ratio, it is likely that they would be explored in the future.

1.5 RESOLVED AND BOOSTED

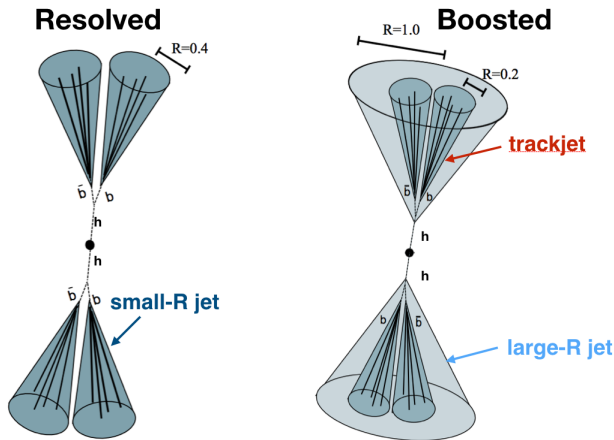


Figure 1.10: Cartoon for $X \rightarrow hh \rightarrow b\bar{b}b\bar{b}$, with resolved event topology (left) and boosted event topology (right).

The thesis focuses on searching for a TeV scale resonance $X \rightarrow hh \rightarrow b\bar{b}b\bar{b}$. The invariant mass of the two-Higgs-boson-candidate system, m_{2J} , is used as the final discriminant between Higgs boson pair production and the SM backgrounds. The Higgs bosons reconstruction affects the m_{2J} invariant mass resolution. Fully reconstructed out-coming b quarks are also necessary to separate the signal from the multi quark production backgrounds.

When the Higgs bosons have Lorentz low boosts, four small- R b -jets with $R = 0.4$ can be reconstructed. This final state is called the *resolved* state, shown on the left of Figure 1.10. The resolved

strategy is effective for resonance M_X from 260 GeV up to 1.2 TeV. It is also good for non-resonance di-Higgs searches.

A different reconstruction strategy is used for di-Higgs systems with higher Lorentz boosts from heavier resonances. For a Higgs boson produced with momentum p_H , the angular separation between the b and \bar{b} quarks, ΔR_{bb} , scales roughly as $\frac{2m_H}{p_H}$. For example, a 1.5 TeV resonance G_{KK}^* is produced roughly at rest in a pp collision. In the lab frame, the two Higgs bosons each get ~ 625 GeV momentum. The ΔR_{bb} is around 0.4. This means that the standard $R = 0.4$ b -jets cannot resolve the $b\bar{b}$ system. Therefore a different analysis strategy is required. Instead, each $b\bar{b}$ system is reconstructed as a single large-radius jet. The large-radius jet contains the decay products of the Higgs boson. The presence of b -quarks is inferred using smaller-radius track jets built from charged-particle tracks. This final state is called the *boosted* state, shown on the right of Figure 1.10. This strategy works for resonance M_X from 1 GeV up to 3 TeV.

In summary, di-Higgs has a small production rate in the SM, but could be significantly enhanced in BSM scenarios. In particular, a heavy resonance spin-0 or spin 2 particle could decay into Higgs boson pair directly. The search sensitivity for massive resonances increases as the center of mass energy of the collision increases. For resonance signals above 1 TeV decaying into di-Higgs, $b\bar{b}b\bar{b}$ channel has the best discovery potential in Run 2. In order to fully reconstruct these $X \rightarrow hh \rightarrow b\bar{b}b\bar{b}$, boosted techniques has to be used. Searching for TeV scale resonance production of di-Higgs $\rightarrow b\bar{b}b\bar{b}$ using the boosted analysis is the goal of thesis.

Pain teaches lessons no scholar can.

2

LHC and ATLAS

The Large Hadron Collider (LHC) is a proton-proton ($p\bar{p}$) collider at the European Organization for Nuclear Research (CERN) laboratory in Geneva, Switzerland²⁷. ATLAS (A Toroidal LHC ApparatuS), CMS (the Compact Muon Solenoid), ALICE (A Large Ion Collider Experiment), and LHC b (Large Hadron Collider beauty experiment)^{28,29,30,31} are the four main experiments. They are located at the Interaction points(IPs) of the accelerator. Figure 2.1 shows a schematic of the LHC ring and its experiments.

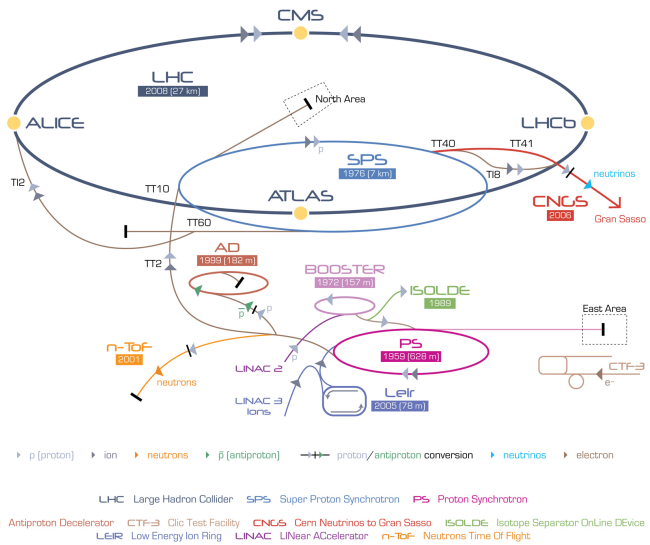


Figure 2.1: A schematic view of the LHC ring³. LINAC2, Booster, PS, SPS, and LHC accelerate the protons in order. Four main experiments are located at interaction points along the ring. ATLAS and CMS are general purpose experiments, while ALICE focuses on heavy ion collisions and LHC b is dedicated to B physics.

2.1 THE LARGE HADRON COLLIDER

Protons accelerated around the LHC originate in a red bottle of hydrogen gas. The whole acceleration, taking around 25 minutes, is accomplished in multiple steps:

- Electrons are stripped from the hydrogens to create protons;
- A linear particle accelerator, Linac 2, accelerates the protons to 50 MeV;
- The Proton Synchrotron Booster (PSB) accelerates the protons to 1.4 GeV;
- The Proton Synchrotron (PS) accelerates the protons to 25 GeV;
- The Super Proton Synchrotron (SPS) accelerates the protons to 450 GeV;
- The 16.7 kilometers LHC accelerates the protons to the final TeV energies.

The instantaneous luminosity, $L (m^{-2}s^{-1})$, at the LHC is defined in Eq2.1 ³:

$$L = \frac{n_b N_b f_{\text{rev}} \gamma_r}{4\pi \epsilon_n \beta^*} F \quad (2.1)$$

In the above Eq2.1:

- n_b is the number of bunches per beam;
- N_b is the number of protons per bunch;
- f_{rev} is the proton revolution frequency;
- γ_r is the relativistic Lorentz factor for the protons;
- ϵ_n is the normalized transverse beam emittance, or the average beam spread length;
- β^* is the transverse beam size; $\sigma_{\text{beam}} = \sqrt{\epsilon \cdot \beta}$;
- F is a reduction factor for the angle beams are colliding.

In $p\bar{p}$ collisions, the rate of a certain physics process is $R_{\text{phy}} = L\sigma$, where $\sigma (m^2)$ the cross section.

The instantaneous luminosity can also be written as the ratio of the rate of inelastic collisions to the inelastic cross section σ_{inel} ³²:

$$L = \frac{R_{\text{inel}}}{\sigma_{\text{inel}}} = \frac{\mu n_b f_{\text{rev}}}{\sigma_{\text{inel}}} \quad (2.2)$$

where, μ is the number of interactions per bunch crossing. At each bunch crossing, the collisions without the highest center of mass energy are called “pileup” interactions.

The main parameters of the LHC beam and performance are shown in Table 2.1. The target peak instantaneous luminosity for both the ATLAS and CMS experiments is $L = 10^{34} \text{ cm}^{-2}\text{s}^{-1}$ ²⁷, which has already been exceeded in 2016. This is partly due to the improved β^* and F . The number of “pileup” interactions also increases, shown in Figure 2.2.

Table 2.1: LHC nominal²⁷ and operational parameters in 2015³³ and 2016³⁴.

Parameter [unit]	Nominal design value	2015 Operating value	2016 Operating value
Beam Energy [TeV]	7	6.5	6.5
Peak L [$10^{34} \text{ cm}^2 \text{ s}^{-1}$]	1	0.5	1.25
Bunch spacing [ns]	25	25	25
f_{rev} [kHz]	11245	11245	11245
n_b [10^{11} p/bunch]	1.15	1.15	1.12
N_b [bunch]	2808	1825	2220
ϵ_n [mm mrad]	3.5	3.5	2
β^* [cm]	55	40	40
F	0.84	0.84	0.59
$\langle \mu \rangle$	19	13	41

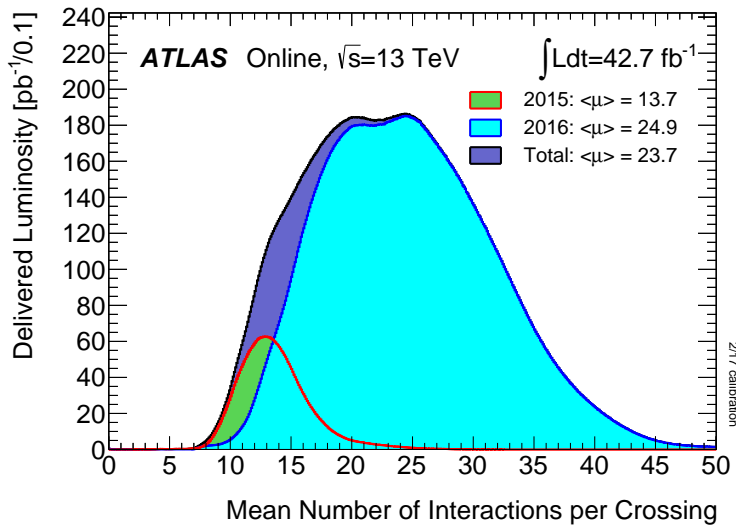


Figure 2.2: The luminosity-weighted distribution of the mean number of interactions per crossing for the 2015 and 2016 pp collision data at 13 TeV center-of-mass energy.⁴

2.2 A TOROIDAL LHC APPARATUS

The ATLAS experiment³⁵ at the LHC is a general-purpose particle detector with a near 4π coverage in solid angle and a forward-backward symmetric cylindrical geometry. The ATLAS detector (Figure 2.3) consists of an inner tracking detector (ID) surrounded by a 2.3 m diameter thin superconducting solenoid providing a 2T axial magnetic field, electromagnetic (EM) and hadronic calorimeters, and a muon spectrometer (MS). Three extra air-core toroid magnets generate the magnetic field in the MS.

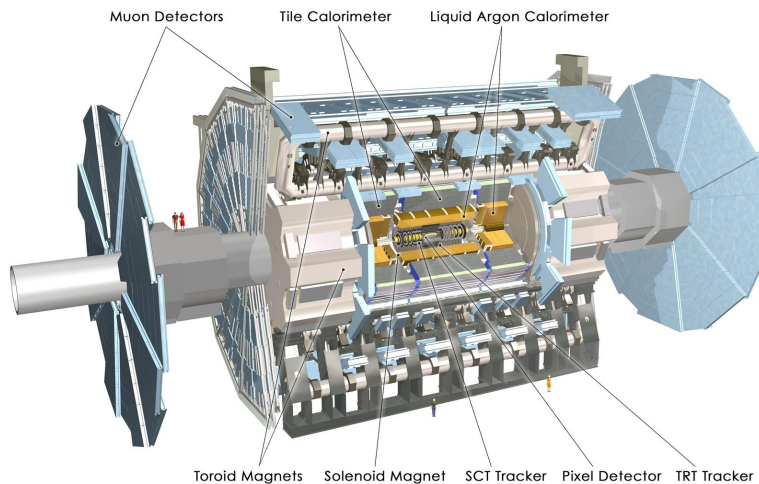


Figure 2.3: A detailed computer-generated image of the ATLAS detector and it's systems.

2.2.1 COORDINATE SYSTEM

ATLAS uses a right-handed coordinate system with its origin at the nominal IP in the center of the detector and the z -axis along the beam pipe. The positive x -axis points from the IP to the center of the LHC ring, the positive y -axis points towards the sky, and the z -axis points straight(like bridges) towards the Geneva airport(A side), back from the Charlie's pub in France(C side). Cylindrical coordinates (r, ϕ) are used in the transverse plane, ϕ being the azimuthal angle around the

z -axis. The pseudorapidity is defined in terms of the polar angle ϑ as $\eta = -\ln \tan(\vartheta/2)$. η the massless approximation of rapidity $y = \frac{1}{2} \ln \frac{E+p_z}{E-p_z}$. ϑ is the angle parameterizing special relativity's boosts along the z -axis. The angular distance is measured in units of $\Delta R = \sqrt{(\Delta\eta)^2 + (\Delta\phi)^2}$.

The region with $|\eta| < 1.5$ is called “central”. It consists of the “barrel” elements, surrounding the beam line cylindrically. For $|\eta| > 1.5$, the region is called “endcap”, and the detector elements are arranged as disks perpendicular to the beam line. At high $|\eta| > 2.5$, the region is referred to as “forward”.

2.2.2 INNER DETECTOR

The ID covers the pseudorapidity range $|\eta| < 2.5$. It consists of three parts: silicon pixel (PIXEL), silicon microstrip (SCT), and straw-tube transition-radiation tracking (TRT) detectors. An additional pixel detector layer (IBL)³⁶, positioned at a mean radius of 3.3 cm, is used in the Run-2 data-taking and improves the identification of b -jets³⁷. A 10GeV charged particle in the barrel region expect 1 IBL hits, 3 PIXEL hits, 8 SCT hits and 36 TRT hits. Figure 2.4a³⁸ shows the R - z distribution of the material for a quadrant of the barrel region PIXEL and SCT. Figure 2.4b shows the distribution of hadronic-interaction vertex candidates in $|\eta| < 2.4$ and $|z| < 400$ mm for 13TeV data. The ID is important for track reconstruction and heavy flavor b -tagging.

2.2.3 CALORIMETER

The Lead/liquid-argon (LAr) finely segmented sampling calorimeters provide EM energy measurements. A steel/scintillator-tile hadronic calorimeter covers the central pseudorapidity range ($|\eta| < 1.7$). The endcap and forward regions are instrumented with copper/tungsten and LAr calorimeters for both the EM and hadronic energy measurements up to $|\eta| = 4.9$. The calorimeters also provide basic EM/Hadronic trigger information, with fast analogue summing in coarse

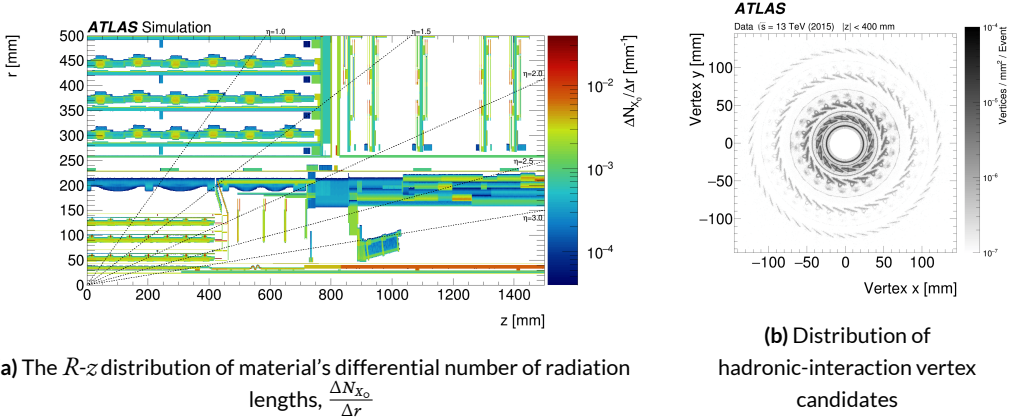


Figure 2.4: Geometrical of IBL, PIXEL and SCT detectors in Run2.

granularity. The calorimeters are important for measuring the energy of the Higgs boson decay productions.

2.2.4 MUON SPECTROMETER

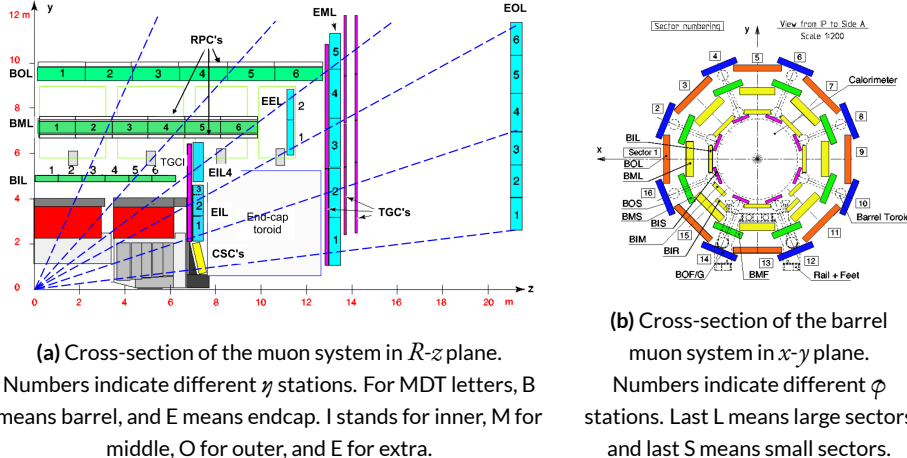


Figure 2.5: The overall layout of the ATLAS MuonSpectrometer.

The muon spectrometer (Figure 2.5) is the largest component of the ATLAS detector. It surrounds the calorimeters and includes three large superconducting air-core toroids. The field integral of the toroids ranges between 2 and 6 T/m for most of the detector. Because of this bending power, the MS measures Muon momentum stand-alone, with $\sigma_{p_T}/p_T \sim 10\%$ at $p_T = 1\text{TeV}$. Muon Drift Tubes (MDT) and Cathode Strip Chambers (CSC) provide precision tracking. Resistive Plate Chambers (RPC) in the barrel and Thin Gap Chambers (TGC) provide triggering, with 1.5-5 ns timing resolution.

2.2.5 TRIGGER AND DATA ACQUISITION

A dedicated trigger system is used to select events³⁹. The first-level trigger (L1) is implemented in hardware and uses the calorimeter and muon detectors to seed regions of interest (RoI) and reduce the accepted event rate to 100 kHz. This is followed by a software-based high-level trigger (HLT) that reduces the accepted event rate to 1 kHz on average. To avoid high rates for certain triggers, the triggers are often prescaled, which means some accepted events get rejected. For example, a prescale of two means only every second event passing all trigger conditions gets accepted.

Over 2015 and 2016, both the LHC and the ATLAS performed outstandingly⁴. The total data recording efficiency for ATLAS is around 92%, shown in Figure 2.6.

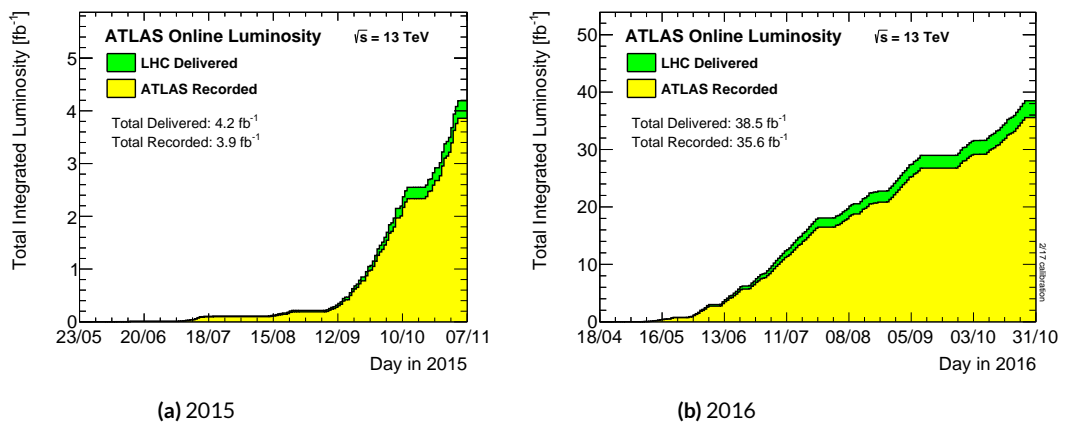


Figure 2.6: Cumulative luminosity vs. time delivered to (green) and recorded by ATLAS (yellow) during stable beams for $p\bar{p}$ collisions at 13 TeV centre-of-mass energy.

A picture is worth a thousand swords.

Tony

3

Reconstruction and Objects

Reconstruction is the construction of particles from raw detector readouts. In each $p\bar{p}$ collision recorded by ATLAS, charged particles bend in the magnetic field and leave tracks in the ID, electrons and photons deposit their energies in ECAL, hadrons are absorbed in HCAL, muons leave extra tracks in the MS, and neutrinos are inferred by the conservation of momentum in the transverse plane. Figure 3.1 gives an overview of the different sub-detectors that each type of particle will interact with in ATLAS. Quark reconstruction and identification is particularly important for this thesis, with di-Higgs decaying to $b\bar{b}b\bar{b}$.

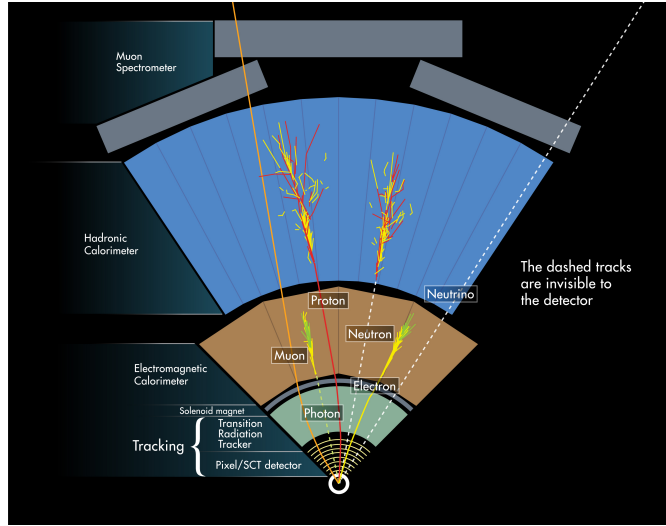


Figure 3.1: Illustration of particle interactions in ATLAS.

3.1 ID TRACKS AND VERTICES

Each beam crossing generates multiple vertices, and the vertices are reconstructed from the available ID tracks. The primary vertex (PV), or the hard-scatter vertex, is selected as the one with the largest $\sum p_T^2$, where the sum is over all tracks with transverse momentum $p_T > 0.4$ GeV that are associated with the vertex. The ID tracks are usually required to have at least 1 PIXEL hit and 6 SCT hits, and to be tightly matched to the primary vertex. The tracks are required to have $p_T > 0.4$ GeV and $|\eta| < 2.5$.

The track reconstruction performance is highly dependent on the momentum of the particle. With higher momentum, the decay tracks have smaller separations in the inner detector, hindering the resolving cluster process, and thus degrading the track identification efficiency. For a 1 TeV b -hadron, the reconstruction track efficiency is 83%, compared to 95% for a 200 GeV b -hadron ⁴⁰.

3.2 JETS

When a quark or gluon is produced in pp collisions, it produces a collimated spray of hadrons, which is known as a jet³. Jets are built from topological clusters of energy deposits in calorimeter cells⁴¹, using a four-momentum reconstruction scheme with massless clusters as input. The directions of jets are corrected to point back to the primary vertex. Typically, jets are reconstructed using the anti- k_t algorithm⁴² with different values of the radius parameter R . R appears in the denominator of the clustering distance metric. This favors clusterings that involve hard particles, and the jets grow outwards around hard “seeds”. It determines the radial size of the jet in η - ϕ plane.

3.2.1 SMALL- R JETS

The jets with $R = 0.4$ (“small- R jets”) are reconstructed from clusters calibrated at the electromagnetic (EM) scale. The jets are corrected for additional energy deposited from pile-up interactions using an area-based correction⁴³. They are then calibrated using p_T - and η -dependent calibration factors derived from simulation, before global sequential calibration⁴⁴ is applied, which reduces differences in calorimeter responses to gluon or quark-initiated jets. The final calibration is based on in situ measurements in collision data⁴⁵.

“Small- R jets” are required to be consistent with the primary vertex, in order to avoid contamination from pileup interactions. The jet vertex fraction (JVF) is a useful variable for this purpose. It is the ratio of tracks associated with a primary vertex to the total number of tracks inside a jet. Jets from the PV should have most tracks consistent with the PV and therefore have a large JVF value.

3.2.2 LARGE- R JETS

The jets with $R = 1.0$ (“large- R jets”) are built from locally calibrated⁴⁴ topological clusters. Two examples are shown in Figure 3.2⁴⁶. Large- R jets are trimmed⁴⁷ to minimize the impact of

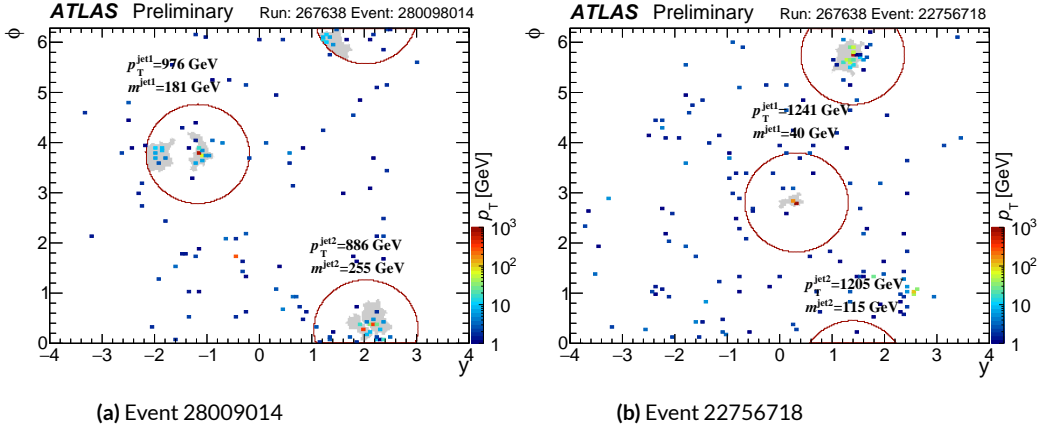


Figure 3.2: Two collision events recorded in June 2015 with a high leading jet p_T shown in rapidity-azimuthal angle parameter space. The dots are calorimeter-cell clusters with positive energy. Only the two leading jets are shown, with their area demarcated by a colored circle, and with grey regions denoting the corresponding k_t sub-jets of size $R_{sub} = 0.2$. The colour of both jets and clusters corresponds to their p_T .

contamination from non-perturbative effects associated with beam-remnants (“pile-up” events).

Trimming proceeds by reclustering the jet with the k_t algorithm⁴⁸ into $R_{sub} = 0.2$ sub-jets and then removing those sub-jets with $p_T^{subjet}/p_T^{jet} < 0.05$, where p_T^{subjet} is the transverse momentum of the sub-jet and p_T^{jet} that of the original jet. Trimming increases the jet mass resolution, as shown in Figure 3.3⁴⁹. The energy and mass scales of the trimmed jets are then calibrated using p_T - and η -dependent calibration factors derived from simulation⁵⁰.

The calorimeter-based jet mass m^{calo} for a large-radius calorimeter jet J is computed from the calorimeter cell cluster constituents i with energy E_i and momentum p_i :

$$m^{calo} = \sqrt{\left(\sum_{i \in J} E_i\right)^2 - \left(\sum_{i \in J} \vec{p}_i\right)^2}. \quad (3.1)$$

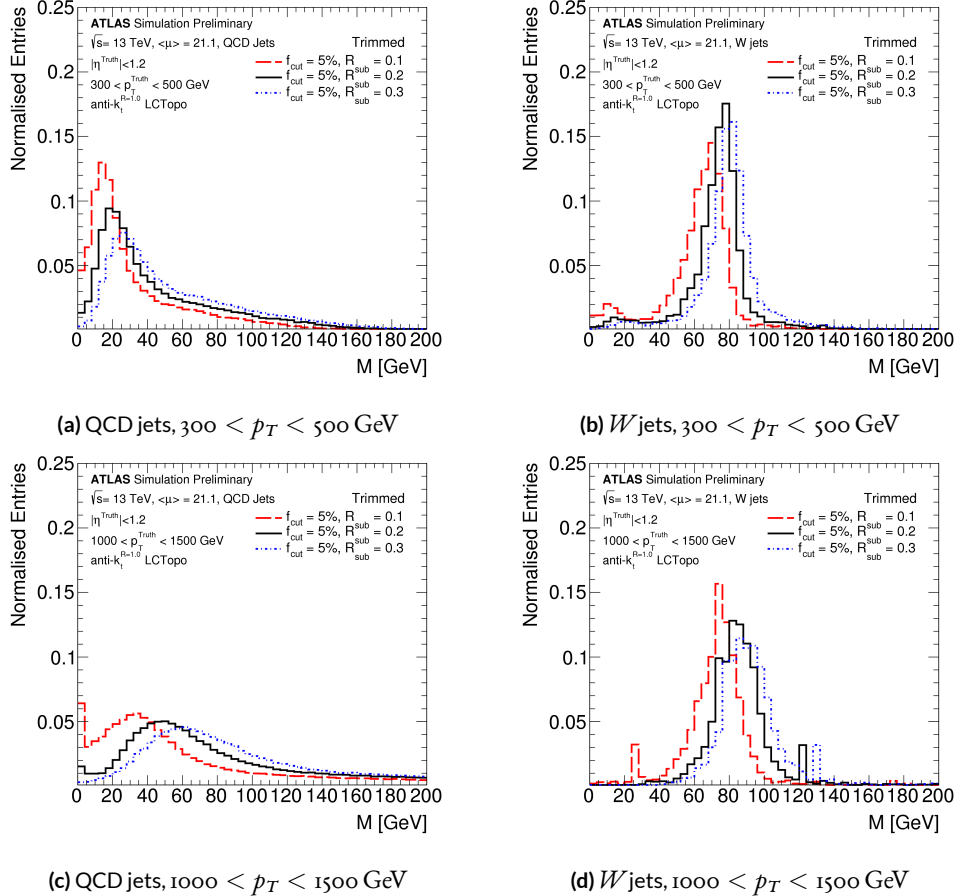


Figure 3.3: For the trimming algorithm using calorimeter cell clusters as inputs to the anti- k_t jet reconstruction algorithm with $R = 1.0$, a comparison of the jet mass distribution for QCD background jets and W boson jets low p_T and high p_T kinematic regions, as determined by the untrimmed truth jet p_T . The trimming parameter choices shown here are $R_{sub} = 0.1, 0.2$, and 0.3 for a fixed cut at 5% .

Tracking information is used to increase the mass resolution. The track-assisted jet mass, m^{TA} , is defined as:

$$m^{TA} = \frac{p_T^{calo}}{p_T^{track}} \cdot m^{track}. \quad (3.2)$$

where p_T^{calo} is the transverse momentum of the large- R calorimeter jet, p_T^{track} is the transverse momentum of the four-vector sum of tracks associated to the large- R calorimeter jet, and m^{track} is the invariant mass of this four-vector sum. This ratio corrects for charged-to-neutral hadron fluctuations, and therefore improves the resolution with respect to track-only jet mass.

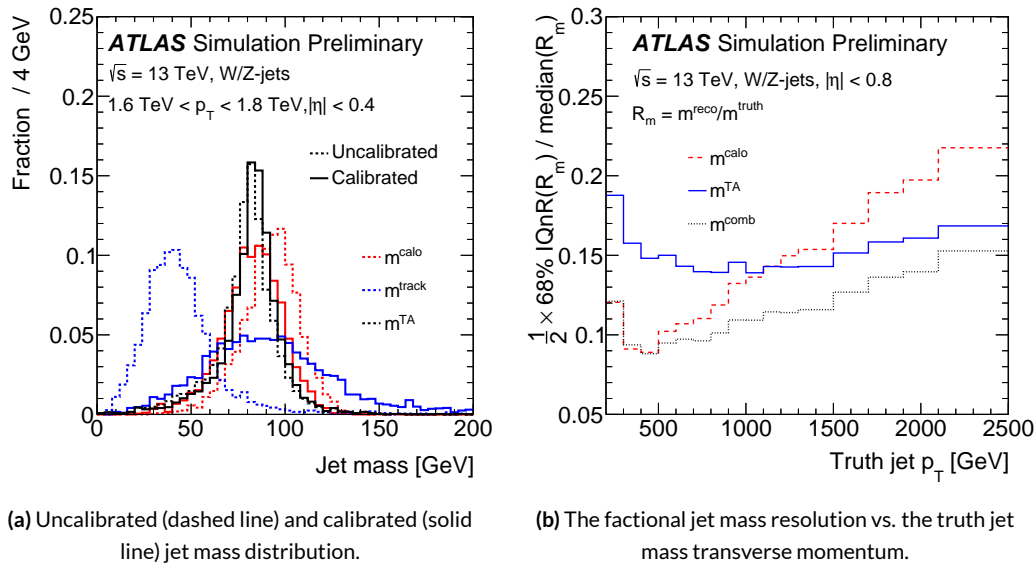


Figure 3.4: Uncalibrated (dashed line) and calibrated (solid line) reconstructed jet mass distribution 3.4a, and the jet mass resolution vs jet p_T 3.4b for calorimeter-based jet mass, m_{calo} (red), track-assisted jet mass m_{TA} (black) and the invariant mass of four-vector sum of tracks associated to the large-radius calorimeter jet m_{track} (blue) for W/Z-jets⁵.

The above two jet mass definitions are only weakly correlated with each other, so they can be linearly combined to the combined mass, m^{comb} , by weighting the components with w :

$$m^{comb} = w \cdot m^{calo} + (1 - w) \cdot m^{TA}. \quad (3.3)$$

where w is determined for each large- R jet from the resolution functions of the calibrated track and calo mass terms. This results in a smaller mass resolution and better estimate of the median mass value than obtained using only calorimeter energy clusters, as shown in Figure 3.4.

3.2.3 TRACK JETS

Track jets are essentially clustered charged hadron tracks. They are reconstructed from ID tracks using the anti- k_t algorithm with a fixed $R = 0.2$. Once the track jet axis is determined, an extra step of track association is performed to select tracks with looser impact parameter requirements, in order to collect the tracks needed for effectively running the b -tagging algorithms. Only track jets with at least two tracks are kept. Track jets are also required to have $p_T > 10$ GeV and $|\eta| < 2.5$, in order to suppress track jets from light flavors.

Track jets are associated to large- R jets using Ghost-Association. “Ghosts” are track jet 4-vectors, with each track jet’s p_T set to an infinitesimal amount, essentially keeping only the direction of the 4-vector. This ensures that Large- R jets reconstruction is not altered by the ghosts when the calorimeter clusters plus ghosts are reclustered. Reclustering is then performed using the anti- k_t algorithm with $R = 1.0$. The calorimeter jets after reclustering are identical to the parents of the trimmed jets used in this analysis, with the addition of the associated track jets retained as constituents. In addition, the track jets corresponding to the ghosts that survive the trimming procedure (and thus are clustered into one of the surviving sub-jets) are the track jets ghost-associated to the trimmed jet. The small radius parameter of the track-jets enables two nearby b -hadrons to be identified when their ΔR separation is small, which is beneficial when reconstructing high- p_T Higgs boson candidates.

3.3 FLAVOR TAGGING

Some jets are formed from quarks with different flavors. Identifying the flavor of a jet is called flavor tagging. Jets originating from a b -quark is referred as a b -jet, from a c -quark is referred as a c -jet, and from a other quarks other than the t -quark is referred as a light jet. b -tagging is particularly useful for this analysis, since there are four b s in the final state.

B -hadrons have a lifetime on the order of 10^{-12} seconds, which makes a flight distance of $0.5\text{ mm}^{\textcolor{red}{1}}$. This results in a displaced decay vertex that can be identified in vertex reconstruction. This allows some b -jets to be distinguished from other flavors of jets theoretically.

ATLAS uses three different basic b -tagging algorithms, which provide complementary information:

- Impact parameter (IP) based algorithm: it uses the transverse and longitudinal impact parameters d_o and z_o of the tracks inside a jet to determine their consistency with the primary vertex. The algorithm uses two or three dimensional templates for light, c , and b jets and evaluates the likelihood of the jet coming from each of these types.
- Inclusive secondary vertex (SV) reconstruction algorithm: it uses tracks inside the jet to fit for vertices that are displaced from the primary vertex. The algorithm provides information on the invariant mass of tracks pointing to same vertex, the number of two track vertices, and the angular separation between the jet and the $\text{PV} \rightarrow \text{SV}$ direction.
- Decay chain multi-vertex reconstruction algorithm, or JetFitter (JF): it reconstructs the full flight path of the b by looking for multiple displaced vertices along the same direction. A Kalman filter is used to find common line for the b and c vertices, and hence the algorithm exploits the topology of the weak b/c -hadron decay chain.

Jets containing b -hadrons are identified using a score value computed from a boosted decision tree(BDT) algorithm $MV_{2c1o}^{\textcolor{red}{6,\texttt{rt}}}$, which makes use of observables provided by three algorithms

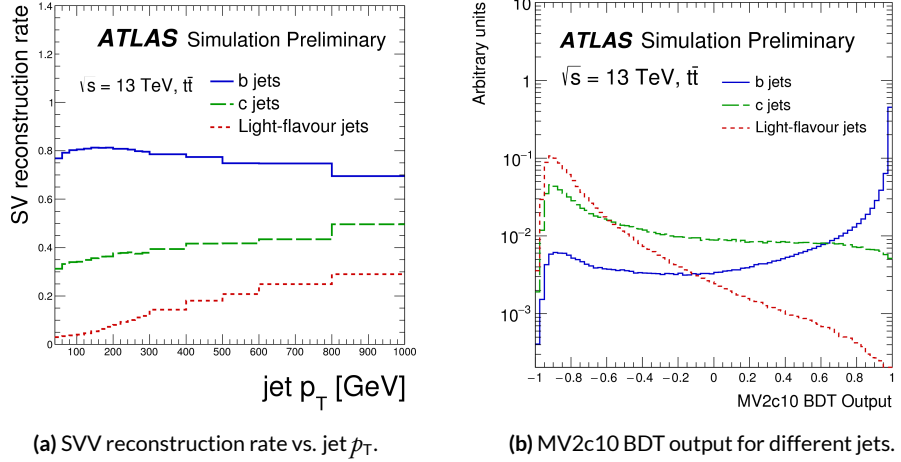


Figure 3.5: Secondary vertex reconstruction rate and MV2c10 output for b-jets (solid blue), c-jets (dashed green) and light-jets (dotted red) evaluated with simulated $t\bar{t}$ events.

above. The $MV2c10$ algorithm is trained on a sample with charm composition of 7%. It is applied to a set of charged-particle tracks that satisfy quality and impact parameter criteria and are matched to each jet. Hence either a small- R jet or a track jet can be b -tagged.

The b -tagging working point (wp) is a fixed cut on the $MV2c10$ value that lead to an efficiency of 70% for b -jets with $p_T > 20 \text{ GeV}$ when evaluated in a sample of simulated $t\bar{t}$ events. This working point corresponds to a rejection rate of jets originating from u, d or s -quarks or gluons of 380 for the jets with $R = 0.4$ and 120 for the track jets. The rejection of jets from c -quarks is 12 for the $R = 0.4$ jets and 7.1 for the track jets.

In this thesis, the track-jets have a wider p_T range, between $50 - 400 \text{ GeV}$, and the same working point leads to b -tagging efficiencies varying from 40% at low p_T , to 80% for p_T values of about 150 GeV, to 60% at high p_T . This can be seen in Figure 3.6. The increase of tracks from fragmentation in the high jet p_T region is the main reason for the performance degradation. As the jet p_T increases, the number of fake vertices is increasing, while the secondary vertex reconstruction efficiency

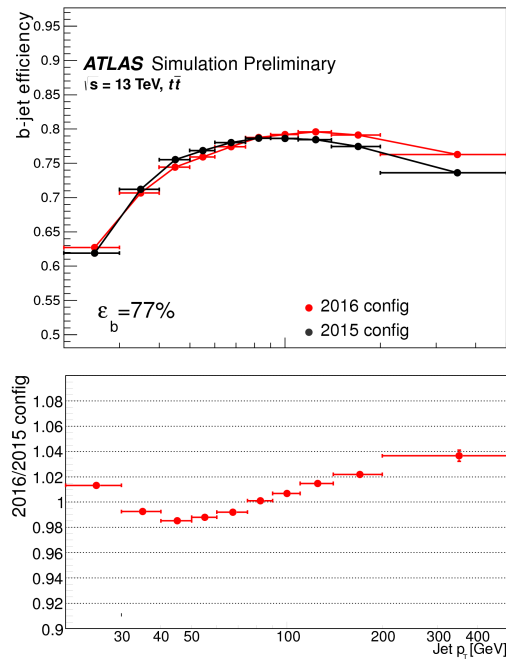


Figure 3.6: b -jet efficiency for the fixed cut working point with a b -jet efficiency of 77% as a function of the jet p_T for the comparison between the MV2c10 b -tagging algorithm employed for the 2016 analyses (2016 config) and the previous version of the tagger, MV2c20 (2015 config), which has 15% c -fraction in the training

for b and c jets decreases with jet p_T . This is shown in Figure 3.7. This non-trivial jet p_T dependence of b -tagging performance is one of the major challenge of this analysis.

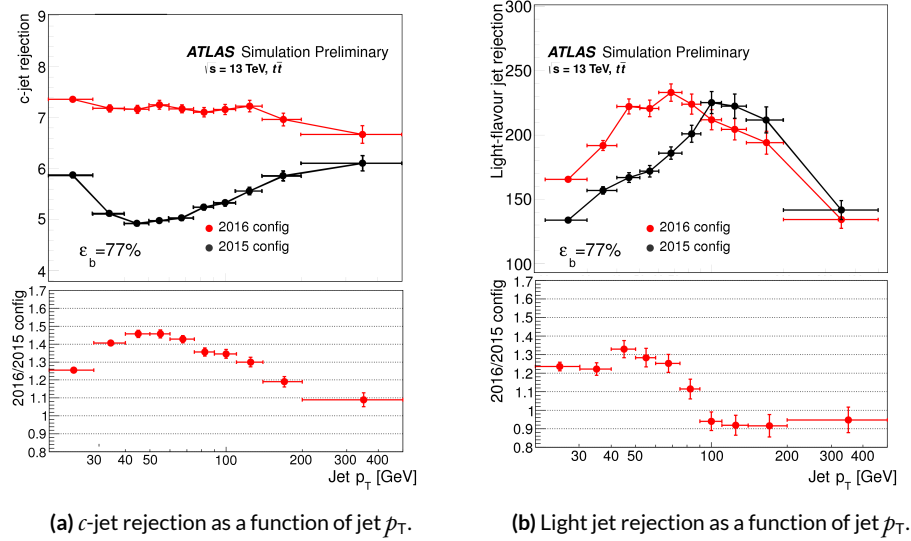


Figure 3.7: Light-flavour jet and c -jet rejection as a function of jet p_T for the previous (2015 config) MV2c20 and the current MV2c10 configuration (2016 config). A fixed cut at 77% b -jet efficiency operating point is used⁶.

Correction factors are applied to the simulated MC samples to compensate for differences between data and simulation in the b -tagging efficiency for b , c and light-jets. The correction for b -jets is derived from $t\bar{t}$ events with final states containing two leptons, and the corrections are consistent with unity with uncertainties at the level of a few percent over most of the jet p_T range.

3.4 LEPTONS

Electron and photon identification is based on matching tracks to energy clusters in the ECAL and relying on the longitudinal and transverse shapes of the EM shower⁵². Well-reconstructed ID tracks matched to EM clusters are classified as electron candidates, while EM clusters without matching tracks are classified as unconverted photon candidates. Clusters matched to a reconstructed con-

version vertex or to pairs of tracks consistent with the conversion hypothesis are classified as converted photon candidates. Electrons and photons are not used in this thesis.

Hadronic tau decays into a tau neutrino and one or three charged pions and up to two neutral pions⁵³. Hence tau reconstruction is seeded by jets, and is matched to one or three associated tracks, with a total electric charge of ± 1 . A Boosted Decision Tree identification procedure, based on calorimetric shower shapes and tracking information is used to reject fakes from jets. Hadronic taus are not used in this thesis.

Neutrinos are inferred from the missing transverse momentum (MET), or E_T^{miss} . Neutrinos do not interact with the ALTAS. Their presence can only be deduced from the conservation of transverse momentum in each collision, as the incoming protons have no net momentum in the transverse plane. MET is calculated as the negative vectorial sum of the p_T of all fully reconstructed and calibrated physics objects. This procedure includes a soft term, which is calculated using the ID tracks that originate from the primary vertex but are not associated with reconstructed objects. MET is not used in this thesis.

Muons are identified by matching ID tracks with reconstructed MS tracks⁵⁴. For this thesis, muons must have $p_T > 4$ GeV, $|\eta| < 2.5$ and to satisfy “medium” muon identification criteria⁵⁴. Muons are used in this thesis, because b hadrons decay to muons with $\sim 20\%$ probability. This will be demonstrated in the later chapters.

Ugliness is in a way superior to beauty because it lasts.

Serge Gainsbourg

4

Data and Simulation

4.1 DATA

This analysis uses 2015 and 2016 LHC $p\bar{p}$ collision datasets at $\sqrt{s} = 13$ TeV recorded by the ATLAS experiment. Data were collected during stable beam conditions and when all relevant detector systems were functional. A Good Run List (GRL) is generated after gathering on-line and off-line data quality reviews of the dataset after reconstruction. Typically, any $> 10\%$ defect in any detector subsystem makes the corresponding Lumiblocks (LB) fail the GRL requirement. The integrated luminosity of the 2015 dataset passing the GRL is 3.2 fb^{-1} , and the 2016 dataset passing a different GRL is 32.9 fb^{-1} . These values are about 82% and 92% of the data ATLAS recorded, in Figure 2.6.

In the resolved analysis, a combination of b -jet triggers is used. Events are required to feature either one b -tagged jet with transverse momentum $p_T > 225$ GeV, or two b -tagged jets, either both satisfying $p_T > 35$ GeV or both satisfying $p_T > 55$ GeV, with different requirements on the b -tagging. Some triggers require additional non- b -tagged jets. Due to a change in the on-line b -tagging algorithm between 2015 and 2016, the two datasets are treated independently until they are combined in the final statistical analysis. After the selection described later, this combination of triggers is estimated to be 65% efficient for simulated signals with a Higgs boson pair invariant mass, m_{HH} , of 280 GeV, rising to 100% efficiency for resonance masses greater than 600 GeV.

During 2016 data-taking, a fraction of the data was affected by a bug. The movement of beam spot was not accounted for in the on-line vertex reconstruction. This reduced the efficiency of the algorithms used to identify b -jets. This reduces the integrated luminosity of the 2016 dataset for the resolved analysis to 24.3 fb^{-1} .

In the boosted analysis, events were selected from the 2015 dataset using a trigger that required a single anti- k_t jet with radius parameter $R = 1.0$ and with $p_T > 360$ GeV. In 2016, a similar trigger was used but with a higher threshold of $p_T > 420$ GeV. The efficiency of these triggers is 100% for simulated signals passing the jet requirements as described later, so the 2015 and 2016 datasets were combined into one dataset.

The data is further skimmed into the Derived Analysis Object Data (DAOD). The ATLAS off-line software 20.7.8.7 derivation cache is used, with version p -tags $p2950$. The boosted slimming keeps events with at least two large- R jets with $p_T > 200$ GeV. The final input data file has name format: *dataYR_13TeV.periodPR.physics_Main.PhysCont.DAOD_EXOT8.grpYR_v01_p2950*, where YR is 15 and PR is DEFGHJ for 2015 data, and YR is 16 and PR is ABCDEFGIKL for 2016 data.

4.2 MC

All Monte Carlo (MC) samples used in this analysis are produced with full simulation. For all simulated samples, charm-hadron and bottom-hadron decays were handled by `EVTGEN 1.2.0`³. To simulate the impact of multiple $p\bar{p}$ interactions that occur within the same or nearby bunch crossings (pile-up), minimum-bias events generated with `PYTHIA 8`⁵⁵ using the A2 set of tuned parameters⁵⁶ were overlaid on the hard-scatter event. The detector response was simulated with `GEANT 4`^{57,58} and the events were processed with the same reconstruction software as that used for the data. Simulated data samples from the ATLAS MC15c campaign are used, corresponding to p -tags p2952–p2949.

4.2.1 BACKGROUNDS

A very small fraction of the background arises from $Z + \text{jets}$ events. The $Z+\text{jets}$ sample was generated using `PYTHIA 8.186` with the NNPDF2.3 LO PDF set.

The $t\bar{t}$ background is modeled using large all-hadronic and non-all-hadronic samples that have both been generated with `POWHEG-BOX v1`⁵⁹ using the CT10 PDF set. The parton shower, hadronization, and the underlying event were simulated using `PYTHIA 6.428` with the CTEQ6L1 PDF set and the corresponding Perugia 2012 set of tuned underlying-event parameters⁶⁰. The t -quark mass in both samples is set to 172.5 GeV. Higher-order corrections to the $t\bar{t}$ cross section were computed with `Top++ 2.0`⁶¹. These incorporate NNLO corrections in QCD, including re-summation of NNLL soft gluon terms. The $t\bar{t}$ MC samples are normalized to the NNLO+NLL predicted inclusive $t\bar{t}$ cross-section of 1821.87 pb multiplied by the all-hadronic branching ratio of 0.457 and non-all-hadronic of 0.543.

In order to keep statistical fluctuations small across the dijet invariant mass spectrum, especially for large values of m_{tt} , additional $t\bar{t}$ samples are generated in slices of $t\bar{t}$ invariant mass. The cross-section of the $t\bar{t}$ process is normalized to NNLO+NNLL in QCD, as calculated by Top++ 2.0. Overlap with the inclusive $t\bar{t}$ samples is removed by a fixed cut on the truth value of m_{tt} at 1100 GeV.

A PYTHIA dijet sample is used to understand the physical processes contributing to the multi-jet background and characteristics of the event selection. This MC sample is generated without a heavy flavor filter, hence is limited by the total generated number of events, given the high background rejection factors of the analysis selection.

4.3 SIGNAL

In all signal samples, the mass of the Higgs boson (m_H) was set to 125 GeV. The signal MC contains truth information, like the two Higgs and the b quark four-momentum before detector interactions. This enables a ΔR truth matching between the reconstructed objects and the Higgs.

SM non-resonant production of Higgs boson pairs via the gluon–gluon fusion process was simulated at NLO with MG5_aMC@NLO, using form factors for the top-quark loop from HPAIR^{62,63}. The simulated events are reweighed to reproduce the m_{hh} spectrum obtained^{64,65}, which calculated the process at NLO in QCD while fully accounting for the top-quark mass. Interference effects between di-Higgs resonant production and SM non-resonant di-Higgs production are not included in the simulated samples.

Signal $G_{KK}^* \rightarrow bb \rightarrow b\bar{b}b\bar{b}$ events were generated at leading order (LO) with MG5_aMC@NLO 2.2.2⁶⁶ interfaced with PYTHIA 8.186 for parton-showering, hadronization and underlying-event simulation. The NNPDF2.3 LO parton distribution function (PDF) set⁶⁷ was used for both MG5_aMC@NLO and PYTHIA. The A14 set of tuned underlying-event parameters was used. These signal samples

were generated with $k/\bar{M}_{\text{Pl}} = 1$ or 2 . Relative to the resonance mass, widths of the graviton signals range from 3% (at low mass) to 13% (at the highest mass) for $k/\bar{M}_{\text{Pl}} = 1$, and 6% to 25% for $k/\bar{M}_{\text{Pl}} = 2$. The graviton samples were normalized using fixed cross sections⁶⁸.

Signal 2HDM Scalar $\rightarrow HH \rightarrow b\bar{b}b\bar{b}$ events were generated at LO in QCD with MG5_aMC@NLO 2.2.3 interfaced with HERWIG++⁶⁹ for parton-showering, hadronization and simulation of the underlying event. CT10⁷⁰ PDF sets were used for MG5_aMC@NLO and CTEQ6L1⁷¹ for HERWIG++. The UE-EE-5-CTEQ6L1 set of tuned underlying-event parameters⁷² was used. The scalar signals were generated with a width of 1 GeV, which represent generic narrow-width scalar signals. Because the width and branching ratios depend on 2HDM parameters, each mass point generated with this fixed width corresponds to a different point in the 2HDM parameter phase space.

Resonant signal samples for the scalar and $k/\bar{M}_{\text{Pl}} = 1$ models were produced in 10 GeV steps between 260 and 300 GeV, in 100 GeV steps up to 1600 GeV, in 200 GeV steps up to 2000 GeV, and in 250 GeV steps up to 3000 GeV. Signal samples for the $k/\bar{M}_{\text{Pl}} = 2$ model were produced with the same spacings but omitting the masses of 270 GeV, 290 GeV and 2750 GeV due to the larger generated width. Unless specified, the MC signal sample used as benchmark is $k/\bar{M}_{\text{Pl}} = 1$ G_{KK}^* , due to its width is medium among the three signal models.

You gotta have a swine to show you where the truffles are.

Edward Albee

5

Event Selection

An example of $X \rightarrow hh \rightarrow b\bar{b}b\bar{b}$ boosted event is shown in Figure 5.1. This chapter explains how this event is selected as a $X \rightarrow hh \rightarrow b\bar{b}b\bar{b}$ candidate.

5.1 DATA CLEANING

The following data cleaning requirements are made:

- Events with problems in SCT/TileCal/LAr are removed.
- Events that fail the jet cleaning procedure are removed. This is designed to exclude jets caused by detector noise, non-collision backgrounds and cosmic rays.
- Incomplete events are removed.

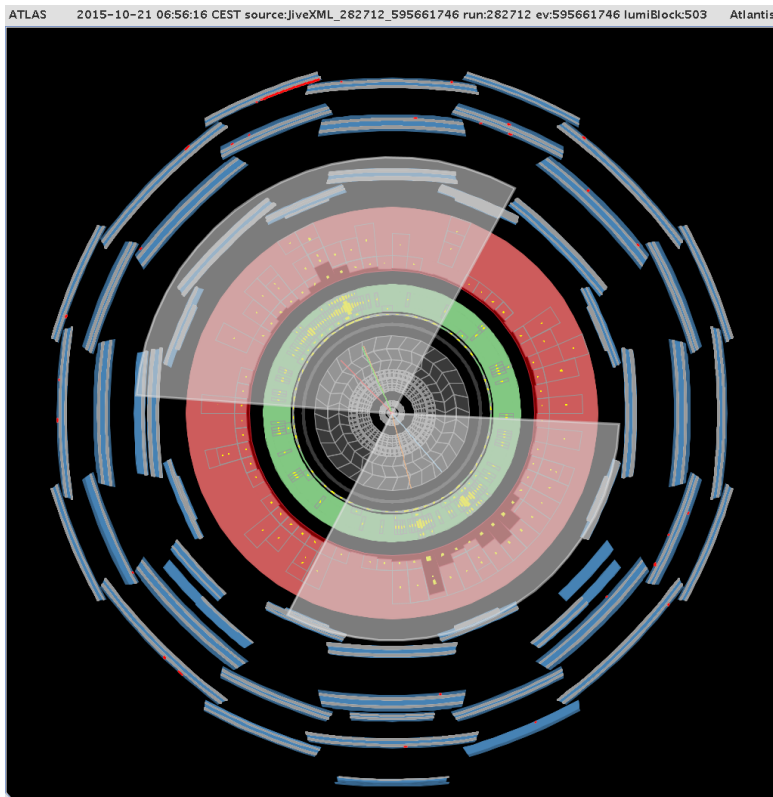


Figure 5.1: 2015 ATLAS boosted di-Higgs event candidate's event display. The data is taken in run 282712, lumiblock 503 and has event number 595661746. ID is in gray, ECAL is in green, HCAL is in red and MS is in blue. Only tracks with $p_T > 25$ GeV are shown. Jets are gray cones, and ID tracks are colored lines in the ID. There are 2 b tagged tracks within each of the large- R jets. The one large- R jet has 119 GeV mass and 543 GeV p_T , and the other one has 127 GeV mass and 413 GeV p_T . The ΔR between the two large- R jets is 3.54 and the invariant mass of the two large- R jets is 1336 GeV.

The analysis also runs over the debug stream, which contains events recorded that couln't be reconstructed on-line due to CPU time constrains. No event passing the full signal selection is found.

5.2 TRIGGER

Events in data and MC are required to pass the lowest unprescaled large- R jet trigger:

`HLT_j360_a10_lcw` in 2015 and `HLT_j420_a10_lcw` in 2016. The triggered jets are topo-cluster jets with local calibration weights and pile-up subtraction. They are seeded by the lowest unprescaled L1 jet trigger, `L1_J100`. LCW cluster trigger is chosen, because the other option, reclustered large- R jet trigger, has slower turn-on in multi-jet events. Other options such as the lowest unprescaled HT trigger, `HLT_ht1000`, has a much slower turn-on compared to large- R jet triggers. Another trigger option is `HLT_4j100`, but because of the boosted jets merging, the trigger efficiency decreases rapidly as the signal mass increases. The results are shown in Figure 5.2.

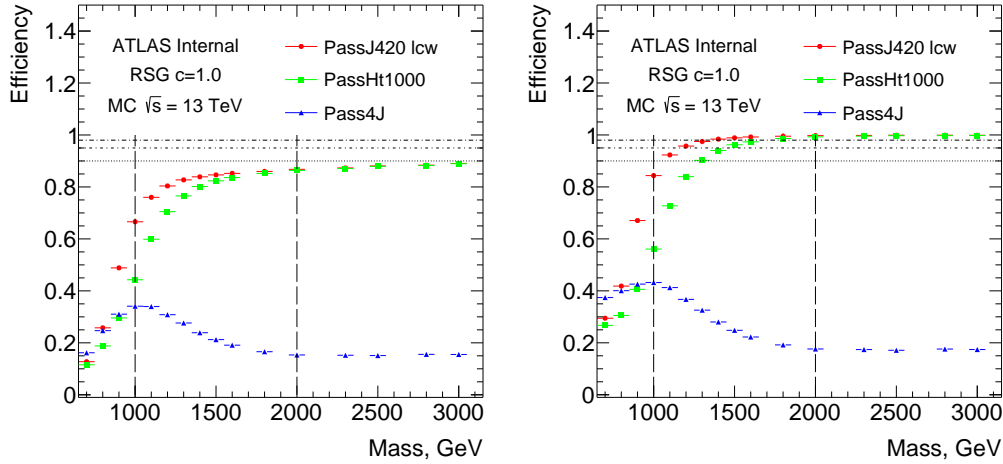


Figure 5.2: Different trigger efficiencies as a function of the signal resonance mass with respect to all events with no selection (left) and with respect to events passing the two large- R jets $p_T > 400$ GeV and leading/subleading jet $p_T > 250$ GeV (right). For 1.4 TeV signal, the trigger efficiency is about 98%.

The selected large- R triggers are found to have $> 98\%$ efficiency for signals with mass above 1400 GeV. The trigger turn-on curve in 2015 and 2016 data, as a function of leading jet p_T , is shown in Figure 5.3.

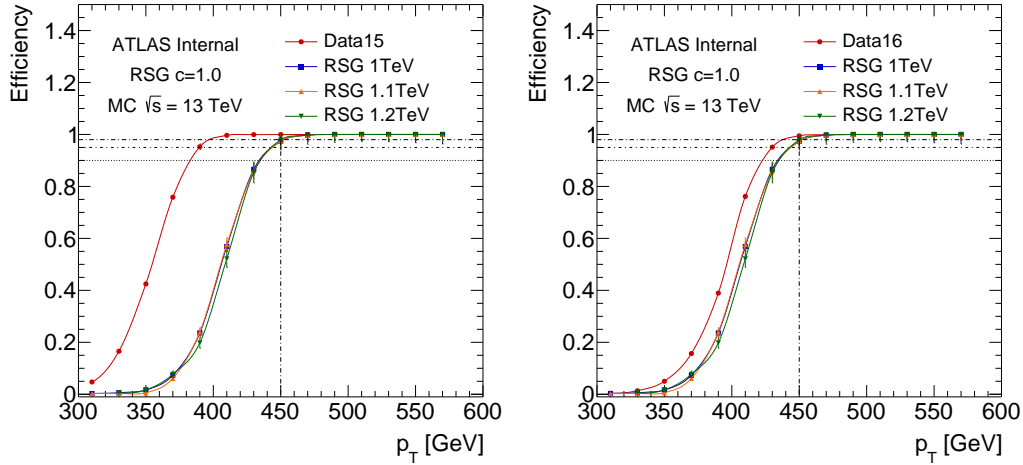


Figure 5.3: Large- R jet trigger efficiencies, defined as the fraction of events fired trigger with a given highest large- R jet p_T , measured in 2015 Data (HLT_j360_a10_lcw, left) and 2016 Data (HLT_j420_a10_lcw, right) and MC.

5.3 OBJECT SELECTION

The specific physics objects used in the boosted analysis are described in previous sections and reiterated in Table 5.1.

Table 5.1: Physics objects and their technical names in the boosted analysis.

object	technical name
large- R calorimeter jets	AntiKt1oLCTopoTrimmedPtFrac5SmallR2oJets
small- R track jets	AntiKt2PV0TrackJets
b-tagging	on track jets, MV2c10, 70% b-tagging wp

Each event must have at least two high momentum large- R jets, each with at least one ghost associated track jets for b -tagging. They are sorted by p_T , and the highest p_T one is named as the leading large- R jet, or the leading Higgs Candidate. The second highest p_T large- R jet is the subleading large- R jet, or the subleading Higgs Candidate. The large- R jets are required to have $p_T > 250$ GeV, $|\eta| < 2$ to guarantee a good overlap with the tracking acceptance, and mass > 50 GeV to avoid over-sized derivations. The leading large- R jet is also required to have $p_T > 450$ GeV to be above the trigger turn on threshold. Only the leading and subleading large- R jets are considered in the rest of this thesis. This selection is $\sim 95\%$ efficient for 1.2 TeV signals, as shown in Figure 5.4. $R = 1.0$ ensures that the two b quarks and their decay products are very likely to be contained within the large- R jet, as shown in Figure 5.5.

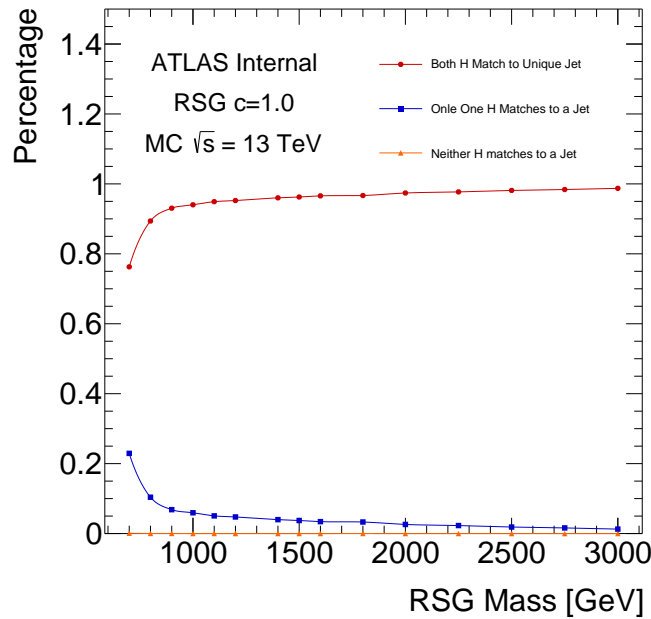


Figure 5.4: Percentages of truth Higgs to large- R jet $\Delta R < 1.0$ matching as a function of G_{KK}^* mass. Both Higgs almost never match to the same large- R jet.

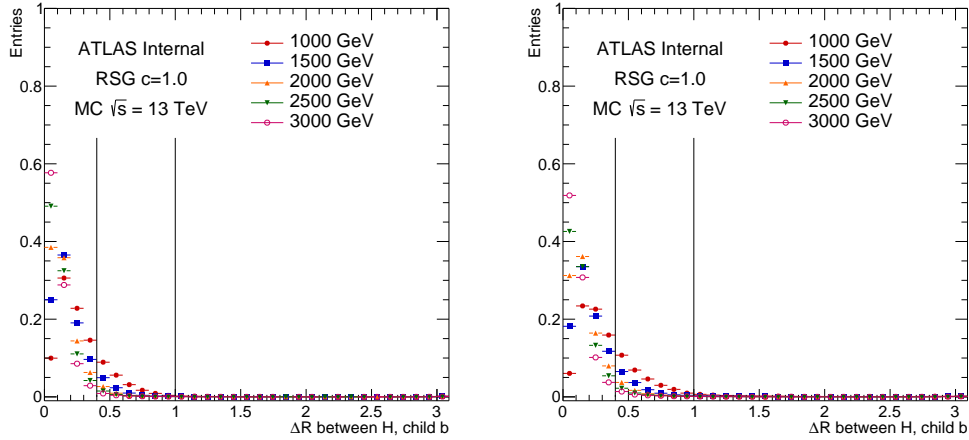


Figure 5.5: Normalized ΔR between the truth Higgs (leading on left, subleading on right) and the truth children b -quarks for G_{KK}^* MCs. Lines are drawn at $\Delta R = 0.4$ (R of small- R jets) and $\Delta R = 1.0$ (R of large- R jets).

The track jets are required to have $p_T > 10 \text{ GeV}$, $|\eta| < 2.5$ and at least two tracks associated with it. A track jet is considered b -tagged if it has $\text{MV}_{2\text{C}10} > 0.6455$, see Section 3.3 for details. Each large- R jet is required to have at least one, not two, track jet Ghost associated with it. This accounts for the $R = 0.2$ track jets merging at really high boost, from signals above 2.5 TeV. If there are more than one track jet contained in the large- R jet, they are also sorted by p_T . The highest p_T track jet is named as the leading track jet, and the second highest p_T one is named as the subleading track jet. Only the two highest p_T track jet is considered in this thesis. The one or two track jets ΔR match to the truth b quarks 80%, as shown in Figure 5.6. In the Figure, red means the truth Higgs doesn't match the large- R jet. Blue means both truth b matches the two track jets. Orange means two truth b matches one same track jet. Green indicates one b quark has $\Delta R < 0.2$ for both leading and sub-leading track jet, and the other b is matched to one of the two track jets. Pink means one b quark matches to one of the two track jets, the other b doesn't match to the two leading track jets.

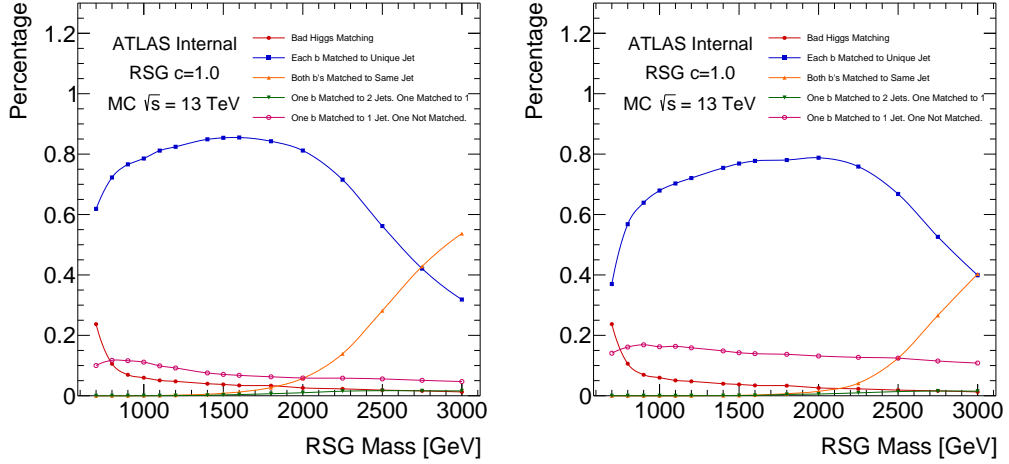


Figure 5.6: Percentage of $\Delta R < 0.2$ matching truth b 's to track jets (leading Higgs on the left, subleading Higgs on the right) for different G_{KK}^* mass. The cases listed in the legend are orthogonal to each other. The cases not listed on the legend (including when a truth b is not contained in the large- R jet) happen in total at most 1.6% of the time for a given G_{KK}^* mass.

A further muon correction accounts for energy loss due to leptonic b -hadron decays with a muon in the final state. The muon-in-jet corrections are applied only after the fiducial large- R jet requirements on p_T and η . The muons are required have $\Delta R < 0.2$ with the b -tagged track jets within each large- R jet. In case more than one muon is found within a track jet, only the muon with the smallest ΔR is considered. If two b -tagged track jets are found to have muons, both corrections are considered. The four-momenta of the matched muon is added to the large- R jet four-momentum, with the muon calorimeter energy deposits subtracted. This correction is only applied to the calorimeter mass portion of the combined mass. The muon-in-jet correction improves the large- R jet mass resolution by approximately 5%, and Figure 5.7 shows the impact of this correction on the 1 TeV G_{KK}^* .

Finally, the Higgs candidates (large- R jets) are also required to have $|\Delta\eta| = |\eta_{\text{leadJ}} - \eta_{\text{subJ}}| < 1.7$. This is because the spin 2 G_{KK}^* are produced mostly through s-channel, while the multijet events could also be produced through t-channels or u-channel. Figure 5.8 shows the distribution for sig-

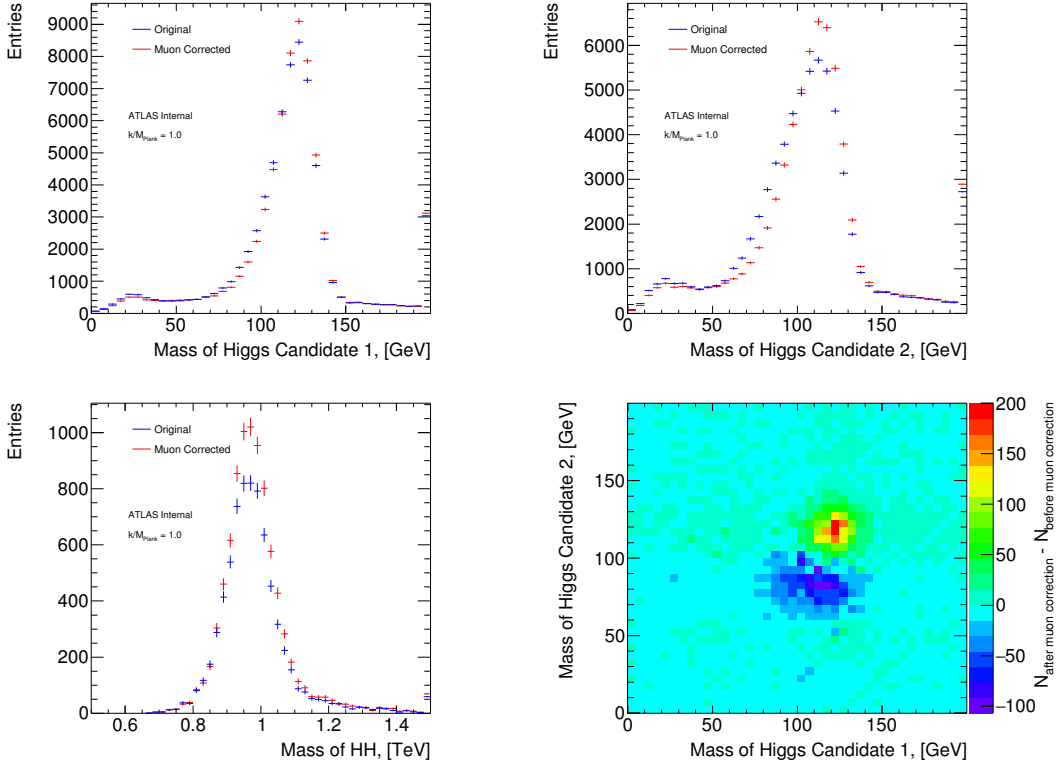


Figure 5.7: Kinematics of 1 TeV G_{KK}^* before and after muon-in-jet corrections. The reconstructed Higgs masses (top row, left for leading large- R jet, right for subleading large- R jet) are closer to 125 GeV after the correction, which improves the signal efficiency for the signal region selection by $\sim 10\%$ (bottom row, left for m_{jj} , right for event distribution differences on the leading-subleading large- R jet mass plane.).

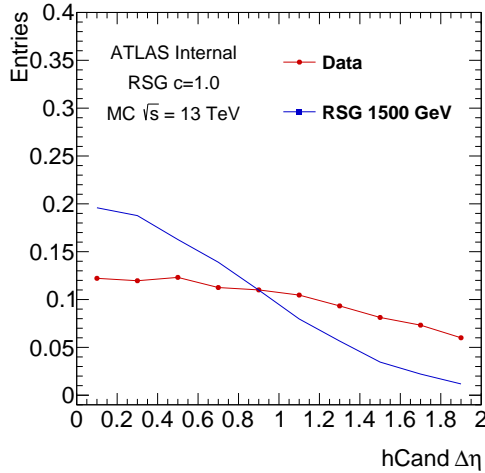


Figure 5.8: After large- R jet requirements, normalized $\Delta\eta_{JJ}$ distribution in $1.5 \text{ TeV } G_{KK}^*$ and data, where the data consists of mostly multijet events ($> 90\%$). The background multijet event is flatter in $\Delta\eta_{JJ}$ distribution.

nal sample and data inclusive b -tag region $\Delta\eta_{JJ}$ distribution. This cut is not entirely optimal for Scalar signals due to the different spin, yet it is fixed for both G_{KK}^* and Scalar selections.

5.4 RESOLVED VETO

Sometimes one event can be reconstructed in both the resolved method as four small- R jets and the boosted method as two large- R jets with track jets. Figure 5.9 shows an example event display of collision data recorded in 2015.

In order to avoid events being reconstructed by both the resolved and the boosted analysis, events that pass the resolved signal region selections are vetoed in the boosted analysis. This is a political decision, and the effect of vetoing boosted event selection in the resolved analysis is never tested. The gain is a full statistical combination of the resolved and boosted result. For boosted analysis, it hurts the sensitivity up to 1.5 TeV for resonance signals. Hence it is necessary to introduce the resolved selection.

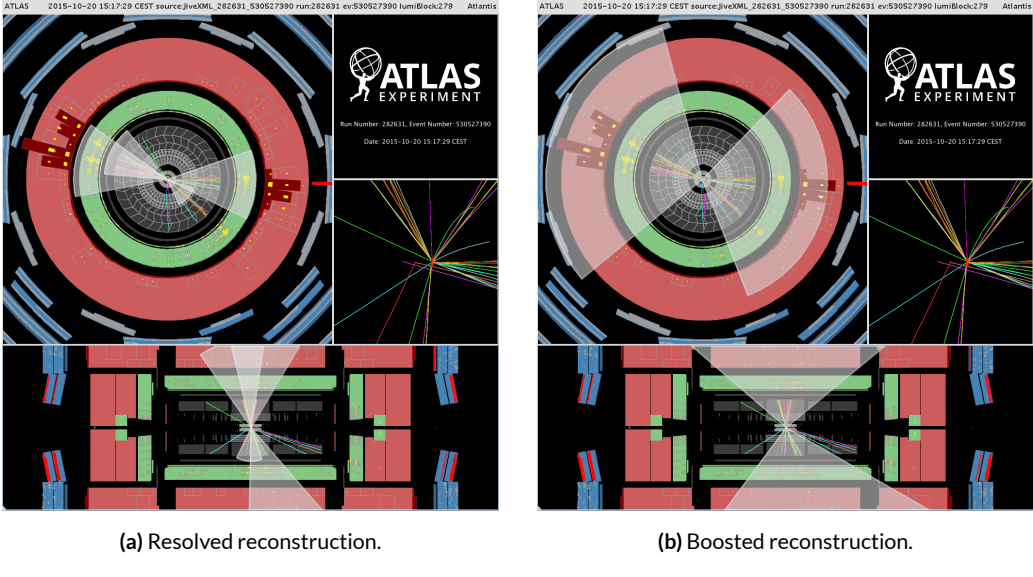


Figure 5.9: Event display of the same event using 5.9a resolved and 5.9b boosted topologies. The resolved reconstruction gives a m_{4j} of 873 GeV, and the boosted reconstruction gives m_{2j} of 852 GeV.

For resolved analysis, four small- R jets with the highest b -tagging score are paired to construct two Higgs boson candidates. Each jet must have $p_T > 40$ GeV, $|\eta| < 2.5$, $\text{MV2c10} > 0.8244$ (small- R jet 70% b -tagging working point). Pairings of jets into Higgs boson candidates are only accepted if they satisfy the following requirements, where m_{4j} is expressed in GeV:

if $m_{4j} < 1250$ GeV:

$$\frac{360 \text{ GeV}}{m_{4j}} - 0.5 < \Delta R_{jj}^{lead} < \frac{653 \text{ GeV}}{m_{4j}} + 0.475; \quad \frac{235 \text{ GeV}}{m_{4j}} < \Delta R_{jj}^{subl} < \frac{875 \text{ GeV}}{m_{4j}} + 0.35 \quad (5.1)$$

if $m_{4j} > 1250$ GeV:

$$0 < \Delta R_{jj}^{lead} < 1; \quad 0 < \Delta R_{jj}^{subl} < 1 \quad (5.2)$$

In these expressions, $\Delta R_{jj,lead}$ is the angular distance between jets in the leading Higgs boson candidate and $\Delta R_{jj,subl}$ for the sub-leading candidate. The leading Higgs boson candidate is defined to be the candidate with the highest scalar sum of jet p_T . This requirement efficiently rejects jet-pairings

where one of the b -tagged jets is not consistent with that originating from a Higgs boson decay. The specific cut values in this and the following requirements were chosen to maximize the sensitivity to the signal.

Also, mass-dependent requirements are made on the leading Higgs boson candidate p_T , and the sub-leading Higgs boson p_T :

$$p_T^{\text{lead}} > 0.5m_{4j} - 105 \text{ GeV}, \quad p_T^{\text{subl}} > 0.33m_{4j} - 75 \text{ GeV} \quad (5.3)$$

where m_{4j} is again expressed in GeV.

A further (m_{4j} -independent) requirement is placed on the pseudorapidity difference between the two Higgs boson candidates, $|\Delta\eta_{bb}| < 1.5$, which rejects multijet events.

$$|\Delta\eta_{bb}| < 1.1 \quad \text{if } m_{4j} < 850 \text{ GeV}, \quad |\Delta\eta_{bb}| < 2 \times 10^{-3}m_{4j} - 0.6 \quad \text{if } m_{4j} > 850 \text{ GeV} \quad (5.4)$$

Events that have multiple Higgs boson candidates satisfying these requirements (which happens often when $m_{4j} < 500$ GeV) necessitate an algorithm to choose the correct pairs. In the absence of energy loss through semi-leptonic decays, the optimal choice would be the combination most consistent with the decays of two particles of equal mass. To account for energy loss, the requirement of equal masses is modified. The distance, D_{bb} , of the pairing's leading and subleading Higgs boson candidate masses, $(m_{2j}^{\text{lead}}, m_{2j}^{\text{subl}})$ from the line connecting $(0 \text{ GeV}, 0 \text{ GeV})$ and $(120 \text{ GeV}, 110 \text{ GeV})$ is computed, and the pairing with the smallest value of D_{bb} is chosen. The values of 120 GeV and 110 GeV are chosen because they correspond to the median values of the narrowest intervals that

contain 90% of the signal in simulations. D_{hh} can be expressed as follows:

$$D_{hh} = \frac{\left| m_{2j}^{\text{lead}} - \frac{120}{\text{no}} m_{2j}^{\text{subl}} \right|}{\sqrt{1 + \left(\frac{\text{no}}{120} \right)^2}}. \quad (5.5)$$

A requirement on the Higgs boson candidates' masses is used to define the resolved signal region:

$$X_{hh-\text{resolved}} = \sqrt{\left(\frac{m_{2j}^{\text{lead}} - 120 \text{ GeV}}{0.1m_{2j}^{\text{lead}}} \right)^2 + \left(\frac{m_{2j}^{\text{subl}} - 110 \text{ GeV}}{0.1m_{2j}^{\text{subl}}} \right)^2} < 1.6, \quad (5.6)$$

where the $0.1m_{2j}$ terms represent the widths of the leading and sub-leading Higgs boson candidate mass distributions, derived from simulation. The signal region is shown as the inner region of Figure ???. In summary, for any event can make a Higgs candidate through the Dhh minimization and passing through the resolved signal region $X_{hh-\text{resolved}}$ cut, it is rejected in the boosted selection.

5.5 2D HIGGS MASS CUT

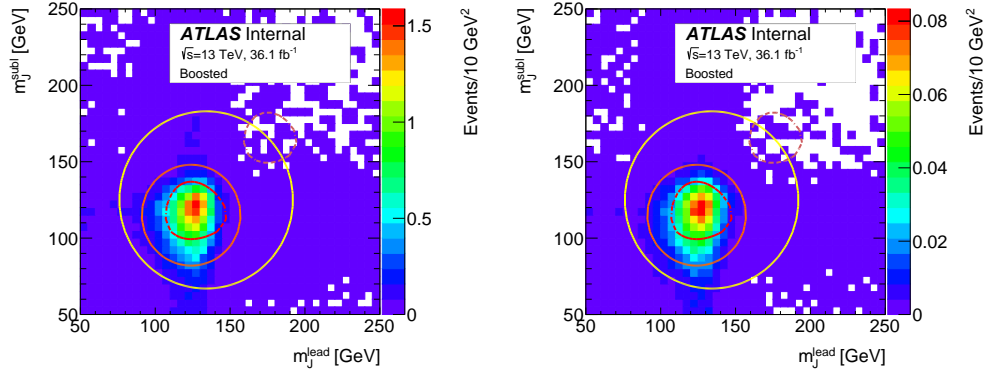


Figure 5.10: For RSG $c = 1.0$ samples, number of events as a function of leading Higgs candidate mass and subleading Higgs candidate mass, for 1.2 TeV (left) signal and 2 TeV (right) signal samples. The red dotted line in the center correspond to the signal region, passing $X_{hh} < 1.6$.

To separate di-Higgs decays from background productions like QCD multi-jets and top, requirements on the leading and subleading large- R jet masses are imposed. The signal region is defined using the expression 5.7:

$$X_{hh} = \sqrt{\left(\frac{m_j^{\text{lead}} - 124 \text{ GeV}}{0.1(m_j^{\text{lead}})}\right)^2 + \left(\frac{m_j^{\text{subl}} - 115 \text{ GeV}}{0.1(m_j^{\text{subl}})}\right)^2} \quad (5.7)$$

The denominator of each term in X_{hh} can be interpreted as a resolution on the reconstructed mass of 10% for the leading and subleading jets, hence X_{hh} can be interpreted as a χ^2 compatibility with the di-Higgs hypothesis. The subleading jet mass value of 115 GeV is chosen after investigating the signal jet masses in MC. The subleading large- R jet typically has a reconstructed mass which is biased downward. This is partly due to the ordering of the large- R jets in p_T , which makes the subleading jet towards lower energy. The energy losses from neutrinos in leptonic b decays, cracks in the calorimeter, and other effects also contributes. The signal region requires $X_{hh} < 1.6$. This cut gives nearly optimal performance. A more optimal signal region definition, using asymmetric signal jet mass resolution and a momentum dependent cut accounting for the higher mass resolution of larger p_T jets, can improve the overall sensitivity by 2 – 8%. Since the gain in sensitivity is small, the signal region is kept to be consistent with the $X_{hh}-\text{resolved}$. Figure 5.10 shows the G_{KK}^* MC m_{2j}^{lead} - m_{2j}^{subl} 2D distribution.

5.6 NUMBER OF b -TAGGING REQUIREMENT

Passing basic object selection and X_{hh} cut, the signal region selection is defined by further requiring multiple b -tags which are consistent with the di-Higgs decay. The presence of two $b \rightarrow b\bar{b}$ decays in the final state naturally suggests requiring 4 track jets passing b -tagging requirements, and this is defined as the $4b$ selection.

The $4b$ requirement has an overall efficiency of roughly ε^4 , where ε is the b -tagging efficiency chosen to be 70%. This means an overall $0.7^4 \sim 0.24$ probability, but having one actual b -jet failing while the other three pass has probability $3 \times 0.7^3 \times (1 - 0.7) \sim 0.31$. Therefore, a $3b$ selection is also introduced to recover the signal efficiency. An event with $3b$ -tags must have at least $3b$ -tagged track jets, but can have any number of additional un-tagged track jets. In $4b$ and $3b$, each Higgs candidate can have at most two b -tagged track jets, hence $\geq 3b$ -tagged track jets cannot be in the same large- R jet.

At the highest resonance mass, the Lorentz boost of the Higgs boson can be large enough to collimate the daughter b -quarks below the distance scale resolvable by the track jets ($R = 0.2$). A third signal region is denoted by two-tag-split or simply $2bs$. It requires exactly one b -tagged track jet is found in each Higgs candidate, plus an arbitrary number of track jets that must fail the b -tag.

$4b$, $3b$, and $2bs$ regions are chosen as three signal regions, also referred to as n - b tag regions. The other b -tagging situations, also referred to as lower- b tag regions, are also sorted and studied. $2b$ region is defined as one large- R jet has two b -tagged track jets, and the other large- R jet has no b -tagged track jet. $1b$ region is defined as one large- R jet has one and only one b -tagged track jets, and the other large- R jet has no b -tagged track jet. $0b$ region is defined as both large- R jets have no b -tagged track jet. They all have relatively small signal acceptance.

The MC events passing all signal region selections are sorted into different b -tagging categories. This is shown in Figure 5.11. For masses above 2.5 TeV, the $2bs$ region (where each large- R jet has exactly one b -tagged track jet) significantly improves the acceptance.

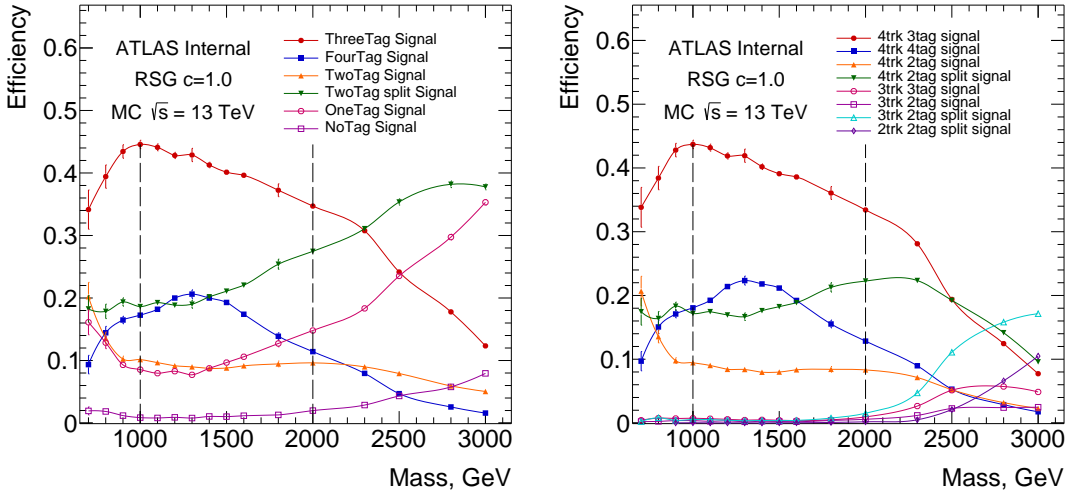


Figure 5.11: Signal fraction in different b -tag categories (left) and detailed fraction in different number of track jet and b -tag categories (right) as a function of signal resonance mass hypothesis for selection cuts. The efficiencies are relative to the total number of events passing the 2D mass cut.

5.7 SIGNAL EFFICIENCY AND CUTFLOW

Acceptance means purely geometric fiducial volume of the detector. Efficiency refers to purely detector effectiveness in finding objects. The signal efficiency as a function of G_{KK}^* resonance mass is shown in Figure 5.12, both for the absolute signal efficiency and for the efficiency relative to the previous cut in the selection. Above a mass of ~ 1 TeV, the reconstruction of high momentum large- R jets with small $\Delta\eta$ is efficient. Across the mass range considered, the signal jet masses requirement (X_{hh}) and b -tagging requirements are $\mathcal{O}(20\%)$ efficient relative to the previous cuts.

The selection efficiency at various stages for G_{KK}^* with $c = 1.0$, G_{KK}^* with $c = 2.0$, and Heavy Scalar signal samples of all mass points can be found in Table 5.2, 5.3 and 5.4.

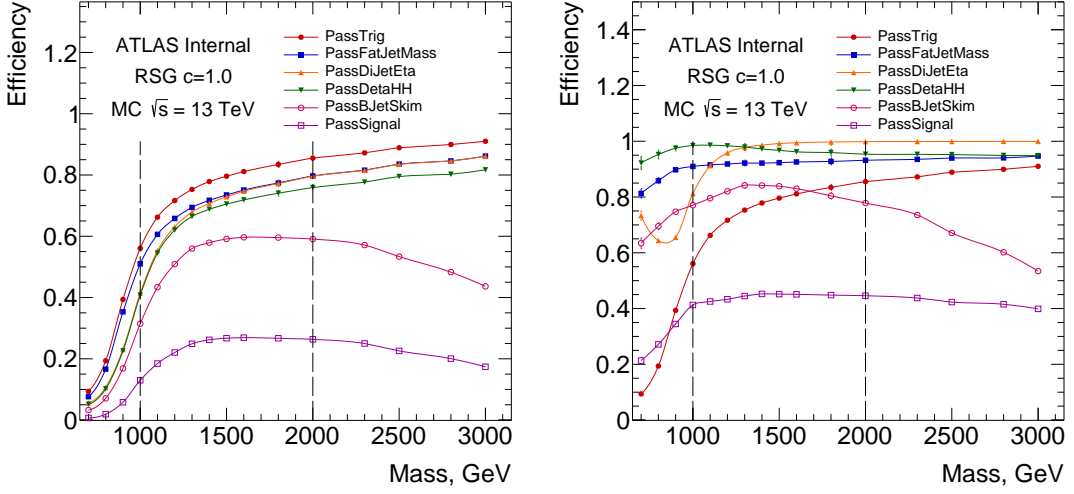


Figure 5.12: Absolute (left) and relative (right) signal efficiency as a function of RSG $c=1.0$ signal resonance mass hypothesis for selection cuts. The relative efficiency is defined from the previous cut, where the order of cuts is given by the legend. PassTrig means the event passes the trigger selection; PassFatJetPt means the event passes the leading and sub-leading jet p_T cuts; PassDiJetEta means the event passes the leading and sub-leading jet η cuts; PassDataH means the events passes the $|\Delta\eta| < 1.7$ cut; PassBJetSkim means the event contains at least two b -tagged track jets, inclusive of $2b, 2bs, 3b$ and $4b$ configurations; PassSignal means the event passes the signal region cut $X_{hh} < 1.6$.

Table 5.2: The selection efficiency for $G_{KK}^* \rightarrow hh \rightarrow b\bar{b}b\bar{b}$ events ($c = 1.0$) at each stage of the event selection. Uncertainties are the MC stat uncertainty only.

Resonance Mass [GeV]	Mini-ntuple Skimming	2 large-R jets	$\Delta\eta$	$X_{hh} < 1.6$	2bs SR	3b SR	4b SR
500	317.31 ± 6.0	295.75 ± 5.79	164.5 ± 4.32	8.45 ± 0.99	1.08 ± 0.37	2.14 ± 0.52	0 ± 0
600	269.07 ± 3.64	247.94 ± 3.5	136.31 ± 2.59	11.31 ± 0.76	2.57 ± 0.37	3.84 ± 0.45	0.66 ± 0.19
700	253.68 ± 3.35	226.93 ± 3.16	124.83 ± 2.35	16.79 ± 0.86	3.74 ± 0.42	6.99 ± 0.56	1.91 ± 0.29
800	286.26 ± 2.28	245.36 ± 2.11	129.2 ± 1.53	24.41 ± 0.67	5.11 ± 0.31	11.27 ± 0.46	4.13 ± 0.27
900	306.51 ± 1.61	275.57 ± 1.52	158.03 ± 1.15	40.72 ± 0.59	8.81 ± 0.28	19.76 ± 0.41	7.5 ± 0.25
1000	238.2 ± 0.98	226.98 ± 0.96	165.2 ± 0.82	52.86 ± 0.47	10.87 ± 0.22	26.0 ± 0.33	10.07 ± 0.2
1100	164.5 ± 0.63	160.94 ± 0.63	132.53 ± 0.57	45.26 ± 0.34	9.55 ± 0.16	21.88 ± 0.23	9.03 ± 0.14
1200	109.24 ± 0.41	107.92 ± 0.4	93.45 ± 0.38	33.53 ± 0.23	6.96 ± 0.11	15.8 ± 0.16	7.38 ± 0.1
1300	72.72 ± 0.59	72.2 ± 0.59	63.74 ± 0.56	24.19 ± 0.35	5.02 ± 0.17	11.33 ± 0.24	5.45 ± 0.16
1400	48.83 ± 0.17	48.61 ± 0.17	42.96 ± 0.16	16.62 ± 0.1	3.72 ± 0.052	7.61 ± 0.07	3.68 ± 0.046
1500	33.13 ± 0.12	33.02 ± 0.12	29.25 ± 0.11	11.31 ± 0.07	2.67 ± 0.036	5.08 ± 0.047	2.44 ± 0.031
1600	22.81 ± 0.08	22.75 ± 0.08	20.16 ± 0.075	7.74 ± 0.048	1.93 ± 0.025	3.48 ± 0.032	1.53 ± 0.02
1800	11.2 ± 0.1	11.18 ± 0.1	9.93 ± 0.094	3.71 ± 0.059	1.1 ± 0.034	1.6 ± 0.038	0.6 ± 0.022
2000	5.72 ± 0.021	5.71 ± 0.021	5.07 ± 0.019	1.83 ± 0.012	0.6 ± 0.0072	0.76 ± 0.0076	0.25 ± 0.0041
2250	2.61 ± 0.0088	2.61 ± 0.0088	2.32 ± 0.0083	0.78 ± 0.005	0.31 ± 0.0032	0.3 ± 0.003	0.078 ± 0.0014
2500	1.24 ± 0.0054	1.24 ± 0.0054	1.11 ± 0.0051	0.33 ± 0.0028	0.16 ± 0.002	0.11 ± 0.0016	0.021 ± 0.00066
2750	0.6 ± 0.0026	0.6 ± 0.0026	0.54 ± 0.0025	0.14 ± 0.0013	0.081 ± 0.00099	0.038 ± 0.00065	0.0055 ± 0.00024
3000	0.3 ± 0.0011	0.3 ± 0.0011	0.27 ± 0.0011	0.058 ± 0.00051	0.039 ± 0.00041	0.013 ± 0.00023	$0.0016 \pm 8e-05$

Table 5.3: The selection efficiency for $G_{KK}^* \rightarrow hh \rightarrow bbbb$ events ($c = 2.0$) at each stage of the event selection. Uncertainties are the MC stat uncertainty only.

Resonance Mass [GeV]	Mini-ntuple Skimming	2 large-R jets	$\Delta\eta$	Xhh < 1.6	2bs SR	3b SR	4b SR
500	3705.15 ± 40.86	3479.44 ± 39.59	2325.18 ± 32.37	568.04 ± 16.17	122.56 ± 7.76	253.49 ± 10.78	100.7 ± 6.53
600	2549.14 ± 22.55	2374.01 ± 21.76	1591.92 ± 17.82	396.96 ± 9.03	89.01 ± 4.46	178.63 ± 6.05	74.31 ± 3.71
700	1928.4 ± 13.57	1782.85 ± 13.04	1183.86 ± 10.63	320.53 ± 5.62	71.38 ± 2.76	148.41 ± 3.81	59.31 ± 2.31
800	1595.14 ± 8.82	1457.71 ± 8.43	958.89 ± 6.84	268.75 ± 3.67	64.14 ± 1.86	123.48 ± 2.47	49.43 ± 1.51
900	1264.78 ± 5.77	1179.88 ± 5.58	819.75 ± 4.65	251.29 ± 2.61	55.63 ± 1.27	119.44 ± 1.79	48.72 ± 1.11
1000	891.0 ± 3.66	856.95 ± 3.59	662.54 ± 3.15	219.04 ± 1.84	49.45 ± 0.91	104.31 ± 1.26	42.97 ± 0.78
1100	595.58 ± 2.98	581.72 ± 2.95	481.67 ± 2.68	167.96 ± 1.61	37.64 ± 0.79	78.28 ± 1.09	34.59 ± 0.7
1200	390.84 ± 1.69	385.41 ± 1.68	330.23 ± 1.55	118.0 ± 0.94	26.23 ± 0.46	54.18 ± 0.64	25.34 ± 0.42
1300	257.66 ± 0.94	255.35 ± 0.94	222.37 ± 0.88	82.11 ± 0.54	19.04 ± 0.27	37.8 ± 0.37	16.99 ± 0.23
1400	172.09 ± 0.72	171.02 ± 0.71	150.22 ± 0.67	56.23 ± 0.42	13.6 ± 0.22	25.36 ± 0.28	11.78 ± 0.18
1500	116.25 ± 0.41	115.72 ± 0.41	101.92 ± 0.39	38.5 ± 0.24	9.94 ± 0.13	17.04 ± 0.16	7.64 ± 0.1
1600	80.09 ± 0.28	79.82 ± 0.28	70.48 ± 0.26	26.24 ± 0.16	7.01 ± 0.09	11.62 ± 0.11	4.92 ± 0.067
1800	38.99 ± 0.14	38.9 ± 0.14	34.39 ± 0.13	12.65 ± 0.081	3.82 ± 0.047	5.46 ± 0.053	2.02 ± 0.03
2000	19.94 ± 0.088	19.91 ± 0.088	17.68 ± 0.083	6.17 ± 0.05	2.15 ± 0.031	2.52 ± 0.032	0.85 ± 0.017
2250	9.02 ± 0.031	9.01 ± 0.031	7.99 ± 0.029	2.62 ± 0.017	1.03 ± 0.011	1.02 ± 0.01	0.28 ± 0.0051
2500	4.28 ± 0.016	4.28 ± 0.016	3.8 ± 0.015	1.13 ± 0.0083	0.52 ± 0.0058	0.4 ± 0.0048	0.098 ± 0.0022
3000	1.07 ± 0.004	1.07 ± 0.004	0.96 ± 0.0038	0.23 ± 0.0019	0.13 ± 0.0015	0.062 ± 0.00097	0.013 ± 0.00043

Table 5.4: The selection efficiency for $H \rightarrow hh \rightarrow b\bar{b}b\bar{b}$ events at each stage of the event selection.

Resonance Mass [GeV]	Mini-ntuple Skimming	2 large-R jets	$\Delta\eta$	Xhh < 1.6	2bs SR	3b SR	4b SR
500	1557.94 ± 136.12	1022.77 ± 110.29	95.14 ± 33.64	11.69 ± 11.69	0 ± 0	11.69 ± 11.69	0 ± 0
600	3289.78 ± 123.99	2542.11 ± 108.99	485.99 ± 47.66	54.55 ± 15.77	18.73 ± 9.39	9.17 ± 6.49	0 ± 0
700	4655.21 ± 94.59	3855.64 ± 86.09	1237.8 ± 48.78	142.42 ± 17.03	28.55 ± 7.74	52.6 ± 10.75	7.69 ± 3.85
800	7506.31 ± 81.79	6020.56 ± 73.25	2150.64 ± 43.78	320.63 ± 17.02	67.63 ± 7.83	139.97 ± 11.23	47.57 ± 6.75
900	9732.89 ± 61.17	8400.91 ± 56.83	3574.63 ± 37.07	806.13 ± 17.76	188.71 ± 8.71	377.92 ± 12.12	127.7 ± 6.99
1000	7516.07 ± 37.72	7033.18 ± 36.49	4496.85 ± 29.18	1351.1 ± 16.2	303.71 ± 7.88	650.89 ± 11.19	234.2 ± 6.57
1100	4731.39 ± 21.54	4563.4 ± 21.15	3485.58 ± 18.49	1135.18 ± 10.7	251.77 ± 5.18	539.51 ± 7.36	215.39 ± 4.5
1200	2853.51 ± 12.23	2782.42 ± 12.07	2253.95 ± 10.87	786.92 ± 6.53	175.53 ± 3.21	366.01 ± 4.44	158.29 ± 2.8
1300	1700.83 ± 7.01	1668.05 ± 6.94	1362.91 ± 6.27	494.36 ± 3.84	107.0 ± 1.86	224.19 ± 2.58	107.55 ± 1.7
1400	1016.14 ± 4.03	999.98 ± 4.0	802.44 ± 3.59	296.46 ± 2.22	65.49 ± 1.1	133.86 ± 1.49	65.58 ± 0.99
1500	621.34 ± 2.41	613.46 ± 2.39	484.92 ± 2.13	179.29 ± 1.32	42.75 ± 0.68	79.32 ± 0.88	36.77 ± 0.56
1600	386.3 ± 1.46	382.44 ± 1.46	297.63 ± 1.28	109.99 ± 0.8	27.68 ± 0.42	49.3 ± 0.53	20.92 ± 0.32
1800	154.8 ± 0.58	153.5 ± 0.57	116.52 ± 0.5	42.24 ± 0.31	12.41 ± 0.18	18.2 ± 0.2	6.66 ± 0.11
2000	65.4 ± 0.24	65.02 ± 0.24	48.57 ± 0.2	16.89 ± 0.12	5.64 ± 0.076	7.01 ± 0.079	2.18 ± 0.041
2250	23.84 ± 0.085	23.73 ± 0.085	17.44 ± 0.073	5.57 ± 0.042	2.25 ± 0.028	2.11 ± 0.025	0.52 ± 0.012
2500	9.2 ± 0.032	9.17 ± 0.032	6.72 ± 0.028	1.9 ± 0.015	0.92 ± 0.011	0.64 ± 0.0086	0.11 ± 0.0034
2750	3.73 ± 0.013	3.73 ± 0.013	2.71 ± 0.011	0.63 ± 0.0054	0.37 ± 0.0042	0.17 ± 0.0027	0.021 ± 0.00093
3000	1.59 ± 0.0054	1.59 ± 0.0054	1.15 ± 0.0046	0.22 ± 0.0021	0.15 ± 0.0017	0.044 ± 0.0009	0.0038 ± 0.00025

*Even in the darkest night. Stars and angels still shine
bright.*

Bear

6

Background Estimation

6.1 OVERVIEW

The invariant mass of the two-Higgs-boson-candidate system, m_{2J} , is used as the final discriminant between Higgs boson pair production and the SM backgrounds. Multi-jet (QCD) is the dominant background. About 40% the QCD events are $gg \rightarrow b\bar{b}b\bar{b}$, and 60% $gg \rightarrow c\bar{c}c\bar{c}$ or $gg \rightarrow q\bar{q}q\bar{q}$ fakes multiple b s. There is no accurate nor high-statistics MC with three or four b -jets collected into two high- p_T large- R jets. Therefore, a data-driven method is used for estimating both the yield and kinematic distribution of the QCD events. For $t\bar{t}$ background, reasonably sized MC samples are available. They provide $t\bar{t}$ kinematic distributions. The $t\bar{t}$ yield is also estimated using a data-driven method to avoid mis-modeling in the MC. The Z +jets background is small, and it estimated by the

Z +heavy flavor jets MC. The SM $ZZ \rightarrow b\bar{b}b\bar{b}$ has been estimated to be completely negligible using a particle-level analysis. For the three signal regions in number of b -tags, the fraction of expected backgrounds are:

- $4b$: QCD $\sim 95\%$, $t\bar{t} \sim 5\%$, $Z+\text{jets} < 1\%$.
- $3b$: QCD $\sim 90\%$, $t\bar{t} \sim 10\%$, $Z+\text{jets} < 1\%$.
- $2bs$: QCD $\sim 80\%$, $t\bar{t} \sim 20\%$, $Z+\text{jets} < 1\%$.

The shapes of the QCD background is estimated from signal depleted data regions. These regions are selected with the signal region selection, except they must have lower number of b -tagged track jets. The differences in kinematic distributions between the lower-tagged and n -tag regions are corrected by reweighting the lower-tagged sample.

The less b -tagged regions only estimate the shapes of the expected background, but not the total yield. The *sideband region* (SB), with the same number of b -tags as the signal regions but a cut on $m_j^{\text{lead}} - m_j^{\text{subl}}$ different from the X_{bb} cut, is used to estimate the yield. A third region, called the *control region* (CR), is used to validate the background estimations. The sideband and control regions are optimized to accurately estimate the rate of QCD and $t\bar{t}$ background.

The definition of SB and CR is introduced in section 6.2. The QCD and $t\bar{t}$ background shape templates are introduced in section 6.3 and section 6.4. The normalization estimation for QCD and $t\bar{t}$ is introduced in section 6.5. The reweighting procedure is explained in section 6.6. The SR prediction is further rescaled and smoothed, discussed in section 6.9. The SB and CR distributions are shown in section 6.7, section 6.8. The yields are listed section 6.10.

6.2 DEFINITION OF THE SIDEBAND AND CONTROL REGIONS

A circular variable R_{hh} is defined in the 2D $m_J^{\text{lead}}\text{-}m_J^{\text{subl}}$ mass plane. It has the same central values as X_{hh} , but without resolution terms in the denominators:

$$R_{hh} = \sqrt{(m_J^{\text{lead}} - 124 \text{ GeV})^2 + (m_J^{\text{subl}} - 115 \text{ GeV})^2} \quad (6.1)$$

Similarly, R_{hh}^{high} , the circular region with the previous central values shifted up by 10 GeV, is defined as:

$$R_{hh}^{\text{high}} = \sqrt{(m_J^{\text{lead}} - 134 \text{ GeV})^2 + (m_J^{\text{subl}} - 125 \text{ GeV})^2} \quad (6.2)$$

The definitions of the SB, CR, and SR in the 2D $m_J^{\text{lead}}\text{-}m_J^{\text{subl}}$ plane are listed in Table 6.1. These regions are shown in Figure 6.1. This Figure also shows the QCD background rate is decreasing from the low $m_J^{\text{lead}}\text{-}m_J^{\text{subl}}$ mass region to high $m_J^{\text{lead}}\text{-}m_J^{\text{subl}}$ mass region on the 2D plane. The $t\bar{t}$ background is also distinguishable as the vertical cyan band where $m_J^{\text{lead}} \sim 173$ GeV.

Table 6.1: Definitions of the signal region, the control region and the sideband region.

Region	Definition
Signal region (SR)	$X_{hh} < 1.6$
control region (CR)	$R_{hh} < 33 \text{ GeV}$ and $X_{hh} > 1.6$
sideband region (SB)	$33 \text{ GeV} < R_{hh}$ and $R_{hh}^{\text{high}} < 58 \text{ GeV}$

The CR is as close to the signal region as possible. The ring shape around the SR allows a good test for the background predictions with all $m_J^{\text{lead}}\text{-}m_J^{\text{subl}}$ combinations, and avoids too few or too many $t\bar{t}$ events. The current CR gives $N_{CR} \sim 2N_{SR}$, which contains good statistics, and not affecting the SB design.

The SB must be a reasonable approximation for the QCD events contained in the CR and SR. It is therefore chosen as the ring outside the CR regions. The shift upwards in R_{bb}^{high} center helps to contain enough $t\bar{t}$ events in the normalization estimates. A larger SB will potentially increase the kinematic differences between different QCD processes in CR/SR and SB. Intrinsically, different $m_J^{\text{lead}} - m_J^{\text{subl}}$ reflects of different portion of $g \rightarrow b\bar{b}$ and $g \rightarrow c\bar{c}/q\bar{q}$ events. This kinematic bias should be reduced as much as possible. A smaller SB will introduce larger statistical uncertainties in the normalization estimation. This is a bias variance trade off. The current design gives roughly $N_{SB} \sim 4N_{SR}$ and $N_{SB} \sim 2N_{CR}$, which provides a good balance of the bias and variance in the background estimation.

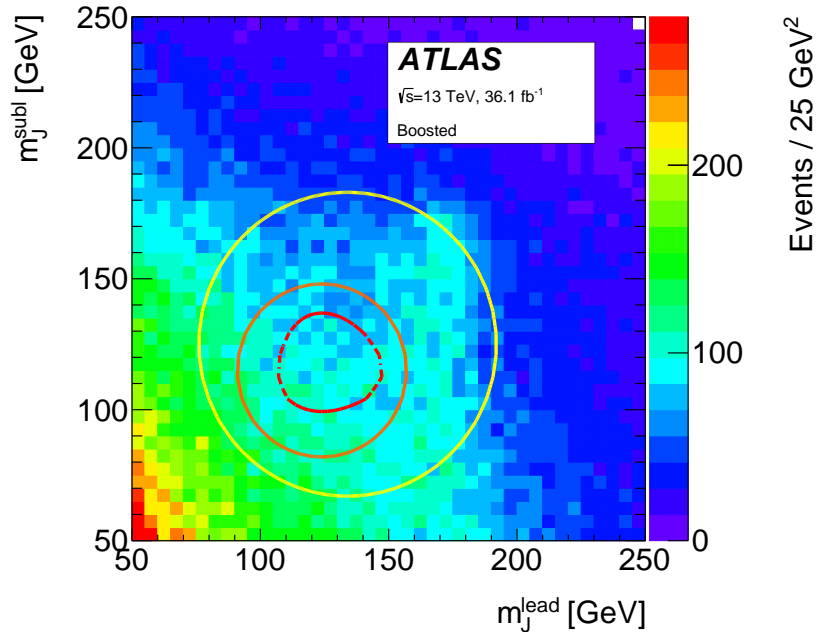


Figure 6.1: The m_J^{lead} vs m_J^{subl} distribution of the $2bs$ data. The signal region is the area surrounded by the inner (red) dashed contour line, centered on $(m_J^{\text{lead}} = 124 \text{ GeV}, m_J^{\text{subl}} = 115 \text{ GeV})$. The control region is the area between the signal region and the intermediate (orange) contour line. The sideband region is the area between the control region and the outer (yellow) contour line.

The fraction of expected events in the control region and sideband region as a function of G_{KK}^* Resonance mass is shown in Figure 6.2. For $4b$, $3b$, and $2bs$, there is no significant signal contamination in the control and sideband regions.

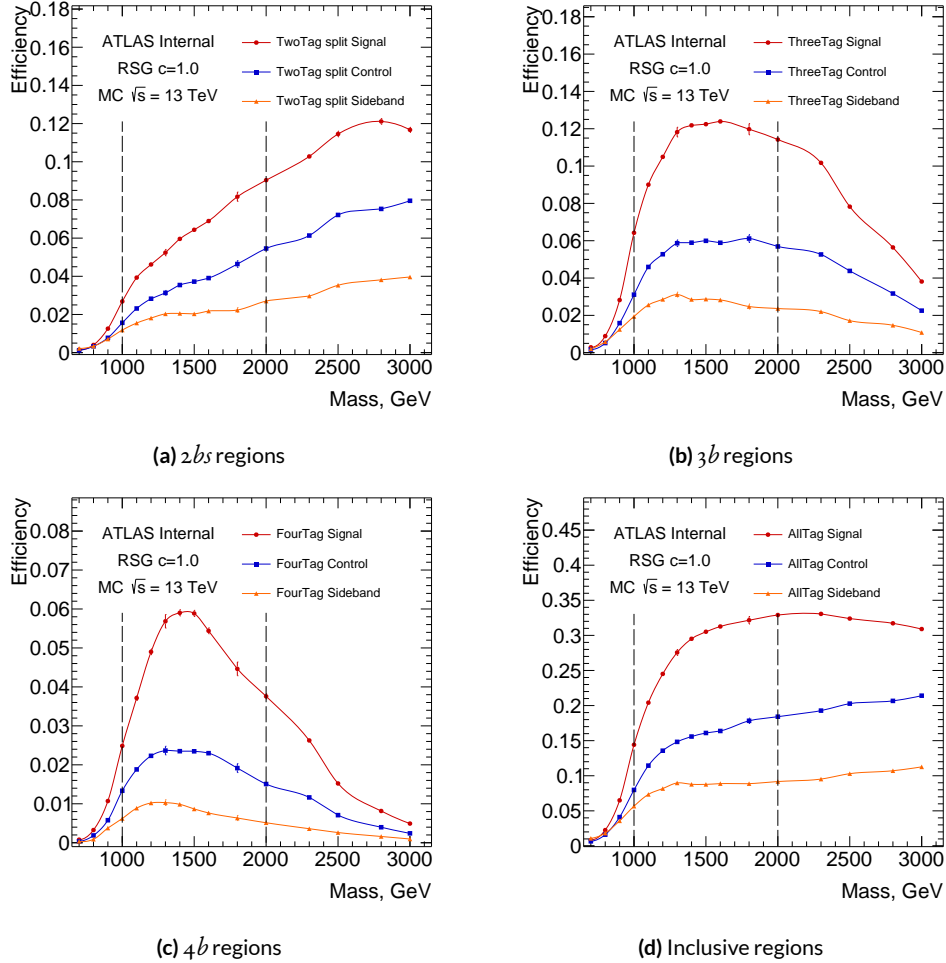


Figure 6.2: Detailed signal efficiency in different signal/control/sideband regions as in n -tag regions and inclusive b-tagged regions, which include $2b$, $1b$ and $0b$ as well, (bottom right) as a function of G_{KK}^* resonance mass for selection cuts. The efficiencies are relative to the total number of events in the preselection.

6.3 QCD MULTI-JETS

The QCD multi-jets prediction relies on finding regions that are similar in signal region event properties. These regions are defined to be identical to the signal regions except requiring fewer number of b -tagged track jets associated with the large- R jets. They are orthogonal to the n -tag regions with no overlapping events:

- For the $2b$ category, $1b$ data events, where one large- R jet has one and only one b -tagged track jets, and the other large- R jet has no b -tagged track jet, is used for modeling.
- For the $3b$ and $4b$ categories, $2b$ data events, where one large- R jet has two b -tagged track jets, and the other large- R jet has no b -tagged track jet, is used for modeling. The $2b$ sample is further split into 80% – 20% parts, where each is used separately for $3b$ and $4b$ background estimations. This ensures the shape estimations of $3b$ and $4b$ QCD estimates are uncorrelated.

The $1b/2b$ MC predicted $t\bar{t}$ and $Z+jets$ events in the $1b/2b$ regions are subtracted from the data distributions to produce the QCD estimation. Therefore, the number of QCD events, N_{qcd} , is estimated in Equation 6.3.

$$N_{\text{qcd}} = N_{\text{data}} - N_{t\bar{t}} - N_{Z+jets} \quad (6.3)$$

The $1b$ -tagged region also requires that each large- R jet has at least one track jet (to model $2b$). Similarly, to model $3b$, the $2b$ -tagged region requires that one large- R jet has at least one track jet and the other one has at least two track jets. To model $4b$, each large- R jet must have at least two track jets (to model $4b$). This prevents biases in m_{2J} distribution from the number of associated track jets.

The resolved signal region events veto impacts the $4b$ background estimation. To account for this effect, a part of $2b$ data events used for $4b$ background estimation are excluded. The vetoed events must have at least two small- R jets that are b -tagged (passing the resolved 70% b -tagging working

point), and in case where the two other non b -tagged resolved jets can make a Higgs candidate, must pass the $X_{bh\text{-resolved}} < 1.6$ cut. This ensures that a similar sculpting effect from the resolved veto is reflected in the background estimation in $4b$ signal region. This reduces the estimated number of events in the signal region by 10%.

Given the $1b/2b$ QCD background shape predictions, the normalization of the QCD background is determined in the sideband by fitting the m_j^{lead} distribution simultaneously with QCD and $t\bar{t}$ background templates, as described in section 6.5. There are kinematic differences between the $1b/2b$ samples and the $4b/3b/2bs$ regions. A kinematic reweighting is applied to correct for such differences, as described in Section 6.6.

6.4 $t\bar{t}$

The $t\bar{t}$ events in the signal region mainly decay to W^\pm s that further decay hadronically. The $t\bar{t}$ MC is scaled by the luminosity in the data. The boosted event selection is applied on the $t\bar{t}$ MC. The estimated $t\bar{t}$'s kinematic distributions come from the MC. To account for possible mismodeling in the MC, a normalization scaling factor is derived from a fit to data in the sideband region, as described in section 6.5.

For $4b$ and $3b$ signal regions, there are not sufficient $t\bar{t}$ MC statistics for high m_{2J} . Instead, the $2bs$ $t\bar{t}$ MC shapes are used. It is rescaled to the $4b$ and $3b$ $t\bar{t}$ MC yields. This reduces the statistical uncertainties for $4b$ and $3b$ $t\bar{t}$ at high m_{2J} . A comparison between the $4b/3b/2bs$ shapes for the m_{2J} distributions in the signal regions is shown in Figure 6.3. The shapes are compatible, with the $4b$ having much larger statistical uncertainties. Differences between these distributions will be used as a systematic, as described in section 7. Since the same $t\bar{t}$ distribution is used for the $4b/3b/2bs$ SR predictions, the $t\bar{t}$ shape systematics are considered correlated in the final results and limit setting.

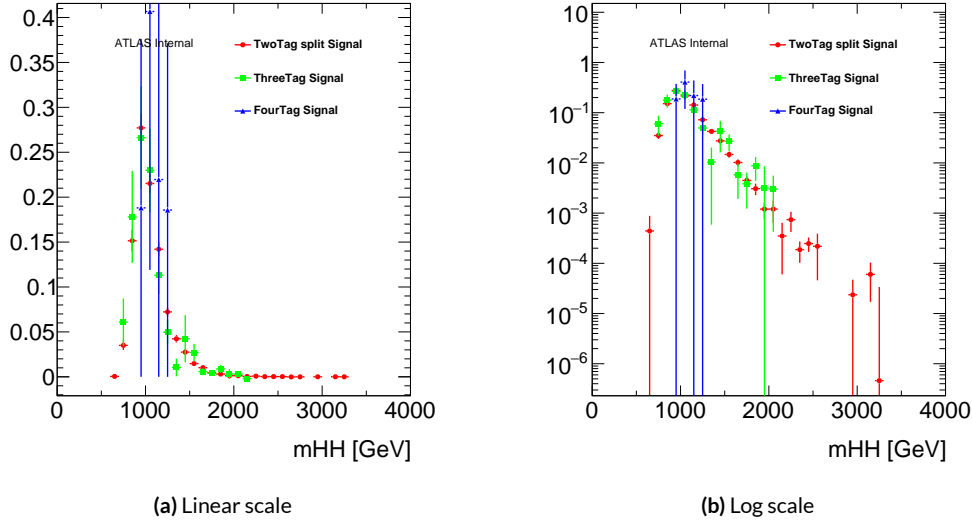


Figure 6.3: Normalized of $2bs$, $3b$, and $4b\bar{t}t$ MC $m_{j^{\text{subl}}}$ distribution in the signal region. The uncertainties are statistical.

6.5 FITTING PROCEDURE FOR QCD AND $\bar{t}t$ NORMALIZATION

The number of $4b/3b/2bs$ background events in a given region R (SB / CR / SR) is shown in

Equation 6.4, 6.5 and 6.6:

$$N_{\text{bkg}}^{4b-\text{R}} = \mu_{\text{qcd}}^{4b} N_{\text{qcd}}^{2b-\text{R}} + \alpha_{\bar{t}t}^{4b} N_{\bar{t}t}^{4b-\text{R}} + N_{Z+jets}^{4b-\text{R}}; \quad \mu_{\text{qcd}}^{4b} \sim \frac{N_{\text{qcd}}^{4b-\text{SB}}}{N_{\text{qcd}}^{2b-\text{SB}}} \quad (6.4)$$

$$N_{\text{bkg}}^{3b-\text{R}} = \mu_{\text{qcd}}^{3b-\text{R}} N_{\text{qcd}}^{2b-\text{R}} + \alpha_{\bar{t}t}^{3b} N_{\bar{t}t}^{3b-\text{R}} + N_{Z+jets}^{3b-\text{R}}; \quad \mu_{\text{qcd}}^{3b} \sim \frac{N_{\text{qcd}}^{3b-\text{SB}}}{N_{\text{qcd}}^{2b-\text{SB}}} \quad (6.5)$$

$$N_{\text{bkg}}^{2bs-\text{R}} = \mu_{\text{qcd}}^{2bs-\text{R}} N_{\text{qcd}}^{1b-\text{R}} + \alpha_{\bar{t}t}^{2bs} N_{\bar{t}t}^{2bs-\text{R}} + N_{Z+jets}^{2bs-\text{R}}; \quad \mu_{\text{qcd}}^{2bs} \sim \frac{N_{\text{qcd}}^{2bs-\text{SB}}}{N_{\text{qcd}}^{1b-\text{SB}}} \quad (6.6)$$

μ_{qcd} is essentially an estimate of the ratio of the number of QCD events with $4b/3b/2bs$ -tagged track jets, to the number of QCD events with $2b/1b$ -tagged track jets. μ_{qcd} is assumed to be a constant over SB/CR/SR $m_j^{\text{lead}}-m_j^{\text{subl}}$ regions. Validation of this assumption can be found in Appendix D. $\alpha_{\bar{t}t}$, applied after the $\bar{t}t$ MC is scaled to the total integrated luminosity, is a correction to

the MC prediction. μ_{qcd} and $\alpha_{t\bar{t}}$ are derived in the sieband region. They are used as multiplicative constants in other regions of the mass plane (i.e. the control region or the signal region).

A binned maximum likelihood fit is used to find the values of μ_{qcd} and $\alpha_{t\bar{t}}$, as well as the correlation between them. These scaling parameters are determined independently using the same procedure in the $4b/3b/2bs$ sideband regions. Due to the $p_T > 450 \text{ GeV}$ cut imposed on the leading large- R jet, the hadronically decaying top quark can be fully reconstructed inside the leading large- R jet. The m_j^{lead} from $t\bar{t}$ events has a clean peak around 170 GeV in the sideband region. It has the best separation between QCD and $t\bar{t}$ shapes. Therefore, the fit is performed on the m_j^{lead} spectrum in the sideband region.

Figure 6.4 shows the post-fit spectrum of m_j^{lead} in the $n\text{-}b\text{tag}$ sideband regions. The m_j^{lead} shapes in data are well modeled by the predicted backgrounds. The fitting errors on μ_{qcd} and $\alpha_{t\bar{t}}$ are applied as systematic uncertainties taking into account their correlation.

The $t\bar{t}$ MC sample normalization is further corrected from the fitted $\alpha_{t\bar{t}}$. At first $\alpha_{t\bar{t}}$ is assumed to be 1. Once the first fit is done, the QCD background is re-estimated using the updated $2bs$ $\alpha_{t\bar{t}}$ value, which has the smallest uncertainty. Then the fit is repeated until the change in $\alpha_{t\bar{t}}$ is less than 0.01. This iterative procedure helps correct the $\alpha_{t\bar{t}}$ bias in the data driven QCD template.

The values of μ_{qcd} and $\alpha_{t\bar{t}}$ estimated by the fits in the $4b/3b/2bs$ sideband regions can be found in Table 6.2, along with the correlation $\rho(\mu_{\text{qcd}}, \alpha_{t\bar{t}}) = \frac{\text{Cov}(\mu_{\text{qcd}}, \alpha_{t\bar{t}})}{\sigma_{\mu_{\text{qcd}}} \sigma_{\alpha_{t\bar{t}}}}$. μ_{qcd} and $\alpha_{t\bar{t}}$ are approximately 70% negatively correlated, due to the two components fit nature. This negative correlation leads to a smaller total normalization uncertainty.

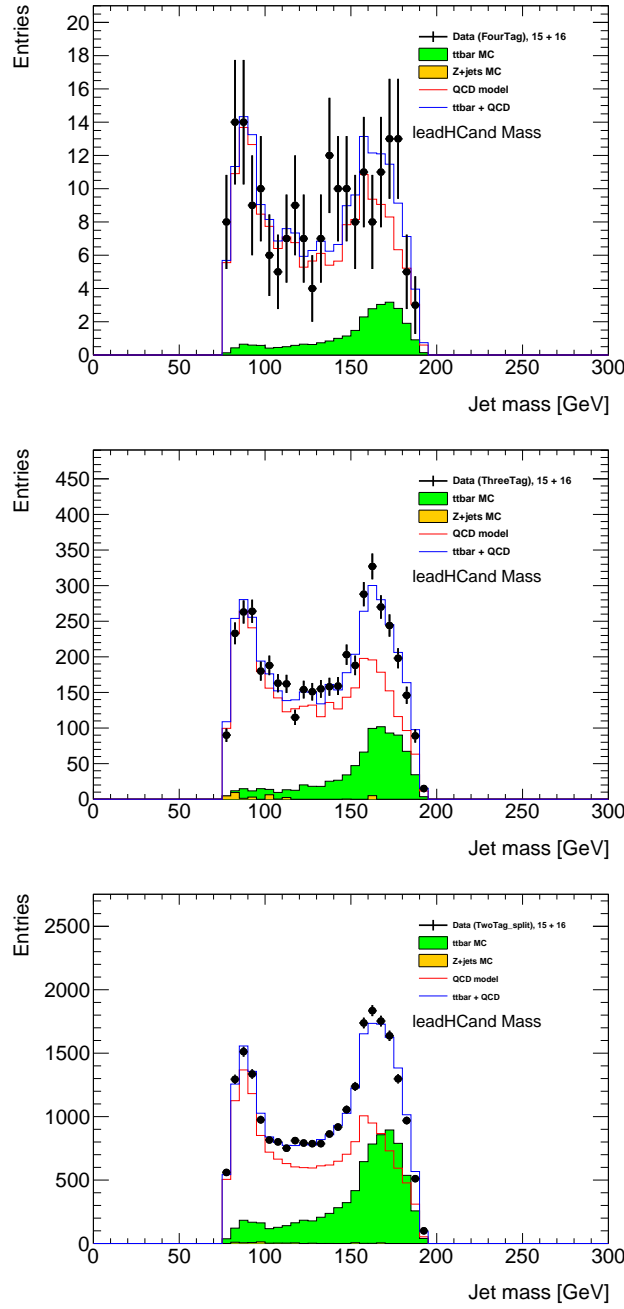


Figure 6.4: Simultaneous fit of μ_{qcd} and $\alpha_{t\bar{t}}$ in $4b$ (top) and $3b$ (middle) and $2bs$ (bottom) sideband region using leading large- R jet mass.

Sample	μ_{qcd}	$\alpha_{t\bar{t}}$	$\xi(\mu_{qcd}, \alpha_{t\bar{t}})$
FourTag	0.033987 ± 0.0043057	1.01697 ± 0.58642	-0.76397
ThreeTag	0.16247 ± 0.0041713	0.86508 ± 0.069019	-0.6778
TwoTag split	0.066713 ± 0.00091137	1.03747 ± 0.026199	-0.74785

Table 6.2: Background scaling parameters (μ_{qcd} and $\alpha_{t\bar{t}}$) estimated from fits to the m_j^{lead} distributions in $4b/3b/2b$ s sideband regions. $\xi(\mu_{qcd}, \alpha_{t\bar{t}}) = \frac{\text{Cov}(\mu_{qcd}, \alpha_{t\bar{t}})}{\sigma_{\mu_{qcd}} \sigma_{\alpha_{t\bar{t}}}}$.

6.6 QCD REWEIGHTING

This is the most time consuming part of this analysis. More supporting plots are shown in Appendix E. It is important to model the QCD background as good as possible in all regions of the analysis. Using the $1/2b$ region to model the $2bs/3b/4b$ regions can introduce discrepancies in the modeling of the estimated QCD background versus the data. These discrepancies arise from the non-trivial effect that b -tagging has on jet kinematics.

In order to account for the b -tagging effect, a reweighting on the $1/2b$ data is adopted. The goal is to reweigh the non b -tagged Higgs candidate to have kinematic distributions just like a b -tagged Higgs candidate. This is motivated by Figure 6.5. ob , $1b$ and $2bs$ data are compared. Except $2bs$ is only showing SB region, ob and $1bs$ are inclusive SB+CR+SR regions. $1b$ sample is further split into four subcategories, depending on which track jet gets b tagged:

- “OneTag lead on lead” means the b tagged track jet is the leading track jet of the leading Higgs candidate;
- “OneTag lead on subl” means the b tagged track jet is the subleading track jet of the leading Higgs candidate;
- “OneTag subl on lead” means the b tagged track jet is the leading track jet of the subleading Higgs candidate;

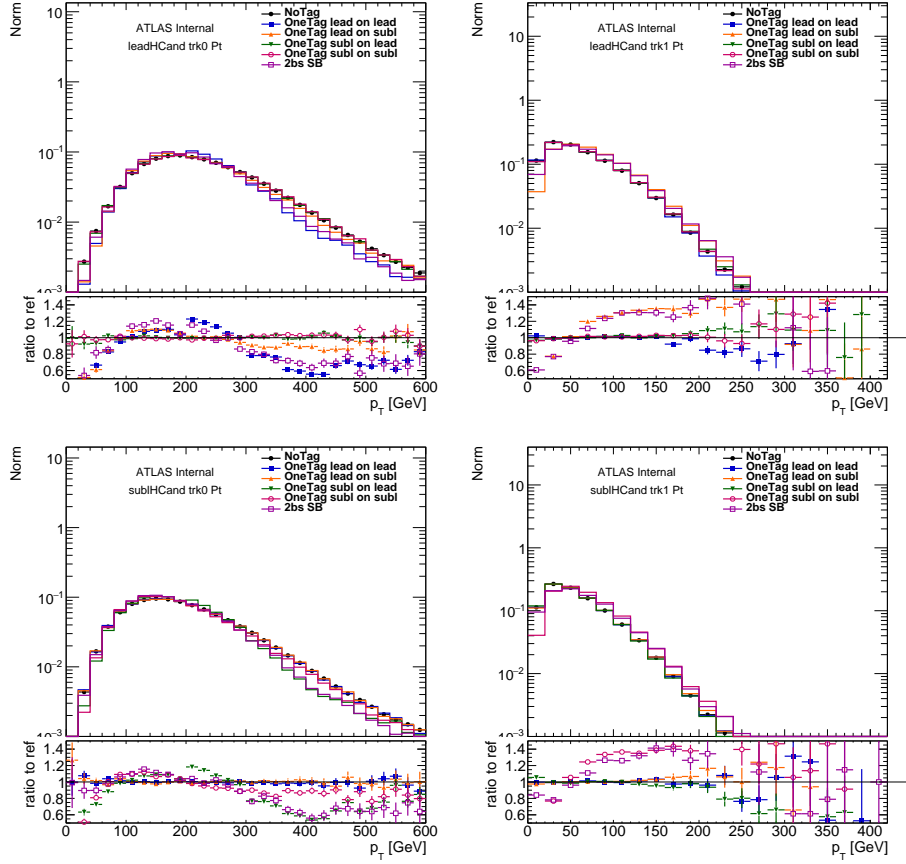


Figure 6.5: Comparison of different track jet p_T distributions. The top row is for leading Higgs candidate, and the bottom row is for subleading Higgs candidate. The left column is for the leading track jet of the Higgs candidate, and the right column is for the subleading track jet of the Higgs candidate. Shown in the plot are data distributions, inclusive of SB, CR, and SR regions for $0b$ and $1b$, while for $2bs$ only the SB region is shown. At the bottom ratio plot, all the ratio are taken with respect to the $0b$ tagged distribution.

- “OneTag subl on subl” means the b tagged track jet is the subleading track jet of the subleading Higgs candidate;

The figure shows that $2bs$ has very similar track jet p_T distributions as the $1b$ sample with a b -tagged track jet. It also shows that in the $1b$ sample, the track jet p_T distribution in the non b -tagged Higgs candidate behaves like the $0b$ sample’s track jet p_T distribution.

To avoid potential biases in the final distributions used for the analysis, this reweighting technique is applied to the $1/2b$ data only. Since each signal region is modeled by a different $1/2b$ tag category, the reweighting procedure is the same for the three different channels. The $2b$ sample is already split into separate parts for $3b$ and $4b$ estimations, as described in section 6.3.

For $2bs$, the $1b$ non- b tagged Higgs candidate is reweighed to be like a $1b$ tagged Higgs candidate; for $3b$, the $2b$ non- b tagged Higgs candidate is reweighed to be like a $1b$ tagged Higgs candidate; for $4b$, the $2b$ non- b tagged Higgs candidate is reweighed to be like a $2b$ tagged Higgs candidate. For each category, the events are split into two orthogonal subgroups, based on whether leading/subleading Higgs candidate is b -tagged. Each event gets a weight, such that the reweighed untagged Higgs candidate’s distributions agree with the corresponding b -tagged Higgs candidate’s.

One natural choice of reweighting variable is the p_T of the track jets in the event, since b -tagging efficiency and b -tagging fake rate have a strong track jet p_T dependence. Also, large- R jet p_T is reweighed to account for the difference from light/ c/b quarks composition in QCD events at different energy scales. The three reweighted variables are the leading large- R jet p_T , leading large- R jet leading trackjet p_T and subleading large- R jet leading trackjet p_T .

The each reweighting iteration is described below:

- Subtract $1/2b$ $t\bar{t}$ and $Z + \text{jets}$ samples in the SB + CR + SR regions from the $1/2b$ tag data in the SB + CR + SR regions to get the $1/2b$ QCD inclusive estimate. Weights from all previous iterations, if applicable, are all applied.
- Separate the $1/2b$ sample into two parts: A. that has the b -tagged Higgs is the leading p_T Higgs candidate, and B. that the b -tagged Higgs is the subleading p_T Higgs candidate.
- For each variable, i.e. the large- R jet p_T : normalize sample A to sample B's total number of events, take the ratio of sample A's distribution over sample B's distribution, and fit the ratio with a smooth spline function. (TSpline3)
- Use this spline function to extract reweighting values for each variable that is considered. Then, the difference from one is scaled by 0.75 to get a new weight. This accounts for over correlation by the spline and accelerates convergence.
- For each event, all the three weights from three variables are multiplied together to get a data event weight. Another constraint is applied, such that each event's total reweighting value is constrained to be within a 0.05 to 1.0 range compared to 1. This avoids over corrections.

A total of ten iterations are used to stabilize the reweighting. The reweighting is almost converging after three iterations. The reweighting value for each variable is also constrained to be within a -30% to $+40\%$ range compared to one, to avoid over corrections and failed fit situations.

Table 6.3: Background scaling parameters (μ_{qcd} and $\alpha_{t\bar{t}}$) estimated from fits to the m_j^{lead} distributions in $4b/3b/2b$ s sideband regions post reweighting. $\xi(\mu_{qcd}, \alpha_{t\bar{t}}) = \frac{\text{Cov}(\mu_{qcd}, \alpha_{t\bar{t}})}{\sigma_{\mu_{qcd}} \sigma_{\alpha_{t\bar{t}}}}$.

Sample	μ_{qcd}	$\alpha_{t\bar{t}}$	$\xi(\mu_{qcd}, \alpha_{t\bar{t}})$
FourTag	0.033167 ± 0.0042799	0.89136 ± 0.59866	-0.7846
ThreeTag	0.16256 ± 0.0043405	0.79989 ± 0.073276	-0.72029
TwoTag split	0.062726 ± 0.00057307	0.98637 ± 0.018582	-0.4698

At the end of reweighting, the μ_{qcd} and $\alpha_{t\bar{t}}$ are re-evaluated. The estimated μ_{qcd} and $\alpha_{t\bar{t}}$ values before reweighting can be found in Table 6.3. The values are statistically consistent with the values in Table 6.2.

6.7 m_{2J} IN THE SIDEband REGION

Figure 6.6 shows comparisons of the predicted m_{2J} background distributions to those observed in the data in the sideband region. The predicted background and observed distributions are in agreement, with no significant excess. Other sideband region distributions are shown in Appendix A.

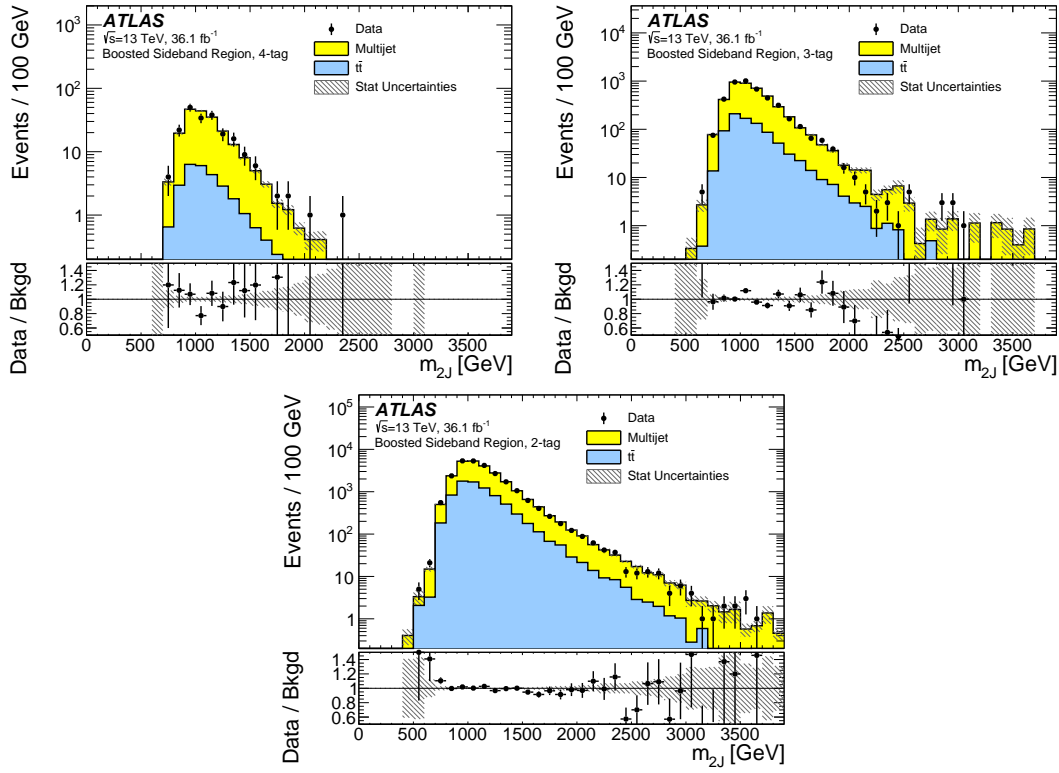


Figure 6.6: The m_{2J} distributions in the sideband region of the boosted analysis for the data and the predicted background for (top left) the four-tag, (top right) the three-tag, and (bottom) the two-tag split samples. The data-to-background ratio (bottom panels) shows the statistical uncertainties as the grey hatched band.

6.8 m_{2J} IN THE CONTROL REGION

Figure 6.7 shows comparisons of the predicted m_{2J} background distributions to those observed in the data in the control region. The predicted background and observed distributions are in agreement, with no significant excess. Other control region distributions are shown in Appendix B.

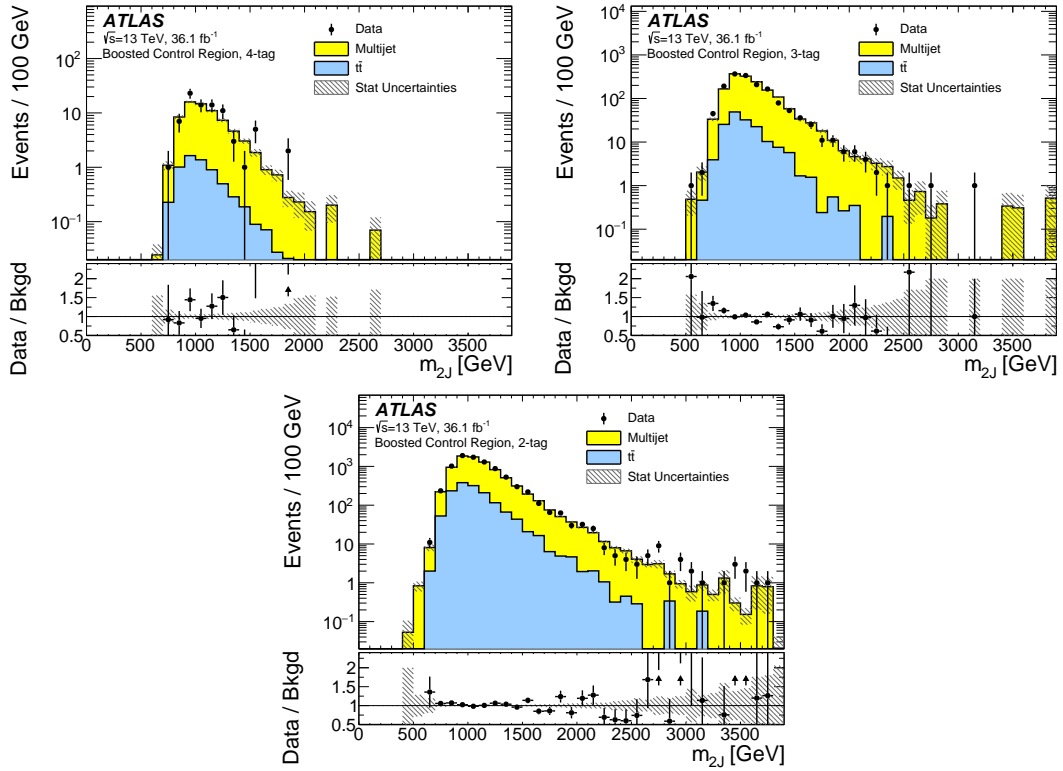


Figure 6.7: The m_{2J} distributions in the control region of the boosted analysis for the data and the predicted background for (top left) the four-tag, (top right) the three-tag, and (bottom) the two-tag split samples. The data-to-background ratio (bottom panels) shows the statistical uncertainties as the gray hatched band.

6.9 m_{2J} RESCALE AND SMOOTHING IN THE SIGNAL REGION

In signal region, the four-momentum of each large- R jet is multiplied with a factor m_H/m_J . From this, a scaled m_{2J} is calculated. This improves the resolution of m_{2J} for signal events by correcting the energy loss. There is little impact on the background distribution. Using the scaled m_{2J} distribution, the expected exclusion limits are slightly better at low mass and slightly worse at high mass, with differences of the order of 10% than the nominal dijet mass limits. The scaled m_{2J} distribution can be found in Figure 6.8.

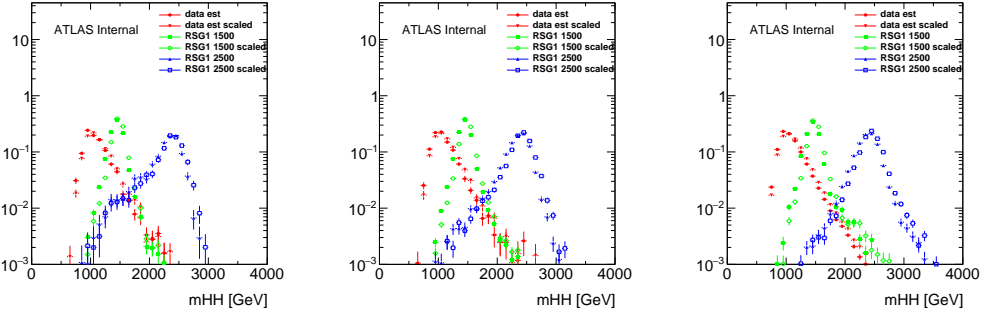


Figure 6.8: Normalized scaled m_{2J} distributions for the $4b$ (left), $3b$ (middle), and $2bs$ (right) signal regions. For comparison, the unscaled m_{2J} distributions are shown on the same plot.

Due to the limited $1/2b$ statistics at high m_{2J} above 2500 GeV and the limited $t\bar{t}$ statistics above 1100 GeV, different fits are performed to smooth the m_{2J} mass distribution in the signal region. The $4/3/2bs$ QCD and $t\bar{t}$ signal region scaled m_{2J} distributions are fitted with the following functional form:

$$y = \frac{a}{\frac{x^2}{\sqrt{s}}} \left(1 - \frac{x}{\sqrt{s}}\right)^{b-c} \log\left(\frac{x}{\sqrt{s}}\right) \quad (6.7)$$

where $\sqrt{s} = 13000$ GeV, the fit range is for $1200 < M_{JJ} < 3000$ GeV, and the three free parameters are a , b and c . The values of the estimated fit parameters in the $4b$ and $3b$ and $2bs$ signal regions can be found in Table 6.4. Figure 6.9 shows the smoothing fits for the QCD background and the $t\bar{t}$

background in the $4b$, $3b$, and $2bs$ signal regions. The smoothing fit statistical uncertainties are also shown on these two plots. Given that the similar $1/2b$ sample is used for deriving the QCD shape for the $4/3/2bs$ signal regions, the slope parameters (a) are similar for $4/3/2bs$ QCD backgrounds.

The final signal region prediction, using scaled di-jet mass distribution, with only statistical uncertainties, are shown in Figure 6.10. This includes smoothing statistical uncertainties only. Uncertainties on the fit parameters are propagated as systematic uncertainties, though they are essentially replacing the bin-by-bin statistical uncertainties of the background estimates (which are not used once smoothing is applied). More details on other systematics, including smoothing systematics, shape uncertainties and other sources of uncertainties would be discussed in Section 7.9.

Table 6.4: Smoothing parameters in $4b$ and $3b$ and $2bs$ signal regions for scaled mass distributions, the correlation between parameters is almost always 0.99.

Region	$a_{t\bar{t}}$	$b_{t\bar{t}}$	$c_{t\bar{t}}$	a_{qcd}	b_{qcd}	c_{qcd}
FourTag	-2.02 ± 1.17	42.46 ± 9.87	1.31 ± 8.98	-0.49 ± 1.59	53.06 ± 15.2	-11.1 ± 12.8
ThreeTag	1.84 ± 1.17	42.45 ± 9.88	1.32 ± 8.98	8.51 ± 0.98	-13.8 ± 9.14	42.58 ± 7.87
TwoTag split	4.22 ± 1.17	42.45 ± 9.88	1.32 ± 8.98	7.06 ± 0.32	11.54 ± 2.77	19.05 ± 2.48

6.10 YIELDS

The event yield results showing the estimated backgrounds, the signal predictions, and the observed data in the $4b$ and $3b$ and $2bs$ signal regions, control regions, and sideband regions can be found in Table 6.5 and Table 6.6 and Table 6.7 respectively. Total background statistical uncertainty is less than the quadratic sum of $t\bar{t}$ and QCD because of the anti-correlation. Z+jets have a negligible yield in the signal regions, therefore, in the later chapters, it is not included in the figures and tables.

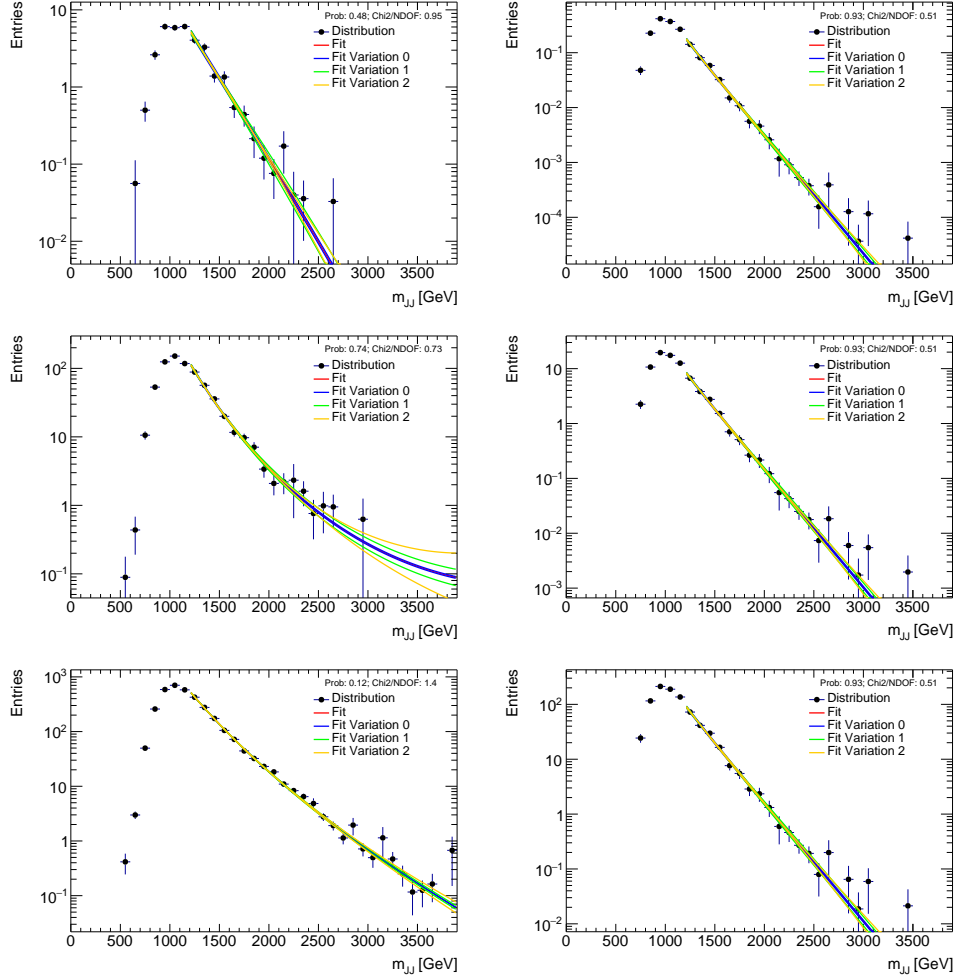


Figure 6.9: Fits for scaled background smoothing are shown for QCD (left column) and $t\bar{t}$ (right column) in the $4b$ (top), $3b$ (middle), and $2bs$ (bottom) signal region. The left figures show the distributions with linear y -axis scale along with the fit central value and variations. The right figures show the distributions with log y -axis scale along with the fit central value and the fit variations as determined by the varying the fit parameters within uncertainties whilst taking into account parameter correlations.

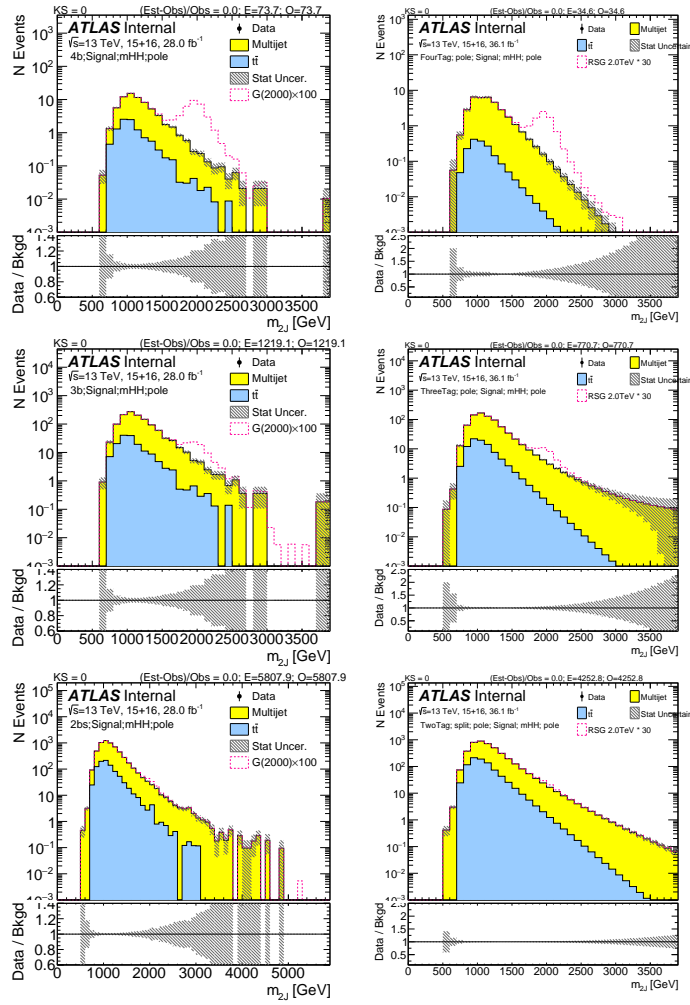


Figure 6.10: Background prediction for $4b$ (top), $3b$ (middle), and $2bs$ (bottom) signal region using scaled di-jet mass before (left) and after smoothing (right). The uncertainty band includes only fit statistical uncertainties.

Table 6.5: Expected yields for backgrounds in the $4b$ signal region, control region, and sideband region, along with the observed number of data events. The signal predictions for $G_{KK}^* m = 1.0, 1.5, 2.0 \text{ TeV}$ with $c = 1.0$. The uncertainty listed is statistical, without fit uncertainty.

FourTag	Sideband	Control	Signal
QCD Est	176.26 ± 2.96	64.21 ± 1.79	32.91 ± 1.25
$t\bar{t}$ Est.	27.86 ± 0.25	6.38 ± 0.13	1.68 ± 0.044
$Z + jets$	0 ± 0	6.18 ± 5.12	0 ± 0
Total Bkg Est	204.12 ± 2.97	76.77 ± 5.43	34.59 ± 1.25
Data	204.0 ± 14.28	81.0 ± 9.0	31 ± 5.57
$c = 1.0, m = 1.0 \text{ TeV}$	2.52 ± 0.1	5.4 ± 0.15	10.07 ± 0.2
$c = 1.0, m = 2.0 \text{ TeV}$	0.034 ± 0.0015	0.1 ± 0.0026	0.25 ± 0.0041
$c = 1.0, m = 3.0 \text{ TeV}$	$0.00032 \pm 3.7e-05$	$0.0008 \pm 5.6e-05$	$0.0016 \pm 8e-05$

Table 6.6: Expected yields for backgrounds in the $3b$ signal region, control region, and sideband region, along with the observed number of data events. The signal predictions for $G_{KK}^* m = 1.0, 1.5, 2.0 \text{ TeV}$ with $c = 1.0$. The uncertainty listed is statistical, without fit uncertainty.

ThreeTag	Sideband	Control	Signal
QCD Est	3518.01 ± 27.48	1413.52 ± 17.36	701.6 ± 11.95
$t\bar{t}$ Est.	852.88 ± 25.72	162.31 ± 11.15	79.34 ± 2.05
$Z + jets$	32.8 ± 11.34	11.21 ± 5.65	0.49 ± 0.49
Total Bkg Est	4403.69 ± 39.31	1587.04 ± 21.4	781.42 ± 12.14
Data	4403.0 ± 66.36	1553.0 ± 39.41	801.0 ± 28.3
$c = 1.0, m = 1.0 \text{ TeV}$	7.86 ± 0.18	12.58 ± 0.23	26.0 ± 0.33
$c = 1.0, m = 2.0 \text{ TeV}$	0.16 ± 0.0035	0.38 ± 0.0054	0.76 ± 0.0076
$c = 1.0, m = 3.0 \text{ TeV}$	0.0036 ± 0.00013	0.0075 ± 0.00018	0.013 ± 0.00023

Table 6.7: Expected yields for backgrounds in the $2bs$ signal region, control region, and sideband region, along with the observed number of data events. The signal predictions for $G_{KK}^* m = 1.0, 1.5, 2.0 \text{ TeV}$ with $c = 1.0$. The uncertainty listed is statistical, without fit uncertainty.

TwoTag split	Sideband	Control	Signal
QCD Est	17216.91 ± 38.33	6821.96 ± 23.49	3393.56 ± 16.64
$t\bar{t}$ Est.	7852.35 ± 70.3	1484.57 ± 29.24	858.27 ± 22.23
$Z + jets$	67.74 ± 16.82	26.44 ± 10.08	0.13 ± 0.091
Total Bkg Est	25137.01 ± 81.82	8332.97 ± 38.84	4251.96 ± 27.77
Data	25137.0 ± 158.55	8486.0 ± 92.12	4376.0 ± 66.15
$c = 1.0, m = 1.0 \text{ TeV}$	4.79 ± 0.14	6.33 ± 0.16	10.87 ± 0.22
$c = 1.0, m = 2.0 \text{ TeV}$	0.18 ± 0.0039	0.36 ± 0.0056	0.6 ± 0.0072
$c = 1.0, m = 3.0 \text{ TeV}$	0.013 ± 0.00025	0.027 ± 0.00034	0.039 ± 0.00041

Every question has a proper answer. Every soul has a proper place.

Tony.

7

Systematics

7.1 OVERVIEW

Theoretical uncertainties in the signal acceptance result from variations of renormalization and factorization scales, PDF set uncertainties, and uncertainties in modeling of the underlying event and hadronic showers (therefore varying initial- and final-state radiation). The total theoretical uncertainty is dominated by the shower variations. The size of the variation of the expected signal yield is typically below 10% but can increase to 23%, depending on the signal hypothesis.

Detector modeling uncertainties (b -tagging efficiencies; jet energy, resolution and mass) are propagated in the analysis. These uncertainties can change both the shape and normalization of the signal and of the MC-based backgrounds. Each uncertainty in the data-driven background estimate is

evaluated for each sample, and these are treated as uncorrelated across the samples in the statistical analysis.

A statistical uncertainty on the value of μ_{qcd} and $\alpha_{t\bar{t}}$ for the $4b$, $3b$ and $2bs$ signal region is determined from the fitting procedure described in section 6.5. Two orthogonal eigenvariations are calculated from the covariance matrix of the normalization fit, which are then applied to the background predictions. Correlations between $\alpha_{t\bar{t}}$ and μ_{qcd} are fully retained this way.

Other background systematic uncertainties in the signal region are further discussed in the following components:

- Non-closure uncertainty on μ_{qcd} found by comparing the value derived from the sideband to the control region normalization.
- Effects on the QCD prediction from variations of the sideBand and control Region Definitions
- The impact of the shape uncertainty of the $t\bar{t}$ distribution in the $3/4b$ signal region.
- The impact of the shape uncertainty of the estimated QCD distribution, derived in the control region.
- The impact of the smoothing function fit range and function choice on the QCD prediction.

7.2 THEORETICAL UNCERTAINTIES

The theoretical uncertainties on the acceptance times efficiency ($\mathcal{A} \times \varepsilon$) are evaluated by analysis of specially-generated, particle-level signal samples. The generation of these samples follows the configuration of the baseline samples, but with modifications to probe the following theoretical uncertainties: uncertainties in the parton density functions; uncertainties due to missing higher order

terms in the matrix elements; and uncertainties in the modeling of the underlying event (including multi-parton interactions), of hadronic showers and of initial and final state radiation.

To evaluate the potential effect of missing higher order terms in the matrix element, the renormalization and factorization scales used in the signal generation are varied coherently by factors of 0.5 and 2 for the signals.

Uncertainties due to modeling of the parton shower and the underlying event (including multi-parton interactions) are evaluated by switching the MC generator used. For the Bulk RS graviton samples, Pythia8 are switched to Herwig++, while for the scalar and non-resonant it is Herwig++ to Pythia8.

PDF uncertainties are evaluated using the PDF4LHC15_nlo_mc set, which combines CT14, MMHT14 and NNPDF3.0 PDF sets⁷³. The uncertainty is evaluated by calculating the acceptance for each PDF replica. The standard deviation of these acceptance values divided by the baseline acceptance is taken as the PDF uncertainty. For each mass point the distribution of these ratio is compatible with a Gaussian centered on one. The uncertainty in acceptance due to PDF uncertainties is less than $\pm 1\%$ across the full mass range considered for the analysis.

These uncertainties are implemented in the final statistical analysis as normalization uncertainties on the signals, with the value taken from the polynomial fit. This smooths out statistical fluctuations and allows interpolation between the generated mass points, if needed.

7.3 UNCERTAINTIES ON DETECTOR AND RECONSTRUCTION

7.3.1 LUMINOSITY UNCERTAINTY

The uncertainty in the integrated luminosity of the combined 2015 and 2016 datasets is $\pm 2.1\%$ ⁷⁴. This uncertainty is applicable to the backgrounds with normalizations determined from simulation, and further propagated to the QCD prediction through data-driven background estimation procedure. This uncertainty is also applied to the signal normalization prediction. It has a small impact on this analysis.

7.3.2 LARGE- R JET RESOLUTION AND SCALE UNCERTAINTIES

There are uncertainties on the large- R jets in both the jet energy scale (JES) and jet energy resolution (JER), as well as the jet mass scale (JMS) and jet mass resolution (JMR). The uncertainties on the JES and JMS are derived in situ from 13 TeV pp collisions, using techniques described in Ref.⁷⁵. Discrepancies observed between data and MC are assigned as uncertainties on the energy/mass scales of the jet. The uncertainties are only correlated between energy and mass.

The uncertainties on the jet mass resolutions (JMR) are estimated by applying a Gaussian smearing. For each signal mass point, the large- R trimmed jets are smeared such that the intrinsic resolution is increased by 20%. For jet energy resolution (JER), the momentum is smeared with an absolute 2% uncertainty. The nominal MC mass resolution (σ_M) for every signal mass point is determined by fitting the reco_M/truth_M distribution with a Gaussian, respectively. The reco_M/truth_M is calculated before the final X_{bb} cut.

7.3.3 b -TAGGING UNCERTAINTIES

The uncertainties related to the b -tagging efficiency calibrations as measured in $t\bar{t}$ events for track jets are considered. The procedure to define these calibrations is similar to that described in reference⁵¹. The uncertainty in the b -tagging efficiency is evaluated by propagating the systematic uncertainty in the p_T -dependent, measured tagging efficiency for b -jets⁵. For b -jets with $p_T > 300$ GeV, systematic uncertainties in the tagging efficiencies are extrapolated with simulation and are consequently larger⁵¹. Uncertainties arising from mis-tagging jets that do not contain b -hadrons are negligible.

Calibrations, or correction factors in the form of scale factors per p_T bin, for the b -tagging efficiency of $R = 0.2$ track jets passing an MV2c10 weight cut corresponding to 77% efficiency have been derived in⁵². These calibrations are applied to the RS graviton signal samples and $t\bar{t}$ simulation. The calibrations also include uncertainties which modify the b -tagging efficiency and thus modify the signal ($t\bar{t}$) acceptance, and thus these uncertainties must be propagated through the analysis. The signal yield uncertainty due to b -tagging is less than 30% for the signal, and less than 12% for the $t\bar{t}$ yield.

A significant reduction of b -tagging systematic uncertainty for resonant signals in $3b$ signal region is observed. The reduced b -tagging uncertainty is due to the requirement that there must be one anti-tagged jet. For the signal, this is likely an anti-tagged b -jet. When a b -tagged jet is calibrated with a scale factor w_{sf} with uncertainties Δw_{sf} , any change in tagging efficiency must be corrected in the opposite direction for the anti-tagged jets in order to ensure that the total number of b -tagged plus anti-tagged jets does not change once the calibration is applied. Therefore, the anti-tagging calibration scale factor would be $w_{sf}^{anti} = (1 - w_{sf}\varepsilon_b)/(1 - \varepsilon_b)$, where ε_b is the tagging efficiency. Based on this equation, a shift in the scale factor for b -tagged jets causes an anti-correlated shift in

the anti-tagging efficiency scale factor. This anti-correlation in turn reduces the overall impact of the b -tagging uncertainty on the $3b$ SR. However, this anti-tagging efficiency scale factor is so large, that in $2bs$ SR, the total uncertainty will be dominated by the square of this factor, and hence it could be larger than $4b$'s b -tagging uncertainty.

This behavior is shown in Figure 7.1. One eigenvariation of b -tagging scale factor is tested on a $2\text{ TeV } G_{KK}^*$ with $c = 1.0$. In the $4b$ plot, no inefficiency scale factor is applied. The variation on the signal yield is only due to w_{sf} . In the $3b$ plot, one inefficiency scale factor is applied. This w_{sf}^{anti} reduces the variation from w_{sf} . In the $2bs$ plot, two inefficiency scale factor is applied. This w_{sf}^{anti} further reduces the variation from w_{sf} , causing the signal yield difference increase compared with the $3b$ case.

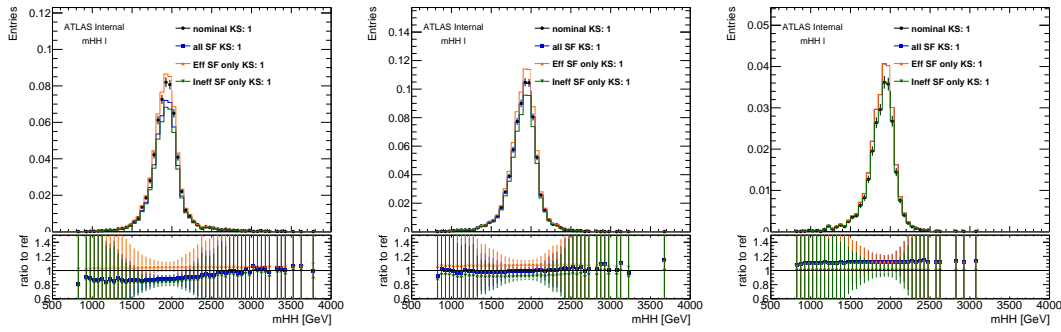


Figure 7.1: Impact of efficiency scale factor w_{sf} and inefficiency scale factor w_{sf}^{anti} on $2\text{ TeV } G_{KK}^*$ with $c = 1.0$. $4b$ signal region (left), $3b$ signal region (middle), and $2bs$ signal region are shown.

7.4 UNCERTAINTY ON $t\bar{t}$ GENERATOR

In addition to the $t\bar{t}$ fit uncertainties, following the recommendations, extra $t\bar{t}$ MC samples are used with different variations: hadronization, fragmentation, matrix element variation and additional radiation. The top quark mass variations are also considered.

These $t\bar{t}$ samples are used to replace the normal had and non-had MCs, stitched with $m_{t\bar{t}}$ slices samples, and the variation in the $t\bar{t}$ yield and background predictions are considered. The variation in total background, with different $t\bar{t}$ MC sample as input is tested. This is shown in Figure 7.2. This uncertainty is considered limited by the MC statistics and not included.

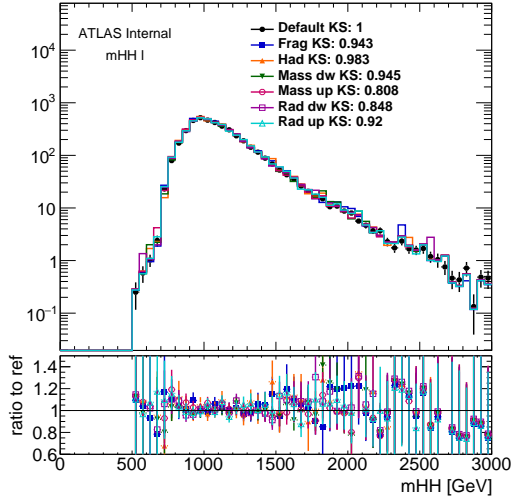


Figure 7.2: Total background estimation ($qcd + t\bar{t}$) with different $t\bar{t}MC$ variations. The different variations agree with the default within the statistical uncertainties.

7.5 UNCERTAINTY ON μ_{qcd} ESTIMATION

A further uncertainty is derived by comparing the value of μ_{qcd} to the overall difference between predicted to observed events in the control region, shown in section 6.10. The number events agrees with the total data in the control region within statistical error, but μ_{qcd} estimation is dependent on the SB and CR choice. An additional systematic on the background prediction in the signal region is assigned. It is the maximum between either the difference between the central value of the prediction to the observed number of events, or the statistical uncertainty of the observed data in the CR. For $4b$ it is 11.1%, for $3b$ it is 2.5%, and for $2bs$ it is 1.1%.

Besides the nominal control region, additional sideband and control region are designed and tested. They are further illustrated in Appendix F, and are listed below:

- Low-mass CR: the center position of the circle that defines nominal CR is moved down by 3 GeV, in both leading and sub-leading large-jet mass.
- High-mass CR: the center position of the circle that defines nominal CR is moved up by 3 GeV, in both leading and sub-leading large-R jet mass.
- Signal-depletion (Small) CR: the X_{hh} cut that defines signal region is increased to 2.0 from 1.6. This variation only affect CR, while SR remains unchanged (i.e. signal region is still defined by $X_{hh} < 1.6$, while CR is defined as $X_{hh} > 2.0$ and $R_{hh} < 33$).
- High-mass SB: The signal region and control region remain unchanged, the center position of the circle that defines nominal SB is moved up by 3 GeV in both leading and sub-leading large-R jet mass.
- Low-mass SB: The signal region and control region remain unchanged, the center position of the circle that defines nominal SB is moved up by 3 GeV in both leading and sub-leading large-R jet mass.
- Large SB: The signal region and control region remain unchanged, while the SB is $33 < R_{hh}$ and $R_{hh}^{\text{high}} < 61$. μ_{QCD} will change.
- Small SB: The signal region and control region remain unchanged, while the SB is $33 < R_{hh}$ and $R_{hh}^{\text{high}} < 55$. μ_{QCD} will change.

To ensure that these value cover the QCD normalization uncertainty, further checks on the effect of adjusting the control and sideband definitions were done. All these tests are done on the control/sideband regions after the full reweighting procedure as described in 6.6, while applying the nominal reweighting values. The results are summarized in Table 7.1, 7.2 and 7.3. Based on all the variations, a final 2.8% normalization uncertainty is assigned to $2b$ s signal region, 4.2% to $3b$ signal region, and a 12.2% normalization uncertainty is assigned to $4b$ signal region.

CR Variations FourTag	Data	Prediction	(Predict - Data)/Data
Nominal	81.0 ± 9.0	76.77 ± 5.43	$-5.22\% \pm 17.23\%$
CR High	76.0 ± 8.72	71.12 ± 5.41	$-6.43\% \pm 17.85\%$
CR Low	91.0 ± 9.54	79.87 ± 5.45	$-12.2\% \pm 15.19\%$
CR Small	58.0 ± 7.62	55.96 ± 5.35	$-3.52\% \pm 21.89\%$
SB Large	81.0 ± 9.0	74.71 ± 5.4	$-7.76\% \pm 16.91\%$
SB Small	81.0 ± 9.0	74.15 ± 5.38	$-8.45\% \pm 16.81\%$
SB High	81.0 ± 9.0	78.72 ± 5.46	$-2.82\% \pm 17.54\%$
SB Low	81.0 ± 9.0	76.51 ± 5.38	$-5.54\% \pm 17.14\%$

Table 7.1: Agreement between data and prediction in 4b tag CR. Showing stat uncertainty only.

CR Variations ThreeTag	Data	Prediction	(Predict - Data)/Data
Nominal	1553.0 ± 39.41	1587.04 ± 21.4	$2.19\% \pm 3.97\%$
CR High	1461.0 ± 38.22	1473.89 ± 20.77	$0.88\% \pm 4.06\%$
CR Low	1628.0 ± 40.35	1697.38 ± 21.75	$4.26\% \pm 3.92\%$
CR Small	1134.0 ± 33.67	1127.34 ± 17.66	$-0.59\% \pm 4.51\%$
SB Large	1553.0 ± 39.41	1574.23 ± 21.47	$1.37\% \pm 3.95\%$
SB Small	1553.0 ± 39.41	1601.44 ± 21.64	$3.12\% \pm 4.01\%$
SB High	1553.0 ± 39.41	1602.74 ± 21.48	$3.2\% \pm 4.0\%$
SB Low	1553.0 ± 39.41	1576.56 ± 21.5	$1.52\% \pm 3.96\%$

Table 7.2: Agreement between data and prediction in 3b tag CR. Showing stat uncertainty only.

CR Variations TwoTag split	Data	Prediction	(Predict - Data)/Data
Nominal	8486.0 ± 92.12	8332.97 ± 38.84	$-1.8\% \pm 1.52\%$
CR High	8174.0 ± 90.41	7937.59 ± 39.61	$-2.89\% \pm 1.56\%$
CR Low	8907.0 ± 94.38	8800.86 ± 39.51	$-1.19\% \pm 1.49\%$
CR Small	5999.0 ± 77.45	5873.52 ± 32.31	$-2.09\% \pm 1.8\%$
SB Large	8486.0 ± 92.12	8341.7 ± 38.44	$-1.7\% \pm 1.52\%$
SB Small	8486.0 ± 92.12	8333.25 ± 39.12	$-1.8\% \pm 1.53\%$
SB High	8486.0 ± 92.12	8378.14 ± 38.45	$-1.27\% \pm 1.52\%$
SB Low	8486.0 ± 92.12	8356.86 ± 39.06	$-1.52\% \pm 1.53\%$

Table 7.3: Agreement between data and prediction in 2bs tag CR. Showing stat uncertainty only.

7.6 VALIDATION IN LOW MASS AND HIGH MASS SIGNAL REGION

Another check is the the so-called “low mass signal region” (or ZZ region) and “high mass signal region” (or TT region). Instead of the signal region around di-Higgs mass region on m_J^{lead} - m_J^{subl} large- R jet mass 2D plane, a separate lower mass (ZZ) and higher mass (TT) signal region are defined:

$$X_{\text{ZZ}} = \sqrt{\left(\frac{m_J^{\text{lead}} - 103 \text{ GeV}}{\text{o.I.}(m_J^{\text{lead}})}\right)^2 + \left(\frac{m_J^{\text{subl}} - 96 \text{ GeV}}{\text{o.I.}(m_J^{\text{subl}})}\right)^2} \quad (7.1)$$

$$X_{\text{TT}} = \sqrt{\left(\frac{m_J^{\text{lead}} - 164 \text{ GeV}}{\text{o.I.}(m_J^{\text{lead}})}\right)^2 + \left(\frac{m_J^{\text{subl}} - 155 \text{ GeV}}{\text{o.I.}(m_J^{\text{subl}})}\right)^2} \quad (7.2)$$

which is also illustrated in Figure 7.3. The analysis is repeated, using the same definition of sideband and control region as the nominal (but with events contained in ZZ signal region excluded) for normalization fit. Then the low mass signal region is unblinded. This helps to validate the background estimation strategy, and the stability for other similar analysis.

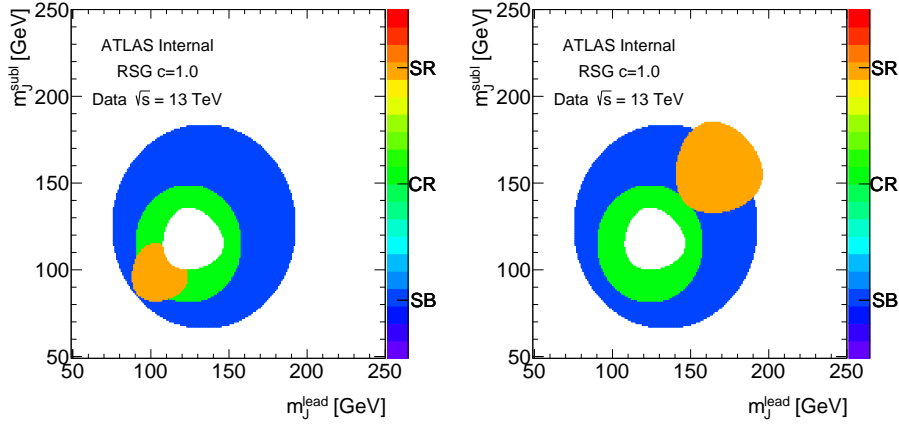


Figure 7.3: Illustration of ZZ (left) and TT (right) signal region as shown in the orange shaded region. Control region shown in green, and sideband region in blue. The white circle in the middle is the real signal region, and it is blinded.

The difference between data and prediction in ZZ signal region is summarized in Table 7.4 for all the regions. The discrepancy between data and prediction is either covered by statistical uncertainty of data or comparable with data statistical uncertainty in $4b$, $3b$ and $2bs$ ZZ SR respectively. The kinematic distribution between data and prediction in ZZ SR are shown in Figure 7.4. The data agrees with prediction well in general, though a few bins might not agree perfectly. The difference from $4b$ CR region test is 17%, which is smaller than the $4b$ ZZ region difference. But the statistical uncertainty in ZZ region (with yield 37) is much higher compared with the CR regions (with minimum yield 76), hence the CR region with more statistical power is still used for the non-closure uncertainty.

The difference between data and prediction in TT signal region is summarized in Table ?? for all the regions. The discrepancy between data and prediction is either covered by statistical uncertainty of data or comparable with data statistical uncertainty in $4b$, $3b$ and $2bs$ TT SR respectively. The kinematic distribution between data and prediction in TT SR are shown in Figure 7.5. The data agrees with prediction well in general, though a few bins might not agree perfectly.

Based on all the variation tests, there is no need to introduce extra uncertainty on non-closure systematics. Most of the data/prediction disagreements are well covered by the data statistical uncertainty.

Table 7.4: Data and prediction in ZZ SR in $4b$, $3b$ and $2bs$ regions.

ZZ Signal Region	Data	Prediction	(Predict - Data)/Data
FourTag	37.0 ± 6.08	27.37 ± 1.16	-26.0 % \pm 15.3 %
ThreeTag	645.0 ± 25.4	671.15 ± 12.11	4.05 % \pm 5.97 %
TwoTag split	3258.0 ± 57.08	3395.59 ± 24.42	4.22 % \pm 2.58 %

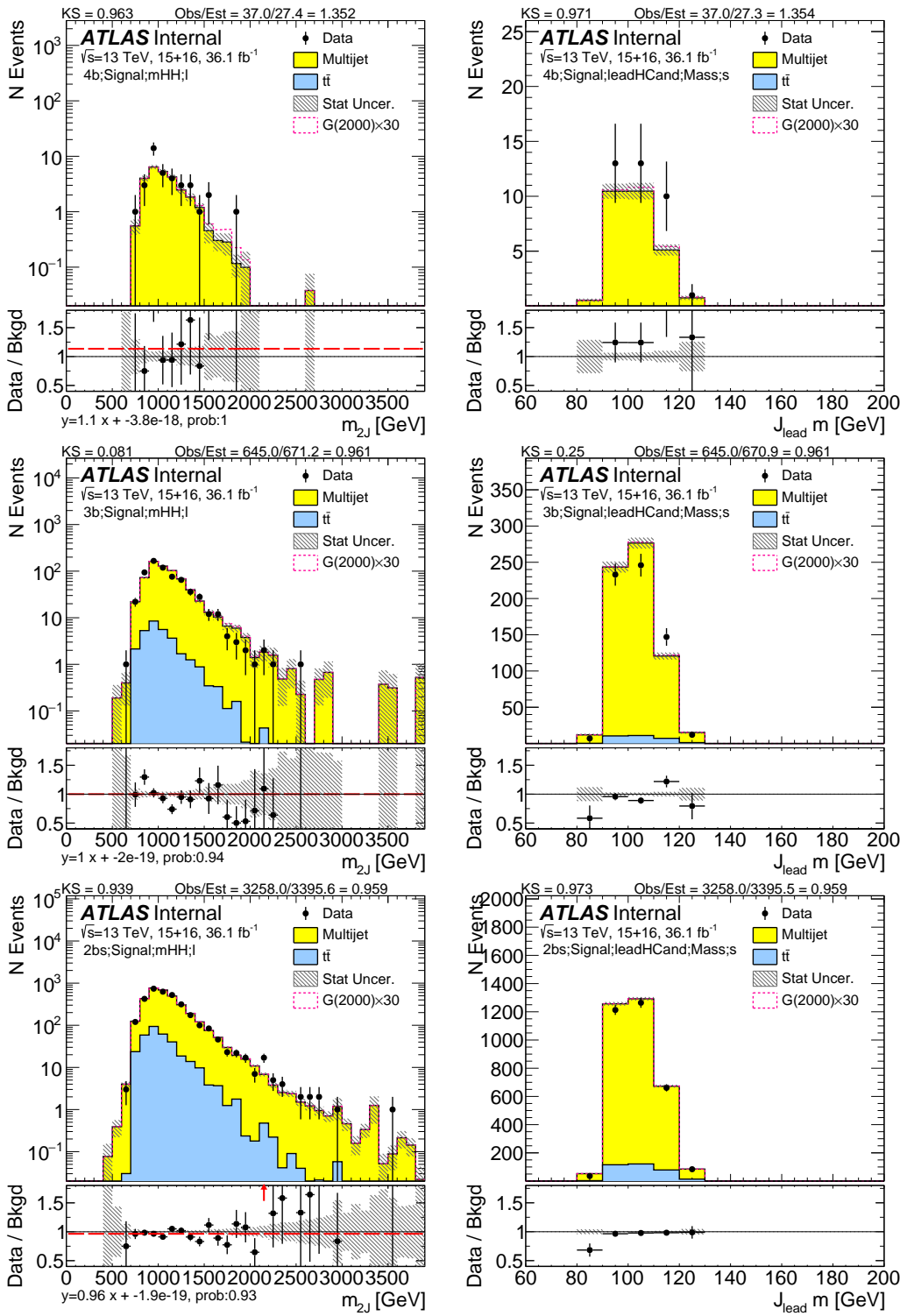


Figure 7.4: ZZ signal region distribution of m_{2J} (left column) and leading large-R jet mass (right column) in low mass signal, for 4b (top row), 3b(middle row) and 2b split (bottom row). The plots are with only statistical uncertainty.

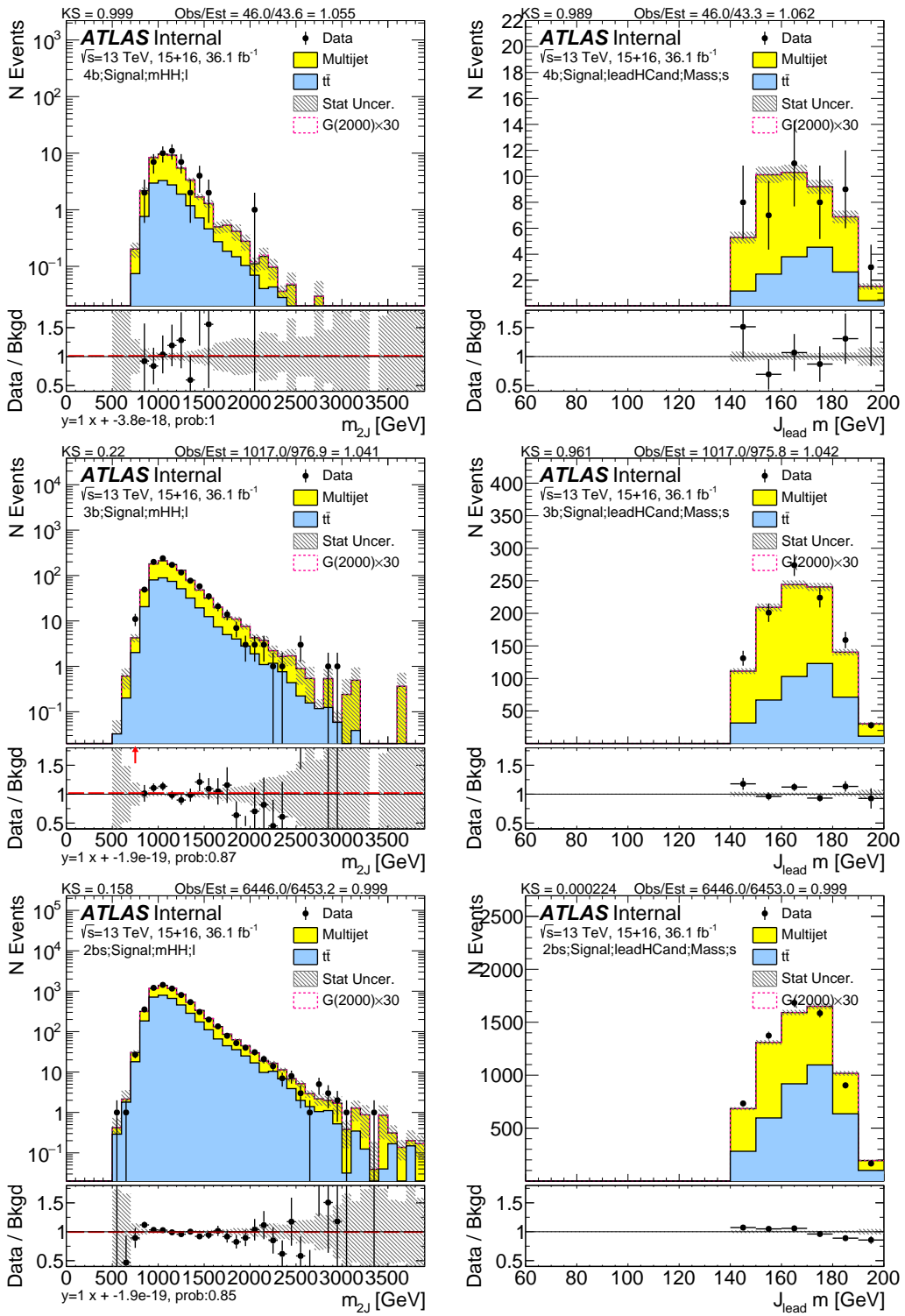


Figure 7.5: TT signal region distribution of m_{2J} (left column) and leading large-R jet mass (right column) in low mass signal, for $4b$ (top row), $3b$ (middle row) and $2b$ split (bottom row). The plots are with only statistical uncertainty.

Table 7.5: Data and prediction in TT SR in $4b$, $3b$ and $2bs$ regions.

TT Signal Region	Data	Prediction	(Predict - Data)/Data
FourTag	46.0 ± 6.78	43.62 ± 1.23	$-5.18\% \pm 16.66\%$
ThreeTag	1017.0 ± 31.89	976.88 ± 12.81	$-3.95\% \pm 4.27\%$
TwoTag split	6446.0 ± 80.29	6453.23 ± 51.41	$0.11\% \pm 2.04\%$

7.7 UNCERTAINTY ON THE SHAPE OF $t\bar{t} m_{2J}$ IN THE $4/3b$ SIGNAL REGION

Because the $4/3b t\bar{t} m_{2J}$ distribution is extremely statistically limited, the $2bs t\bar{t} m_{2J}$ shape is used to predict the final $t\bar{t}$ background shape in the $4/3b$ signal region. In order to estimate the possible shape uncertainty, the $2bs$ and $3b$ sideband shapes are normalized and compared in Figure 7.6. In order to avoid large statistical uncertainties, the distributions of the $3b$ and $2b$ are smoothed. The ratio of the two smoothed distributions is taken as the shape systematic. This ratio is used to apply a bin-by-bin scaling of the $t\bar{t}$ background prediction in the signal region, maintaining the same normalization given by nominal $t\bar{t}$ normalization prediction.

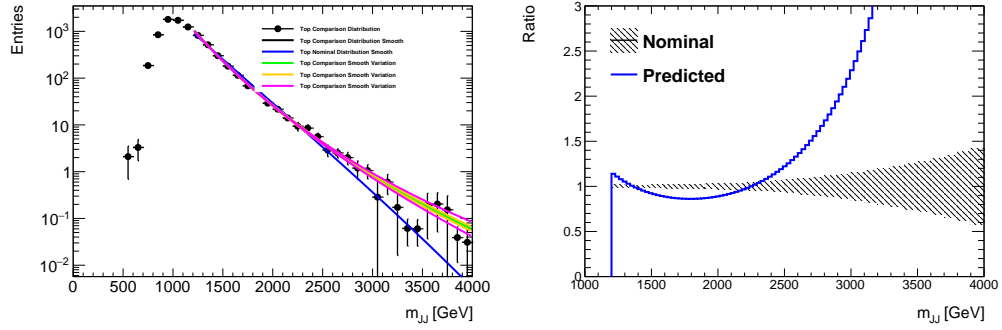


Figure 7.6: The shape of $t\bar{t} m_{2J}$ in the sideband region, comparing the $3b$ shape with that of the $2bs$, in order to assess the systematic effect of additional b -tags changing the dijet mass distribution. The m_{JJ} distributions is shown on the left, and the ratio of $3b$ to $2bs$ distributions on the right.

7.8 UNCERTAINTY ON THE SHAPE OF THE QCD DISTRIBUTION IN THE SIGNAL REGION

As shown in Figures 6.7, the shape of the total predicted background distribution is found to be in good agreement with the $4b$, $3b$, and $2bs$ data in the control region. However due to the low statistics in the high m_{2J} mass bins, there are statistical fluctuations that cannot be ignored. A comparison is performed by first smoothing the prediction and the data distribution in the control region. The ratio of the smoothed QCD distributions to that of the smoothed $4/3/2bs$ data distributions

is taken as the shape systematic. This ratio is then used to apply a bin-by-bin scaling of the QCD background prediction in the signal region, maintaining the same normalization given by μ_{qcd} . The smoothing fit and the ratios can be found in Figure 7.7. This systematics is further split into two parts: one below 2000 GeV and the other above 2000 GeV, to ensure the low and high mass shape variation post-fit pulls can vary independently. This uncertainty is applied for both the m_{2J} , and the scaled m_{2J} distribution, since the scaling correction has small impacts on m_{2J} .

7.9 UNCERTAINTY ON SMOOTHING FUNCTION IN THE SIGNAL REGION

A specific function has been used to fit the QCD background prediction in order to smooth the distribution and provide non-zero background estimates up to dijet masses beyond enough statistics. While this distribution is observed to fit the predicted signal region m_{2J} well, it does not have a concrete physical motivation, and in principle the high mass tail of the distribution could be larger than predicted. Two checks are performed, changing the boundaries where the fit is performed, and changing the fit function. The checks shows the smoothing function range and form variations are almost always smaller than the statistical uncertainties of the distributions. This gives this systematic uncertainty strong correlations with the shape uncertainties discussed in the previous section. As a result, this systematic uncertainty is excluded. Nevertheless, the tests are discussed below.

To test the impact of the region in which the fit is performed, the upper bound on the dijet fit region are varied to be $\{2800, 3000, 3200\}$ GeV and the lower bound are varied to be $\{1200, 1300, 1400\}$ GeV. The ratio of the fits for each upper bound, to that of the nominal (1200–3000 GeV) are shown in Figure 7.8, along with a hash band showing the statistical uncertainty of the nominal fit. This is estimated separately for $2bs$, $3b$, and $4b$ samples.

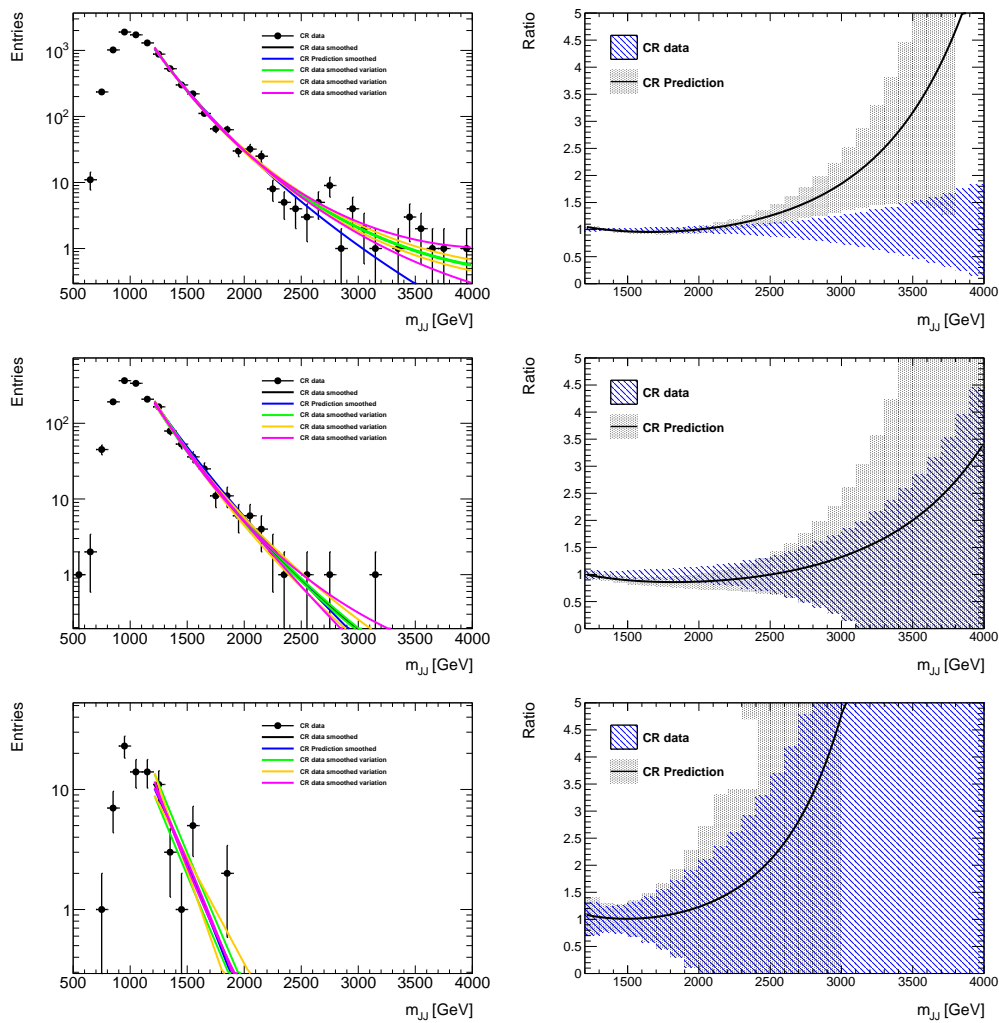


Figure 7.7: Dijet mass distribution in the CR along with the prediction (left) and the ratio of the prediction to the CR distribution (right) for the $2b$ s (top) $3b$ (middle) and $4b$ (bottom) samples. Ratios are from the smoothed distributions, the data uncertainty band contains the smoothing parameter variations, and the prediction uncertainty band also contains smoothing parameter variations.

Fits in which the fit χ^2 probability was less than 0.001%, or in which the fit integrals between 1500-2000 GeV, 2000-2500 GeV, or > 2500 GeV were not in agreement with the original distribution within a factor of 2 or 0.5, are not used to estimate the uncertainty. This ensure that poor fits are not used to estimate the uncertainty.

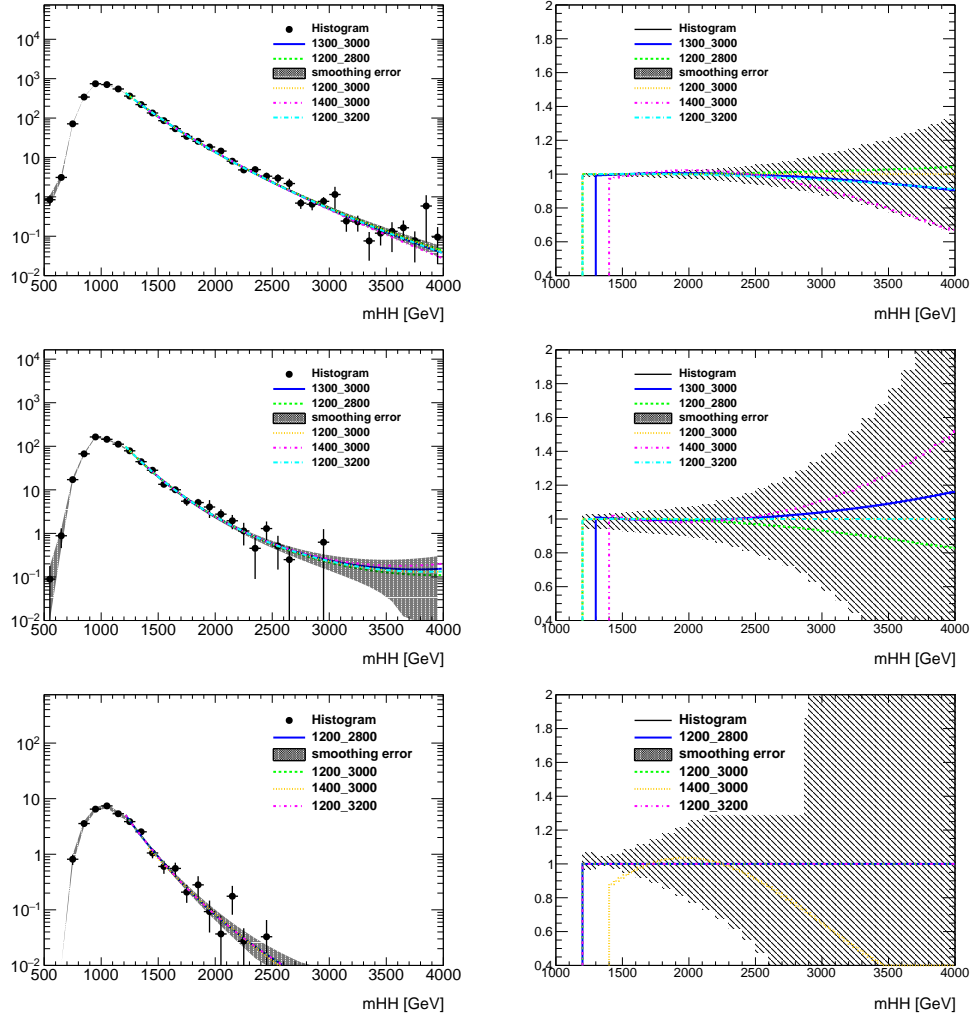


Figure 7.8: Dijet mass distribution SR prediction fit with several fit ranges (left) and the ratio of nominal to fits with different fit ranges (right) for the $2b$ s (top) $3b$ (middle) and $4b$ (bottom) samples.

The signal region QCD prediction is also fitted with a variety of other distributions which can show both power law behavior in the bulk of the distribution. The set of additional functions examined (labelled MJ₁-MJ₇) can be found in Table 7.6, where $x = m_{JJ}/\sqrt{s}$.

Name	Functional Form
MJ ₁ (Dijet)	$f_1(x) = p_o(1-x)^{p_1}x^{p_2}$
MJ ₂	$f_2(x) = p_o(1-x)^{p_1}e^{p_2 x^2}$
MJ ₃	$f_3(x) = p_o(1-x)^{p_1}x^{p_2 x}$
MJ ₄	$f_4(x) = p_o(1-x)^{p_1}x^{p_2 \ln x}$
MJ ₅	$f_5(x) = p_o(1-x)^{p_1}(1+x)^{p_2 x}$
MJ ₆	$f_6(x) = p_o(1-x)^{p_1}(1+x)^{p_2 \ln x}$
MJ ₇	$f_7(x) = \frac{p_o}{x}(1-x)^{p_1-p_2 \ln x}$
MJ ₈	$f_8(x) = \frac{p_o}{x^2}(1-x)^{p_1-p_2 \ln x}$

Table 7.6: Functions used to fit the QCD dijet mass distributions, where $x = m_{JJ}/\sqrt{s}$.

Figure 7.9 shows the fits to the QCD prediction in the $4/3/2bs$ signal regions, and the nominal dijet fit, as well as the ratios of the nominal fit to that of the additional functions. As before, poor fits are not used to estimate the uncertainty..

7.10 SUMMARY OF SYSTEMATICS

Table 7.7 shows the percent impact of systematics used in the boosted analysis on the backgrounds yields and on the expected yields for RSG $c = 1.0$ signals in the $4b$ signal region. The correspondent values are shown for the $3b$ signal region in Table 7.8, and are shown for the $2bs$ signal region in Table 7.9. The systematics that have no impact the yield are not listed. These are uncertainties on the shape of the QCD and $t\bar{t}$ backgrounds in the signal region.

The “Background Normalization Fit” uncertainty comes from summing in quadrature the independent uncertainty components calculated from the correlated statistical errors of μ_{qcd} and $\alpha_{\bar{t}t}$.

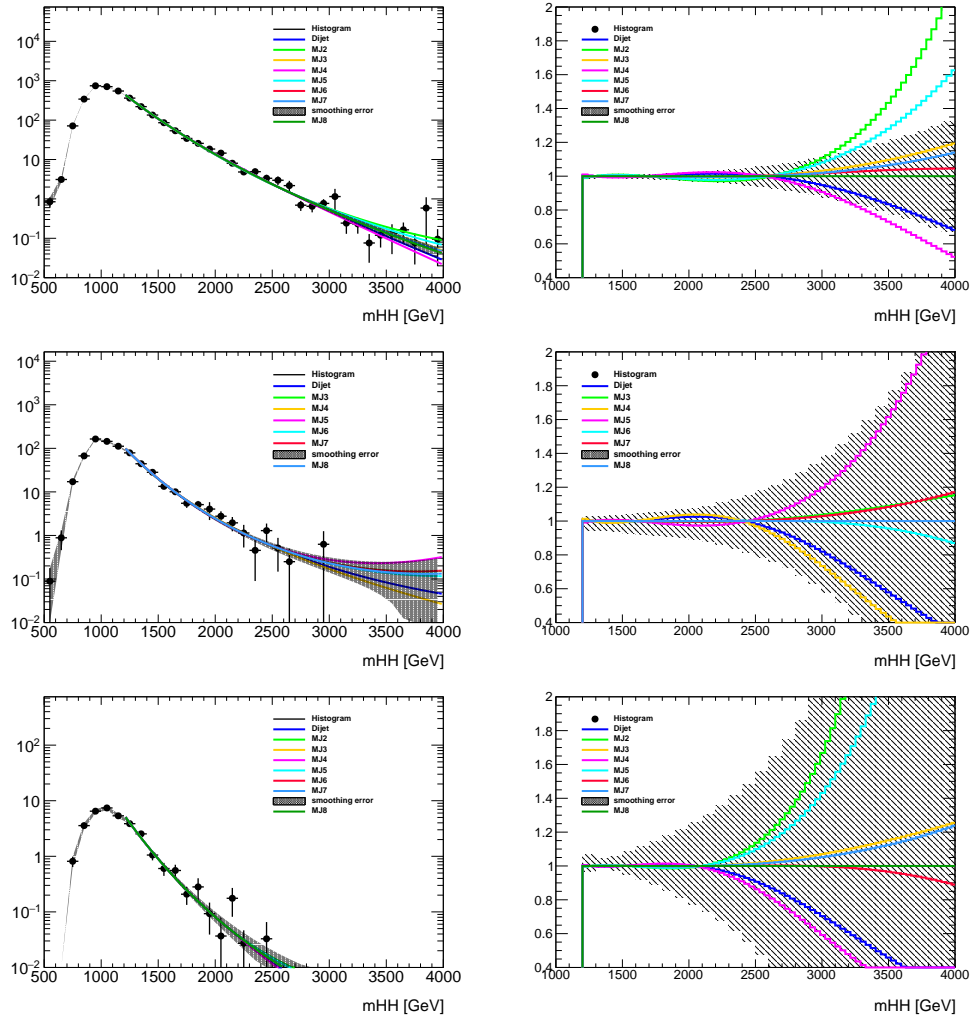


Figure 7.9: Dijet mass distribution SR prediction fit with several fit functions (left) and the ratio of nominal to fits with different fit functions (right) for the 2b (top) 3b (middle) and 4b (bottom) samples. The additional fit functions are from Table 7.6.

The “QCD Non-Closure in CR” systematic is derived as the maximum of the difference between the predicted and observed $4b/3b/2bs$ QCD yields in the control region, or the fractional change in SR predictions from varying the CR and SB definitions. Both options gave similar sized uncertainties, but the uncertainty from the CR/SB variations was found to be larger. All these uncertainties are summed in quadrature and shown in the “Bkg Est” row in the table.

The size of the Monte Carlo modeling systematics on the G_{KK}^* with $c = 1.0$ yield as a function of the signal mass can be found in Figure 7.10. These uncertainties have a similar impact on the other signals. The largest uncertainty in the $4b$ and $2b$ signal region is from b -tagging, followed by the JMR uncertainty. In the $3b$ signal region, although b -tagging systematics is still one of the largest uncertainty, it has been much reduced compared to $4b$ region, as discussed in Section 7.3.3.

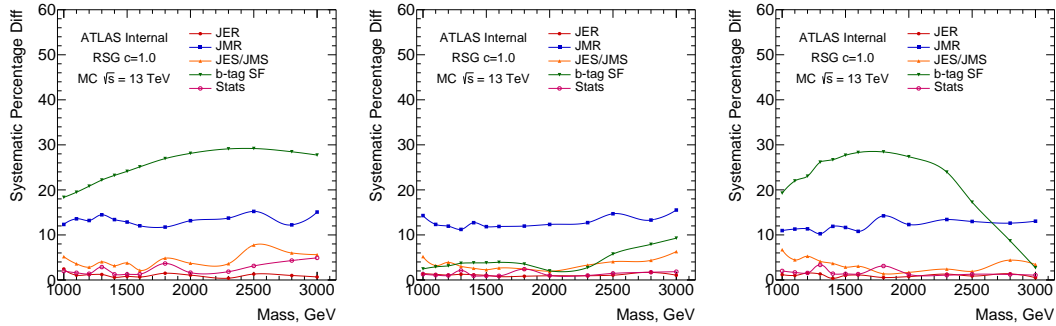


Figure 7.10: Impact of each systematic on the signal prediction as a function of the signal mass, in the $4b$ (left) and $3b$ (middle) and $2bs$ signal regions.

Table 7.7: Percent impact of the dominant systematics on the background acceptance and on the signal acceptance of G_{KK}^* with $c = 1.0$ in the $4b$ signal region.

FourTag	totalbkg	qcd	ttbar	RSG ₁ 1000	RSG ₁ 2000	RSG ₁ 3000
JER	0.45	0.27	3.98	2.44	1.07	0.67
JMR	7.9	10.35	39.95	12.33	13.16	15.08
Top	-	-	-	-	-	-
JES/JMS	1.32	1.49	24.36	5.18	3.72	5.62
Bkg Est	15.67	18.19	67.82	-	-	-
b-tag SF	1.11	0.79	18.85	18.34	28.11	27.73
Total Sys	17.64	21.0	84.62	22.83	31.28	32.07
Stat	3.13	3.29	2.47	1.97	1.63	4.9
Estimated Events	34.59	32.91	1.68	10.07	0.25	0.0016

Table 7.8: Percent impact of the dominant systematics on the background acceptance and on the signal acceptance of G_{KK}^* with $c = 1.0$ in the $3b$ signal region.

ThreeTag	totalbkg	qcd	ttbar	RSG ₁ 1000	RSG ₁ 2000	RSG ₁ 3000
JER	1.38	3.52	17.5	1.41	0.93	1.08
JMR	1.35	4.26	24.38	14.3	12.33	15.53
Top	-	-	-	-	-	-
JES/JMS	2.03	1.26	26.22	5.19	1.94	6.35
Bkg Est	4.84	5.62	9.45	-	-	-
b-tag SF	0.47	0.53	8.45	2.45	2.01	9.27
Total Sys	5.61	8.0	41.82	15.47	12.68	19.2
Stat	1.32	1.44	2.47	1.26	1.0	1.83
Estimated Events	780.89	701.52	79.38	26.0	0.76	0.013

Table 7.9: Percent impact of the dominant systematics on the background acceptance and on the signal acceptance of G_{KK}^* with $c = 1.0$ in the $2bs$ signal region.

TwoTag split	totalbkg	qcd	ttbar	RSG ₁ 1000	RSG ₁ 2000	RSG ₁ 3000
JER	0.25	0.48	3.14	1.18	0.74	0.5
JMR	0.52	1.73	9.43	10.96	12.3	13.03
Top	-	-	-	-	-	-
JES/JMS	0.43	1.67	7.17	6.72	1.7	3.55
Bkg Est	2.7	3.32	2.4	-	-	-
b-tag SF	0.83	1.43	1.82	19.28	27.36	2.72
Total Sys	2.92	4.37	12.62	23.2	30.05	13.79
Stat	0.6	0.41	2.47	2.0	1.2	1.07
Estimated Events	4251.49	3392.79	858.7	10.87	0.6	0.039

*Madness and genius are separated only by degrees of
success.*

Tony

8

Result

8.1 BOOSTED SIGNAL REGION

The unblinded yields are summarized in Table 8.1. The unscaled $2bs/3b/4bs$ m_{2J} distributions are shown in Figures 8.3, 8.2, 8.1. No significant excess of number of events or in the dijet mass distribution is observed. For the scaled m_{2J} distributions are shown in Figures 8.6, 8.5, 8.4. Again, no significant excess of number of events or in the dijet mass distribution is observed. No events are observed with m_{2J} or scaled m_{2J} above 4 TeV. Other distributions in the signal region are shown in Appendix C.

Sample	FourTag	ThreeTag	TwoTag split
qcd	32.92 ± 7.07	702.16 ± 63.12	3393.81 ± 148.78
ttbar	1.68 ± 1.43	79.41 ± 33.12	859.03 ± 107.86
totalbkg	34.6 ± 6.28	781.56 ± 52.42	4252.83 ± 125.73
Data	31.0 ± 5.57	801.0 ± 28.3	4376.0 ± 66.15

Table 8.1: Unblinded Signal Region predictions and results. All systematic uncertainties are included for backgrounds. The Poisson uncertainty in data is shown for comparison.

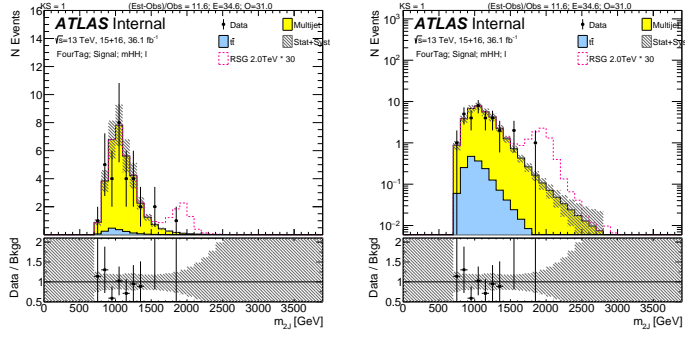


Figure 8.1: Unscaled m_{2j} distribution in the $4b$ Signal Region after unblinding. The left plot is on linear scale and the right plot is on log scale.

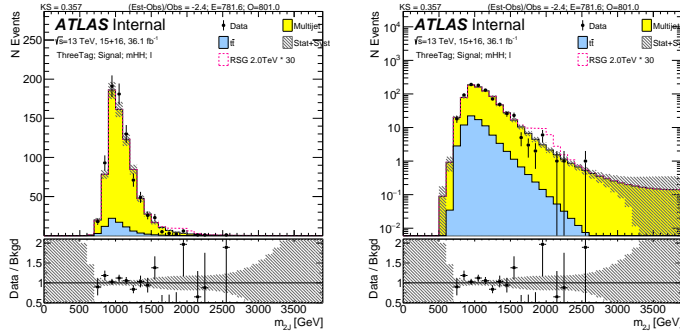


Figure 8.2: Unscaled m_{2j} distribution in the $3b$ Signal Region after unblinding. The left plot is on linear scale and the right plot is on log scale.

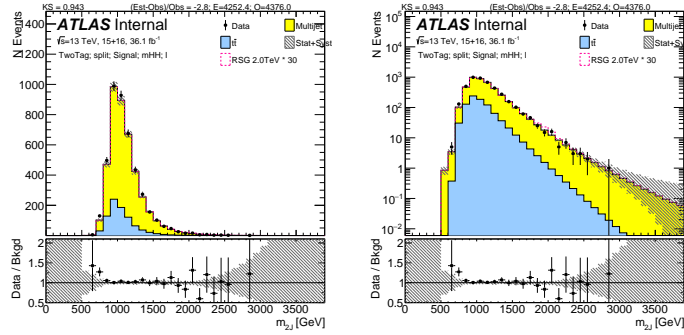


Figure 8.3: Unscaled m_{2J} distribution in the $2b$ Signal Region after unblinding. The left plot is on linear scale and the right plot is on log scale.

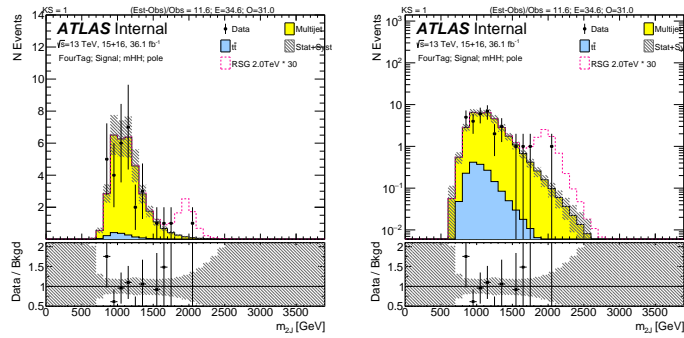


Figure 8.4: Scaled m_{2J} distribution in the $4b$ Signal Region after unblinding. The left plot is on linear scale and the right plot is on log scale.

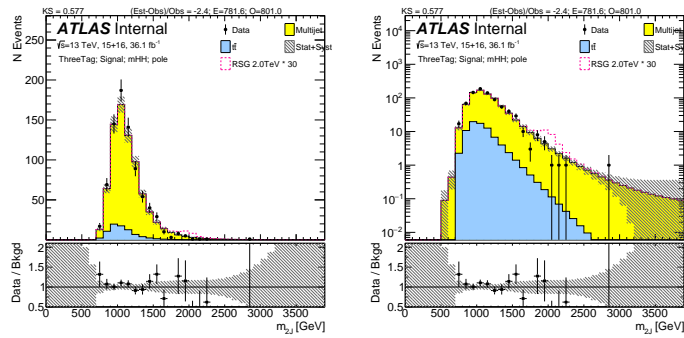


Figure 8.5: Scaled m_{2J} distribution in the $3b$ Signal Region after unblinding. The left plot is on linear scale and the right plot is on log scale.

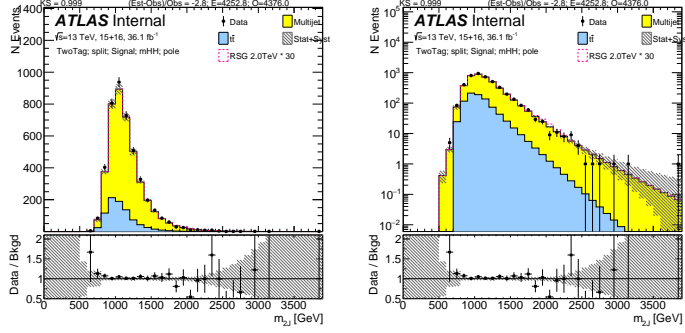


Figure 8.6: Scaled m_{2j} distribution in the $2b\bar{b}$ Signal Region after unblinding. The left plot is on linear scale and the right plot is on log scale.

8.2 RESOLVED SIGNAL REGION

The number of events observed in the data, the predicted number of background events in the signal region, and the predicted yield for three potential signals are presented in Table 8.2 for both the 2015 and 2016 datasets. The numbers of observed and predicted events in the control region are also shown. A discrepancy between data and the total prediction is seen in the 2016 dataset; about half of this excess can be attributed to one bin at $m_{4j} = 280$ GeV. This could be a trigger turn-on effect.

Figure 8.7 shows comparisons of the predicted m_{4j} background distributions to those observed in the 2015 and 2016 datasets. A few signal models are also displayed. The scalar sample shown is normalized to a cross section times $b \rightarrow b\bar{b}$ branching ratio of 2.7 pb, which is the best-fit value (the fit is described in Section ??). The predicted background and observed distributions are mostly in agreement, with an excess above the predicted background in one bin around 280 GeV, which is discussed in Section ??.

Table 8.2: The number of predicted background events in the signal region (SR) for the resolved analysis compared to the data, for the 2015 and 2016 datasets. The yields for three potential signals, an 800 GeV G_{KK}^* -resonance with $k/\bar{M}_{Pl} = 1$, a scalar with a mass of 280 GeV, and SM non-resonant Higgs boson pair production, are also shown. The scalar sample is normalized to a cross section times branching ratio of 2.7 pb. The quoted uncertainties include both the statistical and systematic uncertainties, and the total uncertainty considers correlations. The numbers of observed and predicted events are also given in the control region (CR).

Sample	2015 SR	2016 SR	2015 CR	2016 CR
Multijet	866 ± 70	6750 ± 170	880 ± 71	7110 ± 180
$t\bar{t}$, hadronic	52 ± 35	259 ± 57	56 ± 37	276 ± 61
$t\bar{t}$, semileptonic	13.9 ± 6.5	123 ± 30	20 ± 9	168 ± 40
Total	930 ± 70	7130 ± 130	956 ± 50	7550 ± 130
Data	928	7430	969	7656
$G_{KK}^*(800 \text{ GeV})$	12.5	1.9	89	14
Scalar (280 GeV)	24	7.5	180	57
SM di-Higgs	0.607	0.091	4.43	0.66

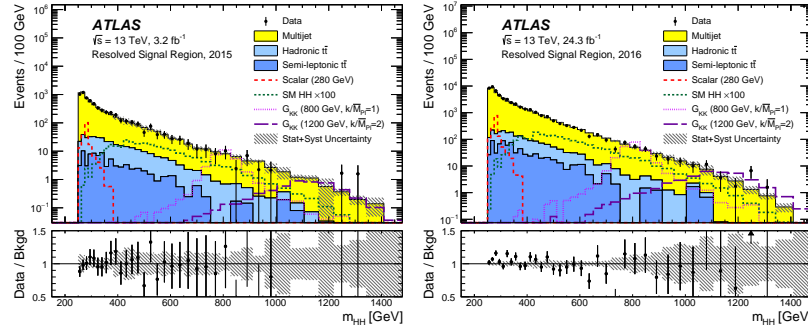


Figure 8.7: Distributions of m_{4j} in the signal region of the resolved analysis for (a) 2015 data and (b) 2016 data, compared to the predicted backgrounds. The hatched bands shown in the bottom panels represent the combined statistical and systematic uncertainties in the total background estimates. The expected signal distributions of G_{KK}^* resonances with masses of 800 and 1200 GeV, the 280 GeV scalar sample and SM non-resonant di-Higgs production ($\times 100$) are also shown. The scalar sample is normalized to a cross section times branching ratio of 2.7 pb.

8.3 STATISTICAL ANALYSIS

Following the statistical procedures outlined in Ref.⁷⁶, a test statistic based on the profile likelihood ratio⁷⁷ is used to test hypothesized values of $\mu = \sigma/\sigma_{\text{model}}$, the global signal strength factor,

separately for each signal model. The exclusion limits are computed using asymptotic formulae⁷⁷ and are based on the CL_s method⁷⁸, where a value of μ is regarded as excluded at the 95% confidence level (CL) when CL_s is less than 5%.

The test statistic used is a one sided profile likelihood ratio:

$$q_o = -2 \ln \frac{L(o, \hat{\vartheta}(o))}{L(\hat{\mu}, \hat{\vartheta})}; \hat{\mu} > o \quad (8.1)$$

$$q_o = o; \hat{\mu} < o \quad (8.2)$$

Where μ is the value of the signal normalization considered, $\hat{\mu}$ is the maximum likelihood (ML) value of μ . ϑ is the set of nuisance parameters (NP): $\hat{\vartheta}$ is the ML value of ϑ and $\hat{\hat{\vartheta}}$ is the ML value of ϑ when μ is fixed at a particular value. L denotes the profile likelihood: $L(\hat{\mu}, \hat{\vartheta})$ is the likelihood where μ is allowed to take any value, the unconstrained likelihood. $L(o, \hat{\vartheta}(o))$ is the likelihood for the value of $\mu = o$, the constrained likelihood.

This tests the compatibility of the data with the background-only hypothesis, $\mu = o$. The local p-value of a set of data, p_o , is defined as the probability for the background-only hypothesis to have a value of q_o that is as high or higher than the value of q_o in that data. In order to obtain p_o , pseudo-experiments are generated with the background only model and the distribution of the test statistic, q_o , is built up from the values of the pseudo-experiments.

The background model is found to describe the data and no significant excess is observed. The smallest local $p_o = 0.175$ (1σ) is found at 1100 GeV when fitting with the narrow scalar model. The local p_o values for the three signal models as a function of the resonance mass are shown in Fig. 8.8.

Figure 8.9 shows the pulls of the systematic uncertainty nuisance parameters and their correlations for the 2000 GeV mass point. The parameters are ranked by their post-fit impact. Only the

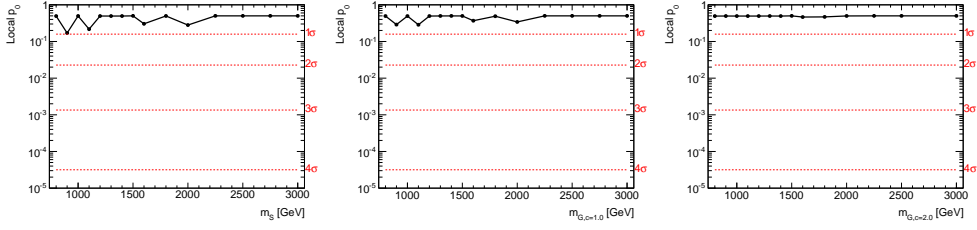


Figure 8.8: Local p_0 of the (a) scalar, (b) $c=1$ Graviton and (c) $c=2$ Graviton.

leading 30 nuisance parameters are displayed. One nuisance parameter (`QCD_ShapeCRHigh`) in both the $2b$ and $3b$ samples shows a significant constraint coming from the signal region data. This nuisance parameter corresponds to the shape uncertainty on the QCD background derived from the $2b$ and $3b$ control regions, as explained in Section 7.8. The prior probability distributions for this nuisance parameter is very broad, with the relative uncertainty on the background prediction reaching 1500% at high m_{bb} . This is because there is very little data in the control region at high mass to constrain the uncertainty. In the signal region however, the two events found suffice to constrain it: very tightly in comparison to the extremely loose prior constraint.

Examples of the fit used to set these limits are shown in Figures 8.10, where a narrow scalar is used for the signal model. In the case the best-fit is negative, the fit is repeated with mu bounded to zero. At 2 TeV, the fitted signal is positive ($\mu = 0.1 \pm 0.25$) though well consistent with the background-only hypothesis. In all fits, good agreement is seen between data and the background only model.

The observed limit for the narrow scalar and G_{KK}^* is shown in Fig. 8.11. The stat-only limit is also shown. The impact of systematic uncertainties is small. These limits do not contain any input from the resolved analysis.

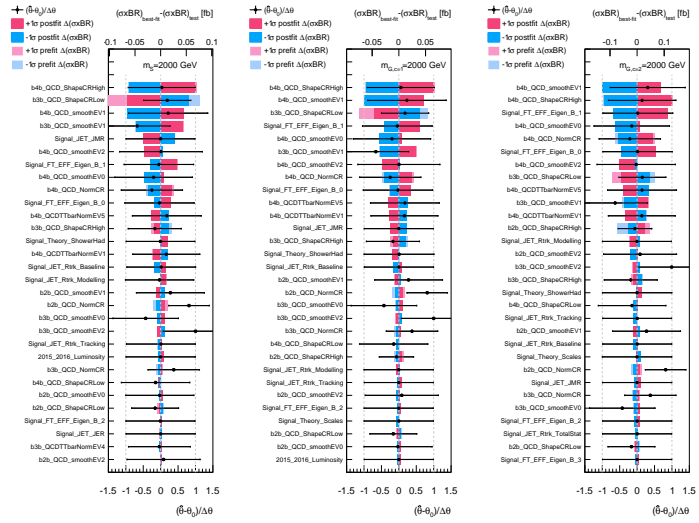


Figure 8.9: The impact of nuisance parameters on the fitted cross section, ranked by their post-fit impact. The signal mass used in this fits is 2000 GeV, and the signal model is (a) narrow scalar, (b) G_{KK}^* with $c = 1$ and (c) G_{KK}^* with $c = 2$.

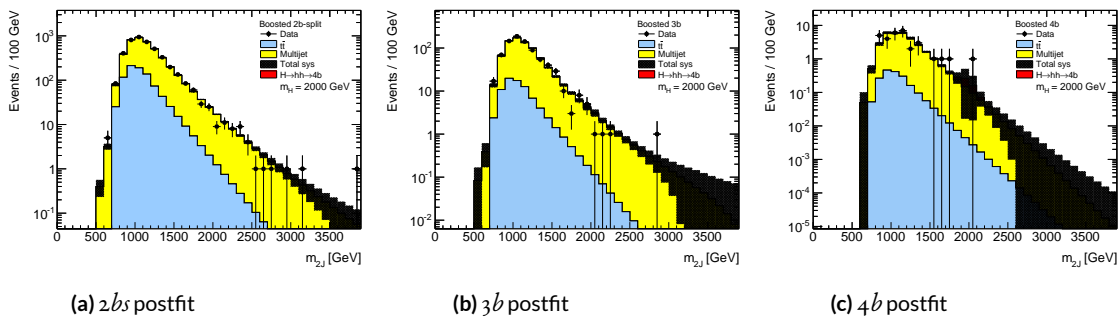


Figure 8.10: Post-fit signal region scaled m_{2j} distributions after fitting the data with the 2 TeV G_{KK}^* with $c = 1.0$ hypothesis. The signal strength is slightly positive.

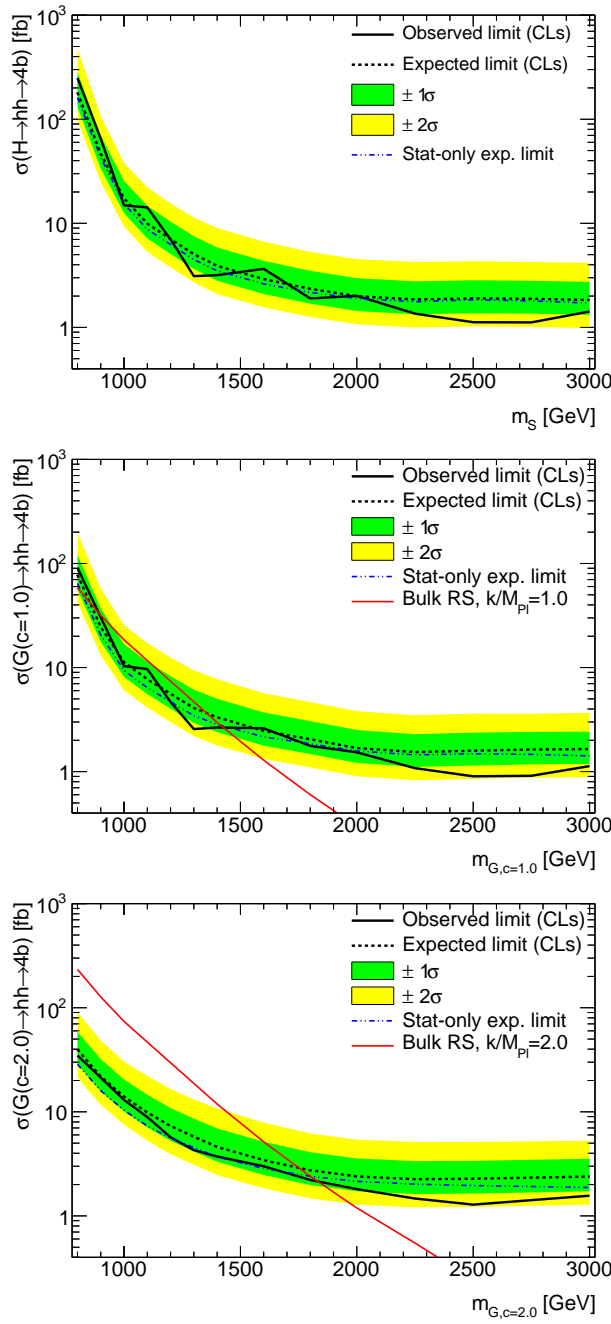


Figure 8.11: The expected and observed 95% C.L. upper exclusion limits for the boosted $4b$ analysis calculated including all systematic uncertainties for the narrow scalar model (top), $G_{KK}^*c = 1.0$ (middle), and $G_{KK}^*c = 2.0$ (bottom). The dot-dashed line shows the expected limit when only statistical uncertainties are included. The limits are derived within the asymptotic approximation.

8.4 BOOSTED AND RESOLVED COMBINED LIMITS

The observed limit for the narrow scalar is shown in Figure 8.14. The observed limits for the Graviton models is shown in Figure 8.12 for $k/\bar{M}_{\text{Pl}} = 1$ and in Figure 8.13 for $k/\bar{M}_{\text{Pl}} = 2$. The bulk RS model with $k/\bar{M}_{\text{Pl}} = 1$ is excluded for masses between 313 and 1362 GeV, and the bulk RS model with $k/\bar{M}_{\text{Pl}} = 2$ is excluded for masses below 1744 GeV. In the heavy Higgs model, the cross section upper limits for $\sigma(pp \rightarrow H \rightarrow hh \rightarrow b\bar{b}b\bar{b})$ range from 1 to 10 fb in the mass range of 1000 to 3000 GeV.

From Figure 8.14, different expected exclusion limit from the analysis can be compared. The resolved analysis is only sensitive for resonance searches up to 900 GeV. The boosted $4b$ is most sensitive for resonances between 1200 and 1800 GeV. The boosted $3b$ is most sensitive for resonances between 2000 and 2500 GeV. The boosted $2bs$ is most sensitive for resonances between 2500 and 3000 GeV. The combination significantly improves the sensitivity between 1 and 1.5 TeV for resonant signals. The result is limited by systematic uncertainties in the background normalization and shape. Since these are data-driven, an increase of the integrated luminosity will improve the sensitivity.

The non-resonant search is performed using the resolved analysis only, since it has much better sensitivity to non-resonant signals than the boosted analysis. Using the SM di-Higgs non-resonant production via gluon–gluon fusion as the signal model, and applying the NNLO and finite top-quark mass correction, the observed 95% CL upper limit is $\sigma(pp \rightarrow hh \rightarrow b\bar{b}b\bar{b}) < 147$ fb. The expected and observed limit values and the uncertainties in the expectation are given in Table 8.3. The observed limit is stronger than the expected due to the light deficit of events in m_{4j} around 500 – 600 GeV.

Table 8.3: 95% CL exclusion limits for SM non-resonant di-Higgs production, in units of the SM prediction for $\sigma(pp \rightarrow hh \rightarrow b\bar{b}b\bar{b})$.

	Observed	-2σ	-1σ	Expected	$+1\sigma$	$+2\sigma$
	13.0	11.1	14.9	20.7	30.0	43.5

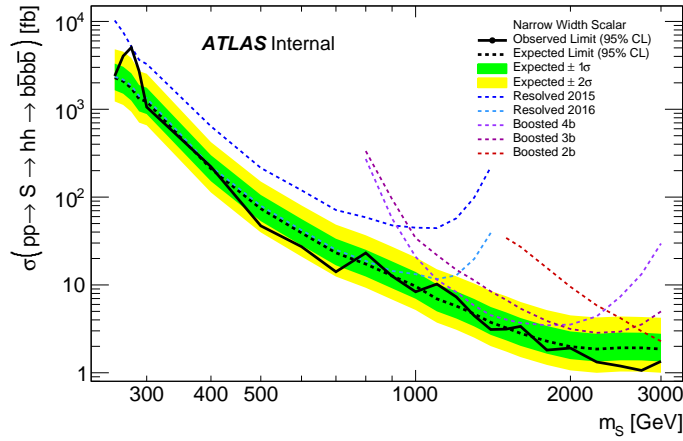


Figure 8.12: The expected and observed 95% C.L. upper exclusion limits for the boosted $4b$ analysis calculated including all systematic uncertainties for the narrow scalar model. The dot-dashed line shows the expected limit when only statistical uncertainties are included. The limits are derived within the asymptotic approximation.

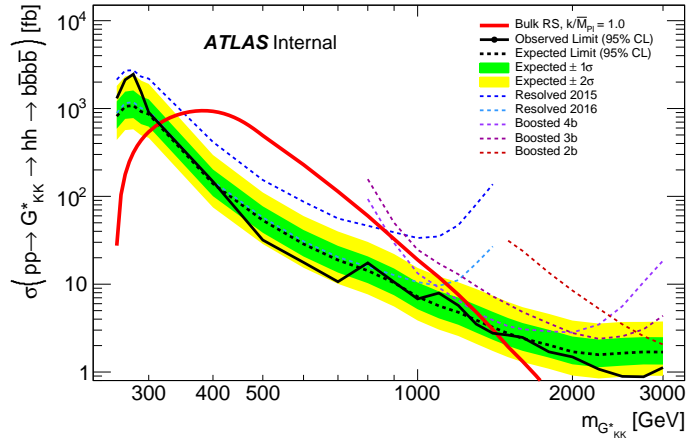


Figure 8.13: The expected and observed 95% C.L. upper exclusion limits for the boosted $4b$ analysis calculated including all systematic uncertainties for the $c=1.0$ Graviton. The dot-dashed line shows the expected limit when only statistical uncertainties are included. The limits are derived within the asymptotic approximation.

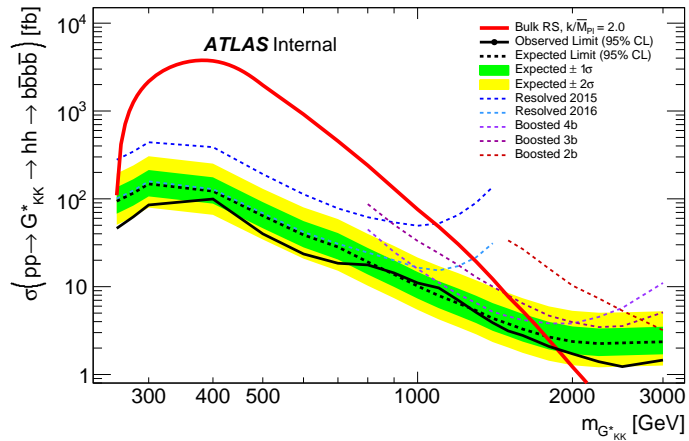


Figure 8.14: The expected and observed 95% C.L. upper exclusion limits for the boosted $4b$ analysis calculated including all systematic uncertainties for the $c=2.0$ Graviton. The dot-dashed line shows the expected limit when only statistical uncertainties are included. The limits are derived within the asymptotic approximation.

*It is a far, far better thing that I do, than I have ever
done; it is a far, far better rest that I go to than I have
ever known.*

Charles Dickens

9

Conclusion

Di-Higgs search has a short history, but will have a long future ahead. This thesis presents a search for both resonant and non-resonant production of pairs of Standard Model Higgs bosons has been carried out in the dominant $b\bar{b}b\bar{b}$ channel, using 36.1 fb^{-1} of LHC $p\bar{p}$ collision data at $\sqrt{s} = 13 \text{ TeV}$ collected by ATLAS in 2015 and 2016. The search sensitivity of this analysis exceeds that of the previous analysis of the $\sqrt{s} = 13 \text{ TeV}$ 2015 dataset³ for non-resonant signal and also across the entire mass range of 260 to 3000 GeV for the resonance search, with significantly improvement in the high mass resonance sensitivities. The resolved analysis has each $h \rightarrow b\bar{b}$ reconstructed as two separate b -tagged jets, and the boosted analysis has each $h \rightarrow b\bar{b}$ reconstructed as a single large-radius jet associated with at least one small-radius b -tagged track-jet. The estimated background consists mainly of multi-jet and $t\bar{t}$ events.

No significant excess is observed in the data. Upper limits on the production cross section times branching ratio to the $b\bar{b}b\bar{b}$ final state are set for a narrow-width spin-0 scalar and for wider spin-2 resonances. The bulk RS model with $k/\bar{M}_{\text{Pl}} = 1$ is excluded for masses between 313 and 1362 GeV, and the bulk RS model with $k/\bar{M}_{\text{Pl}} = 2$ is excluded for masses below 1744 GeV. The 95% CL upper limit on the non-resonant production is 147 fb, which corresponds to 13.0 times the SM expectation.

This result confirms the great success of the Standard Model. The Higgs potential shape couldn't be very different from the SM predictions at TeV energy scale. Without any significant excess, the phase space for Beyond the Standard Model physics is further constrained.

Improvement with future Run 2 data could come b -tagging, especially efficiency increase in high p_T region. Other aspects include advanced trigger technologies, which can increase the signal event rate, and improved jet energy and mass resolution, which can increase the purity in selection. Together with the larger dataset, it is possible to double the current resonance search sensitivity. For non-resonance search, combined $|\frac{\lambda}{\lambda_{\text{SM}}}| \sim 10$ is possible at the end of Run 2 in 2020.

For longer perspectives, di-Higgs searches and measurements will continue to be one of the most important analysis. It can show hints of the physics Beyond the Standard Model. In 2030 to 2040, the High Luminosity LHC will be able to constrain $|\frac{\lambda}{\lambda_{\text{SM}}}| \sim 1$ with all the different channels from both ATLAS and CMS combined.

For even longer future developments in high energy experiments, all aspects—accelerator, detector, computation and theory—must advance together to answer the questions the Standard Model cannot answer, or find questions the Standard Model didn't ask^{79,80}. Life is short for mankind, and the understanding of the universe is an endless journey. I am deeply honored to be a small part of this odyssey by working on the boosted $pp \rightarrow hh \rightarrow b\bar{b}b\bar{b}$ analysis.

A

Boosted sideband region kinematic distributions

This appendix shows comparisons of data with the prediction of QCD multi-jets and $t\bar{t}$ backgrounds in the control region. The definition of the sideband region is discussed in Section 6.2. Because of the fit method in Section 6.5, the predicted normalization agrees perfectly with data. The

agreement of the data and predictions is generally very good, without significant deviations.

Figures A.1, A.2, A.3, and A.4 show predictions of various kinematics of the large- R jets and their associated track jets in the $4b$ selection. Figures A.5, A.6, A.7, and A.8 show predictions of various kinematics of the large- R jets and their associated track jets in the $3b$ selection. Figures A.9, A.10, A.11, and A.12 show predictions of various kinematics of the large- R jets and their associated track jets in the $2bs$ selection.

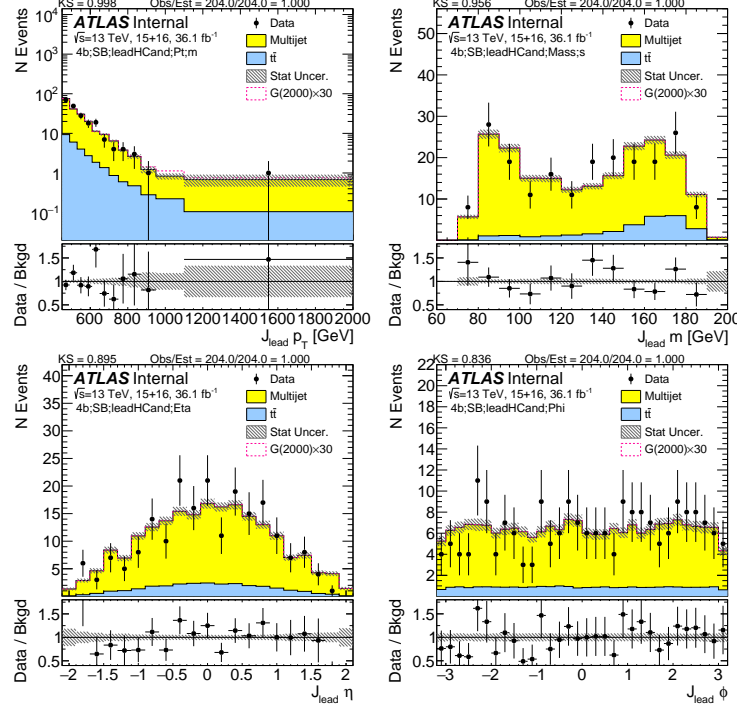


Figure A.1: Kinematics (p_T , mass, η , ϕ) of the lead large- R jet in data and prediction in the sideband region after requiring $4 b$ -tags.

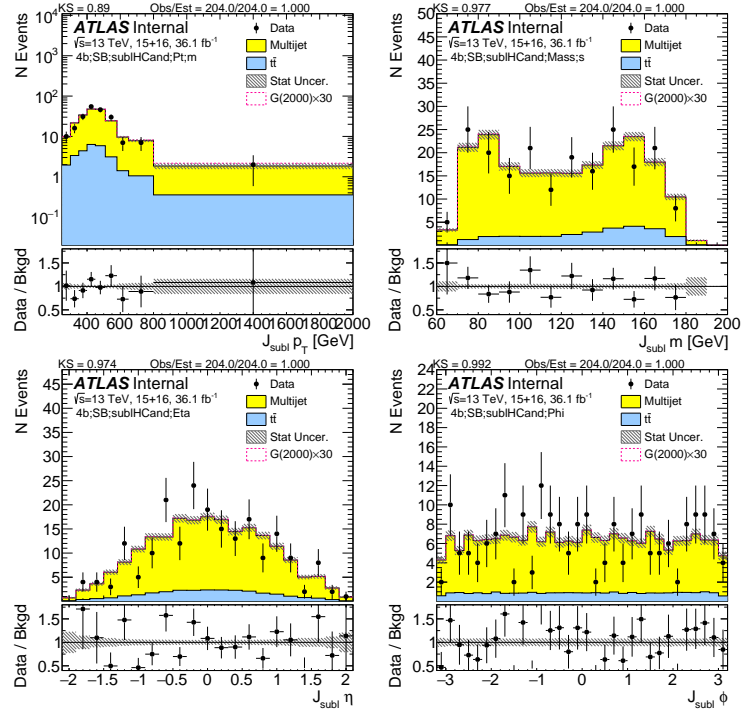


Figure A.2: Kinematics (p_T , mass, η , ϕ) of the subleading large- R jet in data and prediction in the sideband region after requiring 4 b -tags.

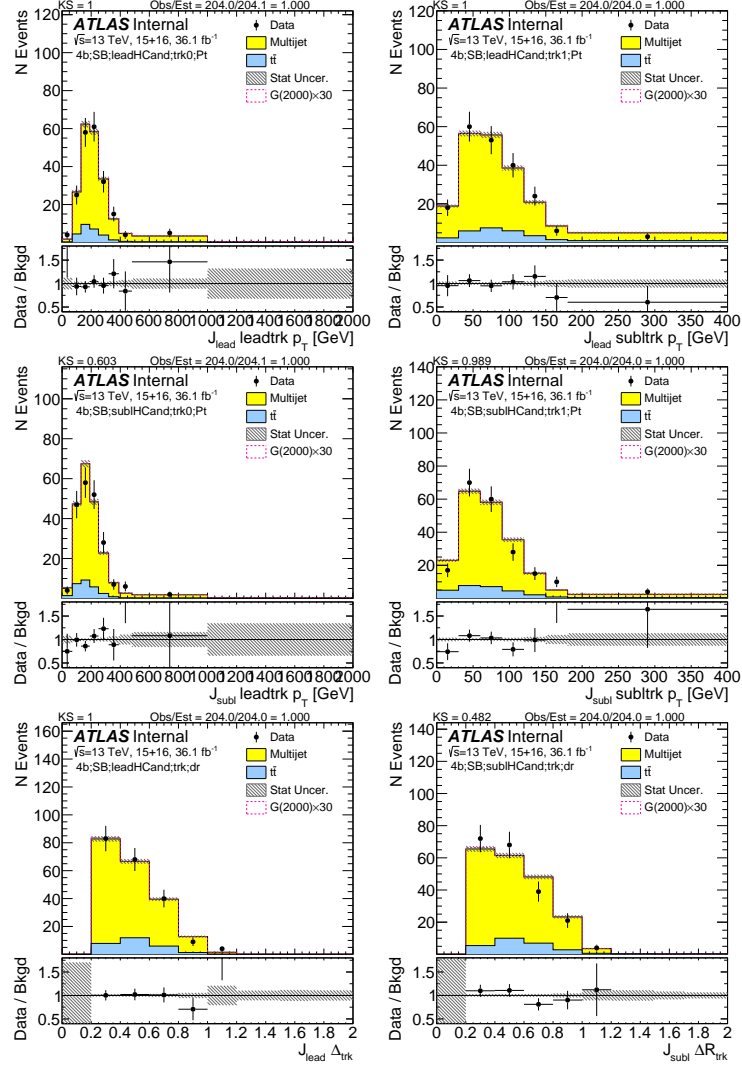


Figure A.3: First two rows show the p_T of the lead (left) and sub-lead (right) small- R track jets associated to the lead (first-row) and sub-lead (second-row) large- R jet in data and prediction in the sideband region after requiring 4 b -tags. Third row shows the ΔR between two leading small- R track-jets associated to the leading (left) and sub-leading (right) large- R jet.

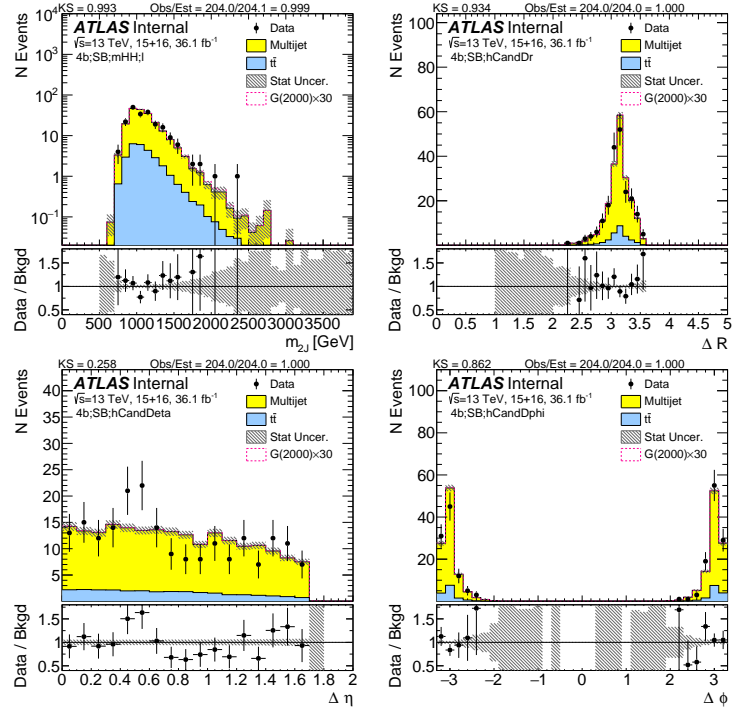


Figure A.4: Kinematics (invariant mass, ΔR , $\Delta\eta$ and $\Delta\phi$) of two large- R jets in data and prediction in the sideband region after requiring 4 b -tags.

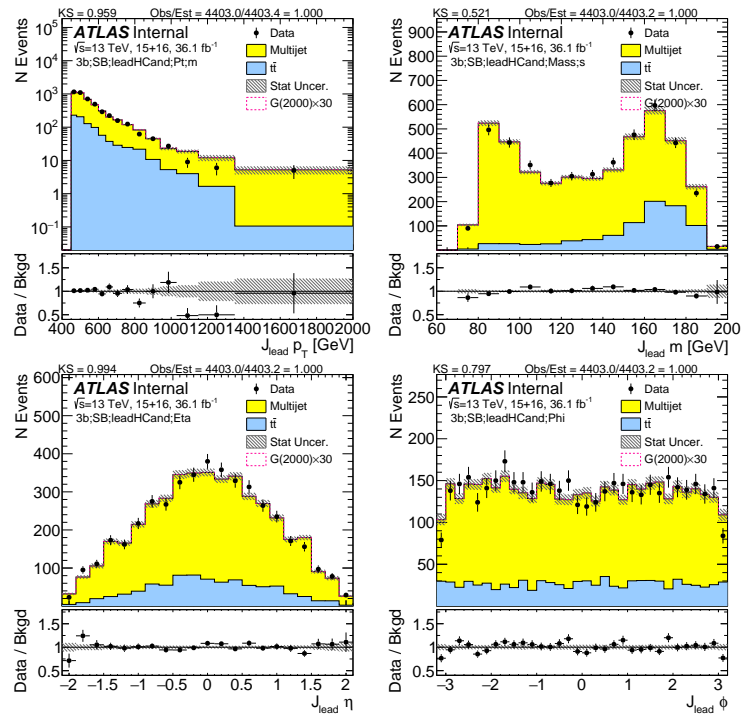


Figure A.5: Kinematics (p_T , mass, η , ϕ) of the lead large- R jet in data and prediction in the sideband region after requiring 3 b -tags.

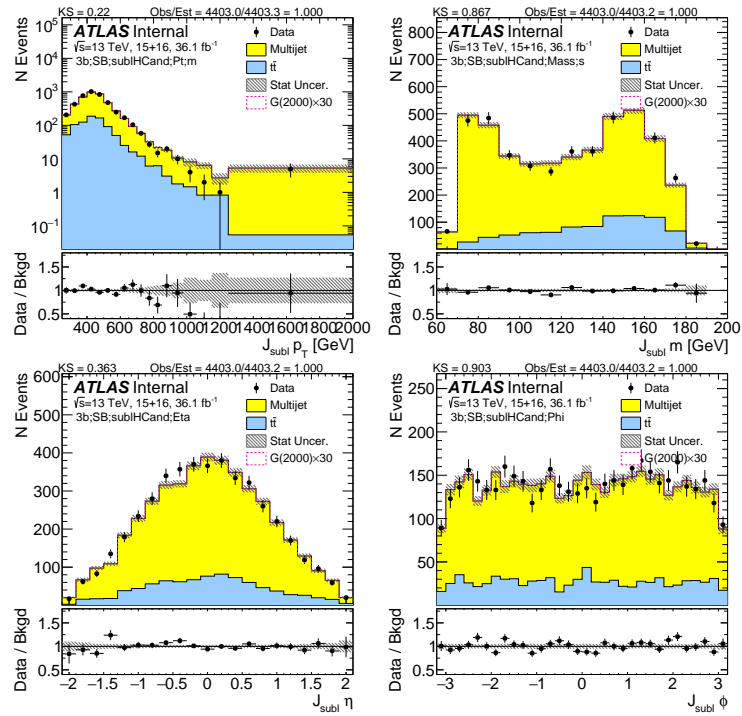


Figure A.6: Kinematics (p_T , mass, η , ϕ) of the subleading large- R jet in data and prediction in the sideband region after requiring 3 b -tags.

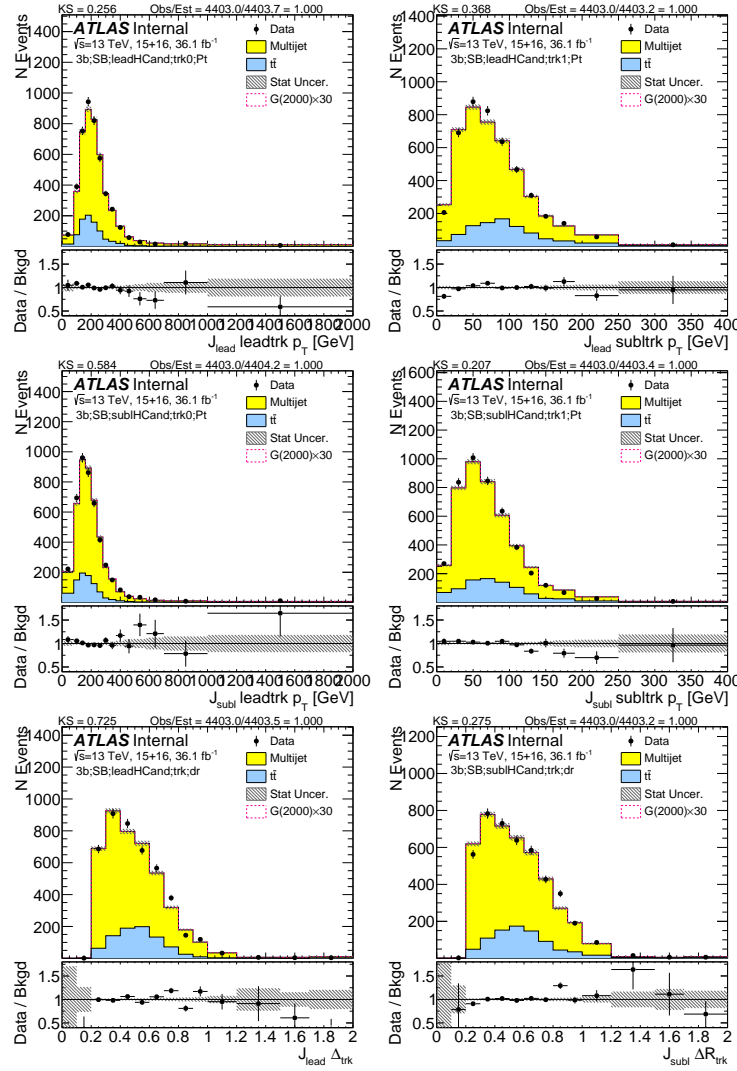


Figure A.7: First two rows show the p_T of the lead (left) and sub-lead (right) small- R track jets associated to the lead (first-row) and sub-lead (second-row) large- R jet in data and prediction in the sideband region after requiring 3 b -tags. Third row shows the ΔR between two leading small- R track-jets associated to the leading (left) and sub-leading (right) large- R jet.

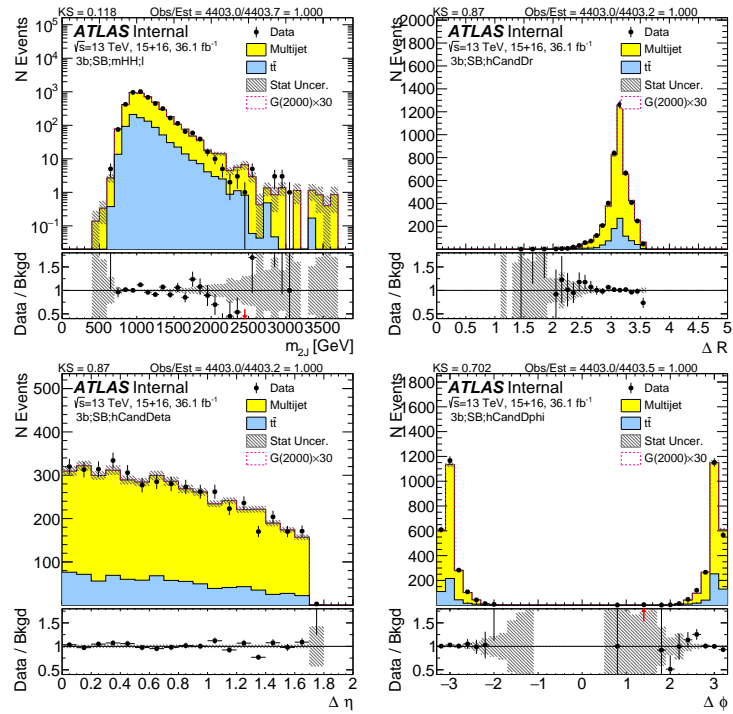


Figure A.8: Kinematics (invariant mass, ΔR , $\Delta\gamma$ and $\Delta\phi$) of two large- R jets in data and prediction in the sideband region after requiring 3 b -tags.

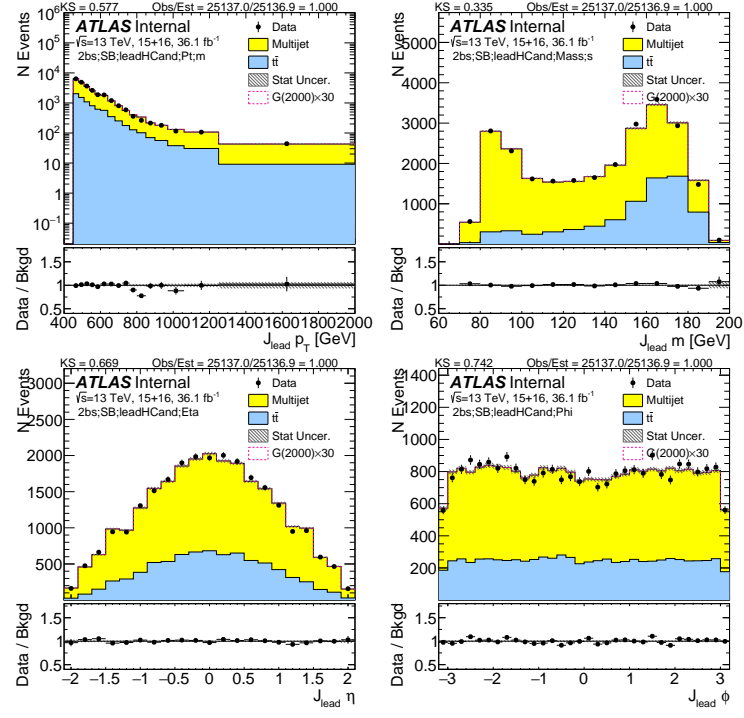


Figure A.9: Kinematics (p_T , mass, η , ϕ) of the lead large- R jet in data and prediction in the sideband region after requiring 2 b -tags split.

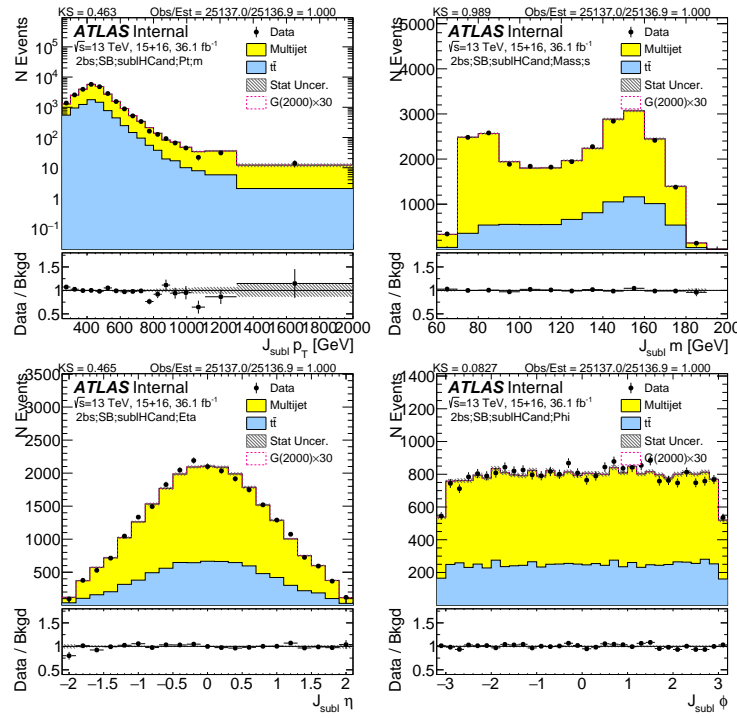


Figure A.10: Kinematics (p_T , mass, η , ϕ) of the subleading large- R jet in data and prediction in the sideband region after requiring 2 b -tags split.

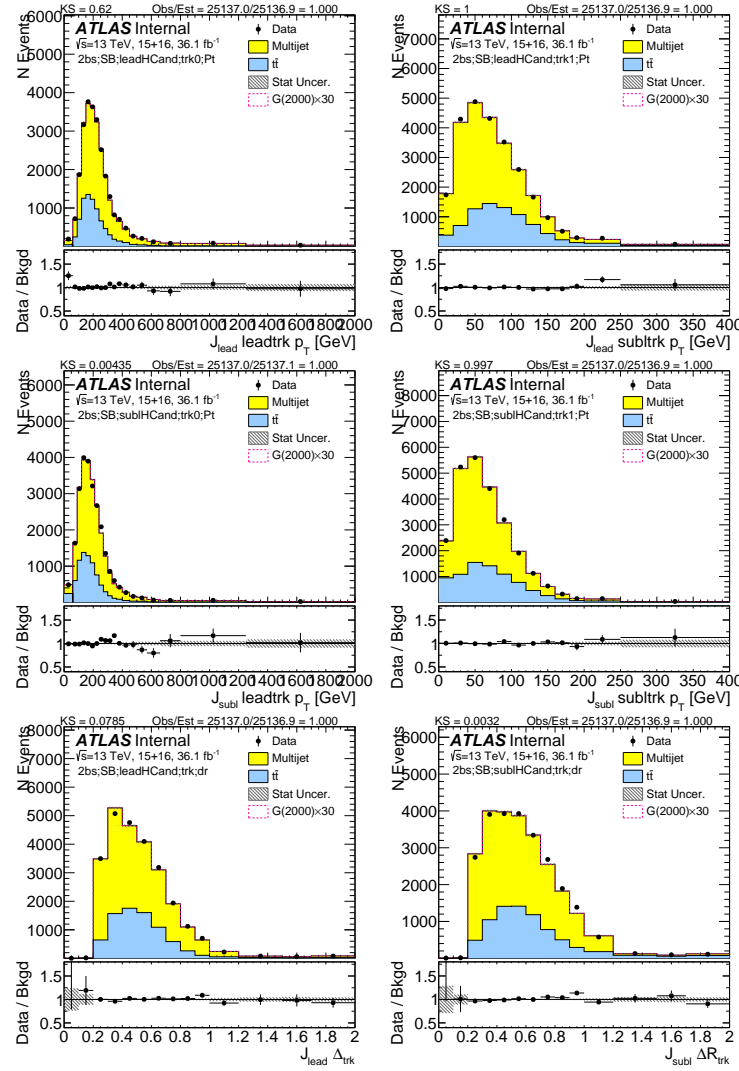


Figure A.11: First two rows show the p_T of the lead (left) and sub-lead (right) small- R track jets associated to the lead (first-row) and sub-lead (second-row) large- R jet in data and prediction in the sideband region after requiring 2 b -tags split. Third row shows the ΔR between two leading small- R track-jets associated to the leading (left) and sub-leading (right) large- R jet.

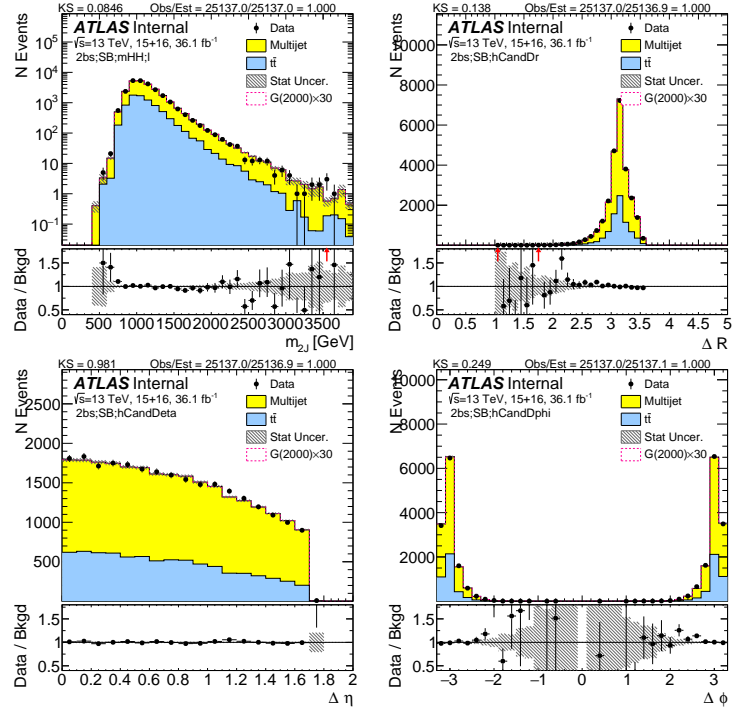


Figure A.12: Kinematics (invariant mass, ΔR , $\Delta\eta$ and $\Delta\phi$) of two large- R jets in data and prediction in the sideband region after requiring 2 b -tags split.

B

Boosted control region kinematic distributions

This section shows comparisons of data with the prediction of QCD multi-jets and $t\bar{t}$ backgrounds in the control region. The definition of the control region is discussed in Section 6.2. The agreement between data and background prediction is generally good, without any systematic biases

observed.

Figures B.1, B.2, B.3, and B.4 show predictions of various kinematics of the large- R jets and their associated track jets in the $4b$ selection. Figures B.5, B.6, B.7, and B.8 show predictions of various kinematics of the large- R jets and their associated track jets in the $3b$ selection. Figures B.9, B.10, B.11, and B.12 show predictions of various kinematics of the large- R jets and their associated track jets in the $2bs$ selection.

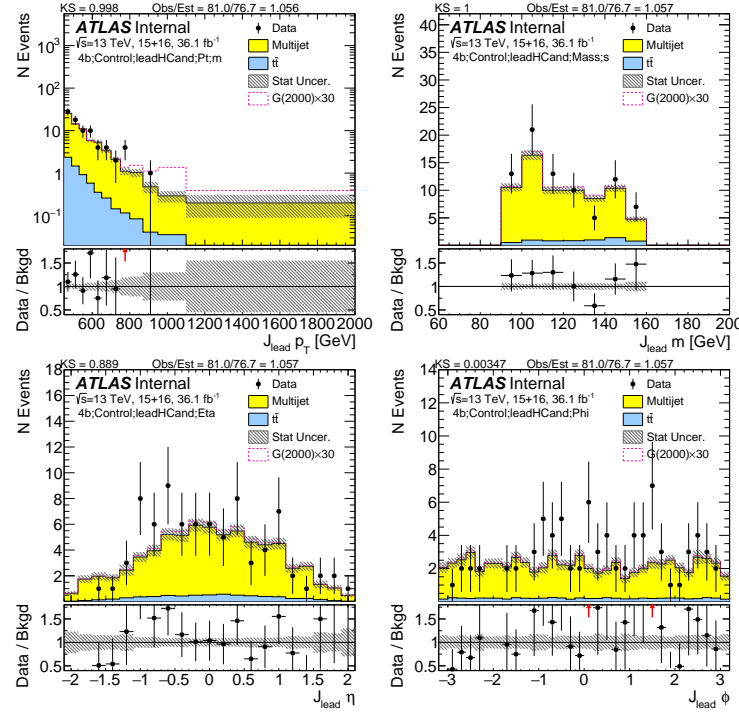


Figure B.1: Kinematics (p_T , mass, η , ϕ) of the lead large- R jet in data and prediction in the control region after requiring $4 b$ -tags.

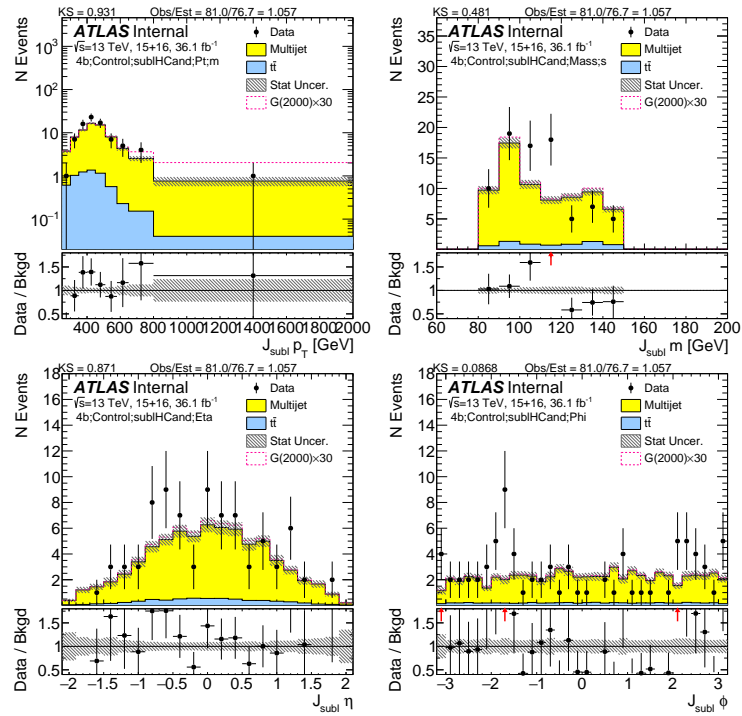


Figure B.2: Kinematics (p_T , mass, η , ϕ) of the subleading large- R jet in data and prediction in the control region after requiring 4 b -tags.

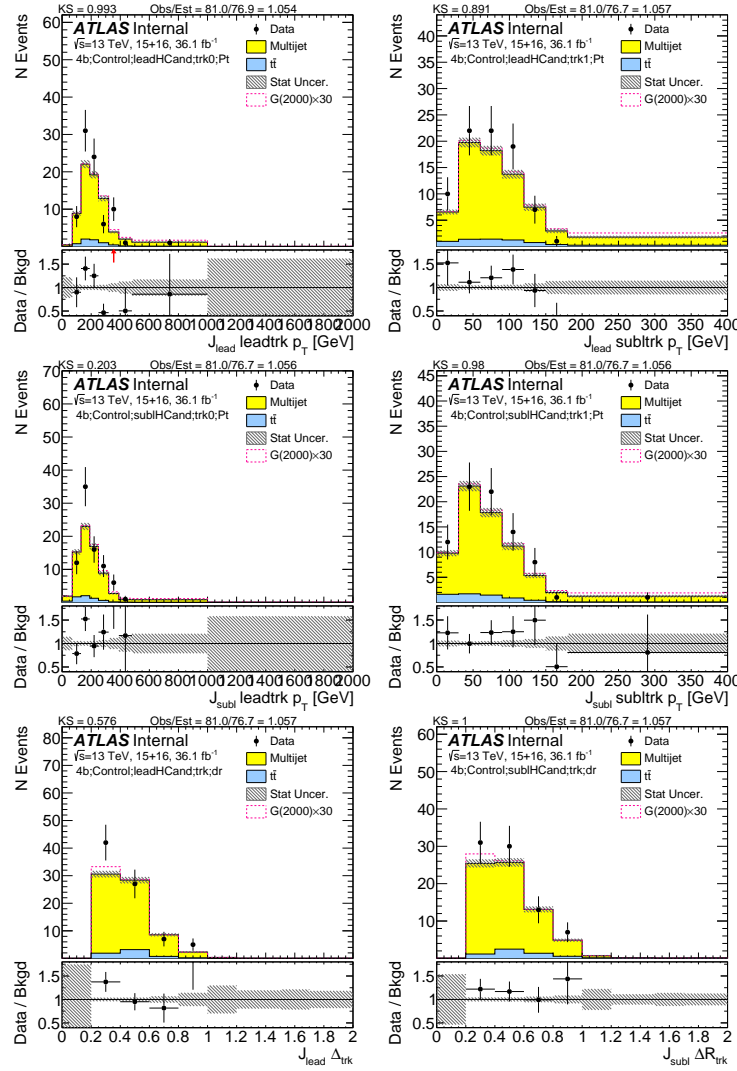


Figure B.3: First two rows show the p_T of the lead (left) and sub-lead (right) small- R track jets associated to the lead (first-row) and sub-lead (second-row) large- R jet in data and prediction in the control region after requiring 4 b -tags. Third row shows the ΔR between two leading small- R track-jets associated to the leading (left) and sub-leading (right) large- R jet.

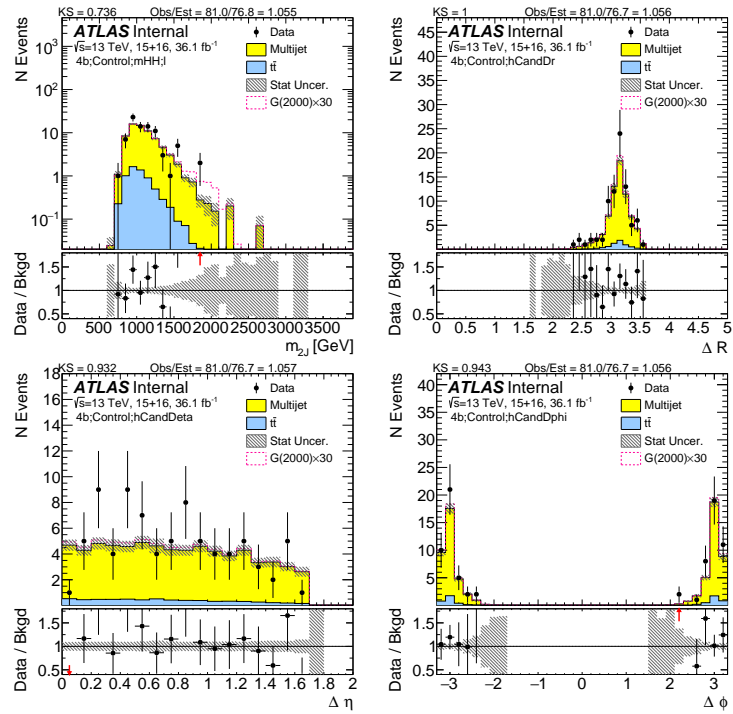


Figure B.4: Kinematics (invariant mass, ΔR , $\Delta\eta$ and $\Delta\phi$) of two large- R jets in data and prediction in the control region after requiring 4 b -tags.

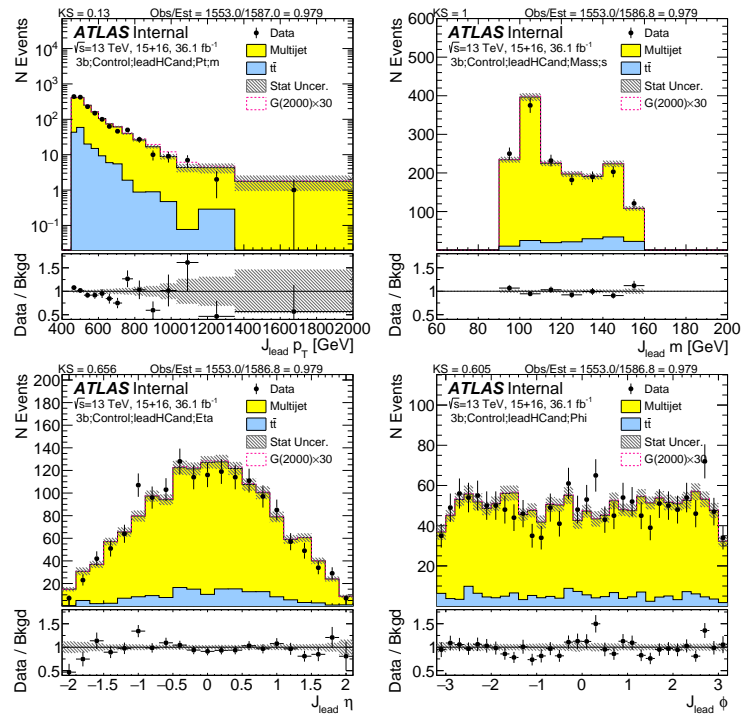


Figure B.5: Kinematics (p_T , mass, η , ϕ) of the lead large- R jet in data and prediction in the control region after requiring 3 b -tags.

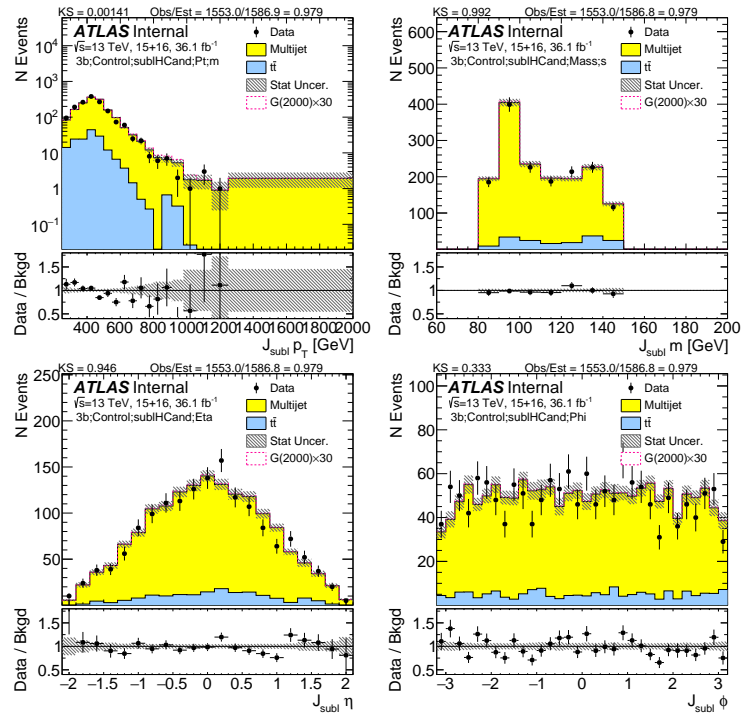


Figure B.6: Kinematics (p_T , mass, η , ϕ) of the subleading large- R jet in data and prediction in the control region after requiring 3 b -tags.

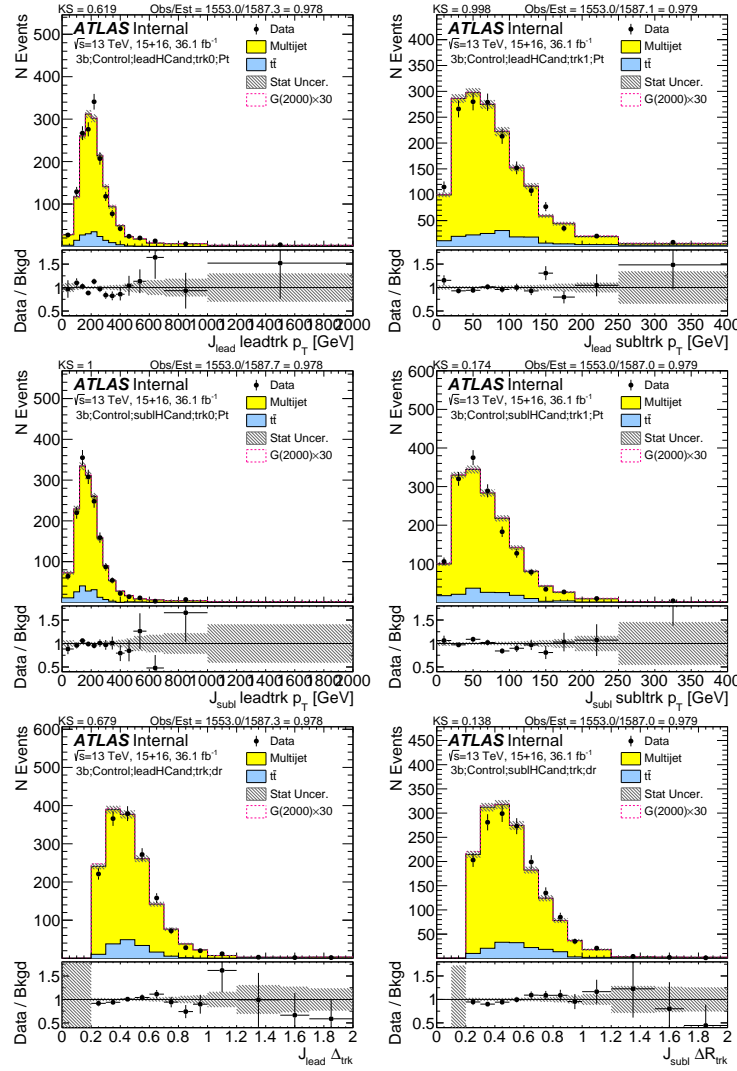


Figure B.7: First two rows show the p_T of the lead (left) and sub-lead (right) small- R track jets associated to the lead (first-row) and sub-lead (second-row) large- R jet in data and prediction in the control region after requiring 3 b -tags. Third row shows the ΔR between two leading small- R track-jets associated to the leading (left) and sub-leading (right) large- R jet.

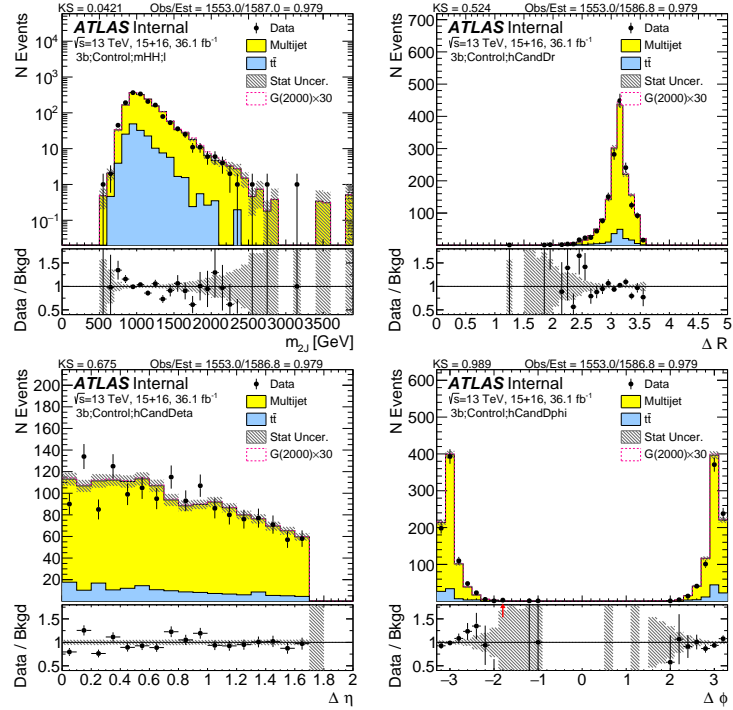


Figure B.8: Kinematics (invariant mass, ΔR , $\Delta \eta$ and $\Delta \phi$) of two large- R jets in data and prediction in the control region after requiring 3 b -tags.

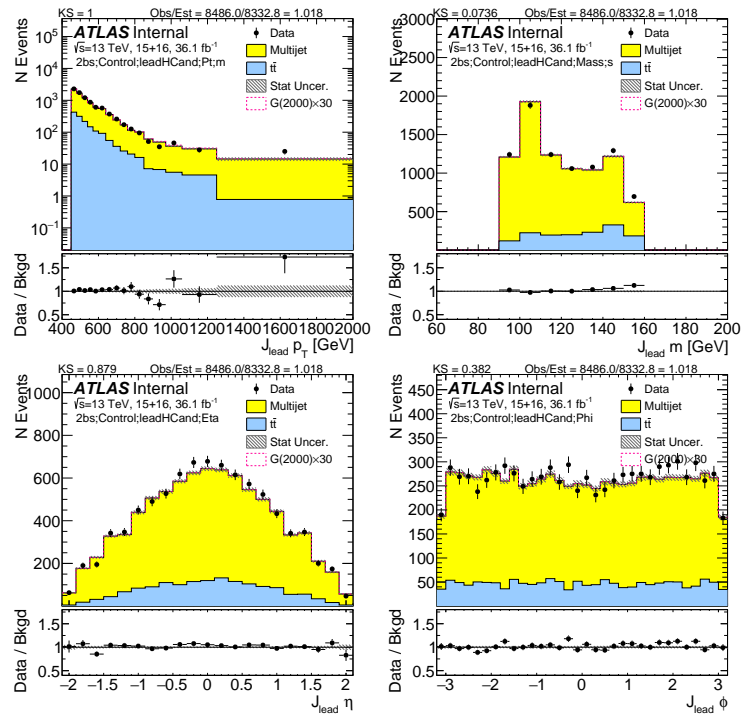


Figure B.9: Kinematics (p_T , mass, η , ϕ) of the lead large- R jet in data and prediction in the control region after requiring 2 b -tags split.

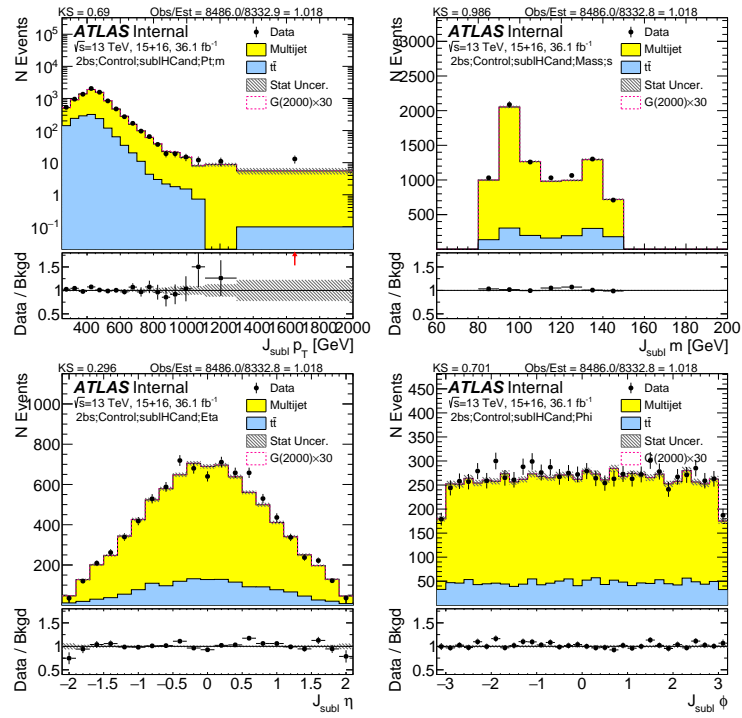


Figure B.10: Kinematics (p_T , mass, η , ϕ) of the subleading large- R jet in data and prediction in the control region after requiring 2 b -tags split.

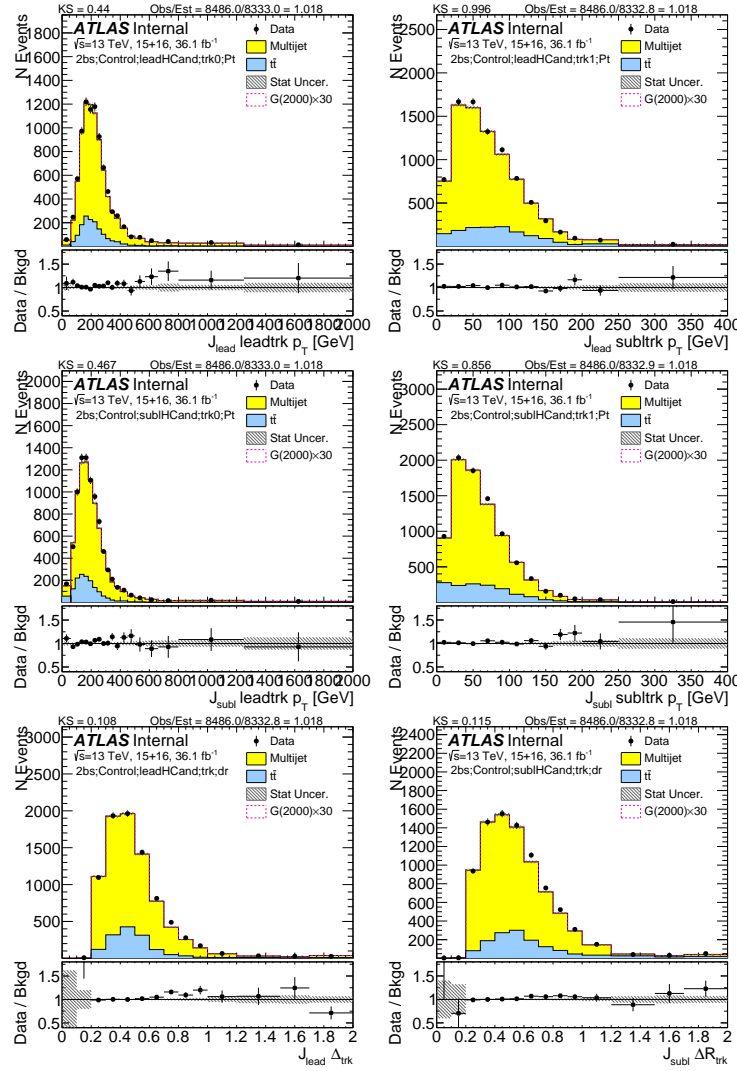


Figure B.11: First two rows show the p_T of the lead (left) and sub-lead (right) small- R track jets associated to the lead (first-row) and sub-lead (second-row) large- R jet in data and prediction in the control region after requiring 2 b -tags split. Third row shows the ΔR between two leading small- R track-jets associated to the leading (left) and sub-leading (right) large- R jet.

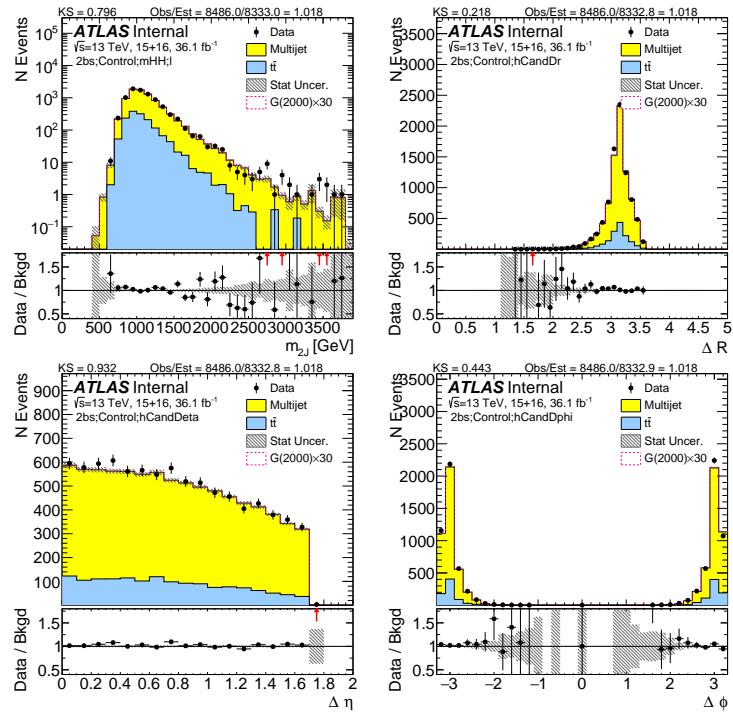


Figure B.12: Kinematics (invariant mass, ΔR , $\Delta\eta$ and $\Delta\phi$) of two large- R jets in data and prediction in the control region after requiring 2 b -tags split.

C

Boosted singal region kinematic distributions

This appendix shows unblinded data with the prediction of QCD multi-jets and $t\bar{t}$ backgrounds in the signal region. Plots shown are with stat uncertainty only.

Tables C.1, C.2, C.3, C.4, C.5, C.6 shows the integrated SR predictions and yields, in different m_{2J} or scaled m_{2J} ranges. The predictions agree with the data fairly well, with the exception of the $3b$ deficient in m_{2J} above 2 TeV.

Mass Range	>1000	>1500	>2000	>2500	>3000
totalbkg	23.09 ± 1.59	1.94 ± 0.15	0.26 ± 0.072	0.061 ± 0.058	0.021 ± 0.047
data	21.0 ± 4.58	3.0 ± 1.73	-	-	-

Table C.1: $4b$ unblinded Signal Region predictions and results. All systematic uncertainties included for backgrounds. For Data, the statistical uncertainty is shown. Mass range is broken into greater than 1 TeV, 1.5 TeV, 2 TeV, 2.5 TeV, and 3 TeV intervals.

Mass Range	>1000	>1500	>2000	>2500	>3000
totalbkg	495.92 ± 12.34	51.72 ± 2.46	10.42 ± 0.95	4.07 ± 0.85	2.21 ± 0.79
data	499.0 ± 22.34	42.0 ± 6.48	3.0 ± 1.73	1.0 ± 1.0	-

Table C.2: $3b$ unblinded Signal Region predictions and results. All systematic uncertainties included for backgrounds. For Data, the statistical uncertainty is shown. Mass range is broken into greater than 1 TeV, 1.5 TeV, 2 TeV, 2.5 TeV, and 3 TeV intervals.

Mass Range	>1000	>1500	>2000	>2500	>3000
totalbkg	2688.71 ± 34.09	288.51 ± 4.96	42.19 ± 2.13	8.85 ± 1.55	2.72 ± 1.09
data	2755.0 ± 52.49	287.0 ± 16.94	38.0 ± 6.16	4.0 ± 2.0	1.0 ± 1.0

Table C.3: $2bs$ unblinded Signal Region predictions and results. All systematic uncertainties included for backgrounds. For Data, the statistical uncertainty is shown. Mass range is broken into greater than 1 TeV, 1.5 TeV, 2 TeV, 2.5 TeV, and 3 TeV intervals.

Figures C.1, C.2, C.3, and C.4 show predictions of various kinematics of the large- R jets and their associated track jets in the $4b$ selection. Figures C.5, C.6, C.7, and C.8 show predictions of various kinematics of the large- R jets and their associated track jets in the $3b$ selection. Figures C.9, C.10, C.11,

Mass Range	>1000	>1500	>2000	>2500	>3000
totalbkg	24.64 ± 1.84	2.84 ± 0.22	0.25 ± 0.044	0.02 ± 0.011	0.0014 ± 0.0026
data	22.0 ± 4.69	4.0 ± 2.0	1.0 ± 1.0	-	-

Table C.4: $4b$ unblinded Scaled dijet mass Region predictions and results. All systematic uncertainties included for backgrounds. For Data, the statistical uncertainty is shown. Mass range is broken into greater than 1 TeV, 1.5 TeV, 2 TeV, 2.5 TeV, and 3 TeV intervals.

Mass Range	>1000	>1500	>2000	>2500	>3000
totalbkg	559.38 ± 14.06	69.27 ± 3.22	13.35 ± 1.14	4.37 ± 0.96	2.0 ± 0.87
data	570.0 ± 23.87	59.0 ± 7.68	4.0 ± 2.0	1.0 ± 1.0	-

Table C.5: $3b$ unblinded Scaled dijet mass Signal Region predictions and results. All systematic uncertainties included for backgrounds. For Data, the statistical uncertainty is shown. Mass range is broken into greater than 1 TeV, 1.5 TeV, 2 TeV, 2.5 TeV, and 3 TeV intervals.

Mass Range	>1000	>1500	>2000	>2500	>3000
totalbkg	2998.69 ± 40.31	377.8 ± 6.39	57.47 ± 2.88	11.78 ± 1.95	3.39 ± 1.27
data	3078.0 ± 55.48	379.0 ± 19.47	47.0 ± 6.86	6.0 ± 2.45	2.0 ± 1.41

Table C.6: $2bs$ unblinded Scaled dijet mass Signal Region predictions and results. All systematic uncertainties included for backgrounds. For Data, the statistical uncertainty is shown. Mass range is broken into greater than 1 TeV, 1.5 TeV, 2 TeV, 2.5 TeV, and 3 TeV intervals.

and C.12 show predictions of various kinematics of the large- R jets and their associated track jets in the $2b$ selection.

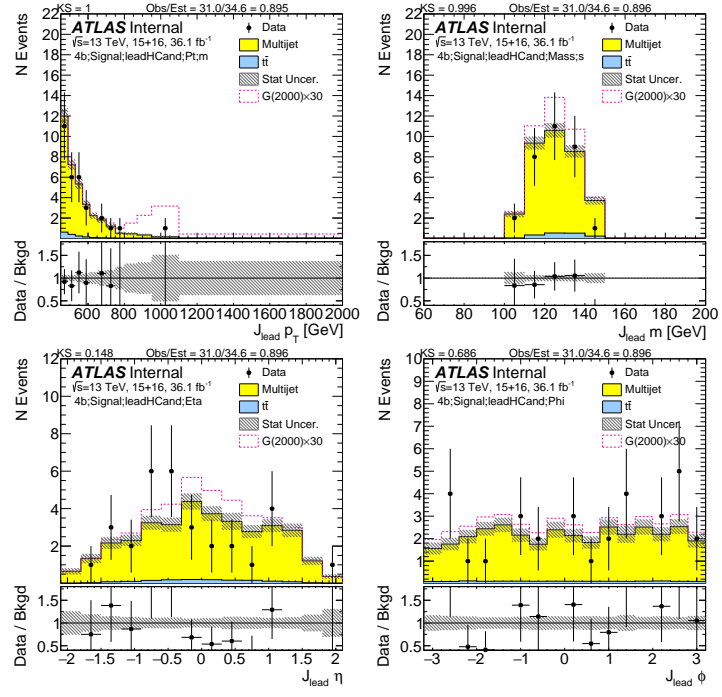


Figure C.1: Kinematics (p_T , mass, η , ϕ) of the lead large- R jet in data and prediction in the signal region after requiring 4 b -tags.

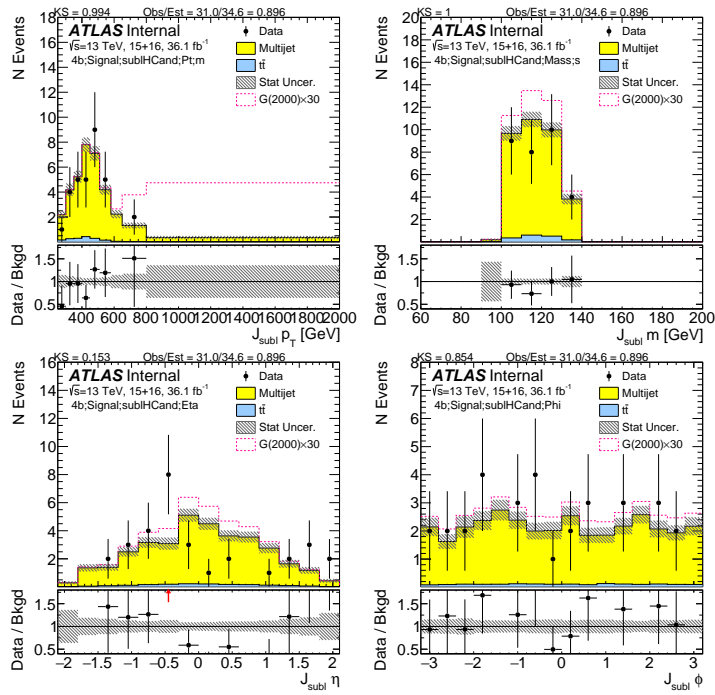


Figure C.2: Kinematics (p_T , mass, η , ϕ) of the subleading large- R jet in data and prediction in the signal region after requiring 4 b -tags.

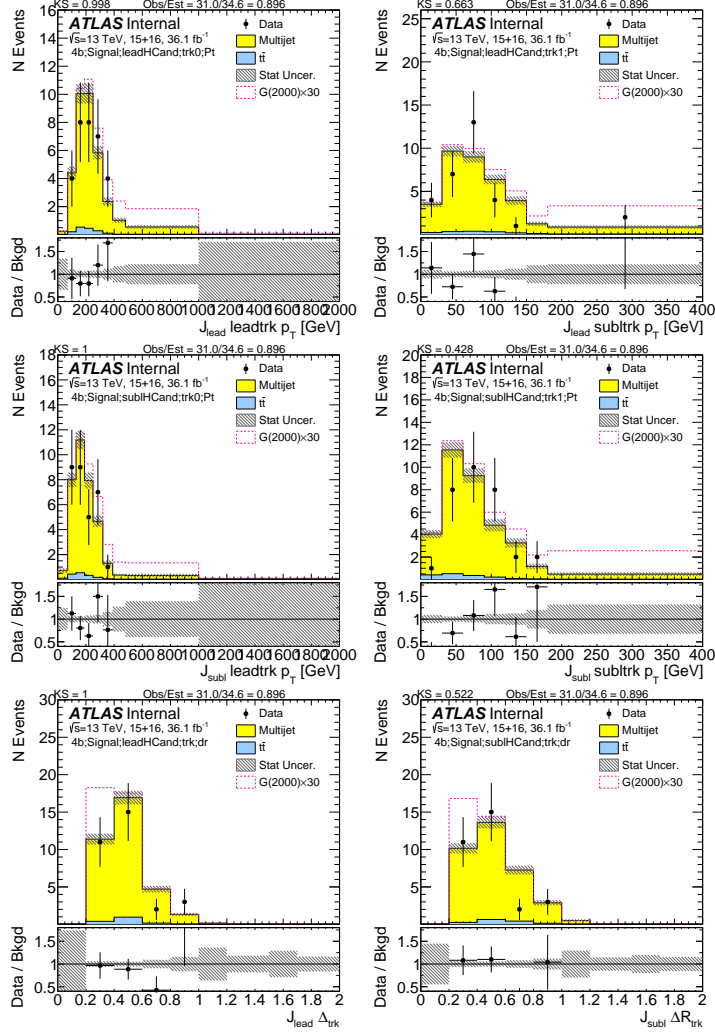


Figure C.3: First two rows show the p_T of the lead (left) and sub-lead (right) small- R track jets associated to the lead (first-row) and sub-lead (second-row) large- R jet in data and prediction in the signal region after requiring 4 b -tags. Third row shows the ΔR between two leading small- R track-jets associated to the leading (left) and sub-leading (right) large- R jet.

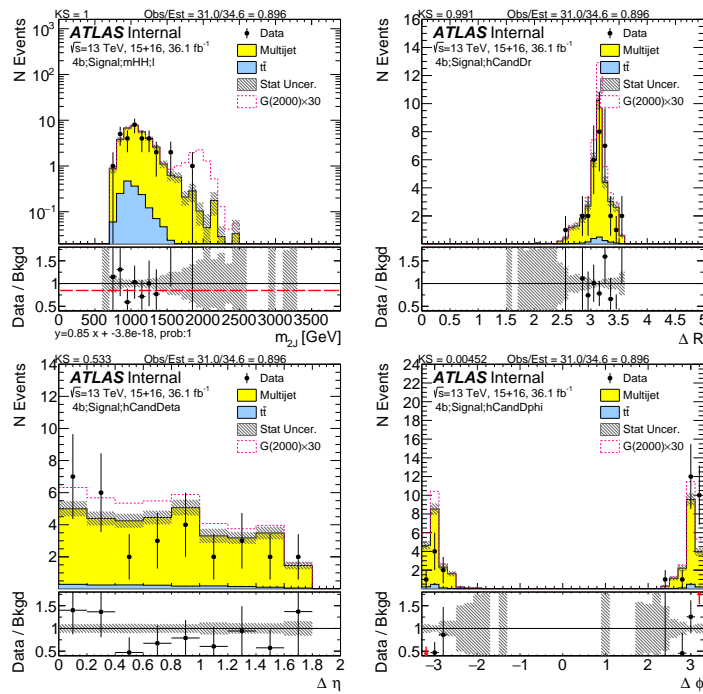


Figure C.4: Kinematics (invariant mass, ΔR , $\Delta\eta$ and $\Delta\phi$) of two large- R jets in data and prediction in the signal region after requiring 4 b -tags.

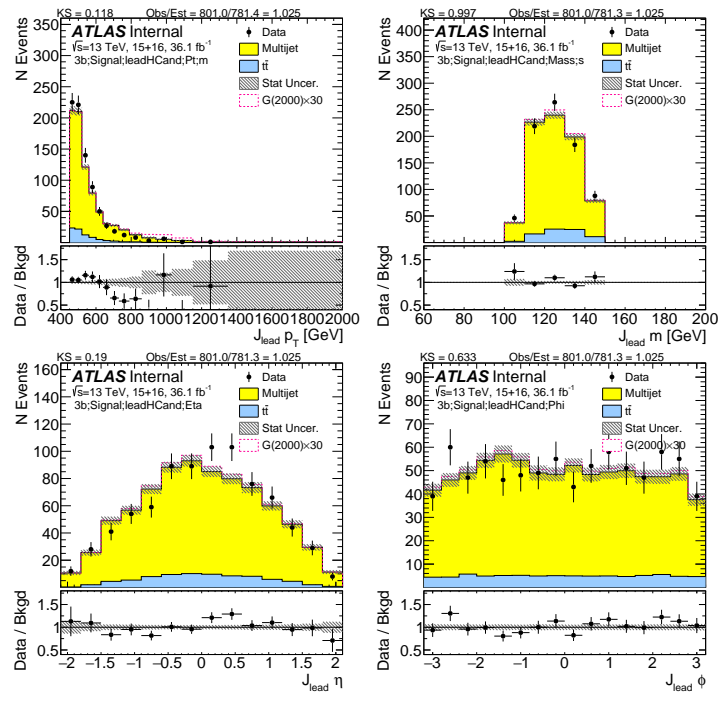


Figure C.5: Kinematics (p_T , mass, η , ϕ) of the lead large- R jet in data and prediction in the signal region after requiring 3 b -tags.

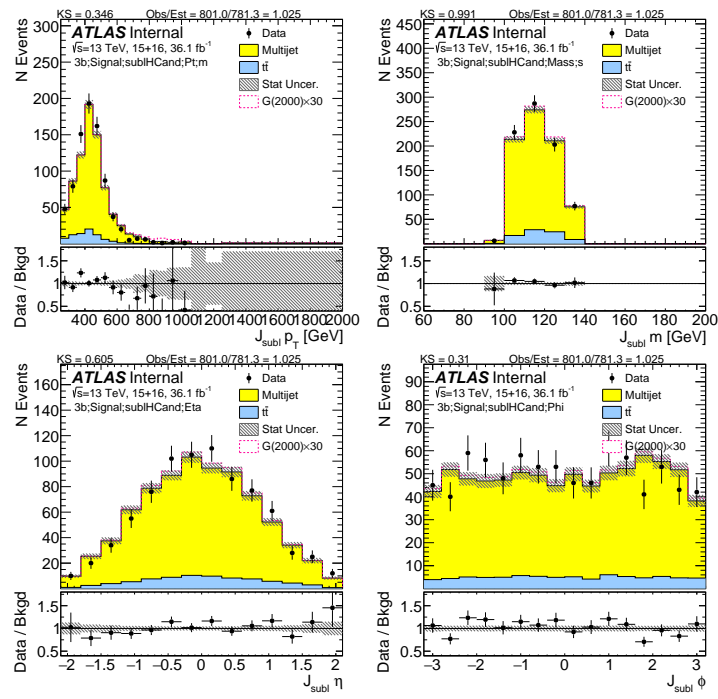


Figure C.6: Kinematics (p_T , mass, η , ϕ) of the subleading large- R jet in data and prediction in the signal region after requiring 3 b -tags.

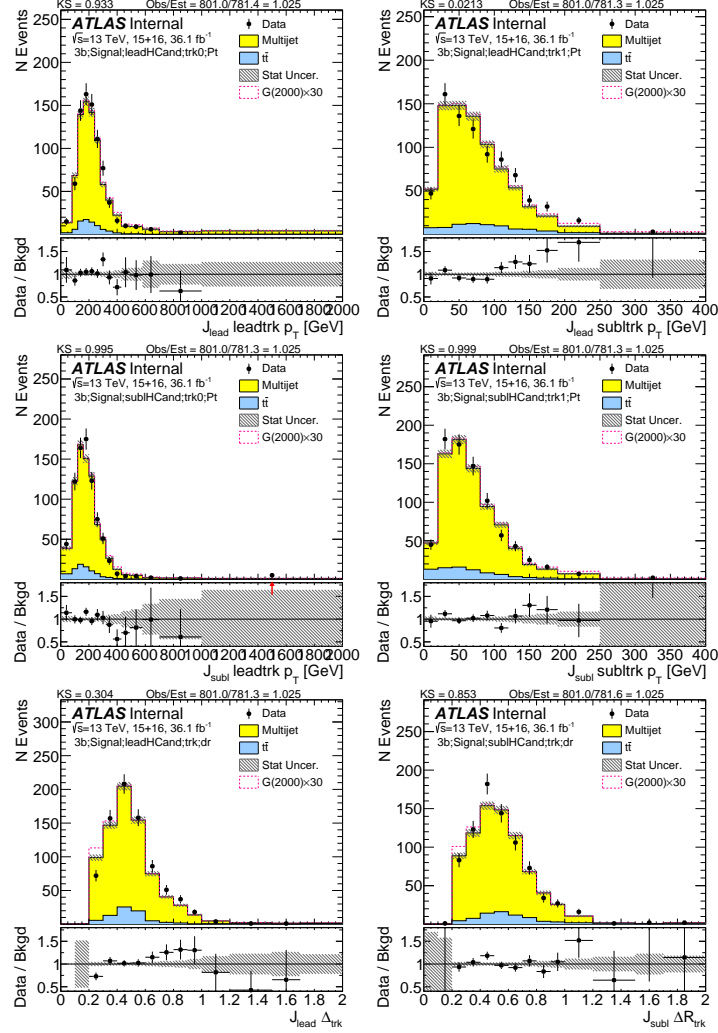


Figure C.7: First two rows show the p_T of the lead (left) and sub-lead (right) small- R track jets associated to the lead (first-row) and sub-lead (second-row) large- R jet in data and prediction in the signal region after requiring 3 b -tags. Third row shows the ΔR between two leading small- R track-jets associated to the leading (left) and sub-leading (right) large- R jet.

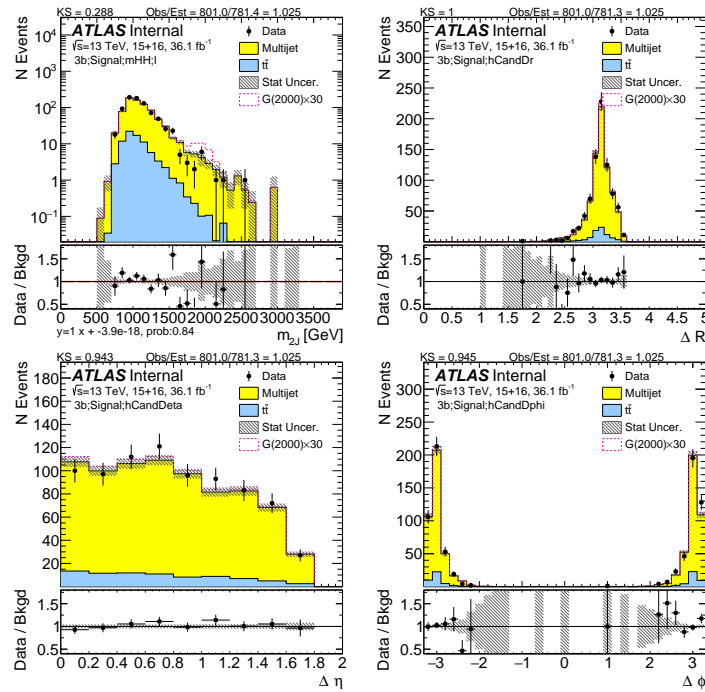


Figure C.8: Kinematics (invariant mass, ΔR , $\Delta\eta$ and $\Delta\phi$) of two large- R jets in data and prediction in the signal region after requiring 3 b -tags.

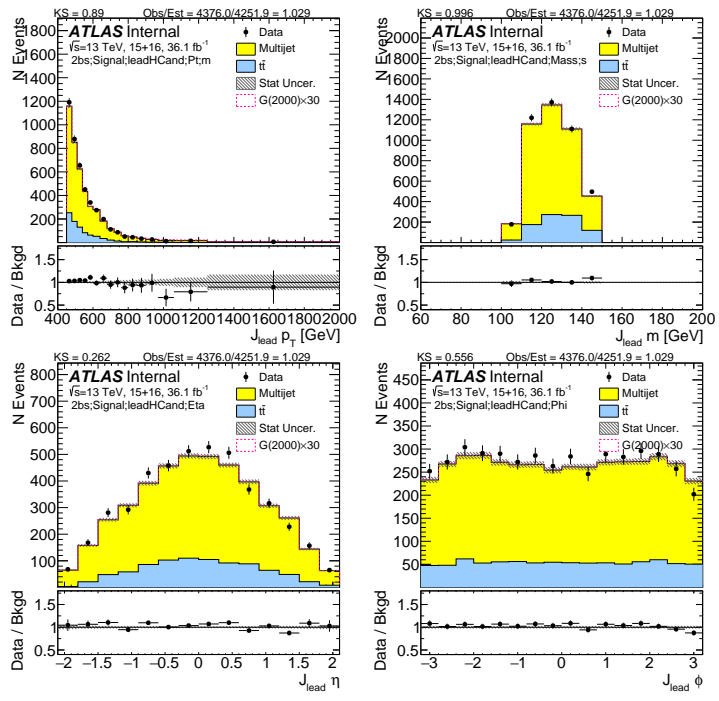


Figure C.9: Kinematics (p_{T} , mass, η , ϕ) of the lead large- R jet in data and prediction in the signal region after requiring 2 b -tags split.

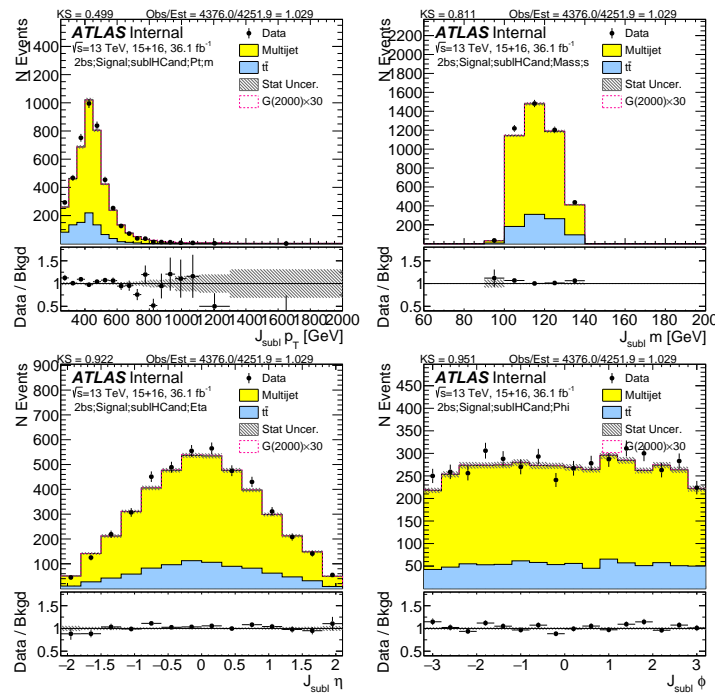


Figure C.10: Kinematics (p_T , mass, η , ϕ) of the subleading large- R jet in data and prediction in the signal region after requiring 2 b -tags split.

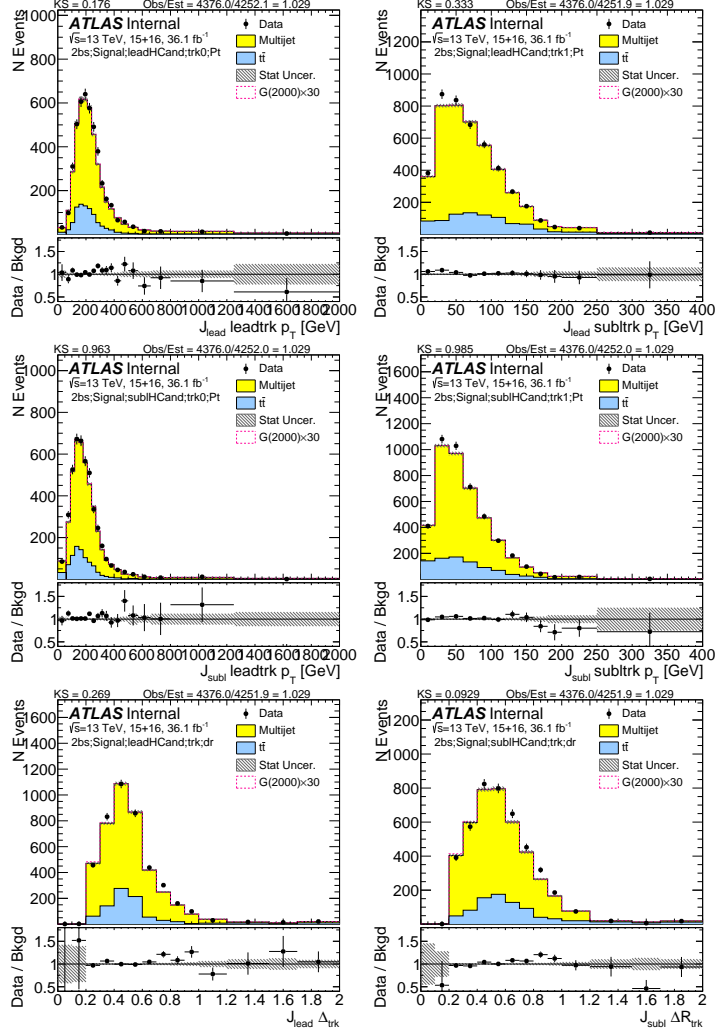


Figure C.11: First two rows show the p_T of the lead (left) and sub-lead (right) small- R track jets associated to the lead (first-row) and sub-lead (second-row) large- R jet in data and prediction in the signal region after requiring 2 b -tags split. Third row shows the ΔR between two leading small- R track-jets associated to the leading (left) and sub-leading (right) large- R jet.

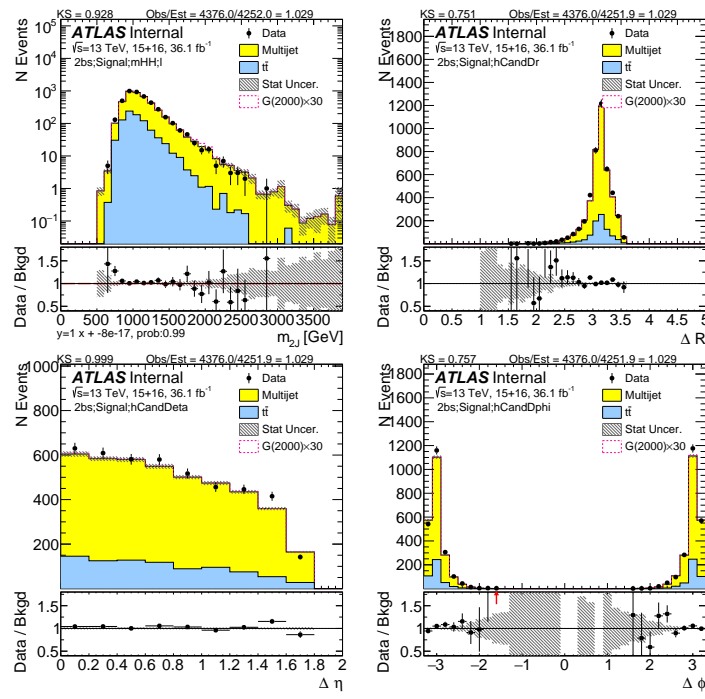


Figure C.12: Kinematics (invariant mass, ΔR , $\Delta \eta$ and $\Delta \phi$) of two large- R jets in data and prediction in the signal region after requiring 2 b -tags split.

D

Constant μ_{qcd} Validation

One important assumption is the constant μ_{qcd} for different regions on the 2D $m_J^{\text{lead}} - m_J^{\text{subl}}$ plane.

This can be validated in data, excluding signal regions which were blinded during this check. The $t\bar{t}$ contribution is estimated directly from MC and subtracted in the data distributions. The ratio of the number of n- b tagged events versus the number of less- b tagged events in each $m_J^{\text{lead}} - m_J^{\text{subl}}$ bin is calculated. The pull of the ratios in SB/CR/SR is also calculated. These two distributions shows the

consistency of μ_{qcd} in SB/CR/SR, as seen in Figure D.1 (1b over ob), D.2 (2b over 1b), D.3 (2bs over 1b), D.4 (3b over 2b), D.5 (4b over 2b). For 4/3/2bs, the μ_{qcd} value can be compared with Table 6.3. This validates the choice of SB region and the constant μ_{qcd} assumption in the analysis.

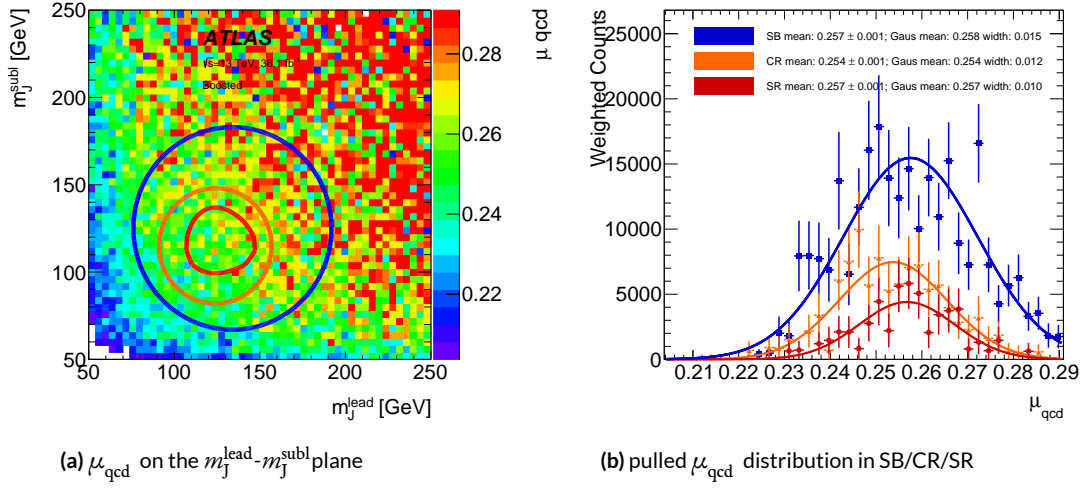


Figure D.1: 1b over ob μ_{qcd} values evaluated in data, with the N_{event} weighted mean and the Gaussian fit mean listed.

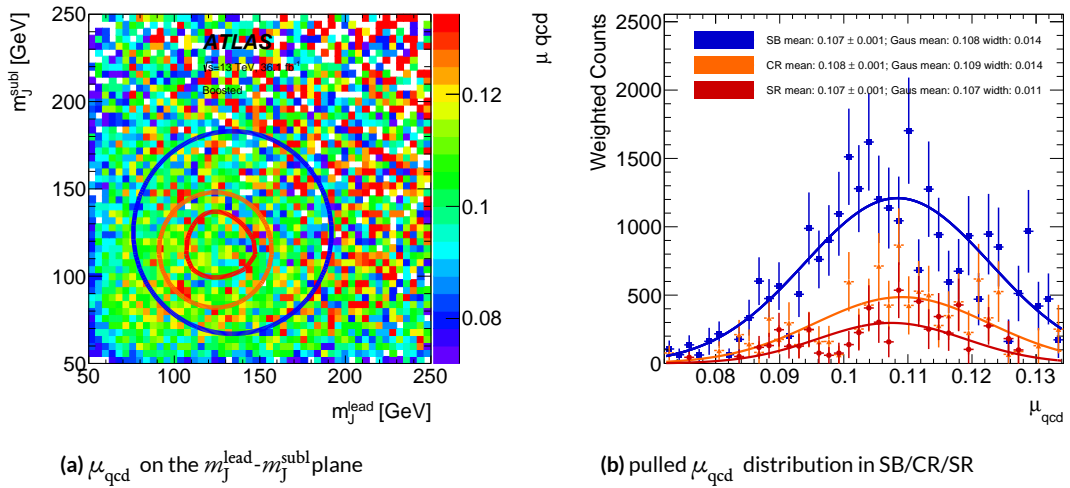


Figure D.2: 2b over 1b μ_{qcd} values evaluated in data, with the N_{event} weighted mean and the Gaussian fit mean listed.

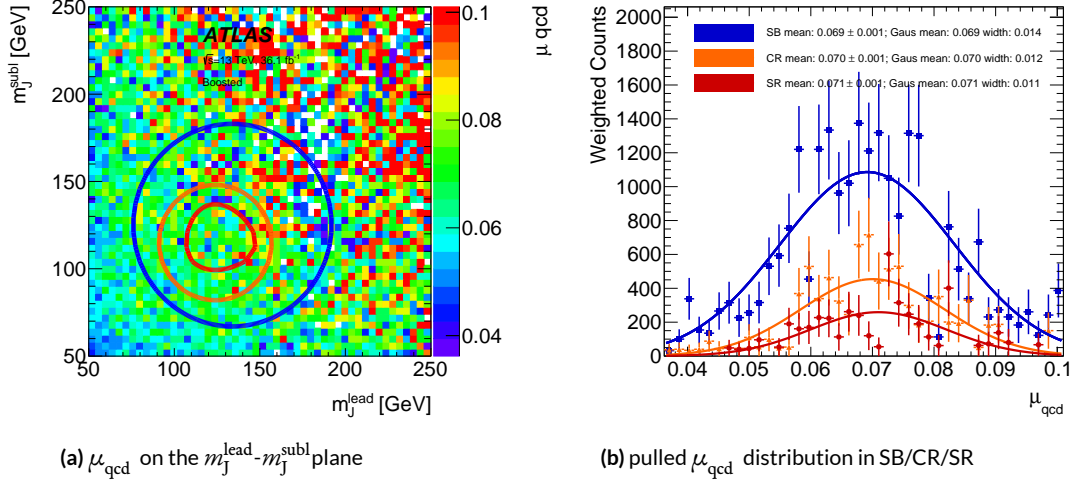


Figure D.3: $2b$ over $1b$ μ_{qcd} values evaluated in data, with the N_{event} weighted mean and the Gaussian fit mean listed.

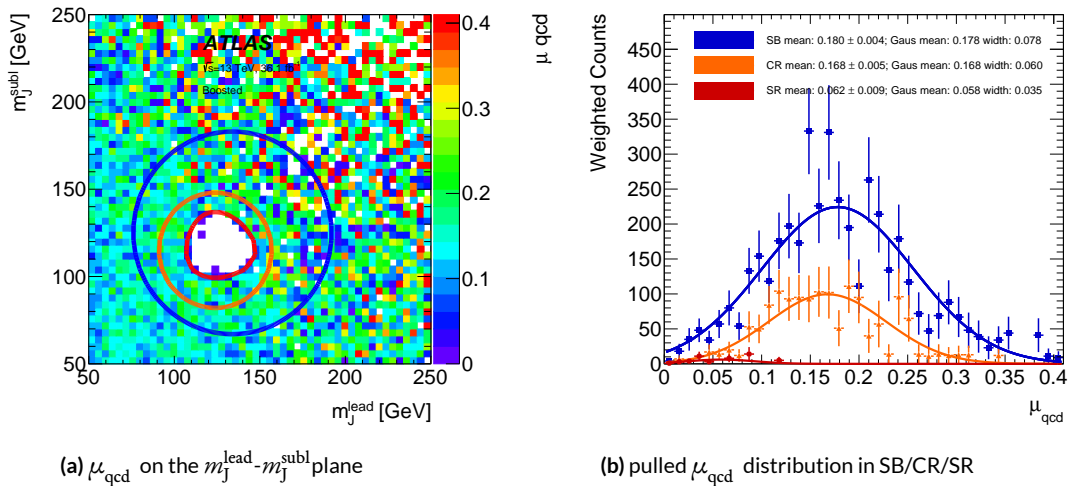


Figure D.4: $3b$ over $2b$ μ_{qcd} values evaluated in data, with the N_{event} weighted mean and the Gaussian fit mean listed.
SR is blinded.

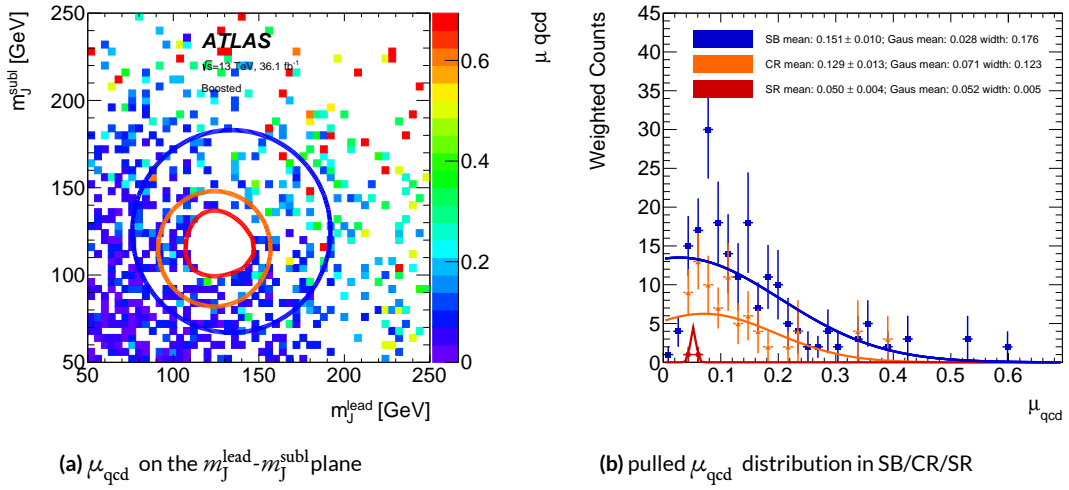


Figure D.5: $4b$ over $2b$ μ_{qcd} values evaluated in data, with the N_{event} weighted mean and the Gaussian fit mean listed. SR is blinded.

Also, the Dijet MC can be used for constant μ_{qcd} validation. The same distributions evaluated in dijet MC are shown in Figure D.6 ($1b$ over ob), D.7 ($2b$ over $1b$), D.8 ($2bs$ over $1b$), D.9 ($3b$ over $2b$), D.10 ($4b$ over $2b$). Poor statistics of the dijet MC affects the pull distributions, especially in $3b$ and $4b$, yet the consistency of μ_{qcd} in SB/CR/SR is still validated. The large difference in μ_{qcd} between data and MC also shows that the dijet MC could not be used directly for background estimation.

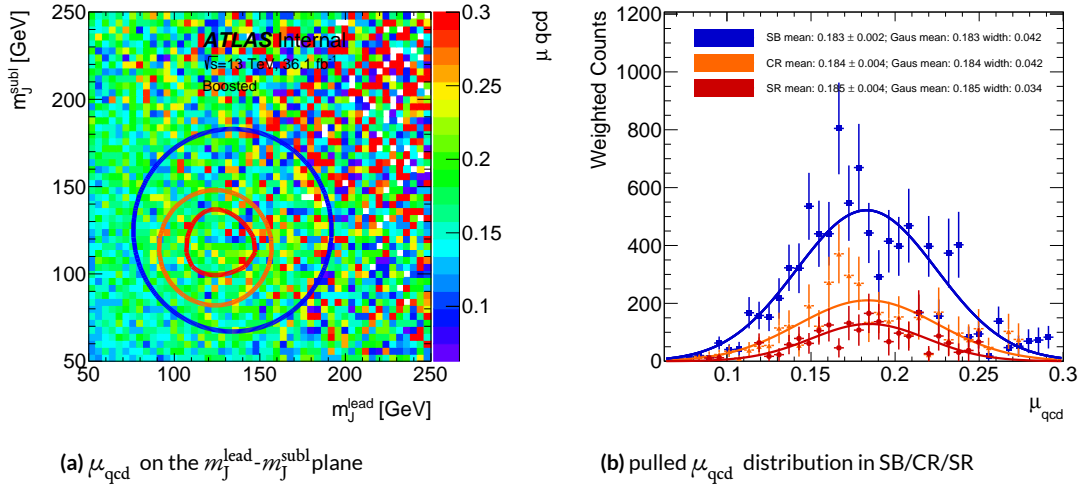


Figure D.6: $1b$ over $0b$ μ_{qcd} values evaluated in dijet MC, with the N_{event} weighted mean and the Gaussian fit mean listed.

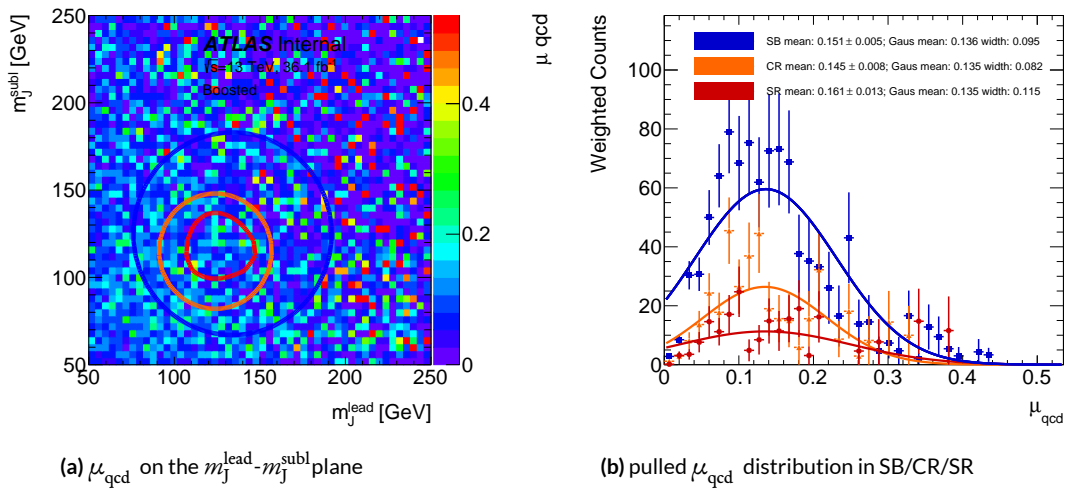


Figure D.7: $2b$ over $1b$ μ_{qcd} values evaluated in dijet MC, with the N_{event} weighted mean and the Gaussian fit mean listed.

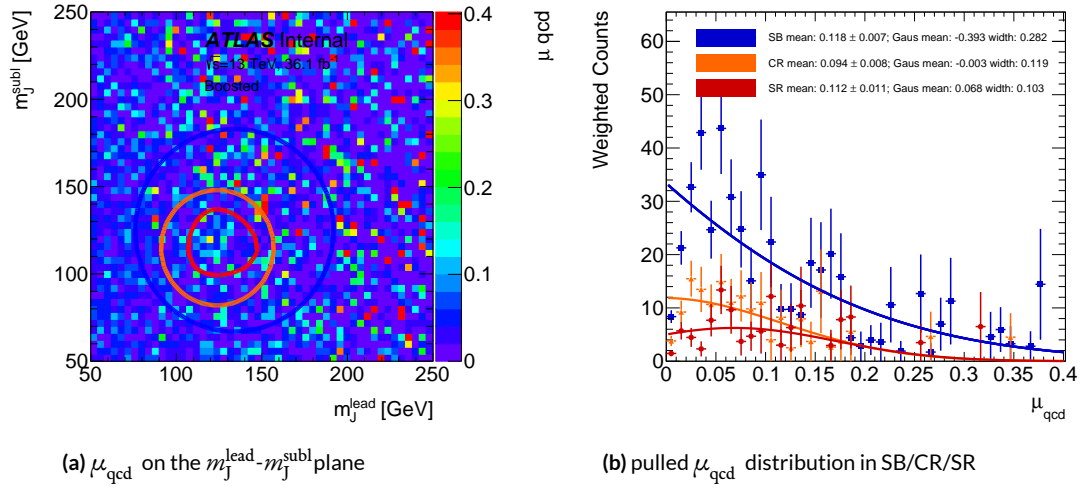


Figure D.8: $2b$ s over $1b$ μ_{qcd} values evaluated in dijet MC, with the N_{event} weighted mean and the Gaussian fit mean listed.

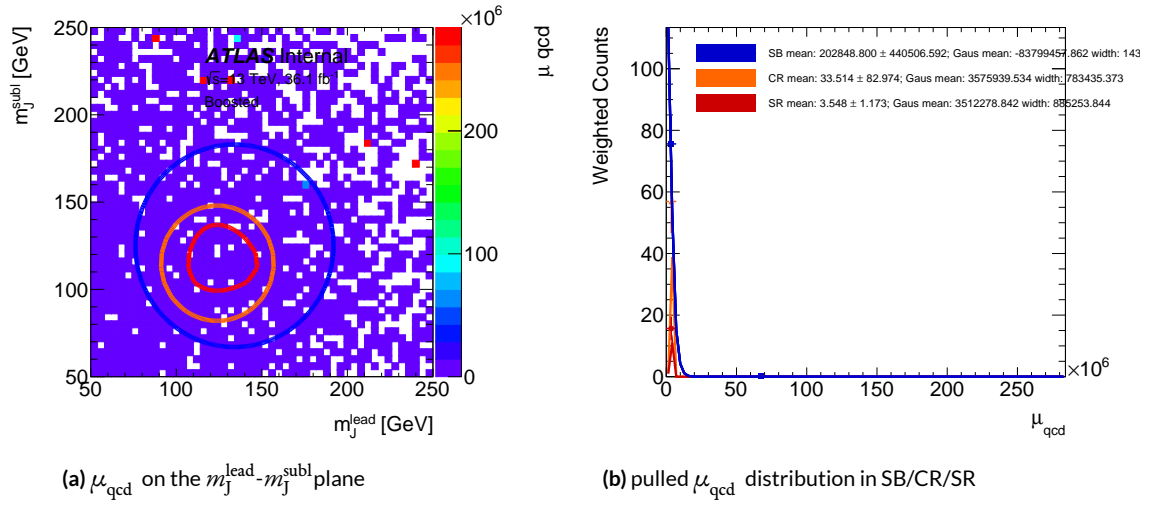


Figure D.9: $3b$ over $2b$ μ_{qcd} values evaluated in dijet MC, with the N_{event} weighted mean and the Gaussian fit mean listed.

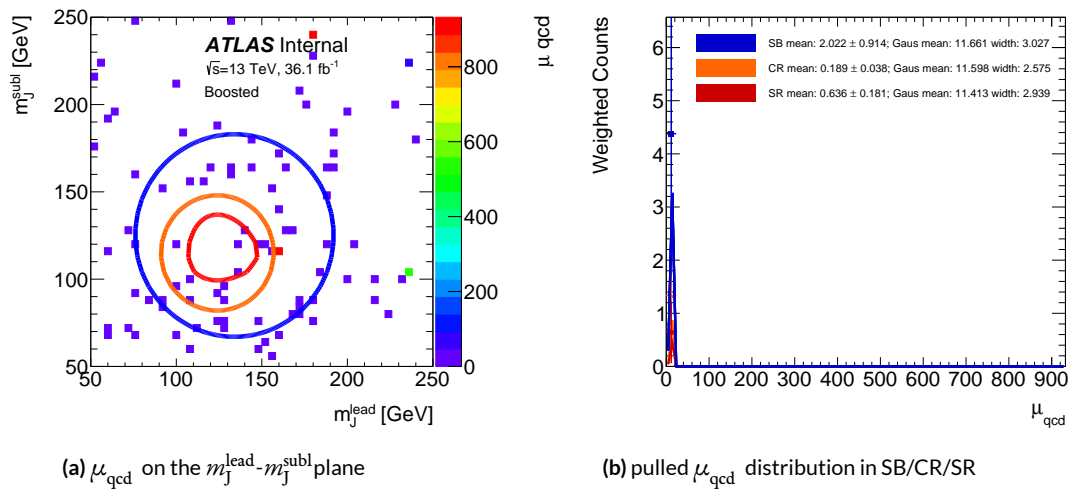


Figure D.10: $4b$ over $2b$ μ_{qcd} values evaluated in dijet MC, with the N_{event} weighted mean and the Gaussian fit mean listed.

E

Reweighting Details

The first iteration, second iteration, and last iteration of fits for $2b$ s, where in $1b$ data, the non- b tagged Higgs candidate are reweighed to be like a $1b$ tagged Higgs candidate, can be seen in Figure E.1 and E.2. Similar distributions for $3b$, where in $2b$ data, the non- b tagged Higgs candidate are reweighed to be like a $1b$ tagged Higgs candidate, are shown in Figure E.3 and E.4. Similar distributions for $4b$, where in $2b$ data, the non- b tagged Higgs candidate are reweighed to be like a $2b$ tagged

Higgs candidate, are shown in Figure E.5 and E.6. The before reweighting distribution (first row), the reweighting result after the first iteration (second row), and the final distribution after reweighting (last row) are presented.

In some plots, like Figure E.5 and E.6, the last ratio bin sometimes still doesn't converge to unity. This is a feature from the limited statistics from the last bin, especially in the $4b$ case, where only 20% number of events in $2b$ is used for background prediction and therefore reweighed. To make this fully converge, a different binning or more iterations could be used. Yet the last bin's few event will also likely to end up with a large unphysical weight and therefore harm the background prediction later.

A comparison of the SB shapes before and after reweighting for $2bs$, $3b$ and $4b$ are shown in Figures E.7, E.8, and E.9. Also, a comparison of the CR shapes before and after reweighting for $2bs$, $3b$ and $4b$ can be seen in Figures E.10, E.11, and E.12. In almost all cases, both the reweighted/non-reweighted prediction agrees fairly well with the data, and the reweighted plots' KS scores are greater than those from non-reweighted distributions.

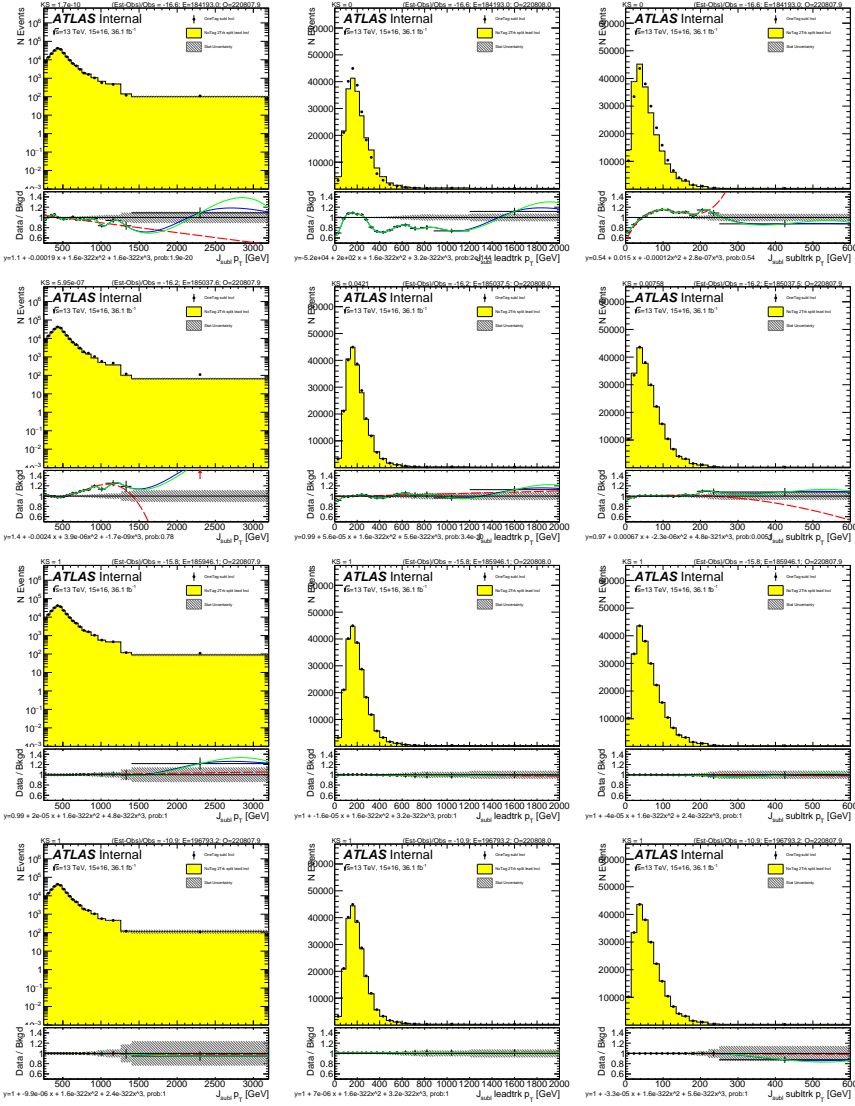


Figure E.1: For $2bs$ background estimate: the fits to the ratio of the data in the $1b$ category, of the subleading Higgs candidate $1b$ -tagged events's subleading Higgs candidate distributions(black point), over the leading Higgs candidate $1b$ -tagged events's subleading Higgs candidate distributions(yellow). Distributions and fits to the estimated QCD background for large- R jet p_T (left), the large- R jet's leading trackjet p_T (middle), and large- R jet's subleading trackjet p_T (right) are shown. Figures are before reweighting (top row), after the first iteration(second row), after the fourth iteration(third row), and after the last iteration (bottom row). The green line is the spline fit; the red line is a polynomial line; the blue line is the spline interpolation.

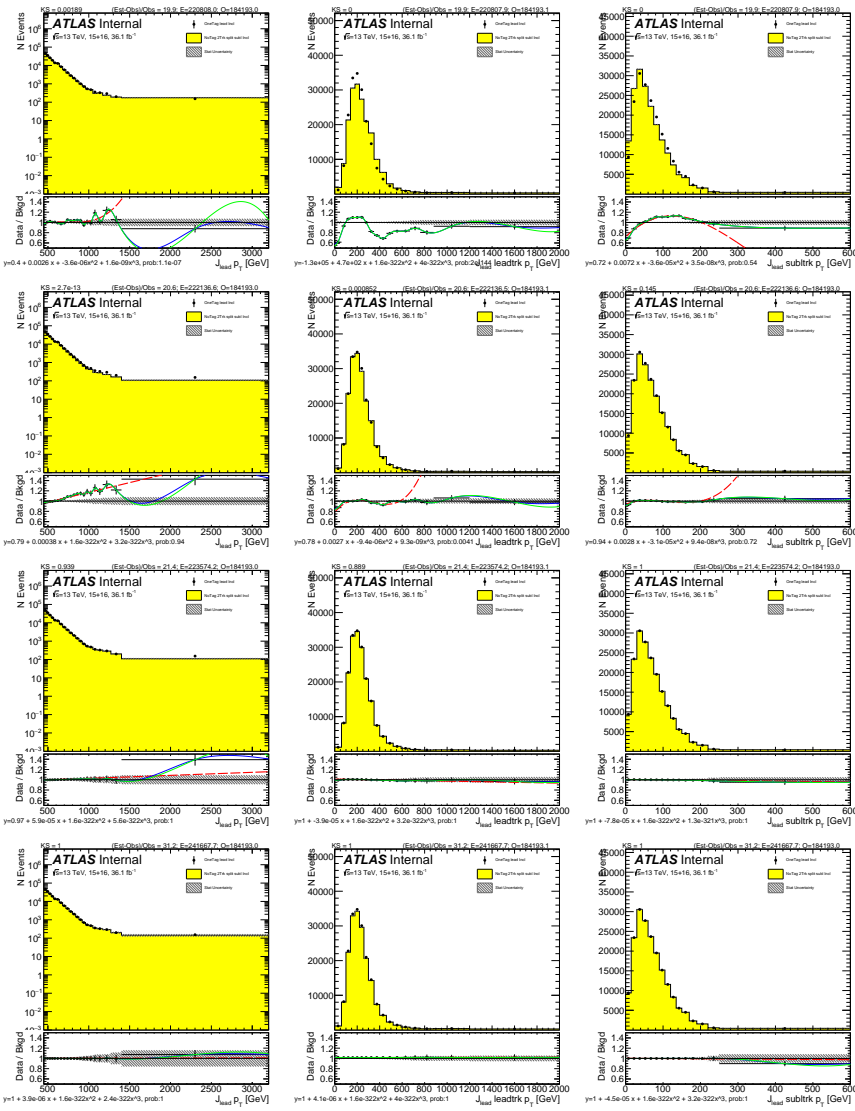


Figure E.2: For zbs background estimate: the fits to the ratio of the data in the $1b$ category, of the leading Higgs candidate $1b$ -tagged events's leading Higgs candidate distributions(black point), over the subleading Higgs candidate $1b$ -tagged events's leading Higgs candidate distributions(yellow). Distributions and fits to the estimated QCD background for large- R jet p_T (left), the large- R jet's leading trackjet p_T (middle), and large- R jet's subleading trackjet p_T (right) are shown. Figures are before reweighting (top row), after the first iteration(second row), after the fourth iteration(third row), and after the last iteration (bottom row). The green line is the spline fit; the red line is a polynomial fit; the blue line is the spline interpolation.

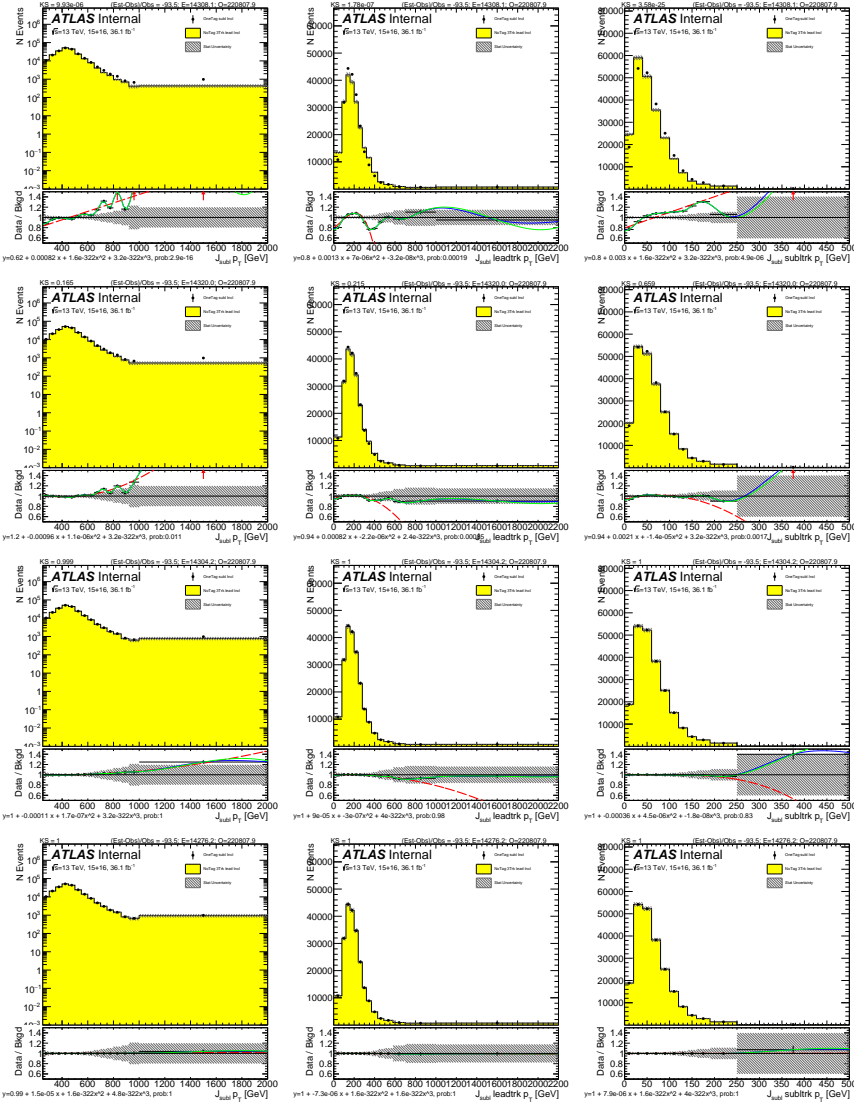


Figure E.3: For $3b$ background estimate: the fits to the ratio of the data in the $2b$ category, of the subleading Higgs candidate $2b$ -tagged events's subleading Higgs candidate distributions(black point), over the leading Higgs candidate $1b$ -tagged events's subleading Higgs candidate distributions(yellow). Distributions and fits to the estimated QCD background for large- R jet p_T (left), the large- R jet's leading trackjet p_T (middle), and large- R jet's subleading trackjet p_T (right) are shown. Figures are before reweighting (top row), after the first iteration(second row), after the fourth iteration(third row), and after the last iteration (bottom row). The green line is the spline fit; the red line is a polynomial fit; the blue line is the spline interpolation.

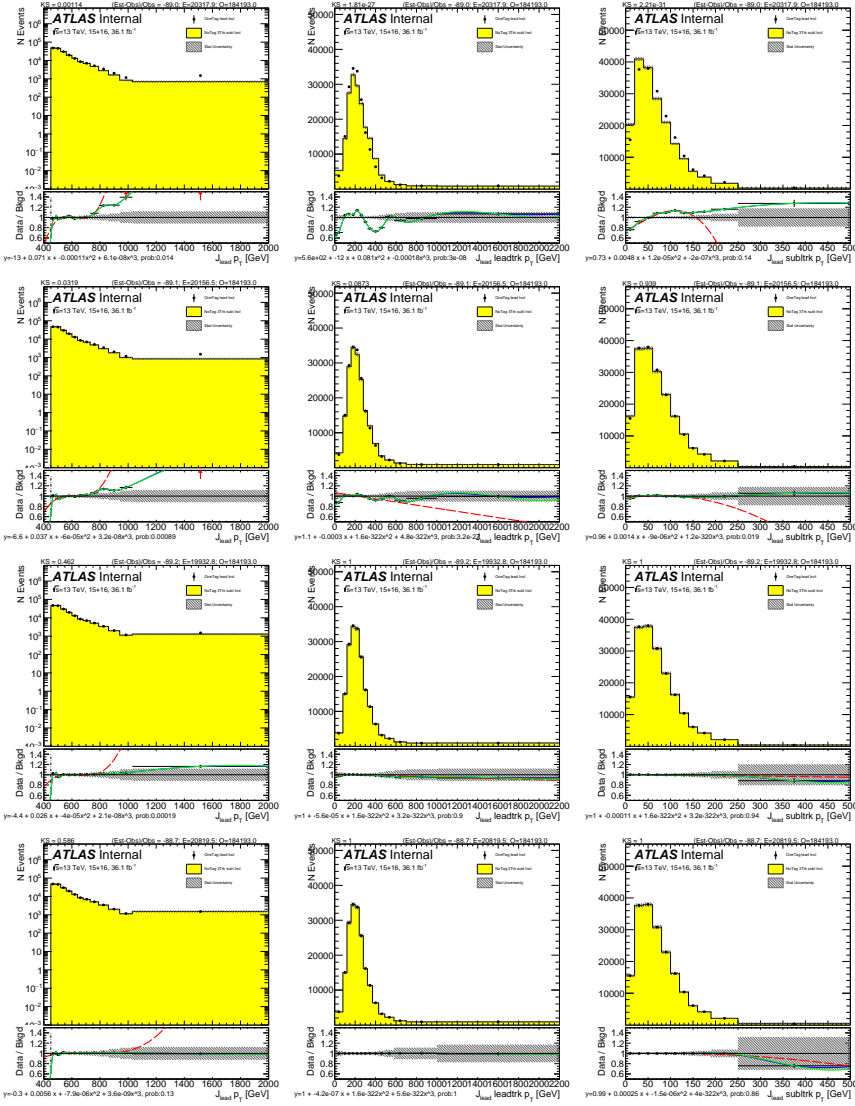


Figure E.4: For $3b$ background estimate: the fits to the ratio of the data in the $2b$ category, of the leading Higgs candidate $2b$ -tagged events's leading Higgs candidate distributions(black point), over the subleading Higgs candidate $1b$ -tagged events's leading Higgs candidate distributions(yellow). Distributions and fits to the estimated QCD background for large- R jet p_T (left), the large- R jet's leading trackjet p_T (middle), and large- R jet's subleading trackjet p_T (right) are shown. Figures are before reweighting (top row), after the first iteration(second row), after the fourth iteration(third row), and after the last iteration (bottom row). The green line is the spline fit; the red line is a polynomial fit; the blue line is the spline interpolation.

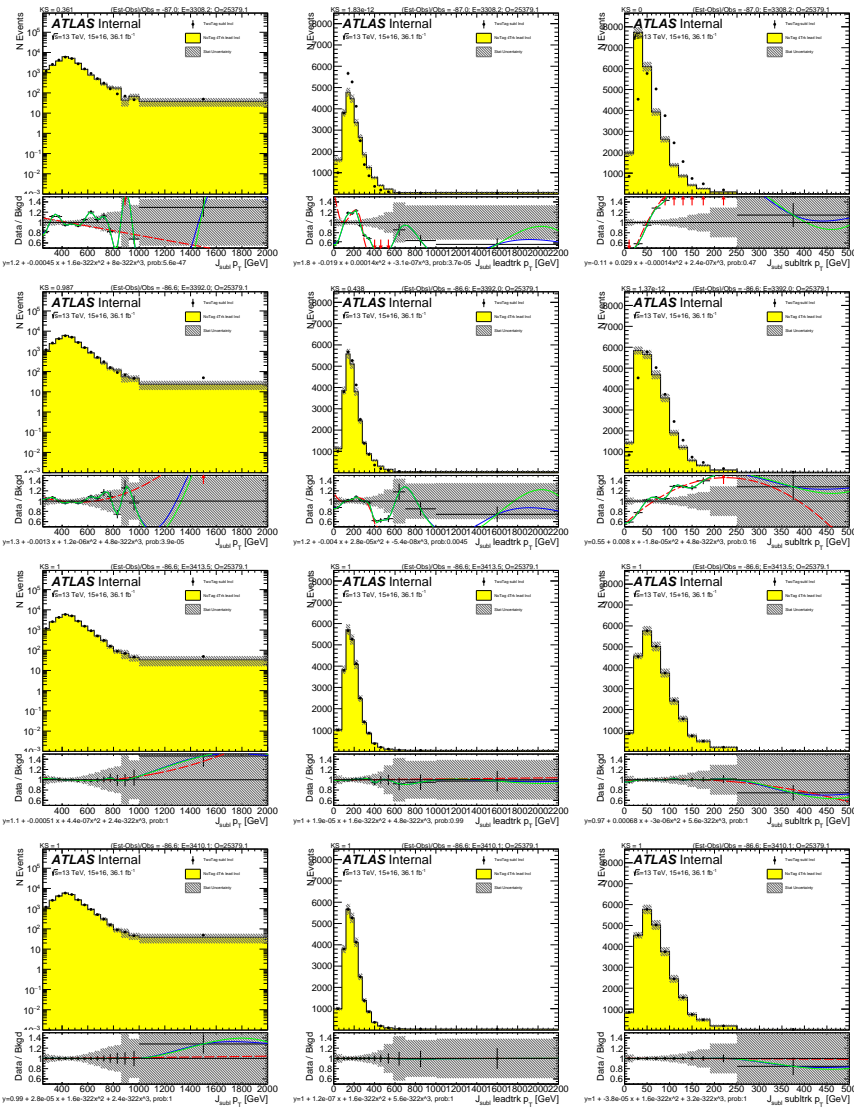


Figure E.5: For $4b$ background estimate: the fits to the ratio of the data in the $2b$ category, of the subleading Higgs candidate $2b$ -tagged events's subleading Higgs candidate distributions(black point), over the leading Higgs candidate $2b$ -tagged events's subleading Higgs candidate distributions(yellow). Distributions and fits to the estimated QCD background for large- R jet p_T (left), the large- R jet's leading trackjet p_T (middle), and large- R jet's subleading trackjet p_T (right) are shown. Figures are before reweighting (top row), after the first iteration(second row), after the fourth iteration(third row), and after the last iteration (bottom row). The green line is the spline fit; the red line is a polynomial fit; the blue line is the spline interpolation.

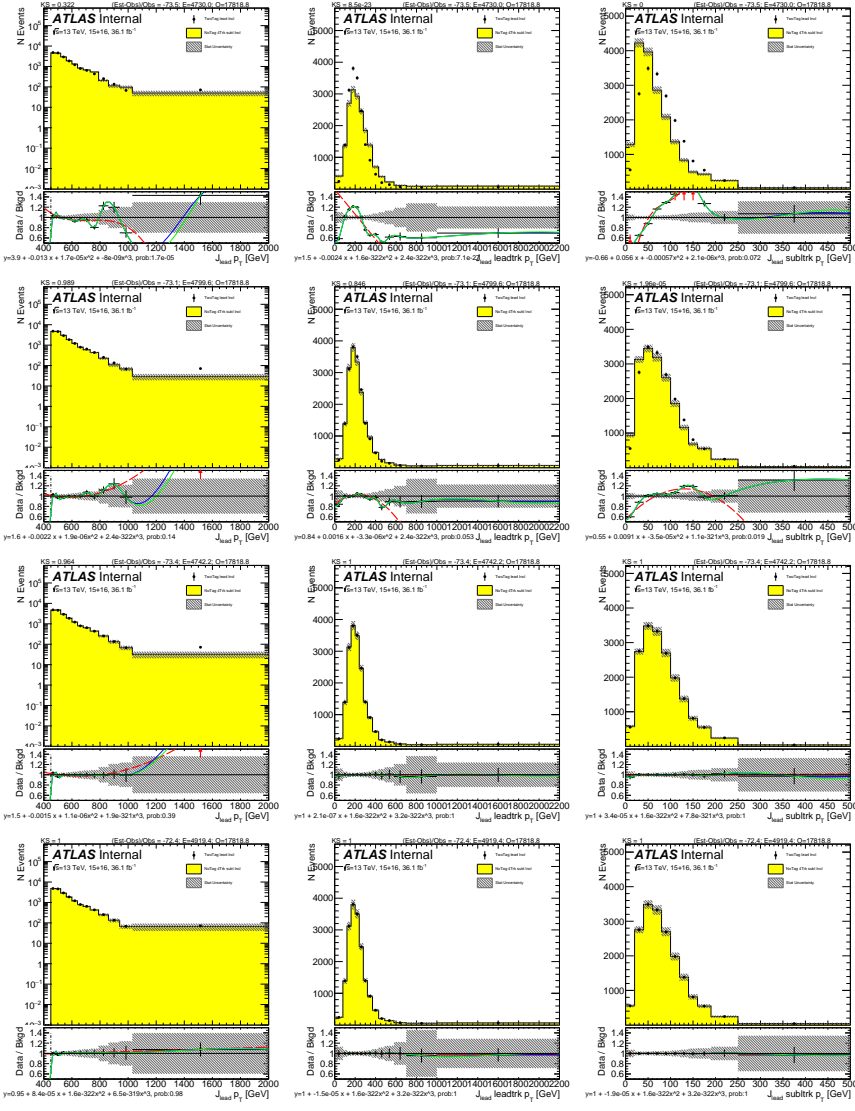


Figure E.6: For $4b$ background estimate: the fits to the ratio of the data in the $2b$ category, of the leading Higgs candidate $2b$ -tagged events's leading Higgs candidate distributions(black point), over the subleading Higgs candidate $2b$ -tagged events's leading Higgs candidate distributions(yellow). Distributions and fits to the estimated QCD background for large- R jet p_T (left), the large- R jet's leading trackjet p_T (middle), and large- R jet's subleading trackjet p_T (right) are shown. Figures are before reweighting (top row), after the first iteration(second row), after the fourth iteration(third row), and after the last iteration (bottom row). The green line is the spline fit; the red line is a polynomial fit; the blue line is the spline interpolation.

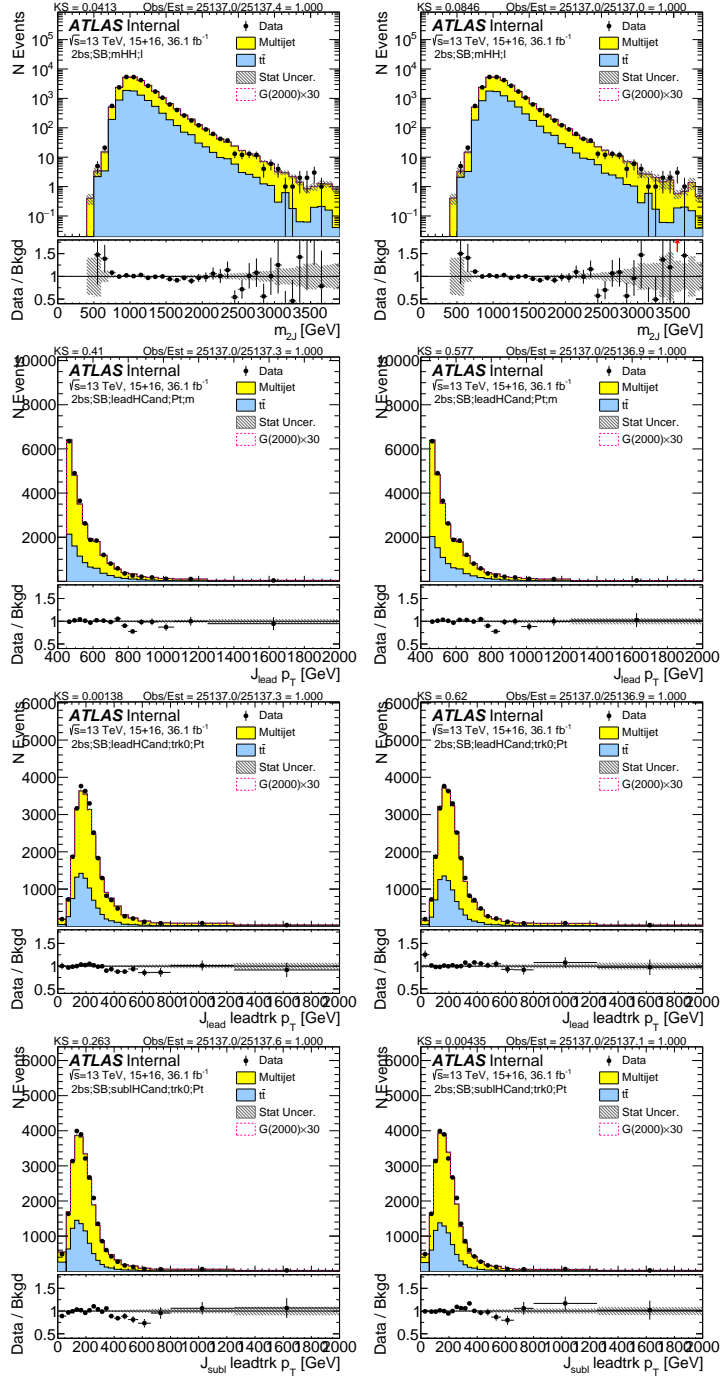


Figure E.7: Reweighted 2bs sideband region predictions comparison. Top row is the dijet Mass, second row is leading large- R jet p_T , third row is the leading large- R jet's leading trackjet p_T and the last row subleading large- R jet's leading trackjet p_T . On the left are the distributions before reweighting, and on the right are the distributions after reweighting.

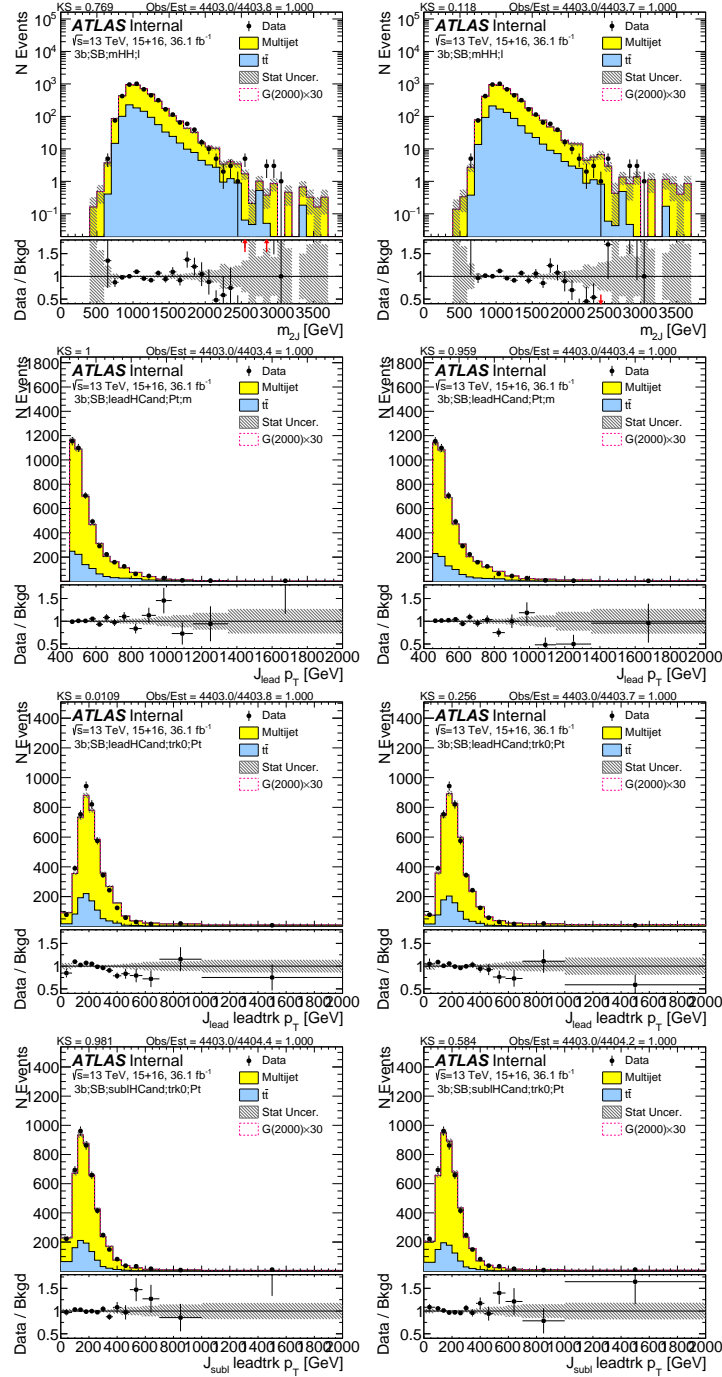


Figure E.8: Reweighted $3b$ sideband region predictions comparison. Top row is the dijet Mass, second row is leading large- R jet p_T , third row is the leading large- R jet's leading trackjet p_T and the last row subleading large- R jet's leading trackjet p_T . On the left are the distributions before reweighting, and on the right are the distributions after reweighting.

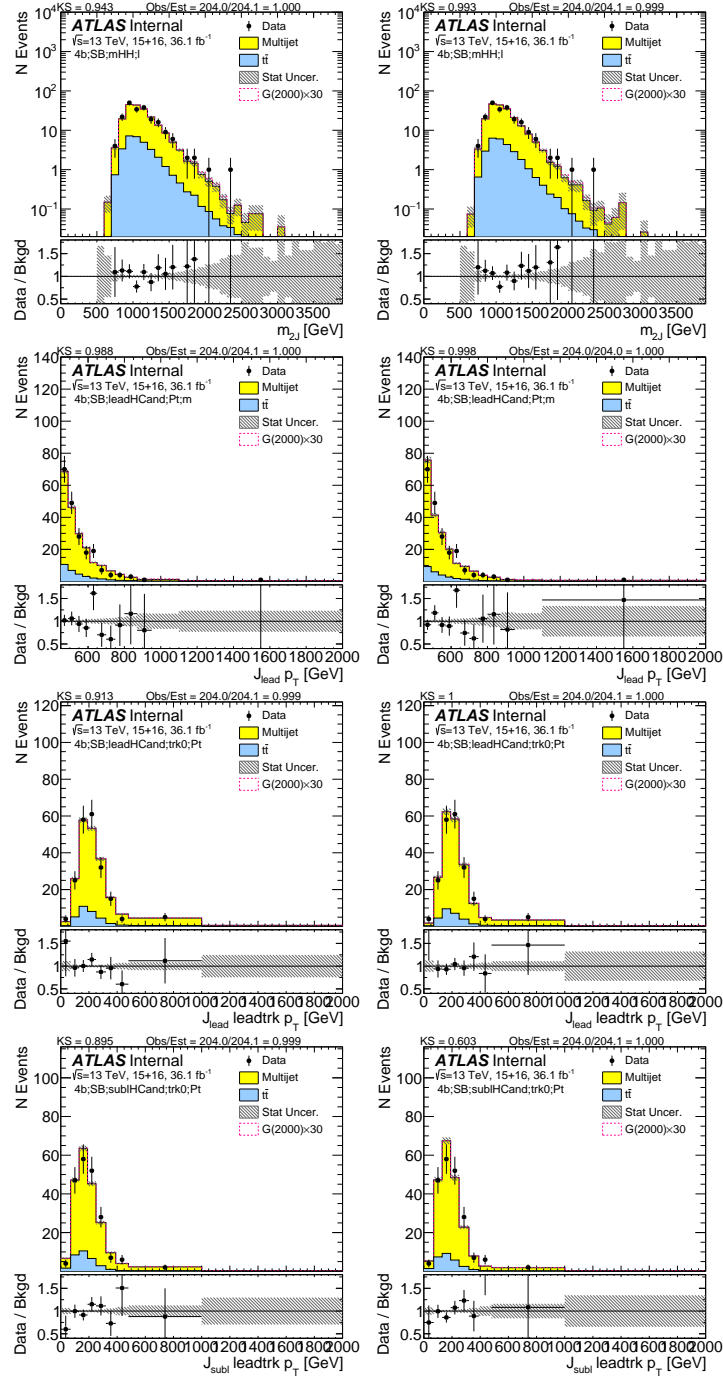


Figure E.9: Reweighted $4b$ sideband region predictions comparison. Top row is the dijet Mass, second row is leading large- R jet p_T , third row is the leading large- R jet's leading trackjet p_T and the last row subleading large- R jet's leading trackjet p_T . On the left are the distributions before reweighting, and on the right are the distributions after reweighting.

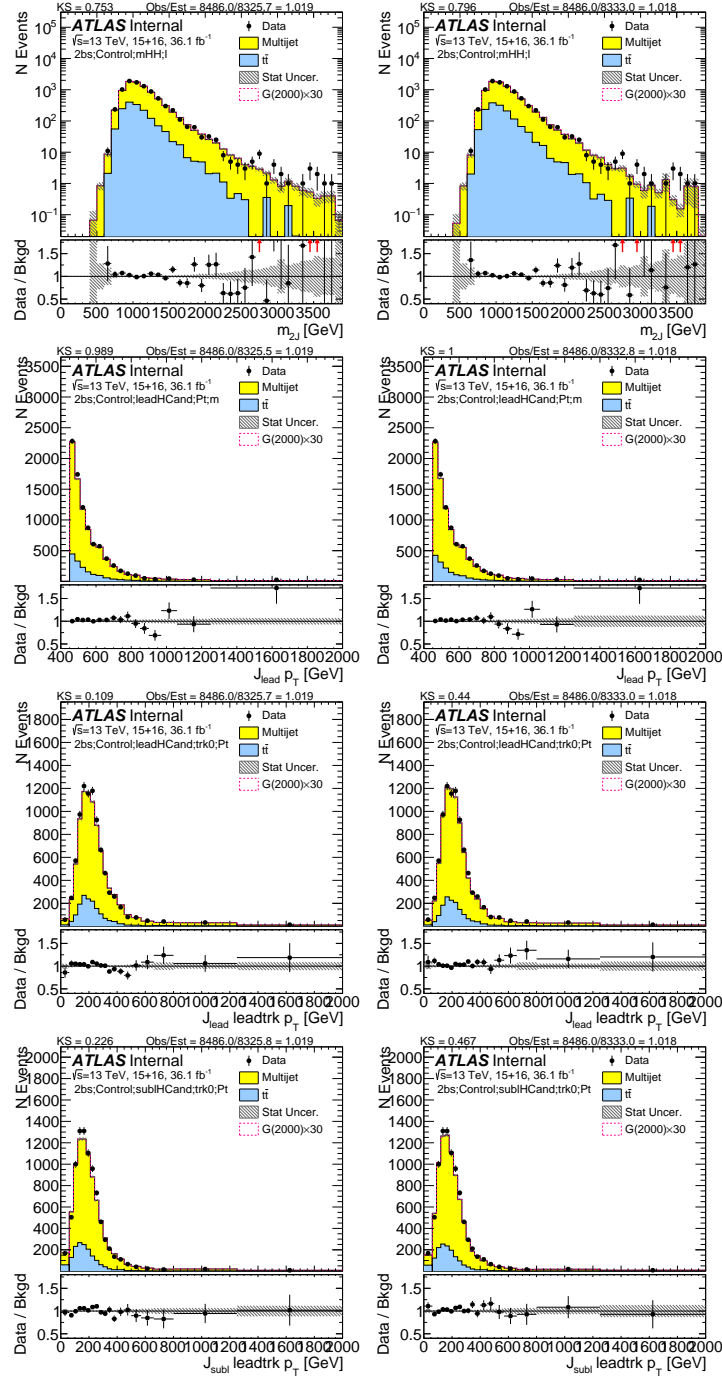


Figure E.10: Reweighted $2bs$ control region predictions comparison. Top row is the dijet Mass, second row is leading large- R jet p_T , third row is the leading large- R jet's leading trackjet p_T and the last row subleading large- R jet's leading trackjet p_T . On the left are the distributions before reweighting, and on the right are the distributions after reweighting.

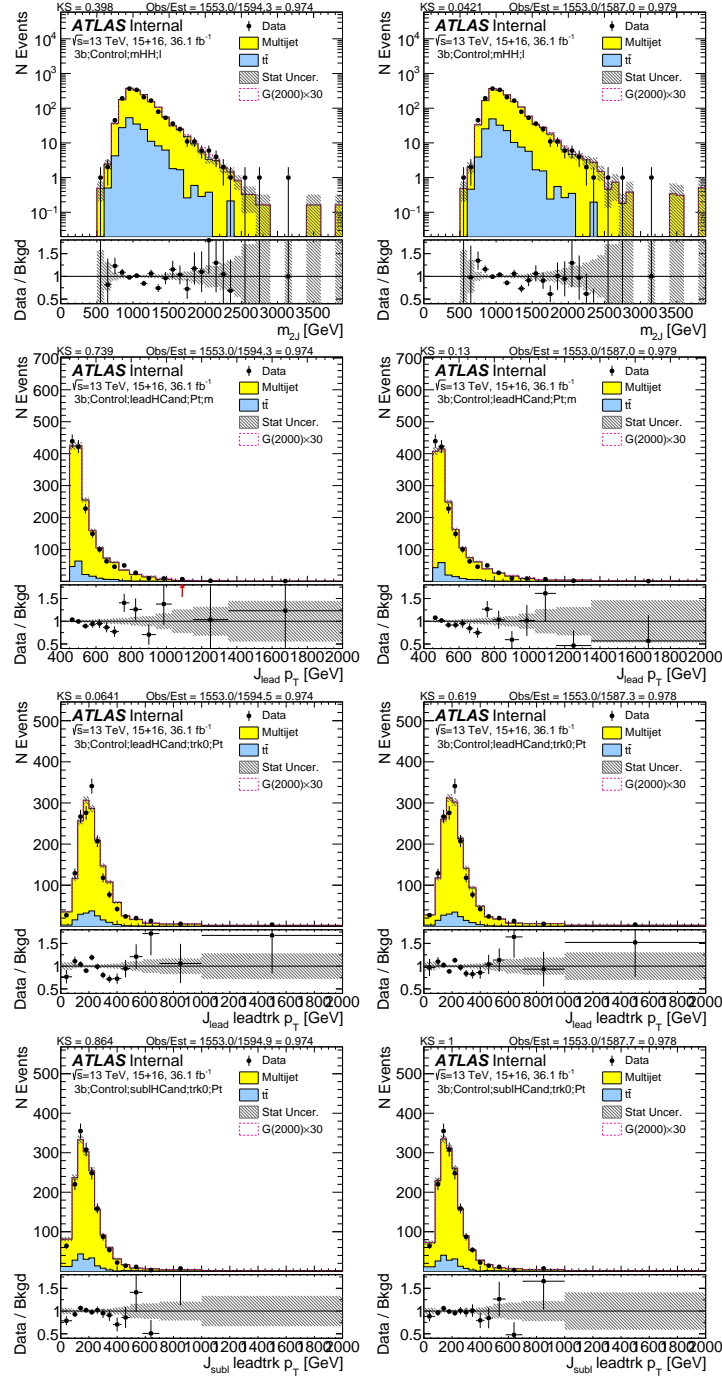


Figure E.11: Reweighted $3b$ control region predictions comparison. Top row is the dijet Mass, second row is leading large- R jet p_T , third row is the leading large- R jet's leading trackjet p_T and the last row subleading large- R jet's leading trackjet p_T . On the left are the distributions before reweighting, and on the right are the distributions after reweighting.

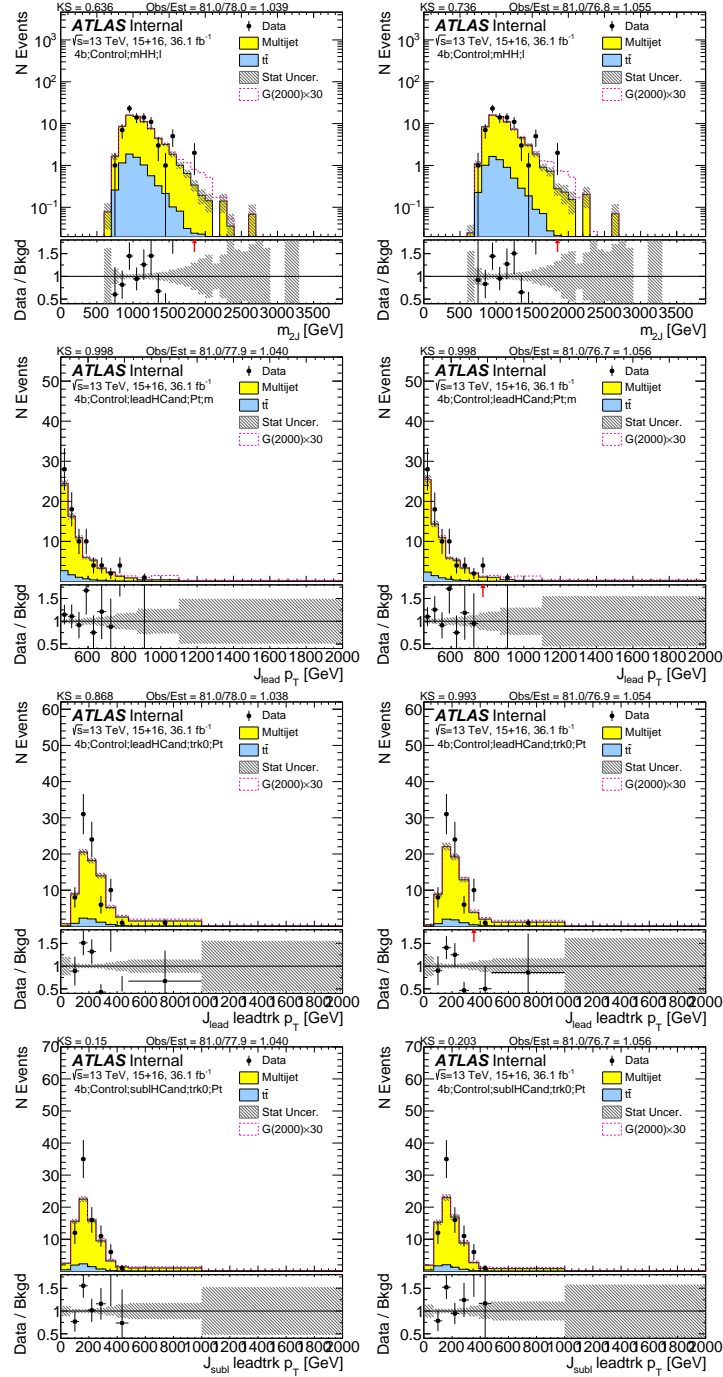


Figure E.12: Reweighted 4b control region predictions comparison. Top row is the dijet Mass, second row is leading large- R jet p_T , third row is the leading large- R jet's leading trackjet p_T and the last row subleading large- R jet's leading trackjet p_T . On the left are the distributions before reweighting, and on the right are the distributions after reweighting.

F

Effects on yield prediction from variations of the sideband and control regions

This Appendix is the supporting material for section 7.5. The effect on signal region yield from different control region and sideband region is tested. All these tests are done on the control/sideband regions after the full reweighting procedure as described in 6.6, while applying the nominal reweight-

ing values.

Besides the nominal control region and sideband region definitions, seven additional variations, as illustrated in Figure F.2, F.1, F.3, F.5, F.4, F.7, F.6, are tested. They are:

- Low-mass control region: the center position of the circle that defines nominal CR is moved down by 3 GeV, in both leading and sub-leading large-jet mass.
- High-mass control region: the center position of the circle that defines nominal CR is moved up by 3 GeV, in both leading and sub-leading large-R jet mass.
- Signal-depletion (Small) control region: the X_{hh} cut that defines signal region is increased to 2.0 from 1.6. This variation only affect CR, while SR remains unchanged (i.e. signal region is still defined by $X_{hh} < 1.6$, while CR is defined as $X_{hh} > 2.0$ and $R_{hh} < 33$).
- High-mass sideband region: The signal region and control region remain unchanged, the center position of the circle that defines nominal SB is moved up by 3 GeV in both leading and sub-leading large-R jet mass.
- Low-mass sideband region: The signal region and control region remain unchanged, the center position of the circle that defines nominal SB is moved up by 3 GeV in both leading and sub-leading large-R jet mass.
- Large sideband region: The signal region and control region remain unchanged, while the SB is $33 < R_{hh}$ and $R_{hh}^{\text{high}} < 61$. μ_{QCD} will change.
- Small sideband region: The signal region and control region remain unchanged, while the SB is $33 < R_{hh}$ and $R_{hh}^{\text{high}} < 55$. μ_{QCD} will change.

The high mass and low mass CR tests how background modeling is sensitive to the exact position of CR. The signal-depletion CR is designed to test whether there is significant signal contamination in the CR. The agreement between data and prediction in the CR would be significantly different

from the number calculated with nominal CR, if there is a large amount of signal contamination in CR. The sideband variations are designed to test how sensitive the normalization fit is to the sideband definition.

The agreement between data and prediction in CR are summarized in Table 7.1, 7.2 and 7.3. For most CR variations, the discrepancy between data and prediction is smaller than statistical uncertainty of data. The only exception is $2bs$ high CR variation, where the prediction is $\sim 1.5\sigma$ away from the data. The variation in signal-depletion CR definition is not significantly deviated from the number derived from nominal CR definition, and the discrepancy is also within the statistical uncertainty of data as well. This shows no significant signal contamination in CR is found.

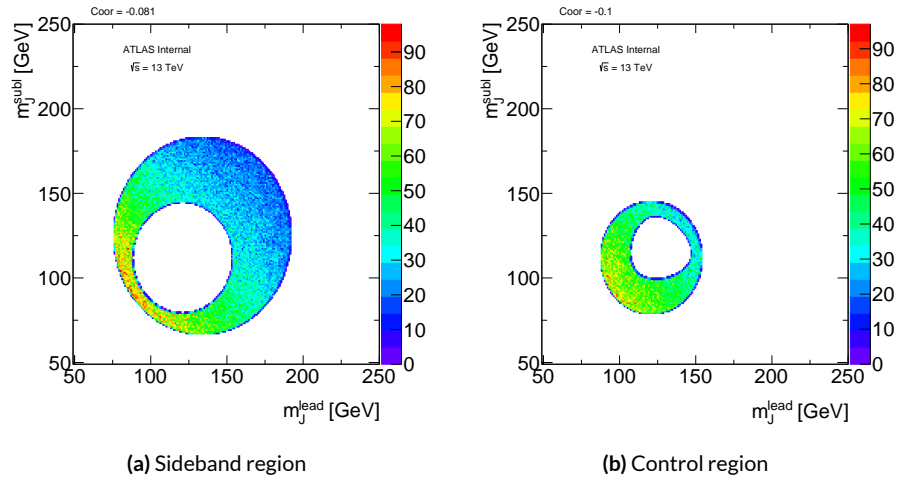


Figure F.1: In $1b$ data, with low-mass CR variation, new SB and CR $m_j^{\text{lead}} - m_j^{\text{subl}}$ distribution.

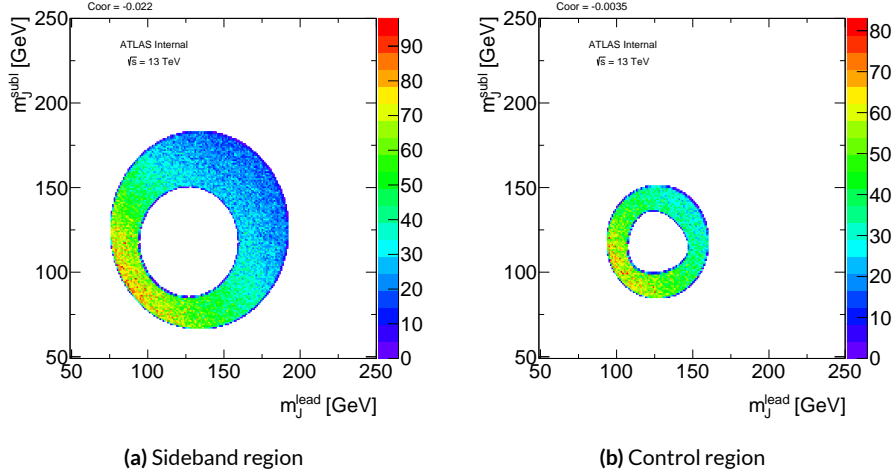


Figure F.2: In $1b$ data, with high-mass CR variation, new SB and CR $m_j^{\text{lead}} - m_j^{\text{subl}}$ distribution.

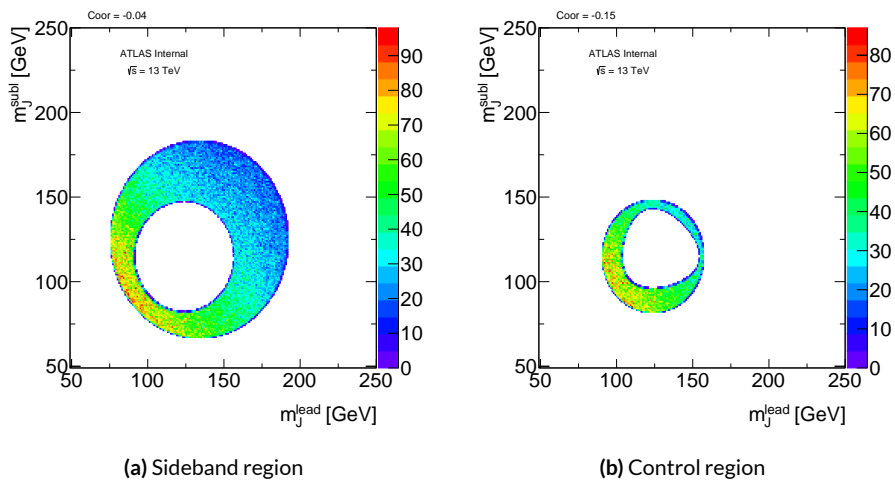


Figure F.3: In $1b$ data, with signal-depletion (small) CR variation, new SB and CR $m_j^{\text{lead}} - m_j^{\text{subl}}$ distribution.

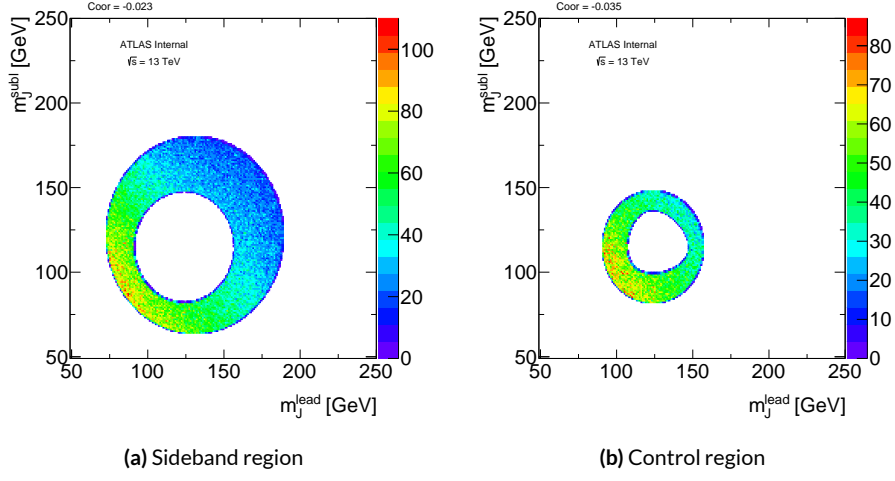


Figure F.4: In $1b$ data, with low-mass SB variation, new SB and CR $m_J^{\text{lead}} - m_J^{\text{subl}}$ distribution.

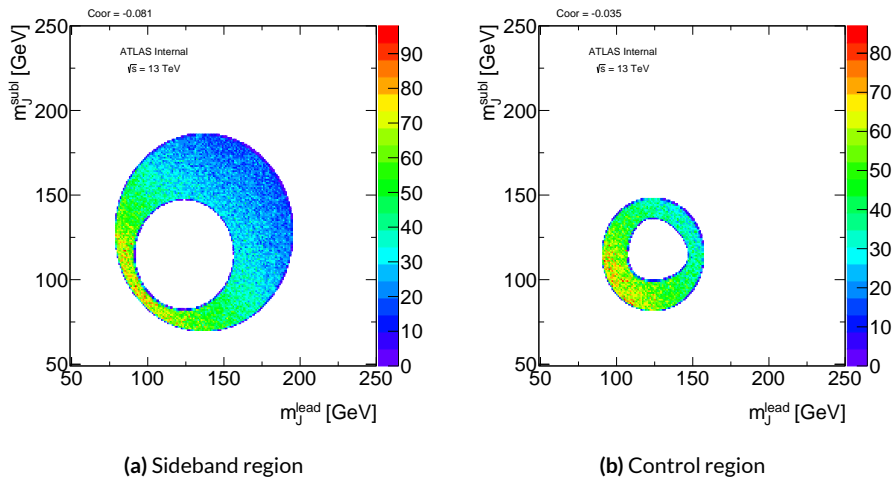


Figure F.5: In $1b$ data, with high-mass SB variation, new SB and CR $m_J^{\text{lead}} - m_J^{\text{subl}}$ distribution.

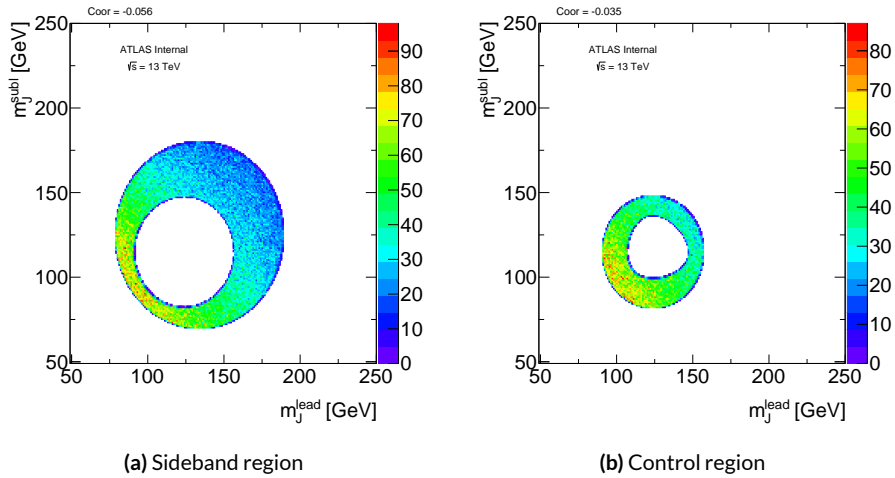


Figure F.6: In $1b$ data, with small SB variation, new SB and CR $m_J^{\text{lead}} - m_J^{\text{subl}}$ distribution.

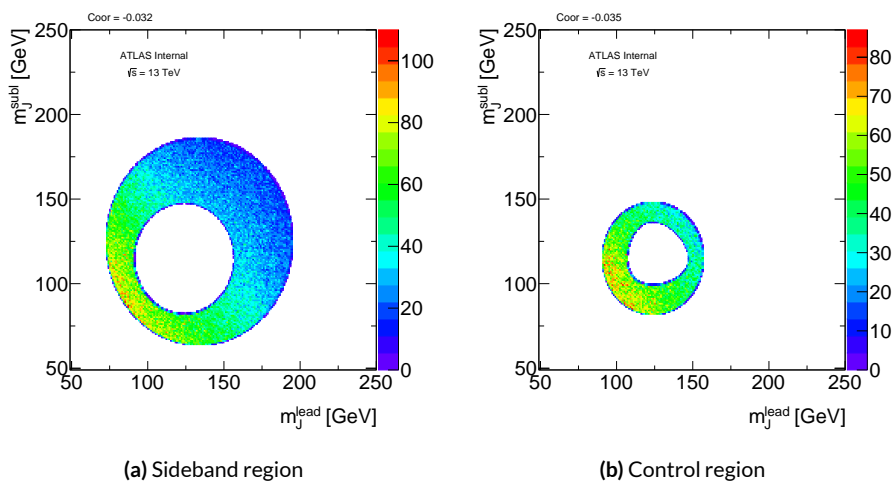


Figure F.7: In $1b$ data, with large SB variation, new SB and CR $m_J^{\text{lead}} - m_J^{\text{subl}}$ distribution.

The whole background estimation procedure is repeated after the variation. The summary of background estimated yields for $4b$ region can be found in Table ??, ??, F.3, F.4, F.5, F.6, F.7, for each variation.

Table F.1: Background prediction in SR/CR/SB for High CR in $4b$ region.

FourTag	Sideband	Control	Signal
QCD Est	183.14 ± 3.02	58.01 ± 1.72	33.01 ± 1.25
$t\bar{t}$ Est.	25.97 ± 0.23	6.92 ± 0.13	1.62 ± 0.042
$Z + jets$	0 ± 0	6.18 ± 5.12	0 ± 0
Total Bkg Est	209.12 ± 3.03	71.12 ± 5.41	34.63 ± 1.25
Data	209.0 ± 14.46	76.0 ± 8.72	31.0 ± 5.57
$c = 1.0, m = 1.0 TeV$	2.68 ± 0.1	5.23 ± 0.14	10.07 ± 0.2
$c = 1.0, m = 2.0 TeV$	0.04 ± 0.0017	0.095 ± 0.0025	0.25 ± 0.0041
$c = 1.0, m = 3.0 TeV$	$0.00032 \pm 3.7e-05$	$0.0008 \pm 5.6e-05$	$0.0016 \pm 8e-05$

Table F.2: Background prediction in SR/CR/SB for Low CR in $4b$ region.

FourTag	Sideband	Control	Signal
QCD Est	165.7 ± 2.84	69.9 ± 1.87	32.26 ± 1.22
$t\bar{t}$ Est.	28.47 ± 0.25	3.79 ± 0.078	1.59 ± 0.041
$Z + jets$	0 ± 0	6.18 ± 5.12	0 ± 0
Total Bkg Est	194.17 ± 2.85	79.87 ± 5.45	33.84 ± 1.23
Data	194.0 ± 13.93	91.0 ± 9.54	31.0 ± 5.57
$c = 1.0, m = 1.0 TeV$	2.66 ± 0.1	5.26 ± 0.14	10.07 ± 0.2
$c = 1.0, m = 2.0 TeV$	0.034 ± 0.0015	0.1 ± 0.0026	0.25 ± 0.0041
$c = 1.0, m = 3.0 TeV$	$0.0003 \pm 3.6e-05$	$0.00082 \pm 5.6e-05$	$0.0016 \pm 8e-05$

Table F.3: Background prediction in SR/CR/SB for Small CR in $4b$ region.

FourTag	Sideband	Control	Signal
QCD Est	176.26 ± 2.96	46.97 ± 1.54	32.91 ± 1.25
$t\bar{t}$ Est.	27.86 ± 0.25	2.81 ± 0.07	1.68 ± 0.044
$Z + jets$	0 ± 0	6.18 ± 5.12	0 ± 0
Total Bkg Est	204.12 ± 2.97	55.96 ± 5.35	34.59 ± 1.25
Data	204.0 ± 14.28	58.0 ± 7.62	31.0 ± 5.57
$c = 1.0, m = 1.0 TeV$	2.52 ± 0.1	2.82 ± 0.11	10.07 ± 0.2
$c = 1.0, m = 2.0 TeV$	0.034 ± 0.0015	0.054 ± 0.0019	0.25 ± 0.0041
$c = 1.0, m = 3.0 TeV$	$0.00032 \pm 3.7e-05$	$0.00048 \pm 4.3e-05$	$0.0016 \pm 8e-05$

Table F.4: Background prediction in SR/CR/SB for High SB in $4b$ region.

FourTag	Sideband	Control	Signal
QCD Est	168.37 ± 2.98	67.36 ± 1.88	34.53 ± 1.31
$t\bar{t}$ Est.	23.75 ± 0.21	5.18 ± 0.1	1.37 ± 0.035
$Z + jets$	0 ± 0	6.18 ± 5.12	0 ± 0
Total Bkg Est	192.12 ± 2.99	78.72 ± 5.46	35.89 ± 1.31
Data	192.0 ± 13.86	81.0 ± 9.0	31.0 ± 5.57
$c = 1.0, m = 1.0 TeV$	2.46 ± 0.098	5.4 ± 0.15	10.07 ± 0.2
$c = 1.0, m = 2.0 TeV$	0.031 ± 0.0015	0.1 ± 0.0026	0.25 ± 0.0041
$c = 1.0, m = 3.0 TeV$	$0.0003 \pm 3.5e-05$	$0.0008 \pm 5.6e-05$	$0.0016 \pm 8e-05$

Table F.5: Background prediction in SR/CR/SB for Low SB in $4b$ region.

FourTag	Sideband	Control	Signal
QCD Est	176.2 ± 2.81	58.42 ± 1.63	29.95 ± 1.14
$t\bar{t}$ Est.	40.93 ± 0.38	11.91 ± 0.23	3.14 ± 0.081
$Z + jets$	0 ± 0	6.18 ± 5.12	0 ± 0
Total Bkg Est	217.12 ± 2.84	76.51 ± 5.38	33.09 ± 1.14
Data	217.0 ± 14.73	81.0 ± 9.0	31.0 ± 5.57
$c = 1.0, m = 1.0 TeV$	2.52 ± 0.1	5.4 ± 0.15	10.07 ± 0.2
$c = 1.0, m = 2.0 TeV$	0.035 ± 0.0015	0.1 ± 0.0026	0.25 ± 0.0041
$c = 1.0, m = 3.0 TeV$	$0.00033 \pm 3.7e-05$	$0.0008 \pm 5.6e-05$	$0.0016 \pm 8e-05$

Table F.6: Background prediction in SR/CR/SB for Large SB in $4b$ region.

FourTag	Sideband	Control	Signal
QCD Est	198.09 ± 3.04	60.63 ± 1.69	31.08 ± 1.18
$t\bar{t}$ Est.	37.04 ± 0.31	7.9 ± 0.16	2.08 ± 0.054
$Z + jets$	0 ± 0	6.18 ± 5.12	0 ± 0
Total Bkg Est	235.12 ± 3.06	74.71 ± 5.4	33.16 ± 1.18
Data	235.0 ± 15.33	81.0 ± 9.0	31.0 ± 5.57
$c = 1.0, m = 1.0 TeV$	2.75 ± 0.1	5.4 ± 0.15	10.07 ± 0.2
$c = 1.0, m = 2.0 TeV$	0.037 ± 0.0016	0.1 ± 0.0026	0.25 ± 0.0041
$c = 1.0, m = 3.0 TeV$	$0.00034 \pm 3.8e-05$	$0.0008 \pm 5.6e-05$	$0.0016 \pm 8e-05$

Table F.7: Background prediction in SR/CR/SB for Small SB in $4b$ region.

FourTag	Sideband	Control	Signal
QCD Est	133.42 ± 2.47	58.2 ± 1.63	29.83 ± 1.13
$t\bar{t}$ Est.	34.72 ± 0.33	9.77 ± 0.19	2.58 ± 0.067
$Z + jets$	0 ± 0	6.18 ± 5.12	0 ± 0
Total Bkg Est	168.13 ± 2.49	74.15 ± 5.38	32.41 ± 1.13
Data	168.0 ± 12.96	81.0 ± 9.0	31.0 ± 5.57
$c = 1.0, m = 1.0 TeV$	2.29 ± 0.095	5.4 ± 0.15	10.07 ± 0.2
$c = 1.0, m = 2.0 TeV$	0.03 ± 0.0014	0.1 ± 0.0026	0.25 ± 0.0041
$c = 1.0, m = 3.0 TeV$	$0.00029 \pm 3.5e-05$	$0.0008 \pm 5.6e-05$	$0.0016 \pm 8e-05$

The summary of background estimated yields for $3b$ region can be found in Table F.8, F.9, F.10, F.11, F.12, F.13, F.14, for each variation.

Table F.8: Background prediction in SR/CR/SB for High CR in $3b$ region.

ThreeTag	Sideband	Control	Signal
QCD Est	3632.79 ± 28.07	1288.95 ± 16.26	700.18 ± 11.93
$t\bar{t}$ Est.	829.13 ± 25.15	174.53 ± 11.64	78.43 ± 2.03
$Z + jets$	33.59 ± 11.36	10.42 ± 5.62	0.49 ± 0.49
Total Bkg Est	4495.51 ± 39.36	1473.89 ± 20.77	779.1 ± 12.11
Data	4495.0 ± 67.04	1461.0 ± 38.22	801.0 ± 28.3
$c = 1.0, m = 1.0 TeV$	8.46 ± 0.19	11.99 ± 0.22	26.0 ± 0.33
$c = 1.0, m = 2.0 TeV$	0.18 ± 0.0037	0.36 ± 0.0052	0.76 ± 0.0076
$c = 1.0, m = 3.0 TeV$	0.0039 ± 0.00013	0.0072 ± 0.00018	0.013 ± 0.00023

Table F.9: Background prediction in SR/CR/SB for Low CR in $3b$ region.

ThreeTag	Sideband	Control	Signal
QCD Est	3412.05 ± 27.11	1542.75 ± 18.27	705.03 ± 12.02
$t\bar{t}$ Est.	887.39 ± 26.48	140.33 ± 10.2	80.32 ± 2.08
$Z + jets$	29.7 ± 11.19	14.3 ± 5.94	0.49 ± 0.49
Total Bkg Est	4329.15 ± 39.51	1697.38 ± 21.75	785.83 ± 12.2
Data	4328.0 ± 65.79	1628.0 ± 40.35	801.0 ± 28.3
$c = 1.0, m = 1.0 TeV$	7.87 ± 0.18	12.58 ± 0.23	26.0 ± 0.33
$c = 1.0, m = 2.0 TeV$	0.15 ± 0.0034	0.39 ± 0.0054	0.76 ± 0.0076
$c = 1.0, m = 3.0 TeV$	0.0036 ± 0.00013	0.0075 ± 0.00018	0.013 ± 0.00023

Table F.10: Background prediction in SR/CR/SB for Small CR in $3b$ region.

ThreeTag	Sideband	Control	Signal
QCD Est	3518.01 ± 27.48	1020.18 ± 14.79	701.6 ± 11.95
$t\bar{t}$ Est.	852.88 ± 25.72	98.31 ± 8.12	79.34 ± 2.05
$Z + jets$	32.8 ± 11.34	8.84 ± 5.19	0.49 ± 0.49
Total Bkg Est	4403.69 ± 39.31	1127.34 ± 17.66	781.42 ± 12.14
Data	4403.0 ± 66.36	1134.0 ± 33.67	801.0 ± 28.3
$c = 1.0, m = 1.0 TeV$	7.86 ± 0.18	7.5 ± 0.18	26.0 ± 0.33
$c = 1.0, m = 2.0 TeV$	0.16 ± 0.0035	0.22 ± 0.0041	0.76 ± 0.0076
$c = 1.0, m = 3.0 TeV$	0.0036 ± 0.00013	0.0043 ± 0.00014	0.013 ± 0.00023

Table F.11: Background prediction in SR/CR/SB for High SB in $3b$ region.

ThreeTag	Sideband	Control	Signal
QCD Est	3244.66 ± 26.66	1431.35 ± 17.56	710.47 ± 12.09
$t\bar{t}$ Est.	889.75 ± 26.15	160.18 ± 11.01	78.3 ± 2.03
$Z + jets$	28.07 ± 10.31	11.21 ± 5.65	0.49 ± 0.49
Total Bkg Est	4162.48 ± 38.74	1602.74 ± 21.48	789.26 ± 12.27
Data	4162.0 ± 64.51	1553.0 ± 39.41	801.0 ± 28.3
$c = 1.0, m = 1.0 TeV$	7.55 ± 0.18	12.58 ± 0.23	26.0 ± 0.33
$c = 1.0, m = 2.0 TeV$	0.14 ± 0.0033	0.38 ± 0.0054	0.76 ± 0.0076
$c = 1.0, m = 3.0 TeV$	0.0032 ± 0.00012	0.0075 ± 0.00018	0.013 ± 0.00023

Table F.12: Background prediction in SR/CR/SB for Low SB in $3b$ region.

ThreeTag	Sideband	Control	Signal
QCD Est	3797.02 ± 28.24	1395.42 ± 17.15	692.6 ± 11.8
$t\bar{t}$ Est.	825.52 ± 25.8	169.94 ± 11.68	83.07 ± 2.15
$Z + jets$	50.5 ± 15.32	11.21 ± 5.65	0.49 ± 0.49
Total Bkg Est	4673.04 ± 41.2	1576.56 ± 21.5	776.15 ± 12.01
Data	4672.0 ± 68.35	1553.0 ± 39.41	801.0 ± 28.3
$c = 1.0, m = 1.0 TeV$	8.09 ± 0.18	12.58 ± 0.23	26.0 ± 0.33
$c = 1.0, m = 2.0 TeV$	0.17 ± 0.0036	0.38 ± 0.0054	0.76 ± 0.0076
$c = 1.0, m = 3.0 TeV$	0.0039 ± 0.00013	0.0075 ± 0.00018	0.013 ± 0.00023

Table F.13: Background prediction in SR/CR/SB for Large SB in $3b$ region.

ThreeTag	Sideband	Control	Signal
QCD Est	4094.15 ± 29.34	1392.94 ± 17.09	691.4 ± 11.77
$t\bar{t}$ Est.	993.33 ± 28.3	170.09 ± 11.69	83.14 ± 2.15
$Z + jets$	44.81 ± 13.44	11.21 ± 5.65	0.49 ± 0.49
Total Bkg Est	5132.28 ± 42.92	1574.23 ± 21.47	775.03 ± 11.97
Data	5132.0 ± 71.64	1553.0 ± 39.41	801.0 ± 28.3
$c = 1.0, m = 1.0 TeV$	8.63 ± 0.19	12.58 ± 0.23	26.0 ± 0.33
$c = 1.0, m = 2.0 TeV$	0.18 ± 0.0037	0.38 ± 0.0054	0.76 ± 0.0076
$c = 1.0, m = 3.0 TeV$	0.0039 ± 0.00013	0.0075 ± 0.00018	0.013 ± 0.00023

Table F.14: Background prediction in SR/CR/SB for Small SB in $3b$ region.

ThreeTag	Sideband	Control	Signal
QCD Est	2935.02 ± 25.3	1424.16 ± 17.5	706.86 ± 12.05
$t\bar{t}$ Est.	765.58 ± 24.63	166.07 ± 11.41	81.18 ± 2.1
$Z + jets$	28.07 ± 10.31	11.21 ± 5.65	0.49 ± 0.49
Total Bkg Est	3728.68 ± 36.78	1601.44 ± 21.64	788.53 ± 12.24
Data	3728.0 ± 61.06	1553.0 ± 39.41	801.0 ± 28.3
$c = 1.0, m = 1.0 TeV$	7.03 ± 0.17	12.58 ± 0.23	26.0 ± 0.33
$c = 1.0, m = 2.0 TeV$	0.14 ± 0.0033	0.38 ± 0.0054	0.76 ± 0.0076
$c = 1.0, m = 3.0 TeV$	0.0032 ± 0.00012	0.0075 ± 0.00018	0.013 ± 0.00023

The summary of background estimated yields for $2bs$ region can be found in Table F.15, F.16, F.17, F.18, F.19, F.20, F.21, for each variation.

Table F.15: Background prediction in SR/CR/SB for High CR in $2bs$ region.

TwoTag split	Sideband	Control	Signal
QCD Est	17680.28 ± 38.67	6283.4 ± 22.64	3382.9 ± 16.59
$t\bar{t}$ Est.	7700.3 ± 69.5	1629.22 ± 30.95	857.59 ± 22.21
$Z + jets$	69.2 ± 16.9	24.98 ± 9.93	0.13 ± 0.091
Total Bkg Est	25449.78 ± 81.31	7937.59 ± 39.61	4240.62 ± 27.72
Data	25449.0 ± 159.53	8174.0 ± 90.41	4376.0 ± 66.15
$c = 1.0, m = 1.0 TeV$	5.21 ± 0.15	5.91 ± 0.16	10.87 ± 0.22
$c = 1.0, m = 2.0 TeV$	0.21 ± 0.0042	0.34 ± 0.0054	0.6 ± 0.0072
$c = 1.0, m = 3.0 TeV$	0.015 ± 0.00026	0.025 ± 0.00034	0.039 ± 0.00041

Table F.16: Background prediction in SR/CR/SB for Low CR in $2bs$ region.

TwoTag split	Sideband	Control	Signal
QCD Est	16635.37 ± 37.77	7376.46 ± 24.35	3390.48 ± 16.64
$t\bar{t}$ Est.	8026.21 ± 71.28	1385.31 ± 28.45	865.13 ± 22.4
$Z + jets$	55.1 ± 15.01	39.08 ± 12.61	0.13 ± 0.091
Total Bkg Est	24716.68 ± 82.06	8800.86 ± 39.51	4255.74 ± 27.91
Data	24716.0 ± 157.21	8907.0 ± 94.38	4376.0 ± 66.15
$c = 1.0, m = 1.0 TeV$	4.62 ± 0.14	6.5 ± 0.17	10.87 ± 0.22
$c = 1.0, m = 2.0 TeV$	0.17 ± 0.0038	0.38 ± 0.0057	0.6 ± 0.0072
$c = 1.0, m = 3.0 TeV$	0.013 ± 0.00025	0.027 ± 0.00035	0.039 ± 0.00041

Table F.17: Background prediction in SR/CR/SB for Small CR in $2bs$ region.

TwoTag split	Sideband	Control	Signal
QCD Est	17216.91 ± 38.33	4909.25 ± 19.86	3393.56 ± 16.64
$t\bar{t}$ Est.	7852.35 ± 70.3	937.99 ± 23.41	858.27 ± 22.23
$Z + jets$	67.74 ± 16.82	26.28 ± 10.08	0.13 ± 0.091
Total Bkg Est	25137.01 ± 81.82	5873.52 ± 32.31	4251.96 ± 27.77
Data	25137.0 ± 158.55	5999.0 ± 77.45	4376.0 ± 66.15
$c = 1.0, m = 1.0 TeV$	4.79 ± 0.14	3.95 ± 0.13	10.87 ± 0.22
$c = 1.0, m = 2.0 TeV$	0.18 ± 0.0039	0.22 ± 0.0044	0.6 ± 0.0072
$c = 1.0, m = 3.0 TeV$	0.013 ± 0.00025	0.016 ± 0.00026	0.039 ± 0.00041

Table F.18: Background prediction in SR/CR/SB for High SB in $2bs$ region.

TwoTag split	Sideband	Control	Signal
QCD Est	15881.71 ± 37.13	6904.39 ± 23.75	3434.67 ± 16.82
$t\bar{t}$ Est.	8012.21 ± 70.33	1447.3 ± 28.51	836.73 ± 21.67
$Z + jets$	53.46 ± 14.13	26.44 ± 10.08	0.13 ± 0.091
Total Bkg Est	23947.39 ± 80.77	8378.14 ± 38.45	4271.53 ± 27.43
Data	23947.0 ± 154.75	8486.0 ± 92.12	4376.0 ± 66.15
$c = 1.0, m = 1.0 TeV$	4.47 ± 0.14	6.33 ± 0.16	10.87 ± 0.22
$c = 1.0, m = 2.0 TeV$	0.16 ± 0.0037	0.36 ± 0.0056	0.6 ± 0.0072
$c = 1.0, m = 3.0 TeV$	0.012 ± 0.00023	0.027 ± 0.00034	0.039 ± 0.00041

Table F.19: Background prediction in SR/CR/SB for Low SB in $2bs$ region.

TwoTag split	Sideband	Control	Signal
QCD Est	18853.52 ± 39.96	6832.97 ± 23.54	3398.98 ± 16.68
$t\bar{t}$ Est.	7470.01 ± 68.56	1497.44 ± 29.5	865.71 ± 22.42
$Z + jets$	72.2 ± 17.11	26.44 ± 10.08	0.13 ± 0.091
Total Bkg Est	26395.73 ± 81.18	8356.86 ± 39.06	4264.82 ± 27.94
Data	26395.0 ± 162.47	8486.0 ± 92.12	4376.0 ± 66.15
$c = 1.0, m = 1.0 TeV$	5.07 ± 0.15	6.33 ± 0.16	10.87 ± 0.22
$c = 1.0, m = 2.0 TeV$	0.2 ± 0.0041	0.36 ± 0.0056	0.6 ± 0.0072
$c = 1.0, m = 3.0 TeV$	0.014 ± 0.00026	0.027 ± 0.00034	0.039 ± 0.00041

Table F.20: Background prediction in SR/CR/SB for Large SB in $2bs$ region.

TwoTag split	Sideband	Control	Signal
QCD Est	20472.06 ± 41.82	6862.72 ± 23.61	3413.92 ± 16.72
$t\bar{t}$ Est.	8569.73 ± 72.85	1452.54 ± 28.61	839.75 ± 21.75
$Z + jets$	73.9 ± 17.45	26.44 ± 10.08	0.13 ± 0.091
Total Bkg Est	29115.69 ± 85.79	8341.7 ± 38.44	4253.81 ± 27.43
Data	29115.0 ± 170.63	8486.0 ± 92.12	4376.0 ± 66.15
$c = 1.0, m = 1.0 TeV$	5.38 ± 0.15	6.33 ± 0.16	10.87 ± 0.22
$c = 1.0, m = 2.0 TeV$	0.2 ± 0.0042	0.36 ± 0.0056	0.6 ± 0.0072
$c = 1.0, m = 3.0 TeV$	0.015 ± 0.00026	0.027 ± 0.00034	0.039 ± 0.00041

Table F.21: Background prediction in SR/CR/SB for Large SB in $2bs$ region.

TwoTag split	Sideband	Control	Signal
QCD Est	14242.66 ± 34.91	6800.86 ± 23.43	3383.0 ± 16.6
$t\bar{t}$ Est.	6985.79 ± 66.42	1505.96 ± 29.67	870.64 ± 22.55
$Z + jets$	55.33 ± 14.25	26.44 ± 10.08	0.13 ± 0.091
Total Bkg Est	21283.78 ± 76.38	8333.25 ± 39.12	4253.77 ± 28.0
Data	21283.0 ± 145.89	8486.0 ± 92.12	4376.0 ± 66.15
$c = 1.0, m = 1.0 TeV$	4.21 ± 0.13	6.33 ± 0.16	10.87 ± 0.22
$c = 1.0, m = 2.0 TeV$	0.16 ± 0.0037	0.36 ± 0.0056	0.6 ± 0.0072
$c = 1.0, m = 3.0 TeV$	0.012 ± 0.00023	0.027 ± 0.00034	0.039 ± 0.00041

The variation of prediction in SR can be found in Table F.22, F.23 and F.24. The variation in signal-depletion variation is not shown since that will be zero by definition. The variation of background prediction in SR is very small and within statistical uncertainty. This is mainly due to the data-driven background estimation technique we are using.

Table F.22: Variation in Prediction in $4b$ SR region.

FourTag	Prediction	Diff	QCD	ttbar
Nominal	$34.59\% \pm 1.25\%$	$0.011\% \pm 7.23\%$	$0.0021\% \pm 7.59\%$	$0.2\% \pm 5.22\%$
CR High	$34.63\% \pm 1.25\%$	$0.1\% \pm 7.24\%$	$0.3\% \pm 7.62\%$	$-3.73\% \pm 5.01\%$
CR Low	$33.84\% \pm 1.23\%$	$-2.16\% \pm 7.08\%$	$-1.98\% \pm 7.44\%$	$-5.6\% \pm 4.92\%$
CR Small	$34.59\% \pm 1.25\%$	$0.011\% \pm 7.23\%$	$0.0021\% \pm 7.59\%$	$0.2\% \pm 5.22\%$
SB Large	$33.16\% \pm 1.18\%$	$-4.13\% \pm 6.88\%$	$-5.57\% \pm 7.17\%$	$24.0\% \pm 6.46\%$
SB Small	$32.41\% \pm 1.13\%$	$-6.31\% \pm 6.67\%$	$-9.35\% \pm 6.88\%$	$53.41\% \pm 7.99\%$
SB High	$35.89\% \pm 1.31\%$	$3.76\% \pm 7.54\%$	$4.91\% \pm 7.96\%$	$-18.7\% \pm 4.24\%$

Table F.23: Variation in Prediction in $3b$ SR region.

ThreeTag	Prediction	Diff	QCD	ttbar
Nominal	$781.42\% \pm 12.14\%$	$0.00026\% \pm 3.11\%$	$-8.8e-05\% \pm 3.41\%$	$-0.0055\% \pm 5.17\%$
CR High	$779.1\% \pm 12.11\%$	$-0.3\% \pm 3.1\%$	$-0.2\% \pm 3.4\%$	$-1.14\% \pm 5.11\%$
CR Low	$785.83\% \pm 12.2\%$	$0.56\% \pm 3.12\%$	$0.49\% \pm 3.42\%$	$1.23\% \pm 5.24\%$
CR Small	$781.42\% \pm 12.14\%$	$0.00026\% \pm 3.11\%$	$-8.8e-05\% \pm 3.41\%$	$-0.0055\% \pm 5.17\%$
SB Large	$775.03\% \pm 11.97\%$	$-0.82\% \pm 3.07\%$	$-1.45\% \pm 3.36\%$	$4.79\% \pm 5.42\%$
SB Small	$788.53\% \pm 12.24\%$	$0.91\% \pm 3.13\%$	$0.75\% \pm 3.43\%$	$2.32\% \pm 5.29\%$
SB High	$789.26\% \pm 12.27\%$	$1.0\% \pm 3.14\%$	$1.26\% \pm 3.45\%$	$-1.31\% \pm 5.11\%$

Besides the normalization, the variation of QCD shape in SR is also tested, as shown in Figure F.8 and Figure F.9. There are very small variations in terms of QCD shape, and such variation is within

Table F.24: Variation in Prediction in $2bs$ SR region.

TwoTag split	Prediction	Diff	<u>QCD</u>	ttbar
Nominal	$4251.96\% \pm 27.77\%$	$-1.4e-05\% \pm 1.31\%$	$-8.2e-05\% \pm 0.98\%$	$-0.00014\% \pm 5.18\%$
CR High	$4240.62\% \pm 27.72\%$	$-0.27\% \pm 1.3\%$	$-0.31\% \pm 0.98\%$	$-0.079\% \pm 5.18\%$
CR Low	$4255.74\% \pm 27.91\%$	$0.089\% \pm 1.31\%$	$-0.091\% \pm 0.98\%$	$0.8\% \pm 5.22\%$
CR Small	$4251.96\% \pm 27.77\%$	$-1.4e-05\% \pm 1.31\%$	$-8.2e-05\% \pm 0.98\%$	$-0.00014\% \pm 5.18\%$
SB Large	$4253.81\% \pm 27.43\%$	$0.044\% \pm 1.3\%$	$0.6\% \pm 0.99\%$	$-2.16\% \pm 5.07\%$
SB Small	$4253.77\% \pm 28.0\%$	$0.043\% \pm 1.31\%$	$-0.31\% \pm 0.98\%$	$1.44\% \pm 5.25\%$
SB High	$4271.53\% \pm 27.43\%$	$0.46\% \pm 1.3\%$	$1.21\% \pm 0.99\%$	$-2.51\% \pm 5.05\%$

QCD shape uncertainty derived from nominal CR.

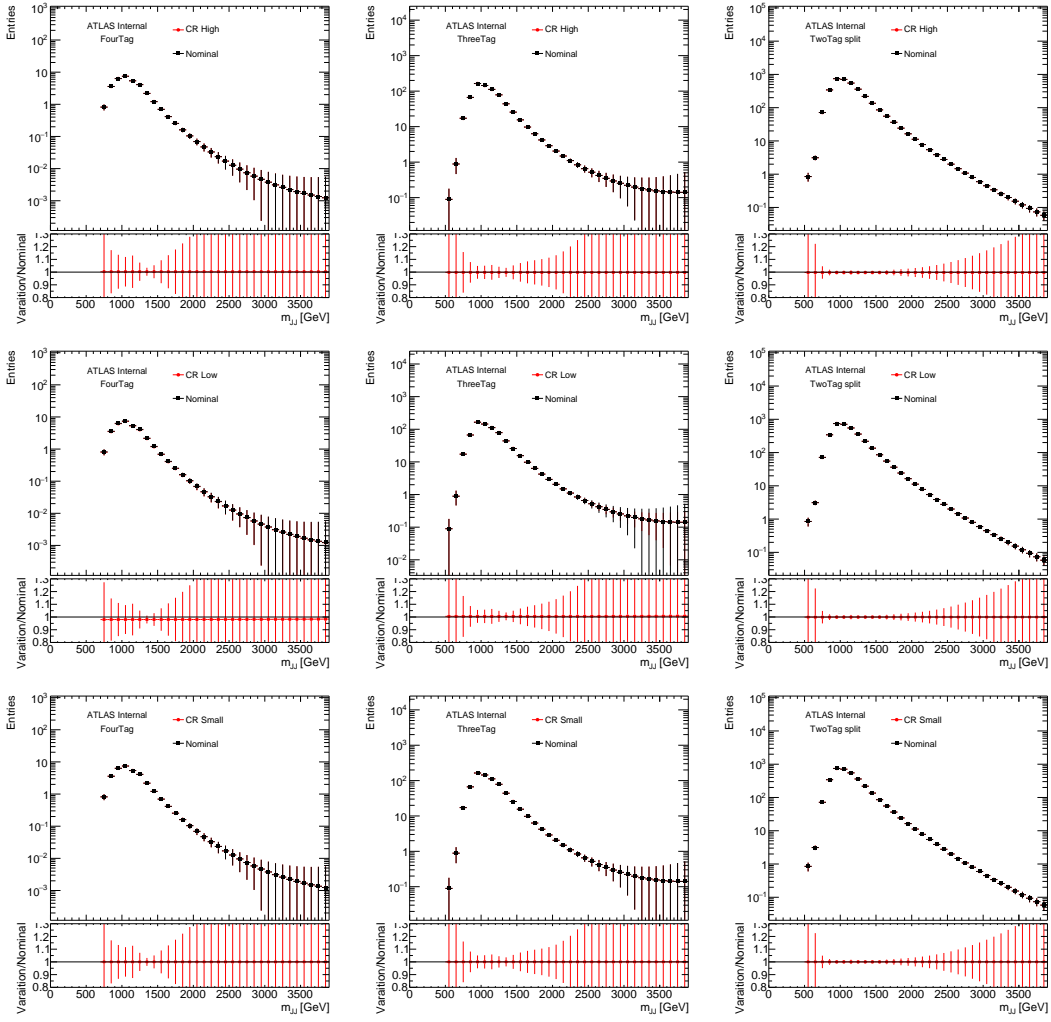


Figure F.8: Comparisons of the nominal QCD shape prediction (black) with the results of control and sideband region variations (red). The ratio of the shape from each variation to the nominal shape is shown in the lower panel. The left column shows the relevant distributions for the 4 b signal region, the middle column is for the 3 b signal region, and the left column is for the 2 b signal region. The top row is for high CR variation, the middle row is for the low CR variation, and the bottom row is for the small CR variation.

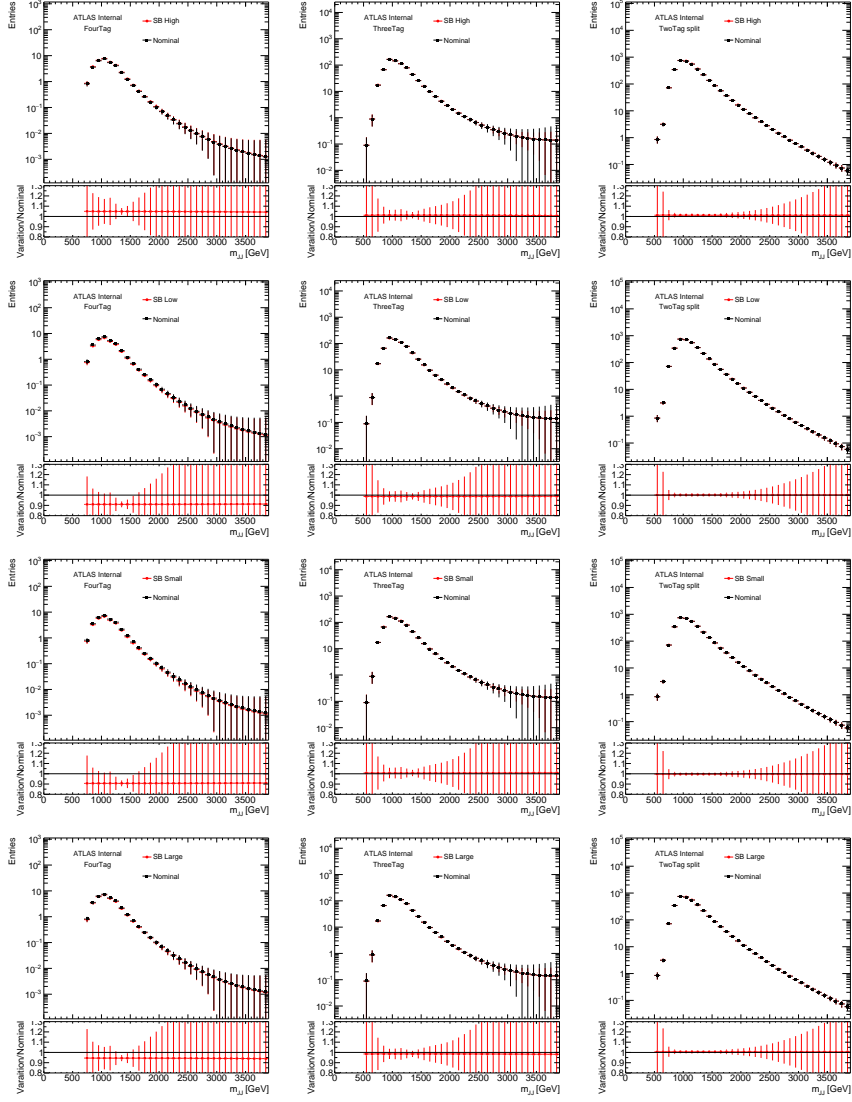


Figure F.9: Comparisons of the nominal QCD shape prediction (black) with the results of control and sideband region variations (red). The ratio of the shape from each variation to the nominal shape is shown in the lower panel. The left column shows the relevant distributions for the $4b$ signal region, the middle column is for the $3b$ signal region, and the right column is for the $2bs$ signal region. The top row is for high SB variation, the second row is for the low SB variation, the third row is for the small SB variation and the large raw is for the large SB variation.

References

- [1] C. Patrignani et al. Review of Particle Physics. *Chin. Phys.*, C40(10):100001, 2016. doi: 10.1088/1674-1137/40/10/100001.
- [2] W.J. Stirling. 7/8 and 13/8 TeV LHC luminosity ratios. 2013. URL http://www.hep.physics.ac.uk/~wstirlin/plots/lhclumi7813_2013_v0.pdf.
- [3] Lyndon Evans. The Large Hadron Collider. *Annual Review of Nuclear and Particle Science*, 61(1):435–466, 2011. doi: 10.1146/annurev-nucl-102010-130438.
- [4] ATLAS Collaboration. ATLAS Luminosity Public Results, Run 2. 2015. URL <https://twiki.cern.ch/twiki/bin/view/AtlasPublic/LuminosityPublicResultsRun2>.
- [5] ATLAS Collaboration. Jet mass reconstruction with the ATLAS Detector in early Run 2 data. ATLAS-CONF-2016-035, 2016. URL <https://cds.cern.ch/record/2200211>.
- [6] ATLAS Collaboration. Optimisation of the ATLAS b -tagging performance for the 2016 LHC Run. *ATL-PHYS-PUB-2016-012*, (ATL-PHYS-PUB-2016-012), Jun 2016. URL <https://cds.cern.ch/record/2160731>.
- [7] ATLAS Collaboration. Search for pair production of Higgs bosons in the $b\bar{b}b\bar{b}$ final state using proton–proton collisions at $\sqrt{s} = 13$ TeV with the ATLAS detector. *Phys. Rev. D*, 94: 052002, 2016. doi: 10.1103/PhysRevD.94.052002.
- [8] David Griffiths. *Introduction to elementary particles*. 2008.
- [9] Christopher G. Tully. *Elementary particle physics in a nutshell*. 2011.
- [10] Matthew D. Schwartz. *Quantum Field Theory and the Standard Model*. Cambridge University Press, 2014. ISBN 1107034736, 9781107034730.
- [11] ATLAS Collaboration. Observation of a new particle in the search for the Standard Model Higgs boson with the ATLAS detector at the LHC. *Phys. Lett. B*, 716:1, 2012. doi: 10.1016/j.physletb.2012.08.020.

- [12] CMS Collaboration. Observation of a new boson at a mass of 125 GeV with the CMS experiment at the LHC. *Phys. Lett. B*, 716:30, 2012. doi: [10.1016/j.physletb.2012.08.021](https://doi.org/10.1016/j.physletb.2012.08.021).
- [13] R. Frederix, S. Frixione, V. Hirschi, F. Maltoni, O. Mattelaer, P. Torrielli, E. Vryonidou, and M. Zaro. Higgs pair production at the LHC with NLO and parton-shower effects. *Phys. Lett.*, B732:142–149, 2014. doi: [10.1016/j.physletb.2014.03.026](https://doi.org/10.1016/j.physletb.2014.03.026).
- [14] D. de Florian et al. Handbook of LHC Higgs Cross Sections: 4. Deciphering the Nature of the Higgs Sector. 2016. doi: [10.23731/CYRM-2017-002](https://doi.org/10.23731/CYRM-2017-002).
- [15] R. Gröber and M. Mühlleitner. Composite Higgs boson pair production at the LHC. *JHEP*, 06:020, 2011. doi: [10.1007/JHEP06\(2011\)020](https://doi.org/10.1007/JHEP06(2011)020).
- [16] Roberto Contino et al. Anomalous couplings in double Higgs production. *JHEP*, 08:154, 2012. doi: [10.1007/JHEP08\(2012\)154](https://doi.org/10.1007/JHEP08(2012)154).
- [17] Graham D. Kribs and Adam Martin. Enhanced di-higgs production through light colored scalars. *Phys. Rev. D*, 86:095023, 2012. doi: [10.1103/PhysRevD.86.095023](https://doi.org/10.1103/PhysRevD.86.095023).
- [18] Graham D. Kribs, Andreas Maier, Heidi Rzehak, Michael Spannowsky, and Philip Waite. Electroweak oblique parameters as a probe of the trilinear Higgs boson self-interaction. *Phys. Rev.*, D95(9):093004, 2017. doi: [10.1103/PhysRevD.95.093004](https://doi.org/10.1103/PhysRevD.95.093004).
- [19] T. D. Lee. A theory of spontaneous t violation. *Phys. Rev. D*, 8:1226–1239, Aug 1973. doi: [10.1103/PhysRevD.8.1226](https://doi.org/10.1103/PhysRevD.8.1226).
- [20] G.C. Branco et al. Theory and phenomenology of two-Higgs-doublet models. *Phys. Rept.*, 516:1, 2012. doi: [10.1016/j.physrep.2012.02.002](https://doi.org/10.1016/j.physrep.2012.02.002).
- [21] Kaustubh Agashe, Hooman Davoudiasl, Gilad Perez, and Amarjit Soni. Warped gravitons at the CERN LHC and beyond. *Phys. Rev. D*, 76:036006, 2007. doi: [10.1103/PhysRevD.76.036006](https://doi.org/10.1103/PhysRevD.76.036006).
- [22] Liam Fitzpatrick, Jared Kaplan, Lisa Randall, and Lian-Tao Wang. Searching for the Kaluza-Klein graviton in bulk RS models. *JHEP*, 09:013, 2007. doi: [10.1088/1126-6708/2007/09/013](https://doi.org/10.1088/1126-6708/2007/09/013).
- [23] Viviana Cavaliere and Gabriel Facini. Summary of Limits on BSM Models from Diboson Searches. Technical Report ATL-COM-PHYS-2016-1071, CERN, Geneva, Sep 2016. URL <https://cds.cern.ch/record/2203605>.

- [24] ATLAS Collaboration. Search for Higgs boson pair production in the $b\bar{b}b\bar{b}$ final state from pp collisions at $\sqrt{s} = 8$ TeV with the ATLAS detector. *Eur. Phys. J. C*, 75:412, 2015. doi: 10.1140/epjc/s10052-015-3628-x.
- [25] ATLAS Collaboration. Search for Higgs Boson Pair Production in the $\gamma\gamma b\bar{b}$ Final State Using pp Collision Data at $\sqrt{s} = 8$ TeV from the ATLAS Detector. *Phys. Rev. Lett.*, 114:081802, 2015. doi: 10.1103/PhysRevLett.114.081802.
- [26] Georges Aad et al. Searches for Higgs boson pair production in the $hh \rightarrow b\bar{b}\tau\tau, \gamma\gamma WW^*, \gamma\gamma bb, bbbb$ channels with the ATLAS detector. *Phys. Rev.*, D92:092004, 2015. doi: 10.1103/PhysRevD.92.092004.
- [27] Lyndon R Evans and Philip Bryant. LHC Machine. *J. Instrum.*, 3:So8001. 164 p, 2008. URL <https://cds.cern.ch/record/1129806>. This report is an abridged version of the LHC Design Report (CERN-2004-003).
- [28] ATLAS Collaboration. The ATLAS experiment at the CERN Large Hadron Collider. *JINST*, 3:So8003, 2008. doi: 10.1088/1748-0221/3/08/So8003.
- [29] CMS Collaboration. The CMS experiment at the CERN LHC. *Journal of Instrumentation*, 3(08):So8004, 2008. URL <http://stacks.iop.org/1748-0221/3/i=08/a=So8004>.
- [30] LHCb Collaoration. The LHCb Detector at the LHC. *JINST*, 3:So8005, 2008. doi: 10.1088/1748-0221/3/08/So8005.
- [31] ALICE Collaboration. The ALICE experiment at the CERN LHC. *Journal of Instrumentation*, 3(08):So8002, 2008. URL <http://stacks.iop.org/1748-0221/3/i=08/a=So8002>.
- [32] ATLAS Collaboration. Luminosity Determination in pp Collisions at $\sqrt{s} = 7$ TeV Using the ATLAS Detector at the LHC. *Eur. Phys. J.*, C 71:1630, 2011. doi: 10.1140/epjc/s10052-011-1630-5.
- [33] Paul Collier for the LHC team. LHC Machine Status. CERN Resource Review Board, 2015. URL <https://cds.cern.ch/record/2063924/files/CERN-RRB-2015-119.PDF>.
- [34] Giulia Papotti for the LHC team. LHC Machine Status Report. CERN Resource Review Board, 2016. URL https://indico.cern.ch/event/563488/contributions/2277292/attachments/1340292/2019570/20160921_LHCC.pdf.

- [35] ATLAS Collaboration. The ATLAS Experiment at the CERN Large Hadron Collider. *JINST*, 3:S08003, 2008. doi: 10.1088/1748-0221/3/08/S08003.
- [36] ATLAS Collaboration. ATLAS Insertable B-Layer Technical Design Report. CERN-LHCC-2010-013. ATLAS-TDR-19, Sep 2010. URL <https://cds.cern.ch/record/1291633>.
- [37] ATLAS Collaboration. Expected performance of the ATLAS b -tagging algorithms in Run-2. ATL-PHYS-PUB-2015-022, 2015. URL <https://cds.cern.ch/record/2037697>.
- [38] Morad Aaboud et al. Study of the material of the ATLAS inner detector for Run 2 of the LHC. *JINST*, 12(12):P12009, 2017. doi: 10.1088/1748-0221/12/12/P12009.
- [39] ATLAS Collaboration. Performance of the ATLAS Trigger System in 2015. *Eur. Phys. J. C*, 77:317, 2017. doi: 10.1140/epjc/s10052-017-4852-3.
- [40] M. Aaboud et al. Performance of the ATLAS Track Reconstruction Algorithms in Dense Environments in LHC Run 2. *Eur. Phys. J.*, C77(10):673, 2017. doi: 10.1140/epjc/s10052-017-5225-7.
- [41] ATLAS Collaboration. Topological cell clustering in the ATLAS calorimeters and its performance in LHC Run 1. *Eur. Phys. J. C*, 77:490, 2017. doi: 10.1140/epjc/s10052-017-5004-5.
- [42] Matteo Cacciari, Gavin P. Salam, and Gregory Soyez. The Anti- $k(t)$ jet clustering algorithm. *JHEP*, 04:063, 2008. doi: 10.1088/1126-6708/2008/04/063.
- [43] Matteo Cacciari, Gavin P. Salam, and Gregory Soyez. The catchment area of jets. *JHEP*, 04:005, 2008. doi: 10.1088/JHEP04(2008)05.
- [44] ATLAS Collaboration. Jet energy measurement with the ATLAS detector in proton-proton collisions at $\sqrt{s} = 7$ TeV. *Eur. Phys. J. C*, 73:2304, 2013. doi: 10.1140/epjc/s10052-013-2304-2.
- [45] ATLAS Collaboration. Jet Calibration and Systematic Uncertainties for Jets Reconstructed in the ATLAS Detector at $\sqrt{s} = 13$ TeV. ATL-PHYS-PUB-2015-015, 2015. URL <https://cds.cern.ch/record/2037613>.
- [46] Performance of jet substructure techniques in early $\sqrt{s} = 13$ TeV pp collisions with the ATLAS detector. Technical Report ATLAS-CONF-2015-035, CERN, Geneva, Aug 2015. URL <http://cds.cern.ch/record/2041462>.

- [47] D. Krohn, J. Thaler, and L.-T. Wang. Jet trimming. *JHEP*, 02:084, 2010. doi: 10.1007/JHEP02(2010)084.
- [48] Stephen D. Ellis and Davison E. Soper. Successive combination jet algorithm for hadron collisions. *Phys. Rev. D*, 48:3160, 1993. doi: 10.1103/PhysRevD.48.3160.
- [49] Impact of Alternative Inputs and Grooming Methods on Large-R Jet Reconstruction in ATLAS. Technical Report ATL-PHYS-PUB-2017-020, CERN, Geneva, Dec 2017. URL <http://cds.cern.ch/record/2297485>.
- [50] ATLAS Collaboration. Performance of jet substructure techniques for large- R jets in proton–proton collisions at $\sqrt{s} = 7$ TeV using the ATLAS detector. *JHEP*, 09:076, 2013. doi: 10.1007/JHEP09(2013)076.
- [51] ATLAS Collaboration. Performance of b -jet identification in the ATLAS experiment. *JINST*, II:P04008, 2016. doi: 10.1088/1748-0221/II/04/P04008.
- [52] Electron efficiency measurements with the ATLAS detector using the 2015 LHC proton–proton collision data. Technical Report ATLAS-CONF-2016-024, CERN, Geneva, Jun 2016. URL <http://cds.cern.ch/record/2157687>.
- [53] Measurement of the tau lepton reconstruction and identification performance in the ATLAS experiment using pp collisions at $\sqrt{s} = 13$ TeV. Technical Report ATLAS-CONF-2017-029, CERN, Geneva, May 2017. URL <http://cds.cern.ch/record/2261772>.
- [54] Georges Aad et al. Muon reconstruction performance of the ATLAS detector in proton–proton collision data at $\sqrt{s} = 13$ TeV. *Eur. Phys. J.*, C76(5):292, 2016. doi: 10.1140/epjc/s10052-016-4120-y.
- [55] Torbjorn Sjostrand, Stephen Mrenna, and Peter Z. Skands. PYTHIA 6.4 physics and manual. *JHEP*, 05:026, 2006. doi: 10.1088/1126-6708/2006/05/026.
- [56] ATLAS Collaboration. Summary of ATLAS Pythia 8 tunes. 2012. URL <http://cdsweb.cern.ch/record/1474107>.
- [57] S. Agostinelli et al. GEANT4: a simulation toolkit. *Nucl. Instrum. Meth. A*, 506:250–303, 2003. doi: 10.1016/S0168-9002(03)01368-8.
- [58] ATLAS Collaboration. The ATLAS Simulation Infrastructure. *Eur. Phys. J. C*, 70:823–874, 2010. doi: 10.1140/epjc/s10052-010-1429-9.

- [59] Simone Alioli, Paolo Nason, Carlo Oleari, and Emanuele Re. A general framework for implementing NLO calculations in shower Monte Carlo programs: the POWHEG BOX. *JHEP*, 06:043, 2010. doi: [10.1007/JHEP06\(2010\)043](https://doi.org/10.1007/JHEP06(2010)043).
- [60] Peter Zeiler Skands. Tuning Monte Carlo generators: The Perugia tunes. *Phys. Rev. D*, 82: 074018, 2010. doi: [10.1103/PhysRevD.82.074018](https://doi.org/10.1103/PhysRevD.82.074018).
- [61] Michał Czakon and Alexander Mitov. Top++: A program for the calculation of the top-pair cross-section at hadron colliders. *Comput. Phys. Commun.*, 185:2930, 2014. ISSN 0010-4655. doi: [10.1016/j.cpc.2014.06.021](https://doi.org/10.1016/j.cpc.2014.06.021).
- [62] S. Dawson, S. Dittmaier, and M. Spira. Neutral Higgs boson pair production at hadron colliders: QCD corrections. *Phys. Rev. D*, 58:115012, 1998. doi: [10.1103/PhysRevD.58.115012](https://doi.org/10.1103/PhysRevD.58.115012).
- [63] T. Plehn, M. Spira, and P.M. Zerwas. Pair production of neutral Higgs particles in gluon-gluon collisions. *Nucl. Phys. B*, 479:46, 1996. doi: [10.1016/0550-3213\(96\)00418-X](https://doi.org/10.1016/0550-3213(96)00418-X). [Erratum: Nucl. Phys. B 531 (1998) 655].
- [64] S. Borowka, N. Greiner, G. Heinrich, S. P. Jones, M. Kerner, J. Schlenk, U. Schubert, and T. Zirke. Higgs boson pair production in gluon fusion at NLO with full top-quark mass dependence. *Phys. Rev. Lett.*, 117(1):012001, 2016. doi: [10.1103/PhysRevLett.117.012001](https://doi.org/10.1103/PhysRevLett.117.012001).
- [65] S. Borowka, N. Greiner, G. Heinrich, S. P. Jones, M. Kerner, J. Schlenk, and T. Zirke. Full top quark mass dependence in Higgs boson pair production at NLO. *JHEP*, 10:107, 2016. doi: [10.1007/JHEP10\(2016\)107](https://doi.org/10.1007/JHEP10(2016)107).
- [66] J. Alwall et al. The automated computation of tree-level and next-to-leading order differential cross sections, and their matching to parton shower simulations. *JHEP*, 07:079, 2014. doi: [10.1007/JHEP07\(2014\)079](https://doi.org/10.1007/JHEP07(2014)079).
- [67] Richard D. Ball et al. Parton distributions with LHC data. *Nucl. Phys. B*, 867:244, 2013. doi: [10.1016/j.nuclphysb.2012.10.003](https://doi.org/10.1016/j.nuclphysb.2012.10.003).
- [68] A. Carvalho. Gravity particles from Warped Extra Dimensions, predictions for LHC. 2017.
- [69] M. Bahr et al. Herwig++ physics and manual. *Eur. Phys. J. C*, 58:639–707, 2008. doi: [10.1140/epjc/s10052-008-0798-9](https://doi.org/10.1140/epjc/s10052-008-0798-9).

- [70] Hung-Liang Lai, Marco Guzzi, Joey Huston, Zhao Li, Pavel M. Nadolsky, Jon Pumplin, and C. P. Yuan. New parton distributions for collider physics. *Phys. Rev. D*, 82:074024, 2010. doi: [10.1103/PhysRevD.82.074024](https://doi.org/10.1103/PhysRevD.82.074024).
- [71] Pavel M. Nadolsky et al. Implications of cteq global analysis for collider observables. *Phys. Rev. D*, 78:013004, 2008. doi: [10.1103/PhysRevD.78.013004](https://doi.org/10.1103/PhysRevD.78.013004).
- [72] Michael H. Seymour and Andrzej Siodmok. Constraining MPI models using σ_{eff} and recent Tevatron and LHC Underlying Event data. *JHEP*, 10:113, 2013. doi: [10.1007/JHEP10\(2013\)113](https://doi.org/10.1007/JHEP10(2013)113).
- [73] et al Jon Butterworth. Pdf4lhc recommendations for lhc run ii. *Journal of Physics G: Nuclear and Particle Physics*, 43(2):023001, 2016.
- [74] ATLAS Collaboration. Luminosity determination in pp collisions at $\sqrt{s} = 8$ TeV using the ATLAS detector at the LHC. *Eur. Phys. J. C*, 76(653), 2016. doi: [10.1140/epjc/s10052-016-4466-1](https://doi.org/10.1140/epjc/s10052-016-4466-1).
- [75] ATLAS Collaboration. Jet mass and substructure of inclusive jets in $\sqrt{s} = 7$ tev pp collisions with the atlas experiment. *JHEP*, 05:128, 2012. doi: [10.1007/JHEP05\(2012\)128](https://doi.org/10.1007/JHEP05(2012)128).
- [76] ATLAS Collaboration. Observation of a new particle in the search for the Standard Model Higgs boson with the ATLAS detector at the LHC. *Phys. Lett. B*, 716:1, 2012. doi: [10.1016/j.physletb.2012.08.020](https://doi.org/10.1016/j.physletb.2012.08.020).
- [77] Glen Cowan, Kyle Cranmer, Eilam Gross, and Ofer Vitells. Asymptotic formulae for likelihood-based tests of new physics. *Eur. Phys. J. C*, 71:1554, 2011. doi: [10.1140/epjc/s10052-011-1554-0](https://doi.org/10.1140/epjc/s10052-011-1554-0).
- [78] Alexander L. Read. Presentation of search results: The CL_s technique. *J. Phys. G*, 28:2693, 2002. doi: [10.1088/0954-3899/28/10/313](https://doi.org/10.1088/0954-3899/28/10/313).
- [79] Burton Richter. High Energy Colliding Beams; What Is Their Future? *Rev. Accel. Sci. Tech.*, 7:1–8, 2014. doi: [10.1142/9789814651493_0001](https://doi.org/10.1142/9789814651493_0001), [10.1142/S1793626814300011](https://doi.org/10.1142/S1793626814300011).
- [80] Stephen Hawking and Gordon Kane. Should China build the Great Collider? 2018.